GRAN SASSO SCIENCE INSTITUTE

DOCTORAL THESIS

Low-frequency sensitivity limitations in current and future gravitational-wave detectors

Author:
Tomislav ANDRIC

Supervisor:
prof. Jan HARMS

A thesis submitted in fulfillment of the requirements for the degree of Doctor of Philosophy

in the

Astroparticle Physics

November 2, 2022

Abstract

Gran Sasso Science Institute
Astroparticle Physics
GSSI Gravity Group

Doctor of Philosophy

Low-frequency sensitivity limitations in current and future gravitational-wave detectors

by Tomislav ANDRIC

Seismic Newtonian noise and controls and sensing noises are the big challenges to extend the observation of terrestrial gravitational wave detectors towards lower frequencies. Improving low-frequency sensitivity is challenging but with high rewards. The motivation to improve the low-frequency sensitivity of the observatories is: to enable the deepest multi-messenger studies of binary neutron-star mergers, study the properties of gravitational wave sources with unprecedented precision, observe black-hole binaries with masses beyond the currently accessible mass range.

In the thesis, SPECFEM3D's, which is a state-of-the-art finite-element simulation software for seismic fields, capabilities to provide estimates of gravitoelastic correlations, which are required for an optimized deployment of seismometers for gravity noise cancelation, are demonstrated. The model on which simulations are run takes into account the local topography at a candidate site of the Einstein Telescope at Sardinia. The work in this thesis provides the first extensive and conclusive study of the impact of topographic scattering on seismic coherence and on the prediction of gravitational coupling between seismic surface displacement and an underground test mass. I found that A3-topography has generally a significant impact on seismic and gravitoelastic correlations. Topography scatters out energy from Rayleigh waves above 4 Hz protecting the test mass from the influence of distant seismic sources. As expected, symmetries of the field of gravitoelastic correlations are broken by topography leading to unique solutions of optimal seismometer placement for gravity-noise cancellation. All pieces together for a Bayesian seismic-array design for Newtonian noise cancelation are outlined.

Another topic elaborated in this thesis is the Angular Sensing and Control system, which suppresses the residual angular motion of suspended test masses. Since during the O3 run the LIGO noise budget was dominated by the angular sensing and controls noise approximately between 10 Hz and 25 Hz, it is crucial to mitigate this noise in order to achieve sensitivity improvements. The Lightsaber, an Angular Sensing and Control system time-domain simulator is presented. The Lightsaber is implemented for LIGO Hanford and for the Input Mode Cleaner (IMC) at the Caltech 40m prototype. The main mechanical degree of freedom simulated in Lightsaber is the pitch motion of the test masses, which introduces the dominant angular noise in gravitational wave measurements. The Lightsaber's plant model is constructed from several static second-order section models representing the mechanical and feedback system together with several nonlinear optomechanical couplings. LIGO-Lightsaber has the linear feedback filters implemented in a global basis as used at LIGO Hanford Observatory during the O3 run.

The mechanical system is simulated in its local degrees of freedom. There is the feed-forward radiation pressure compensation implemented. Lightsaber-IMC is the simulation of the Angular Sensing and Control system of the triangular cavity of the IMC at the Caltech 40m prototype. The main feedback control filters are implemented in a sensing basis. Apart from that, all other filters are in the local basis. For Lightsaber-IMC I did the calibration, obtained input noises, and did comparisons with the real system. I made Simulink block diagrams for both Lightsaber implementations. The Lightsaber is sufficiently accurate to serve, at least, as a useful modeling tool especially when high precision is not required, *i.e.*, for noise budget calculations of current and future gravitational wave detectors. It is possible to modify the mechanical system, angular readouts, etc to represent other detectors. So, the Lightsaber is a more universal simulation tool, and it finds applications in more than one plant model. The Angular Sensing and Control system is a complex component of the detector, which has proven to be difficult to model. The Lightsaber, being a fully nonlinear, time-domain representation, allows researchers to test novel feedback-filter designs before implementation in a detector. This can be especially valuable for certain nonstationary and nonlinear modern control schemes, such as Reinforcement Learning. The Reinforcement Learning based controller can overcome the abilities of the optimal linear filter. What I obtained using Reinforcement Learning is the reduction of the pitch angular motion of 6–8 times in 15–20 Hz frequency band, with respect to the linear controller. First tests at the Caltech 40m prototype with the IMC control successfully demonstrated the use of Reinforcement Learning in interferometer control. The control algorithms were trained with Lightsaber-IMC. The Angular Sensing and Control system remains one of the major challenges of detector control, which needs to be addressed to be able to improve the low-frequency sensitivity of current detectors, and a detailed understanding of noise produced by this system is crucial to plan future generations of gravitational wave detectors.

Acknowledgements

I am indebted to my advisor, professor Jan Harms, for years of patient guidance throughout my studies. I am deeply impressed by the detailed suggestions and comments from Jan during our discussions, which helped me tremendously in my research on gravitational waves detectors. Jan is one of the most genius people I have met, and the conversations with him have been a valuable source of inspiration to me. He was always supportive and optimistic about my work. Without his vision and support, this thesis would never have happened. Thank you, Jan for being a role model on how to approach scientific work.

I also thank Jan for giving me the opportunity to gain experience abroad. During my time at Caltech, I learned many new things. Many people there left a life-long impression on me. Special thanks to brilliant Yuta Michimura, Anchal Gupta, and Francisco Salces-Carcoba for enthusiasm, inspiration, help, and support. Many thanks to Hang Yu and Rana Adhikari for their support, providing most of the information about the LIGO Hanford detector, which is used for the construction of the angular controls model. Many thanks to Christopher Wipf for the useful comments on Lightsaber and for the help with Simulink models. I also thank Jonas Buchli (and others from the computer science team) for their help with Machine Learning and Jenne Driggers for her help with sensing and controls systems. I thank the Sardinia site study team for useful discussions and suggestions for the first paper.

I owe special, tremendous thanks to my computer science colleague and friend, genius Alex Coto. Thank you for enlightening me with your computer science wisdom, for your patience, encouragement, optimism, and support. Thanks to Soumen and Matteo for the company during our Sardinia trips.

Many thanks to my flatmates. Thank you for supporting and encouraging me. Also, thank you for feeding me delicious Italian and Indian food. Thanks to my fellow graduate students and GSSI GW group for many dinners, drinks, and chats. I wouldn't have made it all this way if it weren't for my family, friends, and girlfriend who were making me feel completely comfortable pursuing my interests, including those in science. Most of all, I am grateful to my parents for their unwavering support throughout my entire life. I am proud to share all this with you.

This material is based upon work supported by NSF's LIGO Laboratory, which is a major facility fully funded by the National Science Foundation. The work was also supported by the GSSI's Centre for Urban Informatics and Modelling (CUIM) project. SPECFEM3D is maintained by the Computational Infrastructure for Geodynamics, which is funded by the National Science Foundation under Awards EAR-0949446 and EAR-1550901. The work was supported by the PRIN project Characterization of the Sos Enattos mine in Sardinia as the site for the Einstein Telescope GW observatory. I acknowledge the usage of the high-performance cluster at CNAF, the central computing facility of INFN at Bologna. I also acknowledge the usage of the GPU cluster at LNGS. I'm grateful for the continuous support I received from both clusters' staff.

Contents

List of Figures

List of Tables

List of Abbreviations

GW	**G**ravitational **w**ave
IFO	**I**nter**fe**r**o**meter
ET	**E**instein **T**elescope
CE	**C**osmic **E**xplorer
TM	**T**est **m**ass
BH	**B**lack **h**ole
NS	**N**eutron **s**tar
NN	**N**ewtonian **n**oise
ASC	**A**ngular **S**ensing (and) **C**ontrol
RL	**R**einforcement **L**earning
GR	**G**eneral **R**elativity
EM	**e**lectro**m**agnetic
TT	**t**ransverse-**t**raceless
AS	**a**nti**s**ymmetric
FPC	**F**abry-**P**erot **c**avity
BS	**B**eam**s**plitter
ITM	**I**nput **TM**
ETM	**E**nd **TM**
ETMX	**X**-arm **ETM**
ETMY	**Y**-arm **ETM**
ITMX	**X**-arm **ITM**
ITMY	**Y**-arm **ITM**
PRC	**P**ower **r**ecycling **c**avity
O3	Third Observing Run
SRC	**S**ignal **r**ecycling **c**avity
IMC	**I**nput **m**ode **c**leaner
OMC	**O**utput **m**ode **c**leaner
DARM	**D**ifferential **arm**
DOF	**D**egree **o**f **f**reedom
PD	**p**hoto**d**iode
SNR	**s**ignal-(to)-**n**oise **r**atio
LISA	**L**aser **I**nterferometer **S**pace **A**ntenna
LGWA	**L**unar **G**ravitational **W**ave **A**ntenna
ELGAR	**E**uropean **L**aboratory (for) **G**ravitational (wave and) **A**tom-interferometry **R**esearch
TOBA	**T**orsion **B**ar **A**ntenna
SOGRO	**S**uperconducting **O**mni-directional **G**ravitational **R**adiation **O**bservatory
RF	**R**adio **F**requency
RP	**R**adiation **p**ressure
RPN	**RP n**oise
PSD	**p**ower-**s**pectral **d**ensity
SQL	**S**tandard **Q**uantum **L**imit
DAC	**D**igital-to-**A**nalog **C**onverter

IMBH	**i**ntermediate **m**ass **BH**
SEM	**s**pectral-**e**lement **m**ethod
NLNM	**N**ew **L**ow **N**oise **M**odel
RMS	**r**oot **m**ean **s**quare
CPML	**c**onvolutional **p**erfectly **m**atched **l**ayers
CPSD	**C**ross **PSD**
GPR	**G**aussian **P**rocess **R**egression
LHO	**L**IGO **H**anford **O**bservatory
QUAD	**Quad**ruple pendulum stage
tf	**t**ransfer **f**unction
PUM	**P**en**u**ltimate **m**ass
ISI	**I**nternal **S**eismic **I**solation
SOS	**s**econd-**o**rder **s**ection
RPC	**RP c**ompensation
ZPK	**z**ero-**p**ole-**g**ain
HEPI	**H**ydraulic **E**xternal **P**re-**I**solator
BSC-ISI	**B**asic **S**ymmetric **C**hambers-**ISI**
HAM-ISI	**H**orizontal **A**ccess **M**odule-**ISI**
TOP	**To**p **m**ass
UIM	**U**pper-**i**ntermediate **m**ass
OSEM	**O**ptical **S**ensors (and) **E**lectro-**M**agnetic (actuator)
LED	**L**ight-**E**mitting **D**iode
UGF	**U**nity **g**ain **f**requency
QPD	**Q**uadrant **PD**
WFS	**W**ave**f**ront **s**ensor
OLTF	**o**pen-**l**oop **tf**
RIN	**R**elative **i**ntensity **n**oise
RTCDS	**R**eal-**t**ime **C**ontrols (and) **D**iagnostic **S**ystem
MCx	I**MC** mirror
ASD	**a**mplitude-**s**pectral **d**ensity
PSL	**P**re-**s**tabilized **L**aser
ADC	**A**nalog-to-**D**igital **C**onverter
OPLEV	**Op**tical **Lev**er
MEDM	**M**otif **E**ditor (and) **D**isplay **M**anager
ML	**M**achine **L**earning
MDP	**M**arkov **D**ecision **P**rocess
MPO	**M**aximum (a-posteriori) **P**olicy **O**ptimisation
DMPO	**D**istributional **MPO**
MLP	**m**ulti**l**ayered **p**erceptrons
ELU	**E**xponential **L**inear **U**nit

Physical and Mathematical Constants

Speed of Light	$c = 2.997\,924\,58 \times 10^{8}\,\mathrm{m\,s^{-1}}$
Newton's gravitational constant	$G = 6.674\,30 \times 10^{-11}\,\mathrm{m^{3}kg^{-1}s^{-2}}$
pi	$\pi = 3.141\,592\,653\,59$
Solar mass	$\mathrm{M}_{\odot} = 1.989 \times 10^{30}\,\mathrm{kg}$
Boltzmann's constant	$k_B = 1.380\,649 \times 10^{-23}\,\mathrm{m^{2}kgs^{-2}K^{-1}}$
Planck's constant	$h_p = 6.626\,070\,15 \times 10^{-34}\,\mathrm{m^{2}kgs^{-1}}$
Reduced Planck's constant	$\hbar_p = 1.054\,571\,82 \times 10^{-34}\,\mathrm{m^{2}kgs^{-1}}$
Adiabatic ratio (for a diatomic gas)	$\gamma = 1.4$

List of Symbols / Glossary

$\mathbf{R}_{\nu\rho}$	Ricci curvature tensor
R	scalar curvature
$\mathbf{g}_{\mu\nu}$	spacetime metric tensor
$\mathbf{T}_{\mu\nu}$	stress-energy tensor
$\boldsymbol{\eta}_{\mu\nu}$	flat spacetime Minkowski metric
$\mathbf{h}_{\mu\nu}$	spacetime perturbation / deviation from flatness
h_+, $h_\times$	GW polarizations
ω_{GW}	GW angular frequency
L	length
$\Delta L(t)$	lenght change
h	strain
F	finesse
P_{AS}	light power incident at the photodetector
P_{BS}	light power at BS
ϕ_0	dark-fringe offset
$\Delta\phi$	phase difference
$S_{\mathrm{PD}}^{\mathrm{SN}}$	shot noise's PSD
$S_{\Delta L}^{\mathrm{SN}}$	PSD of DARM length due to shot noise
$S_{\Delta L}^{\mathrm{RPN}}$	PSD of DARM length due to RPN
P_{PD}	mean power on the photodiode
ω_c	carrier angular frequency of the light
P_t	total power in both IFO arms
ω	angular frequency
ρ	density of the surrounding ground or air
$\mathbf{s}$	seismic displacement
T	temperature of the air
p	pressure of the air
Z	impedance
$\mathbf{T}$	stress tensor
$\mathbf{f}$	seismic source
$\mathbf{c}$	elastic tensor
v_{p}	compressional-wave speed
v_{s}	shear-wave speed
d_{minGLL}	minimum distance between Gauss-Lobatto-Legendre interpolation points
e_{max}	the biggest of three dimensions of the single mesh element
$\mathbf{G}$	Green's tensor
$\mathbf{I}$	identity tensor
$\mathbf{\Phi}$	ensemble forward wavefield
c_R	Rayleigh wave speed
C_{ij}	cross-correlation
c_{ij}	coherence

δa_{arm}	horizontal gravitational acceleration in the direction of arm
h_{TM}	depth of the TM
J_x	Bessel function of the first kind
τ_{RP}	RP torque
P_a	arm-cavity power
$y_{\mathrm{ITM,ETM}}$	beam-spot motion on ITM and ETM
$\tau_{S,H}$	torques of soft and hard mode
L_a	arm-cavity length
$R_{\mathrm{ITM,ETM}}$	radius of curvature of ITM and ETM
τ_p	restoring torque of the TM suspension
I	moment of inertia
$\theta_{ITM,ETM}$	pitch angular motion of ITM and ETM
$\theta_{S,H}$	pitch angular motion of soft and hard mode
ΔL_a	arm-cavity length change
P_i	input power
τ_{ITM}	transmissivity of ITM
ρ_{ITM}	reflectivity of ITM
λ	wavelength
M_m	mirror's mass
R_m	mirror's radius
L_m	mirror's thickness
Q	quality factor
ω_{0p}	free pitch angular resonance frequency
y_{MCx}	beam-spot motion on MCx
R_{MC2}	radius of curvature of MC2
L_{IMC}	longer side of the isosceles triangular IMC
d_{IMC}	half of the shorter side of the isosceles triangular IMC
θ_{MCx}	pitch angular motion of MCx
P_{IMC}	IMC cavity power
τ_{MC1}	transmissivity of MC1
ρ_{MCx}	reflectivity of MCx
ΔL_{IMC}	IMC cavity length change

Dedicated to my mother to whom stupidity of patriarchal society didn't allow to go to university.

Introduction

Gravitational waves (GWs) are dynamic strains, disturbances in the curvature of space-time that travel at the speed of light, generated by the non-axisymmetric acceleration of masses, and propagate as waves outward from their source. They proved to be a great window for new research in physics, astronomy, and astrophysics. For detection of the gravitational waves, there are a handful of kilometer-scale, ground-based, laser interferometers (IFOs) of the current generation including Virgo (Acernese et al., 2015), LIGO (Abbott et al., 2016a), KAGRA (Akutsu et al., 2019), and soon LIGO India (Souradeep, 2016). The idea is that through alternating data-taking runs with detector improvements they reach or approach their design sensitivities. They have already demonstrated the effectiveness of the working principle. They are all enhanced Michelson interferometers with super-stabilized lasers operating at 1064 nm. The next generation has also been proposed including Einstein Telescope (ET) (ET Science Team, 2011), Voyager (Adhikari et al., 2020), and Cosmic Explorer (CE) (Reitze et al., 2019). Optics inside of the interferometers, the purest that exist, are housed in enormous vacuum systems and suspended by unprecedented seismic isolation systems (*Look Deeper*). Despite that, they suffer from a big variety of noises (Abbott et al., 2020a). Test masses (TMs) measure the gravitational field distortions due to gravitational waves through the use of coherent light. There is a strong scientific drive to improve the low-frequency sensitivity of the observatories: observing black-hole (BH) binaries with masses beyond the currently accessible mass range, enabling the deepest multi-messenger studies of binary neutron-star (NS) mergers, studying the properties of GWs sources with unprecedented precision (Maggiore et al., 2020; Chan et al., 2018; Sathyaprakash et al., 2012; Abbott et al., 2020; Jani, Shoemaker, and Cutler, 2019).

In chapter 1 I will give you a brief overview of gravitational waves, detectors, and the limiting noises. In the chapter 2 I will demonstrate SPECFEM3D's, which is a state-of-the-art finite-element simulation software for seismic fields, capabilities to provide estimates of gravitoelastic correlations, which are required for an optimized deployment of seismometers arrays for the seismic Newtonian noise (NN) cancelation. I will show you the effects of the topography at the Sardinian candidate site of ET on gravitoelastic correlations. Also, I will give you an interesting starting point to develop the future NN cancellation system for ET. In chapter 3 I will present to you the Lightsaber, a new time-domain simulator of the Angular Sensing and Control (ASC) system for GW detectors. The Lightsaber, being the fully nonlinear, time-domain representation, allows researchers to test ASC controllers before implementing them in a detector. This is especially beneficial for certain nonstationary and nonlinear modern control schemes. So, in chapter 4 I will show you the work on the nonlinear ASC controller based on Reinforcement Learning (RL) to overcome the abilities of the optimal linear filter. The RL control needs to meet the requirements on both the cutoff of high-frequency sensing noise and the suppression of low-frequency input motion.

Chapter 1

Gravitational radiation, its detection, and limiting noises

In this chapter, section 1.1 describes the concept of GWs and the spacetime strain. Also, it describes sources and classes of GWs. Section 1.2 discusses GWs' detectors. Section 1.3 gives a brief overview of the noises limiting the detectors' sensitivity.

1.1 Gravitational Waves

Albert Einstein was the first one to get the right concept about GWs, but he was not the first one to conceive them. Einstein's work was preceded by the work of numerous scientists (Rothman, 2018). From today's perspective, the theory of gravitation started with Newton and it ended with Einstein's General Relativity (GR) in 1916. Despite the introduction of a number of alternative theories, GR continues to be the simplest theory consistent with experimental data. Widely acknowledged as a theory of extraordinary beauty, GR has often been described as the most beautiful of all existing physical theories (Landau and Lifshitz, 1975). GR generalizes special relativity and refines Newton's law of universal gravitation, providing a unified description of gravity as a geometric property of space and time or four-dimensional spacetime. GR predicts novel effects of gravity, such as gravitational waves, gravitational lensing, the precession of the perihelion of the orbits of the planet, the frequency shift of light, the effect of gravity on time known as gravitational time dilation, the existence of black holes, and other compact objects (Einstein, 2014).

The first proof of the existence of GWs came in 1974, almost 20 years after Einstein's death. In that year, Hulse and Taylor using the Arecibo Radio Observatory in Puerto Rico began measuring how the stars' orbits changed over time. After eight years of observations of the binary pulsar PSR B1913+16, 21000 light-years from Earth, they determined that the stars' orbital decay is exactly at precisely the rate predicted by GR if they were radiating GWs (Taylor and Weisberg, 1982; Hulse and Taylor, 1975; *Look Deeper*). On September 14, 2015, LIGO physically sensed the undulations in spacetime caused by GWs generated by two colliding BHs 1.3 billion light-years away (Abbott et al., 2016b; *Look Deeper*). This discovery is one of the biggest scientific achievements in human history. This was the beginning of gravitational wave astronomy and the opening of a new window of the Universe since things like colliding BHs are completely invisible to electromagnetic (EM) astronomers. Gravitational waves transport energy as gravitational radiation, a form of radiant energy similar to EM radiation, but they are very weakly obstructed by matter giving us a clear view of the gravitational-wave Universe. The waves carry

information about their origins that is free of deformations. GWs radiation brings a clean signature of the spacetime geometry and therefore is a crucial tool to understand the behavior of geometry and matter in extreme conditions of relativistic motion, temperature, density, and magnetic fields. Gravitational waves lead to new physics, astronomy, and astrophysics to examine the universe in complement to the existing information such as EM radiation and particles (*LIGO why*; *LIGO what*).

1.1.1 General relativity and gravitational waves

According to GR, gravity is described as a geometric property of space and time. The theory of GR says that the observed gravitational effect between masses is a consequence of the curvature of space and time (or spacetime). One of the basic ideas of GR says that the matter and energy content of spacetime determine the metric (and the associated geometry of spacetime) (Einstein, 2014). The geometry of the spacetime is represented by solutions of Einstein's field equations (Weinberg, 1972):

$$\mathbf{R}_{\mu\nu} - \frac{1}{2}R\mathbf{g}_{\mu\nu} = \frac{8\pi G}{c^4}\mathbf{T}_{\mu\nu} \tag{1.1}$$

where the Ricci curvature tensor

$$\mathbf{R}_{\nu\rho} \overset{\text{def}}{=} \mathbf{R}^{\mu}_{\nu\mu\rho} \tag{1.2}$$

and the scalar curvature

$$R \overset{\text{def}}{=} \mathbf{g}^{\mu\nu}\mathbf{R}_{\mu\nu} \tag{1.3}$$

relate the metric (and the associated curvature tensors) to the stress-energy tensor $\mathbf{T}_{\mu\nu}$ (which measures matter content), and $\mathbf{g}_{\mu\nu}$ is the spacetime metric tensor that represents the solutions of the equations. Here, G is the gravitational constant of Newtonian gravity, and c is the speed of light from special relativity. This tensor equation is a complicated system of second-order partial differential equations for the metric components. The exact solutions to Einstein's field equations are very difficult to find. Einstein's equations are the heart of GR. They use the language of mathematics to formulate precisely the relationship between the properties of matter and spacetime geometry. They are formulated using the concepts of Riemannian geometry. The metric encodes the information needed to compute the fundamental geometric notions of distance and angle in a curved space (or spacetime) (Misner, Thorne, and Wheeler, 1973). A solution of equations 1.1 describes a particular geometry of spacetime; for example, the Schwarzschild solution describes the geometry around a spherical, non-rotating mass such as a star or a black hole (Schwarzschild, 1999), whereas the Kerr solution describes a rotating black hole (Kerr, 1963). Still, other solutions can describe a gravitational wave or, in the case of the Friedmann–Lemaître–Robertson–Walker solution, an expanding Universe (Harada, Carr, and Igata, 2018). The spacetime described by special relativity is the uncurved Minkowski spacetime, and it is the simplest solution to Einstein's equations (Carroll, 1997).

According to Einstein's equations, one of the byproducts of the theory is gravitational radiation from fluctuating energy and momentum. GWs are disturbances in the curvature of spacetime that propagate outward from the source at the speed of light. Near to the source, these ripples can strongly distort the space and time,

but far from the radiator effects of these waves can be expressed as small perturbations to the flat spacetime background. Highly nonlinear dependencies on the metric, hidden in the Ricci tensor and Ricci scalar, make it very difficult and impractical to find the exact solution in most of the systems (Misner, Thorne, and Wheeler, 1973). However, for some systems with small curvature of spacetime (meaning that terms in the Einstein's equations that are quadratic in $\mathbf{g}_{\mu\nu}$ do not contribute much), one can model the solution of the field equations as being the flat spacetime Minkowski metric $\boldsymbol{\eta}_{\mu\nu} = \text{diag}(-1, 1, 1, 1)$ plus a small perturbation term due to the gravity wave, a small deviation from the flatness $\mathbf{h}_{\mu\nu}$. As said, the theory of gravity is not linear, but under the approximation of weak fields the metric describing spacetime in the presence of gravitational radiation is therefore (Carroll, 1997):

$$\mathbf{g}_{\mu\nu} = \boldsymbol{\eta}_{\mu\nu} + \mathbf{h}_{\mu\nu}, \quad \left|\mathbf{h}_{\mu\nu}\right| \ll 1 \tag{1.4}$$

So, doing the substitution of the general metric $\mathbf{g}_{\mu\nu}$ for this approximation results in a simplified expression for the Ricci tensor. The equations are reduced to a linear, second-order partial differential equation in terms of $\mathbf{h}_{\mu\nu}$. This process of decomposing into the Minkowski metric plus a perturbation term is not unique. This is due to the fact that different choices for coordinates may give different forms for $\mathbf{h}_{\mu\nu}$. The gauge symmetry is introduced to capture this phenomenon. In GR there is the freedom in choosing the form of $\mathbf{h}_{\mu\nu}$ to make the calculation easier. A popular and convenient choice, for a GW propagating along z-direction, is the transverse-traceless (TT) gauge:

$$\mathbf{h}_{\mu\nu}(z,t) = \begin{pmatrix} 0 & 0 & 0 & 0 \\ 0 & -h_+ & h_\times & 0 \\ 0 & h_\times & h_+ & 0 \\ 0 & 0 & 0 & 0 \end{pmatrix} \cos\omega_{GW}\left(\frac{z}{c} - t\right) \tag{1.5}$$

where ω_{GW} is the GW angular frequency, and the $+$ and $\times$ are two degrees of freedom that survive fixing this gauge, and they represent two linearly independent polarizations. Without the generality loss, we consider the $h_+(t)$ polarization in the following equations (Misner, Thorne, and Wheeler, 1973; Weinberg, 1972; Hobson et al., 2007).

For a GW which travels along the z-axis, the spacetime metric is given by:

$$ds^2 = -c^2dt^2 + [1 + h_+(t)]\,dx^2 + [1 - h_+(t)]\,dy^2 \tag{1.6}$$

The polarized GWs move particles with respect to each other in the way shown in the figure 1.1. For two free masses at a distance L from each other, along either the x-axis or the y-axis, their separation in the presence of GWs is changed by the factor:

$$\sqrt{1 \pm h_+(t)} \approx 1 \pm \frac{1}{2}h_+(t) \tag{1.7}$$

So, GWs modify their distance in the following way

$$\frac{\Delta L}{L} = \frac{1}{2}h_+ \tag{1.8}$$

where $\Delta L(t)$ is the change in separation between the free masses and this is why GWs are usually said to cause a dimensionless strain in space. For measuring the strain we need to measure $\Delta L(t)$ since, as we saw, the apparent length of each

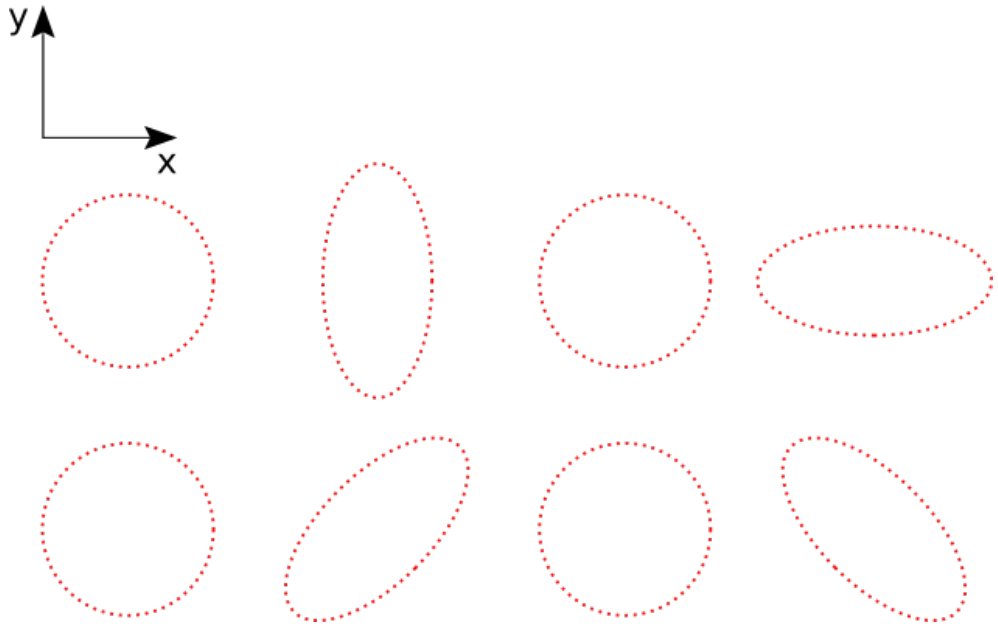

FIGURE 1.1: The effects of + and × polarized GWs propagating in the z direction on a circle composed of test particles in the x-y plane.

arm is compressed and stretched as GWs pass. Using the light beam we can measure the variation in the distance between two inertial TMs. Length measurements interpreted from phase shifts, meaning from measuring the variation in the light travel time is one way of doing this (Adhikari, 2004; Badaracco, 2020).

1.1.2 Sources and types of gravitational waves

Although any object with an accelerating mass quadrupole moment generates GWs, the accelerations and masses of objects on Earth are way too small to make GWs big enough to detect with our instruments. We have to look far outside of our own Solar System in order to find big enough GWs. There are incredibly massive objects in the Universe that experience high accelerations and generate GWs that we can detect. The strain amplitudes are, however, minuscule, *e.g.* in the Virgo Cluster (15 Mpc far away), the system with a mass close to solar mass, produces a maximum strain of 10^{-21} at 800 Hz. Roughly, the strain can be expressed as:

$$h \approx \frac{GMv^2}{Rc^4} \tag{1.9}$$

where M is the source mass, v velocity, and R is the distance from the Earth. The strain amplitude is determined by the quantity $G/c^4 = 8.26 \times 10^{-45}\ \mathrm{m^{-1}\ kg^{-1}\ s^2}$ (Saulson, 1994; Dooley, 2011; *LIGO sources*). Therefore, the most encouraging sources of GWs are fast-moving, massive, nearby objects that include binaries of NSs and BHs, or massive stars exploding at the ends of their lives. In general, the sources of GWs are supernovae (Abbott et al., 2009), binary stars (orbiting or coalescing) (Abadie et al., 2011), spinning NSs (Abadie et al., 2010), cosmological/astrophysical background (Allen and Romano, 1999). Based on the generation mechanism of GWs categories are Continuous, Compact Binary Inspiral, Stochastic, and Burst. Each category of objects generates a characteristic or unique signal

that detectors can sense, and that researchers can look for in detectors' data (*LIGO sources*).

Continuous GWs are typically produced by a single spinning massive object like a neutron star. The source producing the most common monochromatic radiation is a non-axisymmetric pulsar. The time-dependent quadrupole moment necessary to generate GWs can come from any imperfections or bumps in the spherical shape of the star as it spins or from an unsteady rotation (spin axis not aligned with a principal axis). If the spin rate of the star stays constant, GWs have continuously the same frequency and amplitude (Hawking and Israel, 1989; Adhikari, 2004; *LIGO sources*).

The next class, and extensively studied sources of GWs that detectors are hunting for is coming from the decaying orbit of Compact Binary Inspirals. All of the GWs detected so far come from this class. These GWs are produced by orbiting pairs of dense, compact, and massive objects like NSs, BHs, and white dwarfs. Three subclasses detected in this category of generators are NS/NS, BH/NS, and BH/BH. The wave-generation mechanism is the same for all three, but each pair creates a unique pattern of GWs. Searching for these inspiral signals can be done using a matched filtering technique. With time, binary is losing energy through gravitational radiation and orbital separation and period decreases. This can only end with two objects colliding. As objects move closer to each other, frequency increases, and eventually will get into our sensitivity range. This time is usually very brief. Detectors convert these signals into a 'chirp' (an audible sound), so we can 'hear' the last moments of the binaries' lives. Longer signals mean lower-mass objects, like NSs, while shorter signals suggest more massive objects like BHs (Allen, 2005; Adhikari, 2004; *LIGO sources*).

The hypothesis is that many small GWs are passing by all the time, from the entire Universe, mixing together randomly. They make up a 'Stochastic signal', meaning they cannot be predicted precisely but analyzed statistically. This signal can have both astrophysical and cosmological sources such as phase transitions in the early Universe, amplification by inflation of zero-point metric fluctuations, a large number of unresolved foreground sources such as binaries and supernovae, and cosmic strings. These will be the most difficult GWs to detect. Since it is possible that a part of this stochastic signal originates from the Big Bang, it would allow us to see further back into the history of the Cosmos than ever previously. Schemes for detecting this signal typically involve cross-correlating the output of two or more detectors (Allen, 1996; Christensen, 1990; *LIGO sources*).

Searching for the last class of GWs requires being completely broad-minded, since this very large class of events are the unmodeled transients, or bursts. For these GWs, we cannot assume that they have distinct properties like those of compact binary inspiral waves and continuous waves. So, the analyses cannot be restricted to searching only for the GWs that scientists have predicted. For these signals, it is necessary to recognize a pattern even when it has not been modeled before. A typical approach would be searching for the excess power in many narrow bands. Some examples of the expected burst events would be coalescence and merger of intermediate-mass black holes, asymmetrical core collapse in supernovae, and most interestingly, the unknown. The search for GWs' bursts is difficult, but detecting them would reveal revolutionary information about Cosmos (Adhikari, 2004; *LIGO sources*).

1.2 Gravitational Waves' Detectors

As pointed out in equation 1.9, by the time GWs reach the Earth, their amplitudes are tiny, no matter that the processes that generate them can be extremely destructive and violent. In order to directly detect GWs, we need very efficient transducers of spacetime strain to fluctuations in optical power (Barsotti, Harms, and Schnabel, 2018). Weber tried to directly detect GWs using a large aluminum bar (Weber, 1960). The hope was that passing GWs would excite the bar's resonant modes, but no credible evidence was found. In order to improve the directional sensitivity and bandwidth of the resonant mass detectors, ambitious, more sophisticated geometries are proposed (dodecahedrons, spheres, etc) (Cerdonio et al., 2001). The method of detection proposed by Hulse and Taylor, observing the binaries system's rate of change of orbital period, I already mentioned. This method of detection is not direct (Hulse and Taylor, 1975). The most successful method that is being used includes the Michelson interferometer (Bassan, 2013). This configuration is well-known thanks to Michelson and Morley falsifying the aether theory in 1887 (Michelson and Morley, 1887). The principle of work of the Michelson interferometer seems quite simple. Two coherent light beams travel along two perpendicular arms, then the relative phase shift is measured at the antisymmetric (AS) port as shown in figure 1.2. They are measuring the phase shift of light for arm length change of 10^{-18} m and less, so they explore fundamental limits of all kinds. In the following subsection, some of the subcomponents of the Fabry-Perot Michelson power recycled IFO configuration in LIGO are briefly described. All the kilometer-scale IFOs are variants of the power-recycled Michelson scheme. Alternative topologies, for very advanced noise reduction techniques, are Sagnac IFO (Chen, 2003), Fox-Smith cavity (Huang, Huang, and Gong, 2008), Mach-Zehnder IFO (Chen et al., 2006).

1.2.1 The LIGO Interferometers

The heart of the LIGO IFO is a simple Michelson IFO. In order that this kind of IFO detects a GW signal, the arm length should be hundreds of kilometers. For solving this issue, Michelson IFO is altered, including optical resonators known as Fabry-Perot cavities (FPCs) in both arms. Near the beam splitter, 4 km from the end TM, an additional mirror is placed as shown in figure 1.3. Input TM (ITM) and the end TM (ETM) comprise the FPC which increases the path of the light inside the arms. These mirrors are highly reflective, and the light in both arms bounces $F = \frac{\pi\sqrt{r_1 r_2}}{1-r_1 r_2} = 208$ times before exiting and going to the beamsplitter (BS). Here F is the finesse, and r_1, and r_2 are the reflectivities of the FPC mirrors. These reflections build up the light power, which increases the detectors' sensitivity. Since the distance that light travels increases, the detector's sensitivity increases and the length issue is solved. Sensitivity degrades when long-wavelength approximation is no longer valid *i.e.* when the storage time becomes comparable to the GW period (Fabry and Perot, 1901; Bassan, 2013).

While tiny changes in the arm length are amplified by increasing the effective arm length, an increase in light power is needed to increase IFO's resolving power *i.e.* for fringes at the photodetector to become sharper. Also, the shot noise, one of the major noises, is reduced. Power recycling mirrors are used to tackle this issue. These mirrors with BS and the input TMs of the arms, that are almost completely

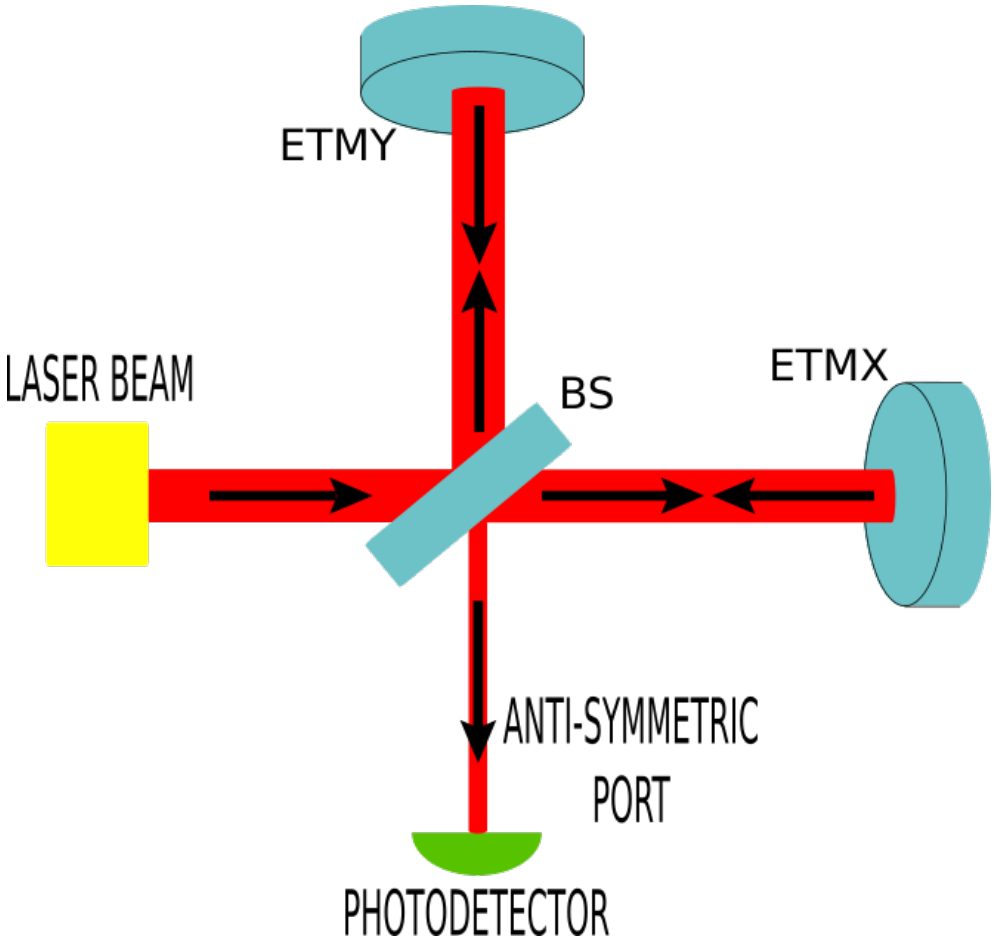

FIGURE 1.2: A basic Michelson IFO. ETMX is the x-arm end test mass (ETM), ETMY is the y-arm ETM, and BS is the beamsplitter. A laser beam is sent to a 50/50 BS. These beams travel perpendicularly to the ETMs, they are reflected back and recombined at the BS. This light then interferes at the AS port.

reflective, form power recycling cavity (PRC). To provide maximum power build-up, PRCs are tuned to the carrier frequency. Almost all the laser light circulating in the arms goes back to the reflective side of the power recycling mirror, and not to the photodetector. The power recycling gain, during the Third Observing Run (O3) in LIGO, was 40-50. The bandwidth of the GW readout at the AS port is not reduced through power recycling, because differential signals created in the arms are not recycled (Schnier et al., 1997; Buikema et al., 2020; Adhikari, 2004).

In order to enhance the signal coming to the photodetector, there is signal recycling mirror at AS port. Signal recycling cavity (SRC), formed with the signal recycling mirror and the input TMs, is affecting the sidebands, partly resending them to the IFO. SRC can be used to reduce/increase the gain (so reduce/increase sensitivity), while increasing/reducing the bandwidth of sensitivity of the detector. This is useful for tuning the detector, depending on the astrophysical sources we want to detect. This IFO enhanced with FPCs, PRC, and SRC is called dual-recycled Fabry-Perot-Michelson IFO. The best sensitivity of IFO is reached when light resonates in the cavities (Bassan, 2013; Harms et al., 2003; Estevez, 2020).

The input mode cleaner (IMC) is placed between the laser and the IFO. It is suppressing the higher-order transverse modes of the light field since the light beam in IFO needs to be in fundamental Gaussian mode (TEM_{00}). IMC reduces the frequency noise and mitigates the beam jitter (Mueller, 2014; Estevez, 2020). As shown in figure 1.3, IMC has a triangular configuration. More about IMC you can find in section 3.2.2. The output mode cleaner (OMC) suppresses the control sidebands and any other higher-order modes and sideband noises of the light beam created in the IFO. OMC is installed just before the photodetector (figure 1.3) (Arai et al., 2013; Fricke et al., 2012).

The differential arm (DARM) length change ($\Delta L = L_X - L_Y$), the most sensitive degree of freedom (DOF) to the passage of GWs, causes GW sidebands (phase modulation sidebands). While the carrier field interferes destructively at the AS port, GW signal sidebands interfere constructively at the BS, reaching the photodetector. The GW sidebands are at $f_{\rm sig} = f_{\rm c} \pm f_{\rm gw}$ where $f_{\rm c}$ is the frequency of the carrier and $f_{\rm gw}$ is the frequency of the GW (typically in the audio band). The photodetector cannot respond to terahertz oscillations of the EM field. An optical oscillator is used to amplify the signal in the resulting photocurrent, and to linearize the photodetector's response to a GW signal. In LIGO, a certain amount of the carrier light leaks to the AS port and serves as a local oscillator. The technique is a special case of homodyne readout, called DC-readout. So, in order to achieve the best possible sensitivity, IFO operates close to, but not at the dark fringe (there is a dark-fringe offset). The power incident at the photodetector can be expressed:

$$\begin{aligned} P_{AS} &= P_{BS} \sin^2(\phi_0 + \Delta\phi) \\ &\approx P_{BS} \sin^2(\phi_0) + 2P_{BS}\phi_0\Delta\phi \end{aligned} \tag{1.10}$$

where P_{BS} is the light power at BS, ϕ_0 is the dark-fringe offset, and $\Delta\phi$ is the phase difference that depends on the optical path difference of the beams in the arms. The photodiode (PD) is the physical detector used for sensing. The PD is sensitive to power, and a phase change at the BS is converted to a change in power (the second term of 1.10):

$$\frac{dP_{AS}}{d\phi_{BS}} = 2P_{BS}\phi_0. \tag{1.11}$$

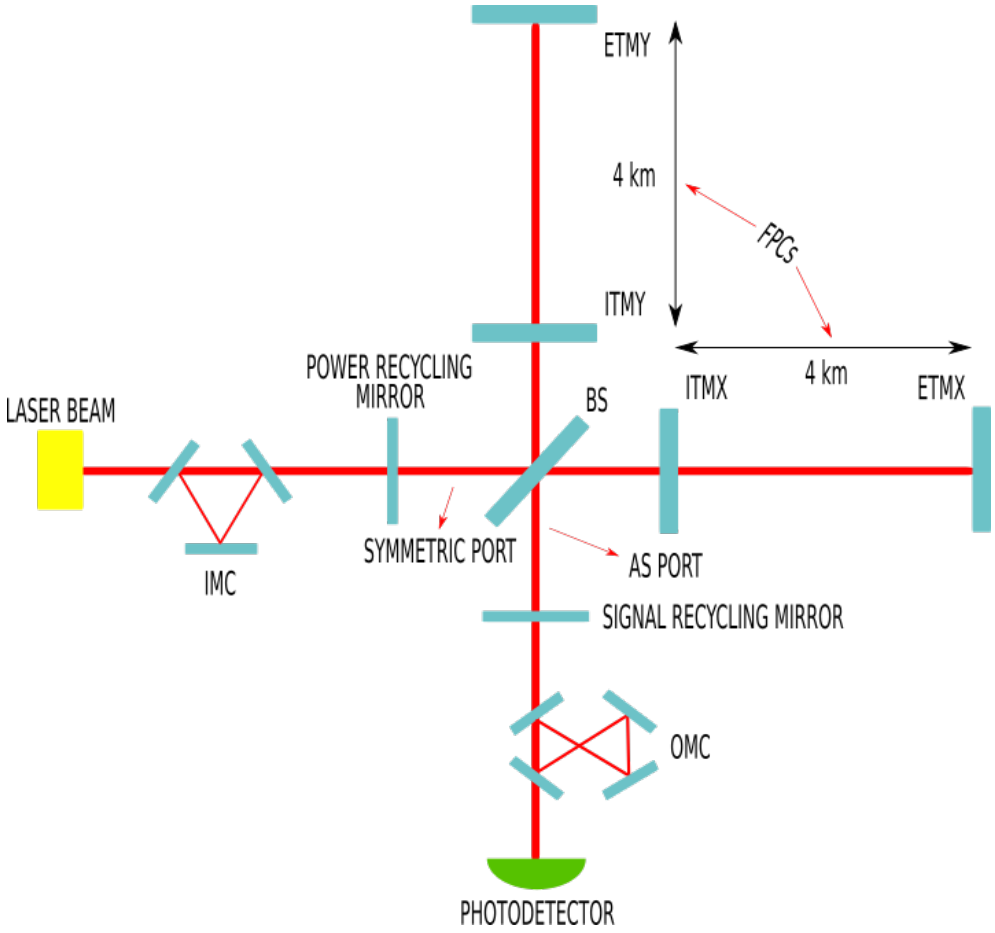

FIGURE 1.3: Simplified optical layout of the LIGO detectors for O3. ITMX is the x-arm input TM (ITM), ITMY is the y-arm ITM. The beam is purified by the triangular input mode cleaner (IMC). Fabri-Perot cavities (FPCs) are formed from input test masses (ITMs) and end test masses (ETMs). The power- and signal-recycling mirrors together with the BS and ITMs form the PRC and SRC, respectively.

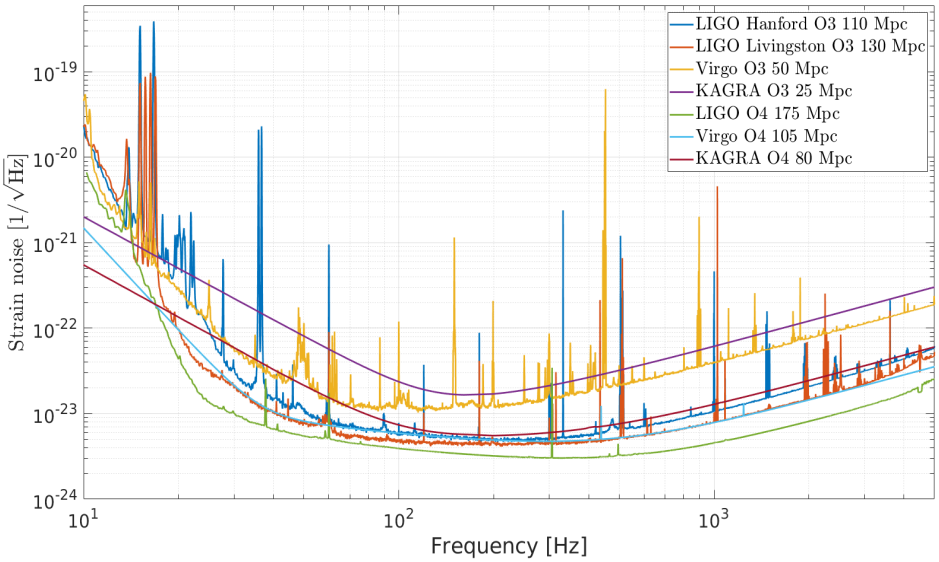

FIGURE 1.4: Strain sensitivities as a function of frequency for GW detectors for O3 and O4 science runs.

For the future, the plan is to use a balanced homodyne detection, which requires a separate laser input for the detection (ET Science Team, 2011; Fricke et al., 2012; Dooley, 2011; Adhikari, 2004).

In figure 1.4 you can see strain sensitivities for detectors for O3 and O4 science runs. For O3, for all the detectors, apart from KAGRA, these sensitivities are observed. For all the detectors for O4, and for O3 for KAGRA they are targeted/simulated (Abbott et al., 2020b).

1.2.2 Future gravitational waves' detectors

The next, third-generation of ground-based, gravitational-wave observatories has been proposed including the European concept Einstein Telescope (ET Science Team, 2011), and the US concepts LIGO Voyager (Adhikari et al., 2020) and Cosmic Explorer (Reitze et al., 2019). These detectors would have greatly improved sensitivity over almost the entire GW observation band compared to current-generation detectors Virgo (Acernese et al., 2015), LIGO (Abbott et al., 2016a), KAGRA (Akutsu et al., 2019), and LIGO India (Souradeep, 2016). Apart from ground-based detectors, there will be space-borne, large-scale GW detector – LISA (Edwards, 2000). The third-generation GW detectors will span the GW spectrum and will be able to determine the nature of the densest matter in the Cosmos, provide an independent probe of the history of the expanding Universe, and expand our knowledge of how massive stars live, die, and create the matter we see today, explore warped spacetime with unprecedented fidelity, and reveal the universe's binary BH population throughout cosmic time. It will improve sensitivity in the low-frequency band, which is important since most of the GW signals are emitted when the compact binary system is in the inspiral phase stage and bodies are far away from each other. This will increase the signal-to-noise ratio (SNR) of the signals. There will be an uncovered gap in frequency band between LISA and ET that might be filled by some ground-based low-frequency GW detector. Seismic and Newtonian noise

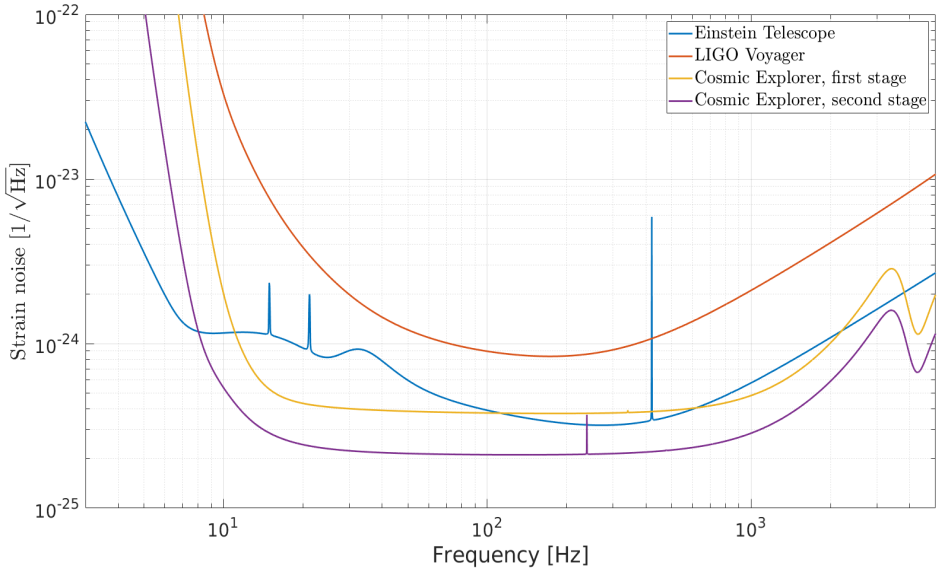

FIGURE 1.5: Targeted strain sensitivities as a function of frequency for the third-generation ground-based Michelson GW detectors.

will not allow detection below 0.1 Hz for ground-based detectors (Harms et al., 2013), so there is the need to construct a space-borne GW detector to cover this frequency band.

The Einstein Telescope is planned to be the European third-generation GW observatory. The low-frequency sensitivity (between 3 Hz and 100 Hz), with respect to previous ground-based detectors, will be significantly improved. It will consist of three nested detectors (ET Science Team, 2011). More information about ET you can find in chapter 2, section 2.2.

The LIGO Voyager, the third-generation detector at the existing LIGO sites, will also be dual-recycled, Fabry-Perot Michelson IFO with the following upgrades: TMs of 200 kg will be made of crystalline silicon, laser wavelength will be longer, optical coatings cryogenically-cooled (123 K, reducing thermal noise), the quantum noise will be reduced, etc. The sensitivity increase should increase the rate of binary BH to around 30 per day, and binary NS mergers to about 10 per day (Adhikari et al., 2020).

The Cosmic Explorer is the U.S. component of the third-generation detectors network. There is a two-stage plan for CE. In the first stage (CE1), CE will scale up Advanced LIGO technologies. It will be an L-shaped IFO. In the second stage (CE2), the 40 km arms long IFO's core optics will be upgraded using cryogenic technologies and new mirror substrates. With this, it will achieve very high sensitivity (figure 1.5), and see GW sources across the history of the universe. It should have a higher sensitivity than ET for frequencies approximately above 10 Hz, but lower sensitivity for frequencies approximately below 10 Hz (Reitze et al., 2019; Evans et al., 2021).

The Laser Interferometer Space Antenna (LISA) will be the first dedicated space-based large-scale GW detector. It will yield a strain sensitivity better than 10^{-20} at about millihertz, and it will be sensitive in the 0.1 m Hz - 1 Hz frequency band (inaccessible from Earth). Three spacecrafts in an equilateral triangle formation will

be separated by 2.5 million kilometers, flying along an Earth-like heliocentric orbit. In each spacecraft, there will be a telescope aimed to receive and transmit a laser beam from and to the other spacecraft, and free-falling TMs (Edwards, 2000; Prince et al., 2006). The Lunar Gravitational Wave Antenna (LGWA) aims to be sensitive in the frequency band between 1 mHz and 1 Hz. The plan is to monitor the vibrations of the Moon, with help of an array of high-end inertial sensors, that should reveal GWs (Harms et al., 2021).

The concepts of low-frequency terrestrial GW detectors are the European Laboratory for Gravitational wave and Atom-interferometry Research (ELGAR) (Canuel et al., 2020), the Torsion Bar Antenna (TOBA) (Ando et al., 2010), the Superconducting Omni-directional Gravitational Radiation Observatory (SOGRO) (Paik, 2018).

1.3 Noises

The interferometer output signal is the sum of GW signal and noises. We search for the displacements induced by GWs which are of the order of $\Delta L = 10^{-18}$ m and smaller. This minuscule displacement is three orders of magnitude smaller than the nucleus of an atom. The transverse size of the laser beam at the TMs is 6 cm for LIGO, and therefore the position of the surface of the TMs is averaged (Maggiore, 2008; Fritschel and LIGO Scientific Collaboration, 2015). There are many noise sources contaminating the detectors' outputs. Two main categories based on the coupling mechanism are displacement noise and sensing noise. Displacement noise moves the suspended mirrors, and sensing noise arises in the process of measuring the electric field and it appears in the readout signal but is not caused by a GW. The displacement noises are for example thermal noise, seismic noise, controls noise. The sensing noises are for example shot noise, frequency noise, PD dark noise. Some noises, like laser amplitude noise, can be assigned to both categories. Another division of the noises can be done based on their nature: fundamental and technical noises. Fundamental noises, like suspension thermal noise, coating Brownian noise, or quantum noise, arise from limitations imposed by the underlying physics of the detector and can be eliminated by a major instrument upgrade. This upgrade would include increasing laser power, size of the beams on the TMs, cryogenics... Technical noises, like noises from controls loops, electronics, auxiliary length loops, and scattered light, can be tackled by understanding and minimizing the coupling of these noises. Non-stationary noise sources (like input beam jitter) and glitches (like cross-talk of Radio Frequency (RF) electronics) are also harmful to the instrument's sensitivity to gravitational waves (Adhikari, 2004; Martynov, 2015). In the subsections below I will briefly describe some of the main noises limiting the sensitivity of GW detectors.

1.3.1 Quantum noise

Gravitational-wave detectors operate near the quantum ground state, despite employing kg-scale optics. Conceptually there are two forms of noise imposed by the quantum nature of the light. Shot noise arising from statistical fluctuations in the arrival time of photons at the antisymmetric port, affecting the high-frequency band, and radiation pressure noise (RPN), due to quantum fluctuations in the photon flux impinging upon the interferometer mirrors, affecting the low-frequency

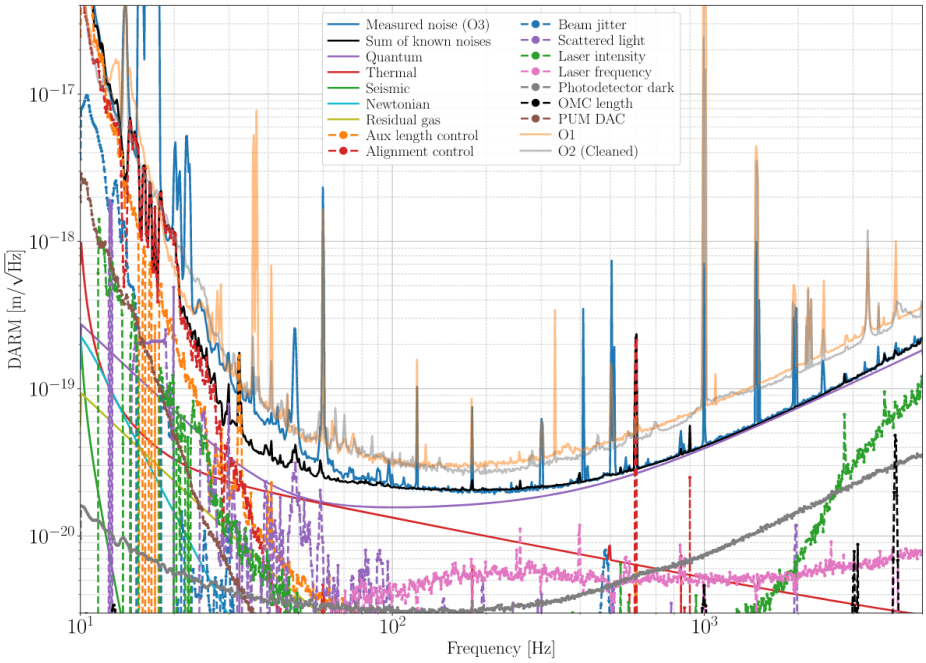

FIGURE 1.6: Noise budget at LIGO Hanford observatory during O3 science run. Figure taken from Cahillane's noise budget.

band (Barsotti, Harms, and Schnabel, 2018; Caves, 1981; Danilishin and Khalili, 2012).

The photons arriving at the photodetector can be described with Poisson statistics. Shot noise appears as a fluctuating power, with power spectral density (PSD):

$$S_{\mathrm{PD}}^{\mathrm{SN}} = 2P_{PD}h_p f_c, \tag{1.12}$$

where P_{PD} is the mean power on the photodiode, h_p is Planck's constant, and f_c is the frequency of the incident light. For small deviations from the 'dark fringe', the calibrated shot noise spectrum in terms of the limited length difference noise ΔL_{SN} in $\mathrm{m}\sqrt{\mathrm{Hz}}^{-1}$ has a white spectrum (Barsotti, Harms, and Schnabel, 2018):

$$\Delta L_{\mathrm{SN}} = \sqrt{S_{\Delta L}^{\mathrm{SN}}} = c\sqrt{\frac{\hbar_p}{2\omega_c P_t}}, \tag{1.13}$$

where P_t is the total power in both IFOs arms. Therefore, by increasing the circulating power the shot noise can be reduced.

Photons impinging on the mirrors transfer momentum. This is not constant in time, it fluctuates according to the Poisson statistics. The radiation pressure noise (or quantum back-action noise), has the PSD of differential arm length that can be written as:

$$S_{\Delta L}^{\mathrm{RPN}}(\omega) = \frac{2\hbar_p \omega_c P_t}{m^2\omega^4 c^2}, \tag{1.14}$$

where m is the mirror mass and ω is the angular frequency. The radiation pressure noise ΔL_{RPN} in $\mathrm{m}\sqrt{\mathrm{Hz}}^{-1}$ (square root of the power spectral density) is therefore

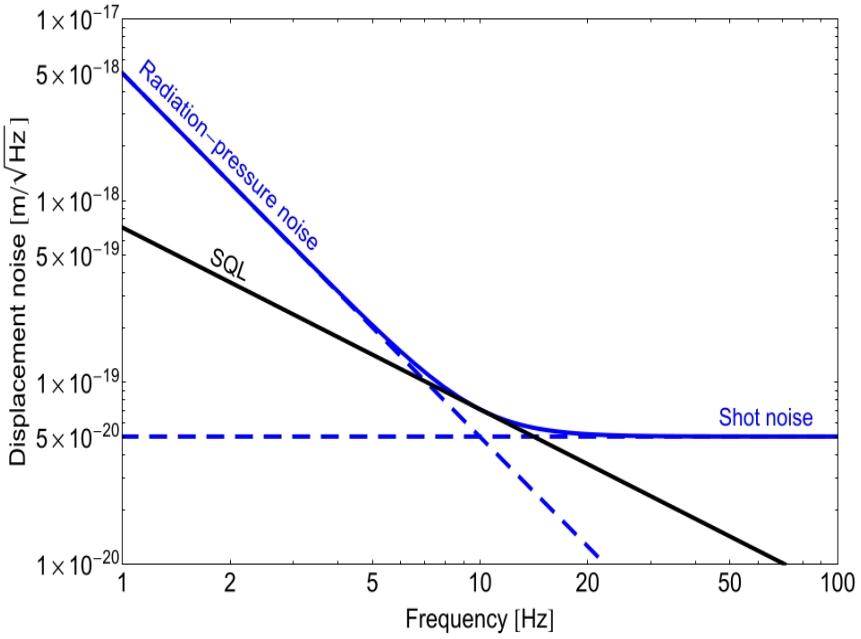

FIGURE 1.7: Displacement noise spectral densities of the quantum noises of a Michelson IFO with a total light beam power of 1 MW and TMs of 10 kg suspended as pendulums. Figure taken from (Barsotti, Harms, and Schnabel, 2018).

given by (Barsotti, Harms, and Schnabel, 2018):

$$\Delta L_{\mathrm{RPN}} = \sqrt{S_{\Delta L}^{\mathrm{RPN}}} = \frac{1}{m\omega^2 c}\sqrt{2\hbar_p \omega_c P_t}. \tag{1.15}$$

In order to decrease it, one can lower the circulating power or increase the mass of the mirrors. The problem is that lowering the arm-cavity power shot noise would increase. Here the concept of Standard Quantum Limit (SQL) comes into play. It is the lower boundary of the summed shot noise and RPN (figure 1.7). Using squeezing, *i.e.* injecting squeezed vacuum states of light, SQL is overcome and detector sensitivity is improved (Barsotti, Harms, and Schnabel, 2018; Caves, 1981; Danilishin and Khalili, 2012).

1.3.2 Seismic noise

The causes of the Earth's ground motion are earthquakes, ocean waves, winds, human activity, and many other sources. The ambient seismic field is a prominent source of disturbance for GW detectors, even if there are no earthquakes. An estimate for the displacement spectral density of the ground noise above 0.1 Hz at a quiet place is $x(f) = \frac{10^{-8}}{f^2}\ \mathrm{ms}^{1/2}$ (Adhikari, 2004). Reducing the seismic noise coupling is important for robust lock acquisition and to reduce optics angular motion. In order to reach desired strain sensitivity, seismic noise needs to be reduced by a factor of 10^9 in the observation band at frequencies higher than 10 Hz for LIGO (Martynov, 2015). For a new generation of GW detectors (*e.g.* ET) critical frequency range is 0.1 - 10 Hz, where the seismic noise is mainly due to microseismic and human activity. Below 1 Hz 'microseismic' noise prevails, depending

on large-scale meteorological and oceanic conditions. Around 1 Hz local meteorological conditions and wind effects show up. Above 1 Hz additional sources are related mainly to human activity (ET Science Team, 2011). At the moment GW detectors are placed on the surface and are sensitive to seismic disturbances. The plan for the future generation of GW detectors is to upgrade further active and passive isolation systems and to go underground. One of the best examples of decay of seismic surface displacement with depth is the reduction of the wind noise by going deeper underground. More on passive and active seismic isolation systems in LIGO is in Chapter 3, section 3.1.

1.3.3 Newtonian noises

One of the fundamental infrastructure limitations, theorised from the beginning of GW detectors, which limits their sensitivity is Newtonian noise. This noise originates from density fluctuations of ground and atmosphere around the TM. Density fluctuations cause the variations in the gravitational field which act on the TM causing noise relevant mostly below 20 Hz. Density perturbations generated by the seismic noise, and in variations in temperature and pressure of the atmosphere are

$$\delta\rho_{\text{seis}}(\mathbf{r},t) = -\nabla\cdot(\rho(\mathbf{r})\mathbf{s}(\mathbf{r},t)), \tag{1.16}$$

$$\delta\rho_{\text{temp}}(\mathbf{r},t) = -\frac{\rho_0}{T_0}\delta T(\mathbf{r},t), \tag{1.17}$$

$$\delta\rho_{\text{press}}(\mathbf{r},t) = \frac{\rho_0}{\gamma p_0}\delta p(\mathbf{r},t), \tag{1.18}$$

respectively (Harms, 2019). Here $\rho(\mathbf{r},t)$ is the density of the surrounding ground or air, $\mathbf{s}(\mathbf{r},t)$ is the seismic displacement, $T(\mathbf{r},t)$ and $p(\mathbf{r},t)$ are the temperature and pressure of the air, ρ_0 , T_0 and p_0 are the average density, temperature, and pressure of the atmosphere, and the adiabatic ratio for a diatomic gas is $\gamma = 1.4$. The assumption is that the density perturbations are much smaller than the average density ($\delta\rho(\mathbf{r},t) \ll \rho(\mathbf{r})$; $\delta\rho(\mathbf{r},t) \ll \rho_0$). The fluctuations of the gravity potential, in the case of seismic displacement, can now be written as:

$$\delta\phi(\mathbf{r}_0,t) = -G\int \mathrm{d}V\rho(\mathbf{r})s(\mathbf{r},t)\cdot\nabla\frac{1}{|\mathbf{r}-\mathbf{r}_0|}, \tag{1.19}$$

and the perturbation of gravity acceleration is:

$$\delta\mathbf{a}(\mathbf{r}_0,t) = G\int \mathrm{d}V\rho(\mathbf{r})\frac{1}{|\mathbf{r}-\mathbf{r}_0|^3}\left(s(\mathbf{r},t) - 3\left(\mathbf{e}_{rr_0}\cdot s(\mathbf{r},t)\right)\mathbf{e}_{rr_0}\right), \tag{1.20}$$

where $\mathbf{e}_{rr_0} \equiv (\mathbf{r}-\mathbf{r}_0)\,/\,|\mathbf{r}-\mathbf{r}_0|$. This form makes it easier to implement gravity perturbations in finite-element simulations. For this equation to be valid continuity equation needs to hold.

For the surface detectors, one idea in order to shield the detector from NN is to construct recess structures or moats (Harms, 2019). In the case of recess structures, the goal is to remove the mass that would be perturbed by seismic fields around the TMs (Harms and Hild, 2014). Another way to reduce NN at a surface is to dig moats around the TMs. In this case, the incident Rayleigh waves are reflected and a region around the TMs that is seismically quieter is created. For this method, the

hypothesis that Rayleigh waves come from external sources needs to hold (Hughes and Thorne, 1998; Harms, 2019).

Another option to reduce NN is to perform coherent noise cancellation. Information that is required to model the noise in data is obtained from the auxiliary sensors that monitor the source of the noise. The noise modeled like this is subtracted from the data during postprocessing or in real-time. The cancellation is limited depending on sensor noise, nonstationarity of the data, and limited information content in sensor data. Auxiliary sensors need to provide information with a high enough SNR. The cancellation scheme that is very well-explored is based on Wiener filters (Harms, 2019; Badaracco and Harms, 2019; Cella, 2000). More about coherent noise cancelation and Wiener filters you can find in Chapter 2, section 2.8.

1.3.4 Thermal noise

The interferometer's strain sensitivity is limited by thermal noise at frequencies where seismic vibrations are sufficiently filtered. Fluctuations in the measured cavity length are produced by the random thermal motion of particles in suspension, mirror substrate, and surface since at temperatures higher than absolute zero atoms are moving randomly around their equilibrium position, and continuously exchanging thermal energy with the environment. The surface distortions affect the phase of light and cause the noise (Saulson, 1990; Bondu, Hello, and Vinet, 1998).

The displacement estimation using the equipartition theorem gives an average displacement that is four orders of magnitude bigger than the one caused by a GW (10^{-18} m). The fluctuation-dissipation theorem gives the PSD of the thermal noise, and the way how to tackle it. If there is more dissipation, there are more fluctuations, and more displacement noise. Choosing materials with low internal dissipation helps to reduce the thermal noise. The temperature and mechanical losses are the important parameters for the thermal noise. The fluctuation-dissipation theorem gives us the relation between the dissipation in the system and the amount of fluctuations (Callen and Welton, 1951):

$$S_x(f) = \frac{k_B T_s}{\pi^2 f^2} \Re \left(Z^{-1}(\omega) \right), \tag{1.21}$$

where $S_x(f)$ is the power spectral density of fluctuations in x DOF, T_s is the temperature of the system, k_B is Boltzmann's constant, f is the frequency of the motion and $Z(\omega)$ is the impedance and it is defined as (Saulson, 1994):

$$Z^{-1}(\omega) = \frac{v(\omega)}{F_{\text{therm}}} = i\frac{\omega x(\omega)}{F_{\text{therm}}}. \tag{1.22}$$

where v is the time-derivative of the readout variable, and where F_{therm} is the thermal driving force.

The thermal noise of the mirror is dominated by the coating Brownian noise. Other thermal noises come from mechanical loss in the mirror substrate, and from thermorefractive and thermoelastic fluctuations in the mirror substrate and dielectric coatings (Braginsky, Gorodetsky, and Vyatchanin, 1999). The biggest care is devoted to the coating. The mirrors' surfaces are coated with several very thin dielectric layers. These layers provide high reflectivity and high sensitivity to the displacements. The proposed coating materials are tantala (Ta_2O_5), silica (SiO_2),

and titania (TiO_2). Depending on the temperature of operation, the best materials for the mirrors are sapphire, silicon, and fused silica (ET Science Team, 2011). Regarding the suspension system, the dissipation comes mostly from the bending of weakly anelastic elements (glass fibers and metallic wires) (Harms and Mow-Lowry, 2018). In order to decrease the thermal noise, monolithic suspensions are used (Amico et al., 2001).

1.3.5 Controls and sensing noises

The alignment of the IFO optics is done by alignment sensing and control systems. In order to maximize optical power, counteract instabilities from radiation pressure, and suppress motion from external sources, the mirrors are actively aligned. The gains of the loops are chosen to be high enough to control IFO but to reinject as less as possible of sensing noise. Even with this optimization, the sensing noise is limiting the detectors' sensitivity. In real-time, noise subtraction is done with feedforward techniques (Buikema et al., 2020; Barsotti, Evans, and Fritschel, 2010).

The biggest known source of the noise contribution to DARM below 25 Hz comes from the Angular Sensing and Control system. This system is particularly challenging in the new detectors, since for high arm-cavity power, significant optomechanical instabilities need to be handled. Angular motion couples linearly and nonlinearly to the longitudinal DOFs (Buikema et al., 2020). The ASC in LIGO is addressed in Chapter 3.

Some of the other noises in this category are actuator noise, Digital-to-Analog Converter (DAC) noise, laser intensity noise, laser frequency noise, auxiliary length control noise, beam jitter noise, scattered light noise, OMC noise, oscillator phase noise, oscillator amplitude noise, etc (Buikema et al., 2020; Martynov, 2015; Adhikari, 2004).

Chapter 2

Simulations of Gravitoelastic Correlations for the Sardinian Candidate Site of the Einstein Telescope

In this chapter, I will demonstrate SPECFEM3D's, which is a state-of-the-art finite-element simulation software for seismic fields, capabilities to provide estimates of gravitoelastic correlations, which are required for an optimized deployment of seismometers for gravity noise cancelation. This chapter is mostly based on the paper by (Andric and Harms, 2020), and in section 2.10, based on the paper by (Andric, 2022), the idea of implementing these simulations as priors to Bayesian array optimization is stated.

2.1 Introduction

Terrestrial gravity noise, also called Newtonian noise (section 1.3.3) or gravity-gradient noise, constitutes one of the fundamental infrastructure limitations, which limits the sensitivity of GW detectors (Harms, 2019). A large sensitivity improvement is targeted with Einstein Telescope in the infrasound observation band (1 – 20 Hz), and even higher, upto 30 Hz, where current generations of detectors have no detection capabilities. This will increase the number and SNR of observable GW signals and therefore greatly enhance the astrophysical impact of third-generation observatories (Hild et al., 2011; Maggiore et al., 2020). In this frequency band, it is possible to follow better the inspiral phase of compact binaries composed of neutron stars and stellar-mass black holes, or open the window to observations of intermediate-mass black holes (IMBH). It is possible to follow the waveform evolution for a longer amount of time and this practically means: more accurate estimates of some of the binary system's parameters including its sky location (Grimm and Harms, 2020), and potentially an early warning for the electromagnetic follow-up of these sources (Chan et al., 2018). ET will also be sensitive to continuous GW emission from a large population of spinning NSs below 10 Hz (Sathyaprakash et al., 2012). Therefore, there is a strong scientific motivation to expand the detection band and to improve the sensitivity in these frequencies.

At very low frequencies the dominant noise sources are those associated with the seismic motion that couples with the detector. One mechanism is the mechanical transmission, in which the vibrations of the ground perturb the motion of the TM via the TM suspension system. This is known as seismic noise, briefly

described in section 1.3.2. Sophisticated vibration-isolation systems are used to suspend the TM, significantly reducing seismic disturbances within the detection band (Acernese et al., 2010; Matichard et al., 2014). These systems in LIGO are discussed in Chapter 3. Another mechanism is by gravitational coupling which generates NN and cannot be shielded in any way (Beker et al., 2011; Beker, Brand, and Rabeling, 2015). A well-explored cancellation scheme is based on Wiener filters (Cella, 2000; Badaracco and Harms, 2019; Coughlin et al., 2016; Coughlin et al., 2018). Wiener filters are linear filters calculated from the correlation between the reference and target channels (Orfanidis, 2007). In the context of seismic NN cancellation, the sensors (seismometers) monitor seismic fields, which means that correlations between them are to be expected (Harms, 2019).

Most of the seismic noise is generated near the surface and it generally decreases significantly with depth. Predictions based on a detailed characterization of the LIGO sites show that seismic surface fields are the dominant contributor to NN (Driggers, Harms, and Adhikari, 2012). Thus, a NN cancellation scheme can be implemented using an array of seismometers deployed at the surface near the TM (Coughlin et al., 2016). ET has been proposed to be built underground, where the amount of seismic motion is expected to be lower and more stable (Harms et al., 2010; Beker, Brand, and Rabeling, 2015; Mandic et al., 2018). NN is about two orders of magnitude smaller underground which is substantial (Amann et al., 2020).

One of the most important things in NN cancellation is the homogeneity of the seismic field. Scattering of seismic fields from an irregular surface topography can cause heterogeneity of the seismic field. It can lead to a more complex field structure that is not fully characterized by surface displacement and will likely pose a major challenge even to 3D seismic surveys with boreholes where effective placement of seismometers needs to be achieved (Badaracco and Harms, 2019). The scattering will especially be the problem if it is strong enough to alter seismic waveforms significantly over very short propagation distances (Driggers, Harms, and Adhikari, 2012). Even if it is identified and fully characterized, scattering could create serious problems for NN subtraction, since it might increase the required effort and therefore cost of a NN mitigation system. Issues of topographic scattering and its connection to NN cancellation are partly examined in (Coughlin and Harms, 2012). They found that the total contribution of waves scattered from topography can be high, which makes topographic scattering relevant to NN subtraction in future low-frequency GW detectors. Seismic scattering was investigated analytically in several publications, see for example (Gilbert and Knopoff, 1960; Abubakar, 1962; Abubakar, 1963; Hudson, 1967; Ogilvy, 1987). An extensive and conclusive study of the impact of topography scattering on coherent cancellation has not been carried out so far.

In this chapter, I present the simulations of the synthetic ambient-noise cross-correlations between stations at the surface of a finite-element model using a 3D spectral-element method (SEM) implemented in SPECFEM3D Cartesian software (Komatitsch and Tromp, 2002a; Komatitsch and Tromp, 2002b; Komatitsch et al., 2018). Cross-correlations are simulated for the flat model and for the topographic model using elevation data at the three (foreseen) vertices of the proposed ET site at Sardinia. Using these correlations I demonstrate the effects of topographic scattering on seismic coherence and on correlations between TM acceleration and

vertical seismic surface displacement. These correlations are crucial when constructing a Wiener-filter. One of the main goals in the future will be to investigate whether high noise cancellation through Wiener filtering or similar methods will be effective at the Sardinia site for ET.

In section 2.2, the ET detector and the ET candidate site at Sardinia are briefly presented. In section 2.3, our main analysis tools SPECFEM3D Cartesian and Trelis are introduced. In section 2.4, the building of the finite-element model is described. In section 2.5, the theory of noise cross-correlation is reviewed with a focus on the method implemented in SPECFEM3D. In section 2.6, ensemble sensitivity kernels and their importance are explained. In section 2.7 topographic scattering and its connection to our research are described. In section 2.8 coherent noise cancelation and Wiener filters are briefly reviewed. In section 2.9, I present the main results of our study concerning the effect of topographic scattering on seismic correlations and the prediction of gravitational coupling between seismic surface displacement and an underground test mass. Finally, in section 2.10, all pieces for Bayesian seismic-array design are put together.

2.2 Einstein Telescope and Sardinia site

The third-generation GW observatory, ET, will be aiming to reach a sensitivity for GW signals emitted by astrophysical and cosmological sources about a factor of 10 better than current detectors over much of the observation band. With such a level of sensitivity, the era of routine GW astronomy will be open. The targeted observation band is from 3 Hz to a few kHz with a strain sensitivity of about $10^{-24}\,\mathrm{Hz}^{-\frac{1}{2}}$ within this band (ET Science Team, 2011; Hild et al., 2011), as shown in figure 1.5. Like all of the GW detectors so far, ET will be a dual-recycled Fabry-Perot Michelson IFO, with suspended mirrors that act as TMs. In its final construction stage, ET should consist of three nested detectors, built a few 100 m underground, which would be arranged in a triangular pattern. The advantages of ET with respect to the traditional L-shaped geometry of current GW detectors are that it will have a more uniform antenna pattern and be sensitive to both GW polarizations independent of the wave-propagation direction (better parameter estimation). Each individual detector will be composed of two interferometers forming a so-called xylophone configuration (Hild et al., 2009), one devoted to detecting low-frequency GWs (low laser power, cryogenic temperature; frequency range from 3 Hz to 50 Hz; seismic, gravity gradient, thermal noise sources will be particularly suppressed) and the other one for the high-frequency part (room temperature, high laser power, frequency range from 50 Hz to 10 kHz; the usage of frequency-dependent squeezed light technologies). Innovative techniques, well beyond the scope of first- and second-generation GW IFOs are required. For seismic noise reduction an extremely long suspension system, composed of five stages, each 10 m tall, will be deployed. Both IFOs will have TM masses around 200 kg (ET Science Team, 2011).

To reduce NN, it is necessary to choose a location for a detector with weak gravity fluctuations. One important observation is that seismic noise, especially above 1 Hz is weaker in regions with high elevation, mostly likely because of smaller population density. In terms of site selection, the challenge is to find a high-elevation site (*i.e.* low seismic noise) with small changes in elevation to minimize scattering. High-frequency seismic spectra (above a few Hz) are all significantly quieter

underground than at typical surface sites (Harms et al., 2010; Beker, Brand, and Rabeling, 2015; Mandic et al., 2018). This can be explained by the exponential decrease of the amplitude of the Rayleigh waves combined with the fact that high-frequency seismicity is typically generated at the surface, and most surface sites are covered by a low-velocity layer of unconsolidated ground. Underground sites are also attractive since the risk that anthropic seismic noise will change in the future due to surface infrastructural developments like the construction of industry or traffic roads is lower (Beker, Brand, and Rabeling, 2015). In addition, atmospheric gravity perturbations are strongly suppressed underground (Fiorucci et al., 2018).

The selected site should provide the possibility for efficient coherent cancellation of NN with surface and borehole seismometer deployment. Two-point spatial correlation of the seismic field determines the efficiency of a cancellation scheme. The strongest scatterer of seismic waves above a few Hz is the surface with rough topography (strong topographic gradients). If scattering is significant then the correlation can be strongly altered, and a seismic array consisting of a potentially large number of seismometers needs to be deployed with difficult to determine sensor positions (Harms, 2019). Since the ground medium near the TM at the Sardinia site is fairly uniform, it is unlikely to observe high scattering cross sections for underground propagation of seismic waves (Driggers, Harms, and Adhikari, 2012). Still, heterogeneity of the ground may add complexity, and a refined model should include information about local geology.

The suggested site at Sardinia (Italy) is near the city Lula (figure 2.1) with approximate vertex coordinates given in table 2.1. The spectral density of the Sardinia site ambient seismic field is close to Peterson's New Low Noise Model (NLNM) and there is no strong seasonal or daily variation above a few Hz. It has a very low seismic occurrence rate, and extremely low noise conditions in the 2 – 10 Hz band, but suffers from an additional peak at around 0.5 Hz as a result of Mediterranean Sea activity (Beker et al., 2012; Beker, Brand, and Rabeling, 2015; Di Giovanni, 2021; Naticchioni et al., 2014). Also, what goes in favor of the Sardinia site is the fact that the most seismically quiet sites are found in hard rock geologies and the Sardinia site is mostly made of granite and schist. Underground, seismic noise at the Sardinia site hits the noise floor of the data acquisition system. In terms of the construction of underground facilities, rock stability is a key factor, which then tends to be more favorable in hard rock (Beker, Brand, and Rabeling, 2015). This is unfavorable for NN reduction with depth, which decreases exponentially with increasing seismic-wave speed. Coordinates of vertices were chosen taking into consideration the quality of the rocks.

Cavern	Latitude	Longitude
A	40°28′	9°27′
B	40°31′	9°21′
C	40°34′	9°28′

TABLE 2.1: Coordinates of vertices of Einstein Telescope.

These vertices make an equilateral triangle with approximately 10.7 km side length. The figure 2.2 shows the surface areas of 3 km $\times$ 3 km size with topographies where the respective ET vertex is located under the center point of the area

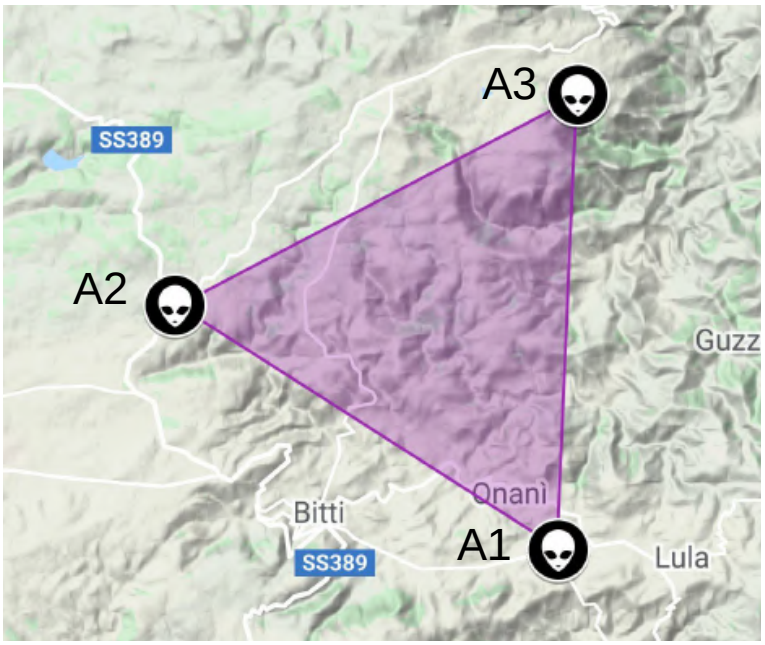

FIGURE 2.1: Sardinia candidate site for Einstein Telescope with marked vertex locations.

[1]. The resolution of elevation data is 30 m. For analysis of seismic coherence and gravity-displacement correlations, due to high computational costs (and, for this study at least, due to limited computational resources of only about 100-200 cores), we chose only vertex A3 because it has the roughest surrounding topography (figure 2.2c) among all three vertices and therefore the largest scattering potential. Roughness can for example be quantified using the root mean square (RMS) value of the elevation data, which are 52.4 m, 43.5 m, 129.6 m for the vertices A1, A2, A3, respectively. As already mentioned, scattering causes heterogeneity of the seismic field, which will be one of the main problems in NN cancellation. If the problem of NN description and cancellation is understood for vertex A3, there will not be any additional challenges when repeating the analysis for vertices A1 and A2.

[1]To prepare the topography data one can get SRTM Digital Elevation Data for a region of interest at SRTM 90m DEM Digital Elevation Database.

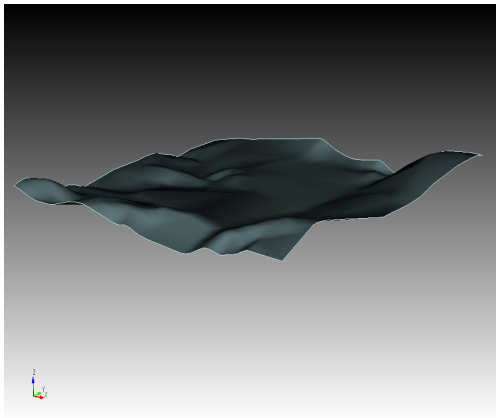

(A) Vertex A1

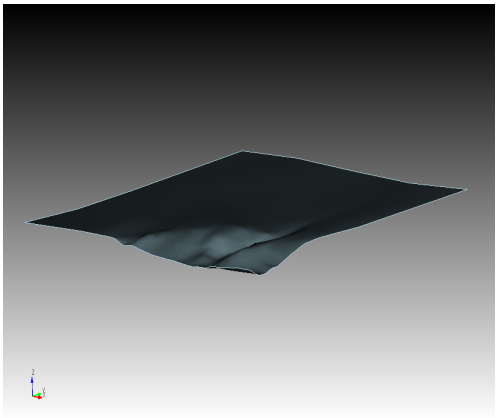

(B) Vertex A2

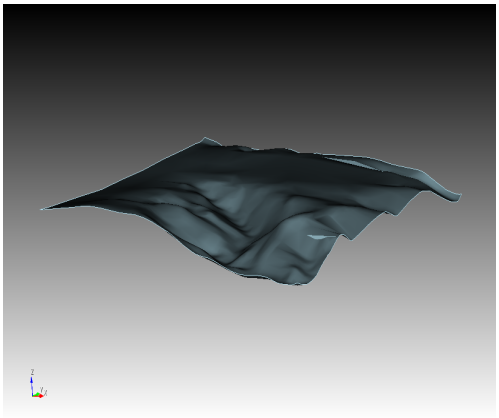

(C) Vertex A3

FIGURE 2.2: Elevation data at the three vertex locations of Einstein Telescope over areas with 3 km side lengths.

2.3 Finite-element simulation and model meshing

SPECFEM3D Cartesian is a powerful software package for local and regional scales seismic-wave propagation modeling and full waveform imaging based on the spectral-element method (Komatitsch and Tromp, 1999; Komatitsch et al., 1999). The SEM, a continuous Galerkin technique (Peter et al., 2011; Tromp, Komatitsch, and Liu, 2008), is a highly accurate numerical method, which combines the geometrical flexibility of the finite-element method with the fast convergence associated with spectral techniques, and it has origins in computational fluid dynamics (Patera, 1984; Maday and Patera, 1989; Seriani and Priolo, 2012). It uses a hexahedral finite element mesh on which the wave field is represented in terms of high-degree Lagrange polynomials on Gauss–Lobatto–Legendre interpolation points. SEM is more accurate than widely used classical techniques such as the finite-difference method (Virieux, 1986; Olsen, Madariaga, and Archuleta, 1997), especially for surface waves (Komatitsch and Tromp, 1999; Komatitsch and Tromp, 2002a), which play an essential role in ground-motion seismology (Komatitsch, 2004). SPECFEM 3D Cartesian has very good accuracy and convergence properties (Deville, Fischer, and Mund, 2003; Maday and Patera, 1989; Priolo, Carcione, and Seriani, 1994). It

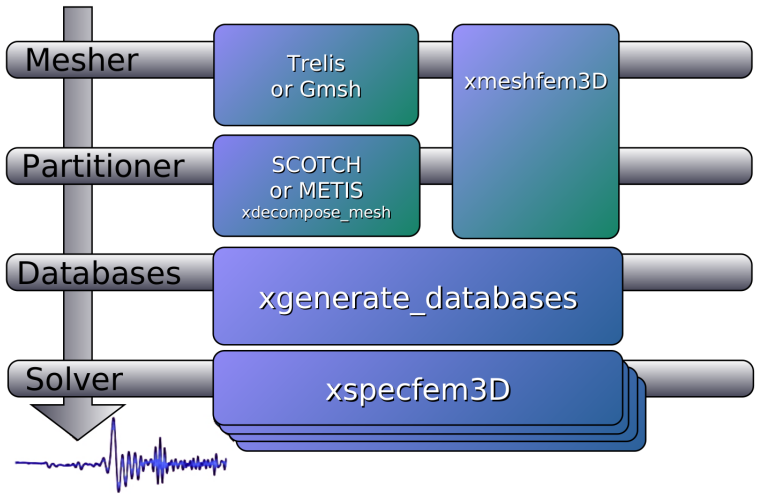

FIGURE 2.3: Schematic workflow for a SPECFEM3D Cartesian simulation. We used Trelis to create meshes, but other packages can be used as well, for instance, Gmsh (Geuzaine and Remacle, 2009). The SPECFEM3D Cartesian software package relies on the SCOTCH library (Pellegrini and Roman, 1996) to partition meshes created with Trelis. METIS (Karypis and Kumar, 1999) can also be used instead of SCOTCH. Meshing and partitioning can be done with internal mesher *xmeshfem3D*. Afterward, distributed databases are created and the solver is run.

is also very well suited to parallel implementation on supercomputers and clusters of CPUs or GPUs (Komatitsch et al., 2003; Komatitsch, Labarta, and Michéa, 2008; Tsuboi et al., 2003; Michéa and Komatitsch, 2010). SPECFEM3D software is written in Fortran2003 with full portability in mind (Komatitsch et al., 2018). The package uses the parallel algorithm based upon the Message Passing Interface (MPI) (Gropp, Lusk, and Skjellum, 1994; Pacheco, 1997). Workflow for a SPECFEM 3D Cartesian simulation is shown in figure 2.3.

We used Trelis (earlier known as Cubit) for the creation of models and their exporting into a SPECFEM3D Cartesian file format. Trelis is a full-featured software for the generation of two- and three-dimensional finite-element grids (meshes) and geometry preparation. Trelis is a solid-modeler based preprocessor that meshes surfaces and volumes for finite element analysis and computational fluid dynamics (Blacker et al., 2019). Generating meshes for complex model-based geometries requires a variety of tools and many of them in Trelis are completely automatic. In creating a load-balanced, partitioned mesh, it is needed to set up a hexahedral mesh, in which goes a large amount of work, then to export that mesh into a SPECFEM3D Cartesian file format and to partition it for a chosen number of cores in SPECFEM3D. The next step is creating the distributed databases in which all the missing information needed by the SEM solver are created. The final step is to run the solver (Komatitsch et al., 2018). Creating the databases and running the solver in SPECFEM3D is done on parallel on a number of cores chosen while partitioning.

2.3.1 Governing equations

For elastic materials, the displacement field $\mathbf{s}(\mathbf{x}, t)$ produced by a seismic source is governed by the momentum equation

$$\rho \partial_t^2 \mathbf{s} = \nabla \cdot \mathbf{T} + \mathbf{f}, \tag{2.1}$$

where ρ denotes mass density, $\mathbf{T}$ the stress tensor, and $\mathbf{f}$ the seismic source (in our case non-uniform noise sources). On the free surface, the traction vector must vanish:

$$\widetilde{\mathbf{n}} \cdot \mathbf{T} = 0, \tag{2.2}$$

where $\widetilde{\mathbf{n}}$ denotes the unit outward normal on the surface. On boundaries between different elastic materials, both traction $\widetilde{\mathbf{n}} \cdot \mathbf{T}$ and displacement $\mathbf{s}$ need to be continuous. The stress tensor $\mathbf{T}$ is linearly related to the displacement gradient $\nabla \mathbf{s}$ by Hooke's law, which in a pure elastic solid may be written in the form (Martin and Komatitsch, 2009):

$$\mathbf{T} = \mathbf{c} : \nabla \mathbf{s}, \tag{2.3}$$

where $\mathbf{c}$ denotes the fourth-order elastic tensor that describes the elastic properties of the medium (Peter et al., 2011).

Besides earthquake simulations, SPECFEM3D Cartesian includes functionality for seismic noise tomography as well. It can perform noise cross-correlation simulations. At the end of noise cross-correlation simulations, two outputs are the most interesting: the simulated ensemble cross-correlations and the so-called ensemble sensitivity kernels, which quantify how much a correlation depends on the properties of the ground medium throughout the model. Cross-correlations are generated based on the SEM (Komatitsch and Vilotte, 1998; Komatitsch and Tromp, 1999) and ensemble finite-frequency sensitivity kernels are generated based on the adjoint method (Tromp, Tape, and Liu, 2005; Liu and Tromp, 2008).

2.4 Model setup

Setting up appropriate absorbing boundary conditions before running simulations using created models is a crucial and time-consuming step. In order to simulate a semi-infinite medium, absorbing conditions are used on all sides of the model except the free surface. If absorbing boundary conditions are not adequate there are significant artificial boundary reflections from the numerical model which affect cross-correlations. The convolutional perfectly matched layers (CPML) absorbing boundary condition is very efficient from a numerical point of view for the elastic-wave equation in absorbing body waves with non-grazing incidence and surface waves (Komatitsch and Martin, 2007). CPML has better absorbing efficiency, especially in the case of small mesh size, than commonly used Clayton-Enquist absorbing boundary conditions which are mostly satisfactorily in the case of large mesh size (Komatitsch, 2004).

To create a high-quality absorbing boundary layers out of the edge elements/layers of the meshed model, it is important to have those elements/layers as regular as possible with constant thickness and aligned with the coordinate grid axes (X, Y, and/or Z). The CPMLs' thickness can be different for the X, Y, and Z sides, but must have a fixed, specific value for each coordinate individually. Typically, three or four CPMLs on each of the five absorbing model surfaces are sufficient, but

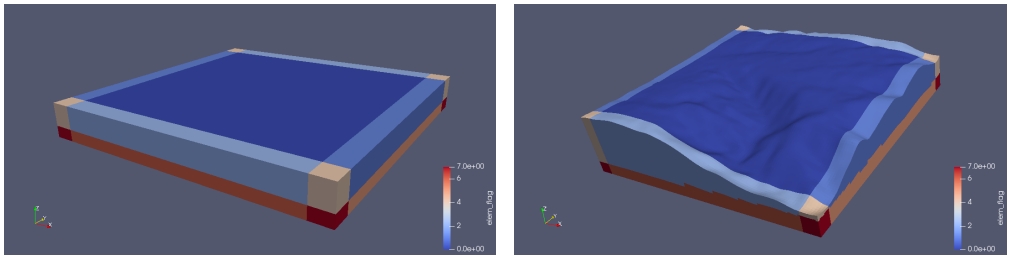

(A) Flat (B) Topography (A3)

FIGURE 2.4: Models with convolutional perfectly matched boundary layers (CPML).

as simulations showed, having more CPMLs on each of the absorbing surfaces suppressed reflections more, regardless of the thickness of the single CPML. Although CPML is very efficient, it does not completely absorb incident waves (see figure 2.9). To prevent remaining parasitic waves to affect cross-correlations *i.e.* to reach receivers, simulation time is set to be quite low (0.94 s). The thickness of the overall CPML used for the flat-surface model is 210 m, 210 m, 120 m for the X, Y and Z boundary planes, respectively (figure 2.4a), and for the topography model 179 m, 174 m, 179 m (figure 2.4b). These and many other figures of models, and waves propagation later in this chapter are visualized using the software Paraview (Ayachit, 2019). More information about CPML can be found in (Martin and Komatitsch, 2009; Komatitsch and Martin, 2007; Martin et al., 2010; Xie et al., 2014). CPML absorbing boundary condition is only supported in CPU mode for now (so one cannot use GPUs). Using GPUs would, of course, make the running of simulations much faster. Also, CPML is still under test for the third step of cross-correlation simulations – adjoint simulations.

The important parameter values of the model are $v_p = 3500\,\mathrm{m/s}$ compressional-wave speed, $v_s = 2000\ \mathrm{m/s}$ shear-wave speed, and $\rho = 2750\,\mathrm{kg/m^3}$ for the uniform mass density based on the fact that at the suggested site, granite and partly schist dominate, and also based on recent geoseismic studies (Giunchi et al., 2020). The simulations were performed without taking into account attenuation and anisotropy. We do not have any robust information about attenuation and anisotropy in this area yet. In addition, attenuation is not yet supported for noise cross-correlation simulations with SPECFEM3D. However, it can also be expected that attenuation plays a minor role over the small extent of the medium relevant to gravity-noise calculations.

The horizontal size of the models is $3\,\mathrm{km}\times3\,\mathrm{km}$ with a depth of 360 m in the flat free surface case (figure 2.5a) and with variable depth in the case with A3-topography. The minimum depth is 192 m and the maximum is 798 m (figure 2.5b). The mesh size of the flat free surface model is 30 m (for all three dimensions). For the topography model, it varies from 12 m to 71 m in Z dimension. For X and Y dimensions, it is 25 m. Mesh properties play an important role in estimating the stability of the simulation and estimating the maximum frequency, up to which synthetics are valid. The stability of simulations depends on P-wave velocity, time step size, and minimum distance between Gauss-Lobatto-Legendre interpolation points. From these parameters, one can calculate the Courant number that is used as measure of simulation's stability ($C = \frac{v_p \Delta t}{d_{minGLL}} \leqslant 0.55$). Courant number resolved in each element of the A3-topography model is shown in figure 2.6. We also made

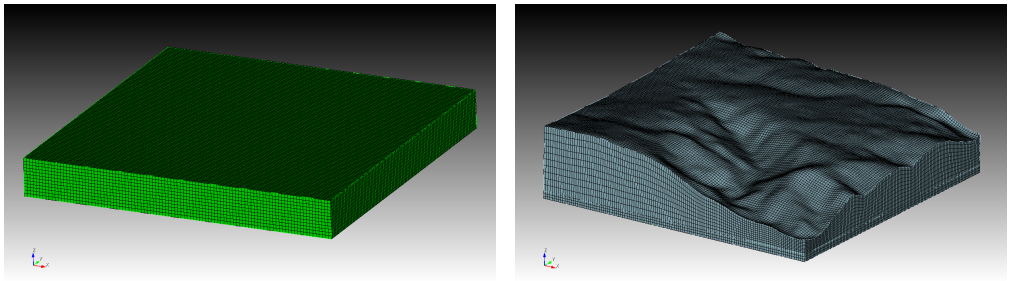

(A) Flat (B) Topography

FIGURE 2.5: Meshed models.

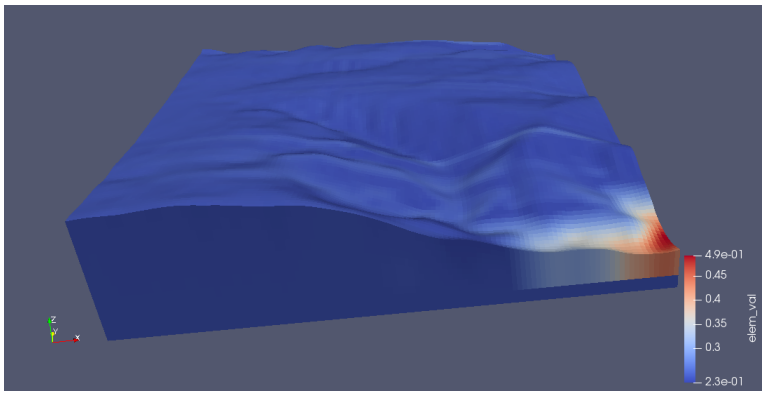

FIGURE 2.6: Courant number resolved in each element of A3-topography model.

sure that the maximum frequency lies above the target band, *i.e.*, above 30 Hz. Other important aspects of mesh design are governed by the meshing software Trelis.

As already mentioned, the simulations' results are valid up to a certain maximum frequency (minimum period). This maximum frequency depends on the mesh size and S-wave velocity ($f_{max} = \frac{4v_s}{5e_{max}}$, where e_{max} is the biggest of three dimensions of the single mesh element) and for the flat, free surface model, it is 53 Hz (and it is constant throughout the model) and for the topography model, it varies between 22 Hz and 66 Hz. Minimum periods up to which simulations at the A3 vertex are valid in specific mesh elements are shown for the topography model in figure 2.7. The minimum period is an estimation, and there is no sharp cut-off period for valid synthetics. Correlations become just more and more inaccurate for periods shorter than this estimate. Based on what we saw from simulations, they are usually sufficiently accurate only up to about 10 Hz from estimated values, and this value does not only depend on the mesh size and density, but also on details of the seismic-source modeling.

Source distribution affects surface-waves amplitudes (Tsai and Moschetti, 2010), it influences correlograms and its knowledge is important for correct interpretation of the data (Hanasoge et al., 2012; Basini, Liu, and Tape, 2012). For cross-correlation simulations, the distribution of noise sources in SPECFEM3D Cartesian is constrained to the surface, which is not a major disadvantage since the most relevant seismic sources in the NN band are expected to be surface sources. We also defined the ensemble of seismic sources used for the cross-correlation simulation

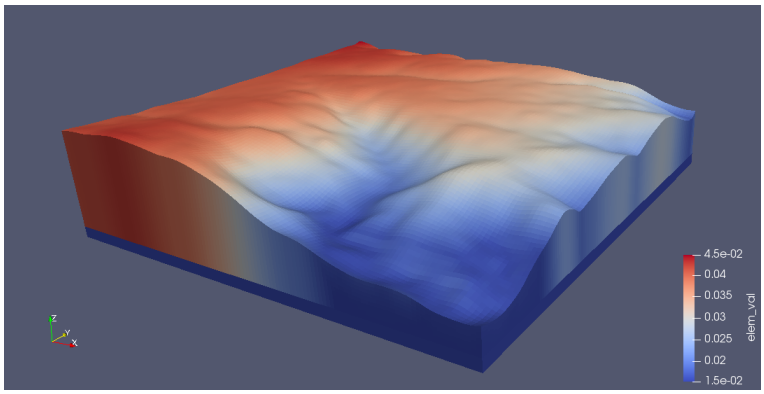

FIGURE 2.7: Minimum wave period resolved in each element of A3-topography model.

to have a minimum distance to the center of the model surface since we assume that these areas will be protected in the future, *i.e.*, excluding the presence of strong seismic sources inside the protected area. The radius of this area was also varied in our study to see the effect on seismic spectra and correlations. This also implies that the ET infrastructure must not introduce significant perturbations itself, which requires a novel low-noise infrastructure design avoiding some of the errors made with the current detectors infrastructure.

2.5 Noise cross-correlation simulations

Ambient-noise seismology is very important for high-resolution crustal imaging. Thanks to the unprecedented dense data coverage, it can be used even in regions with low seismic activity (Basini, Liu, and Tape, 2012). Cross-correlations between seismograms that recorded diffuse seismic wavefields created by stochastic wave excitation at the Earth's surface at different seismographic stations show statistically significant signals to be present (Tromp et al., 2010). According to the general interpretation of noise cross-correlations, they are related to a form of the Green's function between two receivers (Lobkis and Weaver, 2001; Wapenaar, Slob, and Snieder, 2006; Fan and Snieder, 2009; Montagner et al., 2012). The method implemented in SPECFEM3D is best described in (Tromp et al., 2010), where it extends to the application of tomography and evaluating misfits between models and observations.

The solution for boundary problems of the elastodynamic equation given by equation 2.1 can be expressed with the help of the Green's tensor $\mathbf{G}$

$$\mathbf{s}(\mathbf{x},t) = \int_{-\infty}^{t} \int_{\Omega} \mathbf{G}\left(\mathbf{x},\mathbf{x}';t-t'\right) \cdot \mathbf{f}\left(\mathbf{x}',t'\right) \mathrm{d}^3\mathbf{x}'\mathrm{d}t'. \tag{2.4}$$

where the Green's tensor $\mathbf{G}\left(\mathbf{x},\mathbf{x}';t-t'\right)$ is the response to the source $\mathbf{f}(\mathbf{x},t) = \mathbf{I}\delta\left(\mathbf{x}-\mathbf{x}'\right)\delta\left(t-t'\right)$, and $\mathbf{I}$ is the identity tensor. The Green's tensor satisfies the relationship (Aki and Richards, 2009; Dahlen, and Tromp, 1998)

$$\mathbf{G}\left(\mathbf{x},\mathbf{x}';t-t'\right) = \mathbf{G}^T\left(\mathbf{x}',\mathbf{x};t-t'\right). \tag{2.5}$$

In frequency domain, the solution can be expressed using the Fourier transform

$$\mathbf{s}(\mathbf{x},\omega) = \int_{\Omega} \mathbf{G}\left(\mathbf{x},\mathbf{x}';\omega\right)\cdot\mathbf{f}\left(\mathbf{x}',\omega\right)\mathrm{d}^3\mathbf{x}'. \tag{2.6}$$

In practice, an 'ensemble average' of many cross-correlations are used, which we will refer to as the *ensemble cross-correlation*. Ensemble averaging is one of the most important data-processing techniques in all of ambient-noise seismology, which makes it possible to reduce the effects of a set of scatterers and sources randomly distributed in time and space to those of a diffuse wavefield (Basini et al., 2013). From the observational point of view, ensemble average would mean stacking months of noise cross-correlation data. It could be done by stacking numerical simulations involving random noise (Cupillard and Capdeville, 2010), but it is computationally too expensive. What is following is a practical approach for calculating synthetic ensemble cross-correlations. Ensemble-averaged cross-correlations between synthetic seismograms at two geographically distinct locations on the free surface are determined under the assumption that noise is spatially uncorrelated but non-uniform. Despite the advantages of deeper seismometer installations, we focus our study on seismic surface measurements (Mandic et al., 2018).

Let's take into consideration the $\hat{\boldsymbol{v}}^{\alpha}$ component of the displacement at location $\mathbf{x}^{\alpha}$, and the $\hat{\boldsymbol{v}}^{\beta}$ component of the displacement at location $\mathbf{x}^{\beta}$:

$$s^{\alpha}(t) \equiv \hat{\boldsymbol{v}}^{\alpha}\cdot\mathbf{s}\left(\mathbf{x}^{\alpha},t\right), \quad s^{\beta}(t) \equiv \hat{\boldsymbol{v}}^{\beta}\cdot\mathbf{s}\left(\mathbf{x}^{\beta},t\right) \tag{2.7}$$

The cross-correlation between these two time-series is given by

$$C^{\alpha\beta}(t) = \int s^{\alpha}(t+\tau)s^{\beta}(\tau)\mathrm{d}\tau \tag{2.8}$$

We assume that sources of the field are spatially uncorrelated, which implies

$$\left\langle f_j\left(\mathbf{x}',t'\right) f_m\left(\mathbf{x}'',t''\right)\right\rangle = S_{jm}\left(\mathbf{x}',t'-t''\right)\delta\left(\mathbf{x}'-\mathbf{x}''\right) \tag{2.9}$$

where $< \cdot >$ denotes an ensemble average (Woodard, 1997). S_{jm} describes the geographic and geometric properties and ω-dependence of the noise sources, it is non-zero only at the (surface) locations of the seismic sources.

Using Fourier transform, a representation in terms of the Green's tensor, and taking into consideration ensemble average and equation (2.5), the analytical expression for ensemble cross-correlation is:

$$\left\langle C^{\alpha\beta}\right\rangle(t) = \frac{1}{2\pi}\hat{v}_i^{\alpha}\hat{v}_{\ell}^{\beta}\iint S_{jm}(\mathbf{x},\omega)G_{ji}\left(\mathbf{x},\mathbf{x}^{\alpha};\omega\right)G_{m\ell}^{*}\left(\mathbf{x},\mathbf{x}^{\beta};\omega\right)\exp(\mathrm{i}\omega t)\mathrm{d}^3\mathbf{x}\mathrm{d}\omega. \tag{2.10}$$

One may notice that ensemble cross-correlations have the symmetry:

$$\left\langle C^{\alpha\beta}\right\rangle(t) = \left\langle C^{\beta\alpha}\right\rangle(-t). \tag{2.11}$$

The more detailed calculation can be found in (Tromp et al., 2010).

Our noise cross-correlation simulations require two steps. In the first step, we calculate a generating wavefield, which is obtained by inserting a source-time

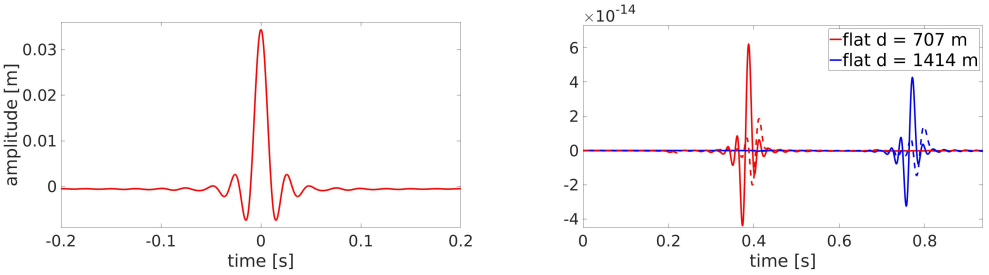

(A) (B)

FIGURE 2.8: Source time function corresponding to the noise spectrum (a) and vertical displacement of generating wavefield for the flat and topography models at the locations with 707 m and 1414 m distance from the source (b). The dashed, colored curves in (b) mark with corresponding colors the vertical displacement of generating wavefield with topography.

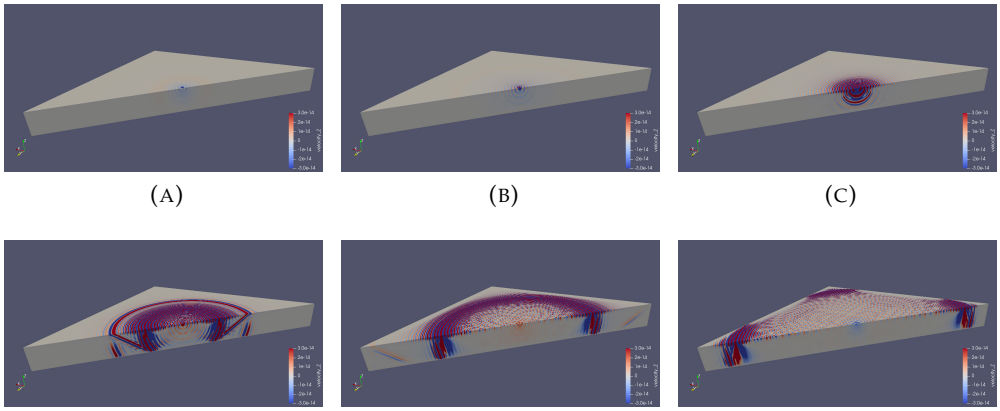

(A) (B) (C)

(D) (E) (F)

FIGURE 2.9: Propagation of seismic waves for the flat-surface model using a source time function determined by the spectrum of the ensemble-averaged noise.

function at the location of the first receiver. The source-time function of the generating wavefield is obtained using the spectrum of the ensemble-averaged noise, and it is narrowly concentrated around zero time. We use a source-time function shown in figure 2.8a representing a frequency-independent seismic spectrum in the interesting frequency range (1 – 30 Hz), since the absolute values of the seismic spectrum are not relevant for this research. Generally, results in the frequency domain can be rescaled using observed / realistic seismic spectra when needed. A sequence of snapshots resulting from a simulation of the wavefield with a source at the center of the model surface with the source time function as in figure 2.8a can be seen in figure 2.9 for the flat model and in figure 2.10 for the A3-topography model.

The results of the generating wavefield are saved at each time step at locations where the actual noise sources are located, which in our simulation covers an area of the free surface. Figure 2.8b shows displacement in the vertical direction of the generating wavefield for the flat and topography models at two locations with

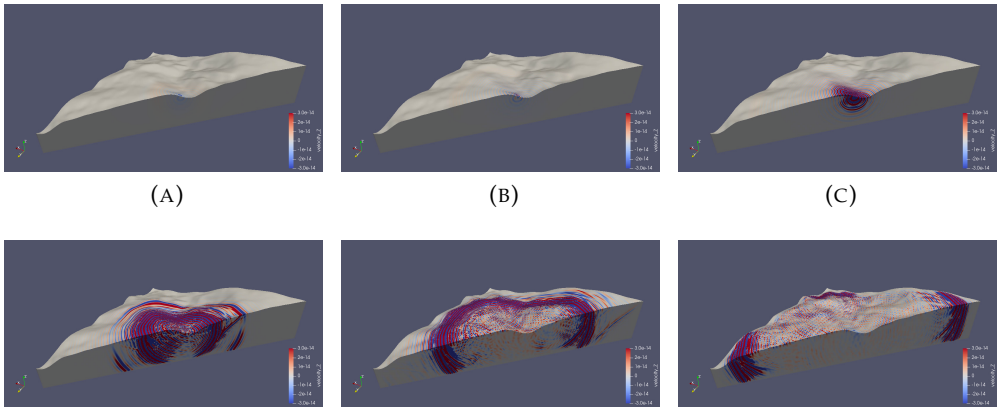

(A) (B) (C)

(D) (E) (F)

FIGURE 2.10: Propagation of seismic waves for the A3-topography model using a source time function determined by the spectrum of the ensemble-averaged noise.

different distances from the source.

Next, in the second step, one uses this generating wavefield at the locations of the noise sources as sources of the ensemble forward wavefield associated with the first receiver. We assume that the excitation is along the vertical direction of the surface. In the case of vertical forces, more than two-thirds of the total energy is radiated as Rayleigh waves (Woods, 1968). For our application, at the surface, the relative amount of Rayleigh waves is even larger (Sanchez-Sesma and Campillo, 1991). It should also be noted that in our models, which essentially represent a homogeneous halfspace, no other modes of Rayleigh waves, apart from the fundamental Rayleigh mode, are possible. The source of the ensemble forward wavefield is just the time-reversed generating wavefield. The ensemble cross-correlation is equal to the $\hat{v}^{\alpha}$ component of the ensemble forward wavefield $\mathbf{\Phi}^{\beta}$ evaluated at location $\mathbf{x}^{\alpha}$:

$$\left\langle C^{\alpha\beta} \right\rangle (t) = \hat{\boldsymbol{v}}^{\alpha} \cdot \mathbf{\Phi}^{\beta} \left(\mathbf{x}^{\alpha}, t \right). \tag{2.12}$$

Given the equation (2.11), it is clear that knowing either $\mathbf{\Phi}^{\alpha}$ or $\mathbf{\Phi}^{\beta}$ the ensemble cross-correlation can be calculated. The examples of surface propagation of the simulated ensemble forward wavefield is shown in the sequence of snapshots in appendix A, in the figures A.1 and A.2 for flat and A3-topography models, respectively. More details can be found in (Tromp et al., 2010).

2.6 Sensitivity kernels

Another step can be taken with noise cross-correlation simulations to obtain ensemble sensitivity kernels, which quantify the sensitivity of the cross-correlations to parameters of the ground medium such as mass density and seismic speeds, and the spatial distribution of noise. In addition to the generating and ensemble forward wavefield described in section 2.5, the calculation of sensitivity kernels requires another wavefield called ensemble adjoint wavefield. The sensitivity kernel results from an interaction between the ensemble forward wavefield and the ensemble adjoint wavefield. This interaction 'paints' ensemble sensitivity kernels.

This makes it possible to estimate ensemble sensitivity kernels without the need to use computationally expensive ensemble averages as done in practice in seismic data analysis (substituting ensemble averages with temporal averages). As a technical note, the calculation of sensitivity kernels with SPECFEM3D does not currently support CPML. For these simulations, the Clayton-Enquist boundary conditions are used.

In seismology, sensitivity kernels are very important for tomographic inversion and can be used to improve Earth and source models. They shed light on those parts of models that are inaccurate. In other words, using observed correlations and making simulations of synthetic correlations, one can use the cross-correlation misfit to iteratively improve the model. More about ensemble adjoint wavefield and sensitivity kernels can be found in (Liu and Tromp, 2006; Tromp, Tape, and Liu, 2005; Tromp, Komatitsch, and Liu, 2008; Tromp et al., 2010; Peter et al., 2011). Sensitivity kernels are not directly relevant to our work, but they provide additional information on whether the model size is sufficiently large for the simulation of correlations, in which case sensitivity kernels should be small towards the boundaries of the model. For the future, they can guide the development of more sophisticated models with heterogeneous geology.

The theoretical study by (Tromp et al., 2010) shows how adjoint techniques (*e.g.* Tromp, Tape, and Liu, 2005; Peter et al., 2007) can be applied to ambient-noise seismology given the non-uniform distribution of noise sources. The ensemble adjoint wavefield is produced by a source located at the second receiver whose time function depends on the misfit between simulated and observed correlations. There are numerous possibilities to evaluate cross-correlation misfits. The method chosen in SPECFEM3D is based on the misfit of cross-correlation delay times. For example, the cross-correlation delay time would be responsible for a complex phase of cross-spectral densities between sensors. Since we are only interested in the sensitivity kernel and not in the actual inference of ground properties using seismic observations, an arbitrary misfit of $\Delta T = 1\,\mathrm{s}$ is chosen (Tromp et al., 2010).

The ensemble adjoint source corresponding to a delay-time misfit involves the first-time derivative of the simulated ensemble cross-correlation $\langle \dot{C}^{\alpha\beta} \rangle$. As will be shown afterward, ensemble cross-correlations are dominated by Rayleigh surface waves, whose main sensitivity is to shear-wave speed (often given the symbol β). So here, we focus on beta kernels. The beta kernel is a volumetric field representing the gradient of the misfit function with respect to S-wave speed.

The beta kernel is shown in figure 2.11 for the flat (top) and for the A3-topography model (bottom). One can see that ensemble cross-correlations are most sensitive to properties of the ground near to and between the two receivers and close to the surface (*i.e.* seismic waves are mostly sensitive to the near-surface structures between receivers). Note that the kernel is asymmetric with respect to an exchange of receivers. This asymmetry comes from the fact that kernels are defined for two branches, the so-called positive and negative branches (the positive branch being shown). The positive branch describes cross-correlations whose time delays are consistent with waves reaching the second receiver before the first.

If we interpreted the 1 s time delay as an observed misfit, then the plots in figure 2.11 would tell us that the S-wave speed in the region between the two receivers, since the kernel is negative here, would have to be decreased to reduce the time-delay misfit between observation and model. The sign of the kernel would be inverted in the negative branch since the model would have to be corrected to

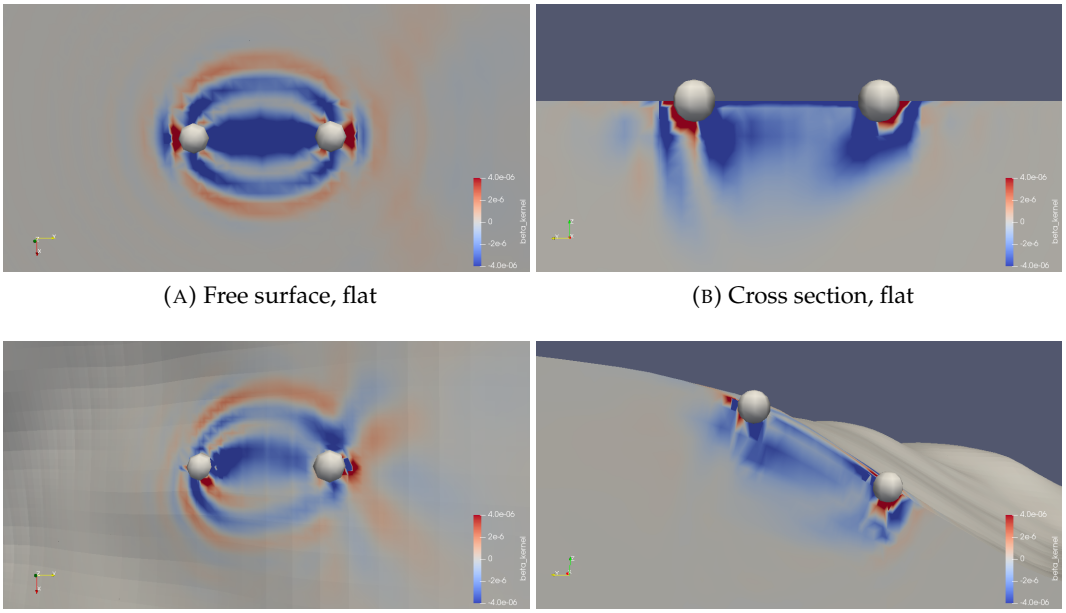

(A) Free surface, flat

(B) Cross section, flat

(C) Free surface, topography

(D) Cross section, topography

FIGURE 2.11: Beta kernel for flat (top row) and topography surface model (bottom row). White spheres represent receivers at a distance of 130 m from each other.

increase a negative time delay.

2.7 Seismic scattering

The effect of scattering of seismic waves from surface topography on seismic correlation and gravity perturbations of TMs needs to be quantified using the methods described in section 2.5. As mentioned earlier, because of the way we choose to excite seismic waves in this analysis, the ensemble forward field is mainly composed of Rayleigh surface waves. For flat, free surfaces, Rayleigh waves, once decoupled from the near field of the seismic sources, propagate without conversion into other seismic modes.

The scattering by topography depends on the area of contact, the size of elevation changes, and the scale of the length of the irregularity. It also depends significantly on the angle of incidence and type of seismic waves propagating through the area. Amplitudes of scattered waves should increase linearly with the size of elevation changes for small obstacles according to perturbation theory based on the first-order Born approximation (Gilbert and Knopoff, 1960). Born approximation breaks down for steeper slopes (steeper than approximately 30°) and higher elevations of topography (depending on the wavelength of seismic waves and horizontal dimension of topography), for which there is strong amplification of scattered waves (Snieder, 1986; Hudson et al., 1973). Therefore, the scattering should be much reduced in the case of irregularities with gentle curvature when compared with irregularities (mountains) with abrupt discontinuities in curvature (bluff topography) (Gilbert and Knopoff, 1960). An important point is that the incident wave is essentially 'blind' to features that are much smaller

than a wavelength (Otto, 1977). Scattering always becomes weaker at smaller frequencies if all other parameters are kept constant, but generally, there is no simple frequency scaling valid for the entire wavenumber space. Scattering coefficients in wavenumber space are mainly proportional to the topographic spectrum (Coughlin and Harms, 2012). The maximum scattering is generally present when seismic wavenumbers match the wavenumbers of the topographic spectrum (Hudson and Knopoff, 1967).

There is also body-wave content in our ensemble forward wavefield. Therefore, it is interesting to see what happens with body waves during scattering in addition to the dominant Rayleigh-wave field. For incident S-waves, if the dominant horizontal length scales of the surface spectrum are small compared with the length of incident waves, the amplitudes of some of the scattered waves decrease exponentially with depth similar to Rayleigh waves. A periodic surface characterized by short horizontal length scales captures more of the incident energy than one characterized by longer length scales, but the amount of trapped energy also depends on the associated amplitudes of the topographic spectrum. This trapped energy feeds into the surface waves (Abubakar, 1962).

For the incident P-waves, scattered waves are predominantly Rayleigh waves followed by a weaker (horizontal) P-wave (Bard, 1982). The amplitude ratio of scattered Rayleigh to incident longitudinal wave depends mostly on the angle of incidence and horizontal and vertical dimensions of the corrugation. For example, for normally incident longitudinal waves, with Rayleigh wavelength equal to the width of corrugation, the amplitude ratio grows linearly with the ratio of horizontal and vertical dimensions of the corrugation. Scattered Rayleigh wave has surface amplitude that is greater than that of the incident longitudinal wave alone already at ratios of horizontal and vertical dimensions less than one (Hudson et al., 1973). In conclusion, a significant portion of bulk waves scatter into Rayleigh waves, and additionally, that scattering is driven by high-wavenumber components of the surface topography, which usually have weaker amplitudes.

Scattering effects in the case of incident Rayleigh waves, which is the most interesting case for us, were investigated in (Maradudin and Mills, 1976). The main conclusion that one may infer from there is that the predominant contribution from the roughness-induced scattering of the incident Rayleigh wave is into other Rayleigh waves. At low frequencies, the ratio between scattered Rayleigh and bulk waves is about 10, and it increases as the frequency increases. So Rayleigh wave/Rayleigh wave scattering contribution is approximately an order of magnitude larger than the bulk wave contributions. However, details depend on the topography.

In particular, scattering from Rayleigh waves into Rayleigh waves is a very efficient scattering channel, but since it does not cause a change in wave type, its impact on NN cancellation can easily be modeled. However, it is found that topographic scattering might be relevant to NN subtraction in regions with rough topography (Coughlin and Harms, 2012). Fields of scattered waves do not generally permit a one-to-one correspondence between frequency and wavelength, and the wavenumber spectrum of the scattered field is typically continuous at each frequency. This is the main challenge for the design of a NN cancellation system in seismic fields where scattered waves make significant contributions. It should be noted that also scattering from underground caverns of the Einstein Telescope would significantly modify the seismic field in the vicinity of the cavern, but as

long as the caverns are much smaller than the seismic wavelengths in the relevant frequency range the impact on NN remains small (Harms, 2019).

2.8 Coherent noise cancellation and Wiener filters

Einstein Telescope targets GW observations down to a few Hz (Punturo et al., 2010), which means that seismic NN will play an important role in instrument design. The detector will be hosted in an underground infrastructure, which creates a low-noise environment providing an essential reduction of NN. Detector infrastructure including ventilation and pumps must not disturb the underground environment or be at a safe distance from the TMs. Further mitigation of NN can be achieved by noise cancellation using an extensive monitoring system of the ambient seismic field (Harms, 2019). Coherent noise cancellation, also known as active noise cancellation, of seismic NN, is based on techniques that have been already successfully used in GW detectors to tackle other forms of noise (Giaime et al., 2003; Driggers et al., 2019; DeRosa et al., 2012; Driggers et al., 2012). The noise in the data can be modeled from the information obtained from auxiliary sensors that monitor the source of the noise (*e.g.* seismometers). To minimize the noise, this noise 'model' is then subtracted from the data. Coherent noise cancellation is limited by available quality and type of sensors, non-stationarity of noise, back-action of the sensors on the monitored field, the available number of sensors, etc (Harms, 2019).

The idea is to pass seismic data through a filter such that its output can be understood as a coherent estimate of seismic NN and be subtracted from the GW data (Cella, 2000). These filters may be in the form of linear Wiener filters calculated from the correlations between the reference channel (seismometers) and the target channel (GW detector) (Orfanidis, 2007). The residual of the target channel after subtraction is given by:

$$r_n = y_n - \mathbf{w} \circ \mathbf{x}_n, \tag{2.13}$$

where y_n is the target channel (GW strain contaminated by NN), $\hat{y}_n = \mathbf{w} \circ \mathbf{x}_n$ a coherent estimate of NN contribution to the target channel, $\mathbf{w}$ is the filter, and $\mathbf{x}_n$ is the seismic noise signal. The coefficients of the Wiener filter are calculated by minimizing the mean-square error between the target channel and filter output ($\left\langle (y_n - \hat{y}_n)^2 \right\rangle$) (Benesty, Huang, and Chen, 2008; Harms, 2019). If the noise sources and target channel are wide-sense stationarity (meaning that noise moments are independent of time up to second order), and if all forms of noise are additive, then the Wiener filter is known to be the optimal linear filter for a given configuration of the sensor array (Rey Vega and Rey, 2013). The most challenging aspect of this technology is to determine the locations of a given number of sensors that optimize the cancellation performance (Coughlin et al., 2016; Badaracco and Harms, 2019). More about these topics one can find in (Harms, 2019).

2.9 Results

It is predicted that Rayleigh waves will give the dominant contribution to NN in surface detectors (Coughlin et al., 2016; Harms et al., 2020) and even underground detectors can still be limited by gravitational noise from Rayleigh waves

depending on the detector depth (Badaracco and Harms, 2019). The Rayleigh field produces surface displacement and density perturbations beneath the surface at the same time (Hughes and Thorne, 1998; Beccaria et al., 1998), which leads to gravity perturbations. Even if the wave composition of the seismic field at a site is unknown, it is still reasonable in many cases to assume that Rayleigh waves dominate the normal surface displacement at frequencies in the range 1 Hz – 20 Hz produced by surface or near the surface seismic sources (Mooney, 1976; Bonnefoy-Claudet, Cotton, and Bard, 2006). Only at exceptionally quiet (necessarily remote) surface sites or underground sites, body-wave content is expected to be significant or dominant in this band (however, mode content can change significantly with time if due to natural sources (Coughlin et al., 2019)).

In the following, I present the results of our analyses of spatial correlations in an ambient seismic field simulated with SPECFEM3D Cartesian software, and I predict the correlation between surface seismometers and the gravity perturbation experienced by an underground TM, which is crucial information for the optimization of surface arrays for NN cancellation. As already explained, our analyses are constrained by the computational resources that were available to us. One consequence is that it was not possible to run a simulation with a TM depth greater than 100 m (while 200 m – 300 m is the envisioned depth of ET test masses), since this would have required a dense set of receivers spread over a much larger surface area. These results show how topography affects correlations, which we expect to be the main site effect on seismic correlations and seismic gravitational noise.

As an initial characterization of topographic scattering, we calculate the ratio of power spectral densities at the center of our models with and without topography. The ratio is shown in figure 2.12 between 1 Hz and 30 Hz for three different minimal distances of seismic sources to the center point. The plot shows that the topography scatters higher frequencies more than lower frequencies. In other words, topography acts as a low-pass for Rayleigh waves protecting a point to some extent from the influence of distant seismic sources. At the A3 vertex of the Einstein Telescope, topographic protection is provided down to about 4 Hz. As can be seen, the ratio depends weakly on the minimal distance of seismic sources, which can be explained by the contribution of increasingly large topographic scales to the scattering coefficients. Of course, the absolute value of power spectral density reduces significantly when sources are more distant.

2.9.1 Seismic coherence

The SPECFEM3D simulation of seismic correlations yields a time-domain correlation $C_{ij}(\tau)$ between two receivers. Our analysis requires the Fourier transform,

$$S_{ij}(f) = \int_{-\infty}^{\infty} \mathrm{d}\tau \, C_{ij}(\tau) \mathrm{e}^{\mathrm{i}2\pi f\tau}, \tag{2.14}$$

which, according to the Wiener-Khinchin theorem (which is proved as a consequence of Parseval's theorem), is the cross power-spectral density (CPSD) between

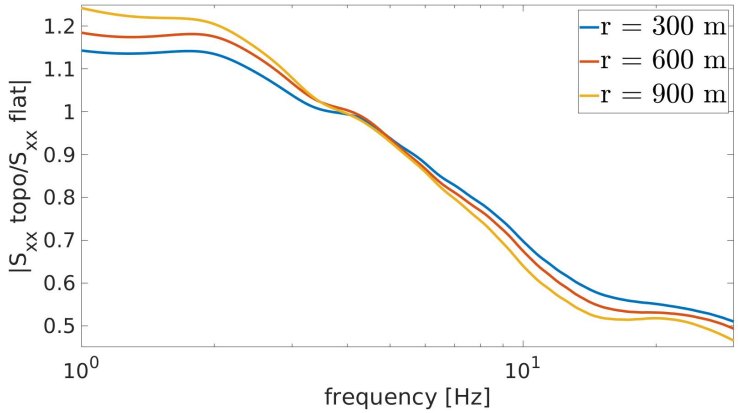

FIGURE 2.12: Ratio of seismic spectral densities at the center of topographic (A3 vertex) and flat models for different values of the minimal distance of seismic sources.

the two sensors. The CPSD can be normalized so that its absolute value lies between 0 and 1, a quantity called *coherence*:

$$c_{ij}(f) = \frac{S_{ij}(f)}{\sqrt{S_i(f)S_j(f)}}. \tag{2.15}$$

Figure 2.13 summarizes four analyses of seismic coherence with SPECFEM3D. In plot (a), we show the absolute value of coherence for the flat-surface and A3-topography models with varying minimal distances of seismic sources of the ambient field. While the coherence is significantly different between the two models, it only depends weakly on the minimal distance of sources. The plot also contains an analytical prediction of coherence for the flat-surface, isotropic Rayleigh-wave field, where the coherence is given by a Bessel function

$$c_{ij}(f) = J_0(2\pi f|\vec{r}_j - \vec{r}_i|/c_R) \tag{2.16}$$

with a Rayleigh-wave speed of $c_R = 1840\,\mathrm{m/s}$. In this simple case, the coherence is real-valued, but it is generally a complex quantity. The distance between the two receivers is 130 m.

Plot (b) shows the absolute value of coherence for varying distance between the two receivers. Again, the coherence obtained from the A3-topographic model is qualitatively different from the flat-surface coherence for all distances between receivers. With the A3-topographic model, $|c_{ij}(f)|$ does not vanish at any frequency, which is likely due to a mixed wave content with Rayleigh waves and scattered waves of different wavelengths.

In plot (c), we verify that the size of the standard finite-element model (3 km $\times$ 3 km) was not chosen too small for analyses in this research, *i.e.*, that coherence changes weakly when increasing model size. While some change in coherence can be observed, it is minor especially in the frequency band of interest 3 Hz – 10 Hz, where NN might limit the sensitivity of Einstein Telescope.

Finally, in plot (d), $|c_{ij}(f)|$ is shown as a function of distance at 5 Hz frequency. The aforementioned qualitative difference between the flat-surface and A3-topographic models can be seen again. The flat-surface model closely follows the analytical

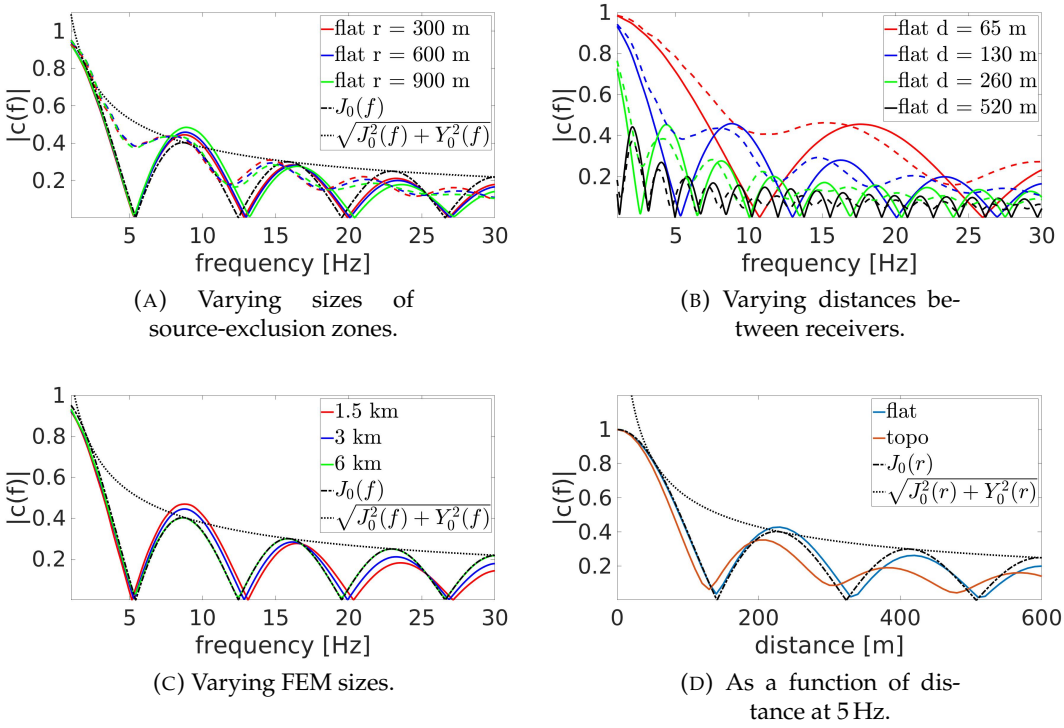

(A) Varying sizes of source-exclusion zones.

(B) Varying distances between receivers.

(C) Varying FEM sizes.

(D) As a function of distance at 5 Hz.

FIGURE 2.13: Plots of seismic coherence calculated by SPECFEM3D. The dashed, colored curves in (a) and (b) mark with corresponding colors the coherence with topography.

model of an isotropic, flat-surface Rayleigh-wave field.

2.9.2 Gravity-displacement correlation

The gravity perturbation produced by a seismic field can be expressed in terms of an integral over seismic correlations (Harms, 2019). It is possible to separate contributions from decompression and compression of the ground medium by seismic waves and from surface displacement. Surface displacement is usually much stronger than underground displacement due to the presence of surface waves such as Rayleigh waves. One of the reasons why Einstein Telescope is proposed as an underground infrastructure is to avoid the relatively strong gravitational noise from surface displacement (Amann et al., 2020).

As a consequence, and as a first step, we attempt to model the gravitational coupling between seismic surface fields and underground gravitational perturbations. The equation to be used takes the form of a surface integral (Harms, 2019)

$$C\left(\delta a_{\mathrm{arm}}(\boldsymbol{r_0}), s_z(\boldsymbol{r}); f\right) = G\rho_0 \int \mathrm{d}^2\boldsymbol{r'} C\left(s_n(\boldsymbol{r'}), s_z(\boldsymbol{r}); f\right) \frac{(\boldsymbol{r'}-\boldsymbol{r_0})\cdot \boldsymbol{e}_{\mathrm{arm}}}{|\boldsymbol{r'}-\boldsymbol{r_0}|^3}, \tag{2.17}$$

which is the CPSD between vertical seismic displacement s_z monitored at $\boldsymbol{r}$ and horizontal gravitational acceleration δa_{arm} at the location $\boldsymbol{r}_0$ of an underground TM. Here, G is Newton's gravitational constant, ρ_0 is the mass density of a homogeneous ground, and $\boldsymbol{e}_{\mathrm{arm}}$ is the unit vector pointing along the detector arm of Einstein Telescope. The integral contains the CPSD between vertical and normal

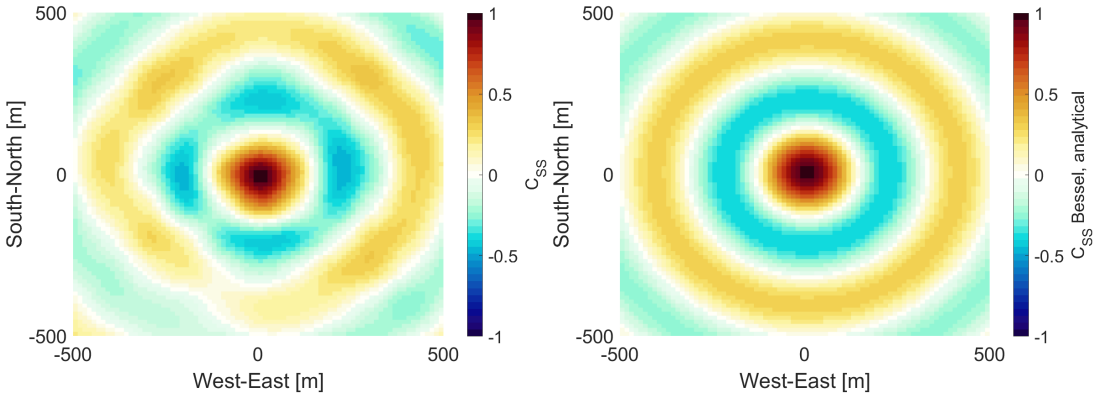

(A) SPECFEM3D simulation.

(B) Flat-surface, isotropic.

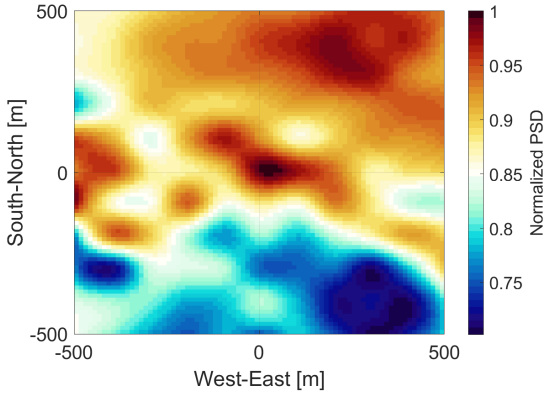

(C) Simulated vertical seismic displacement.

FIGURE 2.14: Normalized correlations (a) and spectral densities (c) calculated for an ambient field with SPECFEM3D at 5 Hz. The ideal (normalized) seismic correlations in the case of a flat-surface and isotropic field is shown in (b).

surface displacement provided by SPECFEM3D simulations. The A3-topography surface normals are shown in appendix A, figure A.3. We focus on normal surface displacement typically associated with Rayleigh waves since lateral surface displacement does not produce gravity perturbations. This also explains why in this study we are not interested in contributions from Love waves, which can only generate gravity perturbations by displacement of underground cavern walls of the detector. In any case, our homogeneous model does not support the simulation of Love waves. Since a homogeneous medium is simulated here, Love waves do not play a role, but it is still convenient for practical reasons (when comparing with other work or seismic observations) to focus on vertical displacement.

The seismic CPSD $C\left(s_n(\boldsymbol{r}'=\boldsymbol{0}), s_z(\boldsymbol{r}); f\right)$ for the A3-topographic model is shown in plot (a) of figure 2.14. It only represents a small subset of all seismic correlations required for equation (2.17). The result can be compared with the seismic CPSD in the case of a flat-surface, isotropic Rayleigh wave field shown in plot (b). Topography has a significant impact on seismic correlations, but the pattern of concentric rings is approximately preserved. The third plot shows the variation of power spectral densities of vertical surface displacement. Again, topography leaves a clear imprint on the seismic field in the form of an inhomogeneity. This plot in the case of the flat free surface model is shown in appendix A, figure A.4.

Equation (2.17) can be solved analytically in the case of a flat-surface, isotropic Rayleigh field, which yields (Harms, 2019)

$$C\left(\delta a_{\text{arm}}(\boldsymbol{0}), s_z(\boldsymbol{r}); f\right) = 2\pi G\rho_0 S\left(s_z; f\right) \mathrm{e}^{-h_{TM}k(f)} \cos(\phi) J_1\left(k(f)r\right), \tag{2.18}$$

with $\boldsymbol{r} = (r\cos(\phi), r\sin(\phi), h_{TM})$, ϕ being the angle between detector arm and the horizontal projection of $\boldsymbol{r}$, and $k(f)$ is the wavenumber of plane Rayleigh waves. According to this model, the CPSD between vertical displacement and gravity perturbation vanishes for $\boldsymbol{r} = \boldsymbol{0}$, as shown in plot (a) of figure 2.15. Instead, plot (b) is calculated by inserting the isotropic, flat-surface correlation of equation (2.16) into equation (2.17), but with a kernel that depends on topography. This shows that the kernel has an important impact on the seismic-gravitational CPSD, *e.g.*, the nodal line along the west-east direction seen in plot (a) is not present in the plot (b). Finally, the seismic-gravitational CPSD calculated with the seismic CPSD from SPECFEM3D and topographic kernel in equation (2.17) is shown in plot (c).

The result in plot (d) tells us where a single seismometer should be placed to obtain the best reduction of NN by coherent cancellation with a Wiener filter. The plotted quantity is

$$S(w; f) = \left|C\left(\delta a_{\text{arm}}(\boldsymbol{r_0}), s_z(\boldsymbol{r}); f\right)\right|^2 / C\left(s_z(\boldsymbol{r}), s_z(\boldsymbol{r}); f\right), \tag{2.19}$$

which is the power spectral density of the output of the Wiener filter (Cella, 2000; Harms, 2019). The higher it is, the more NN the Wiener filter is able to cancel in the data of the Einstein Telescope. This optimal placement of a seismometer is at (-38 m, -113 m). This plot in the case of the flat free surface model is shown in appendix A, figure A.5. The problem gets significantly more complicated if one wants to deploy multiple seismometers since the placement of sensors also depends on their mutual CPSDs. Nonetheless, the quantities required for such a multi-sensor optimization are provided by SPECFEM3D. They need to be used in numerical optimization routines (Badaracco and Harms, 2019).

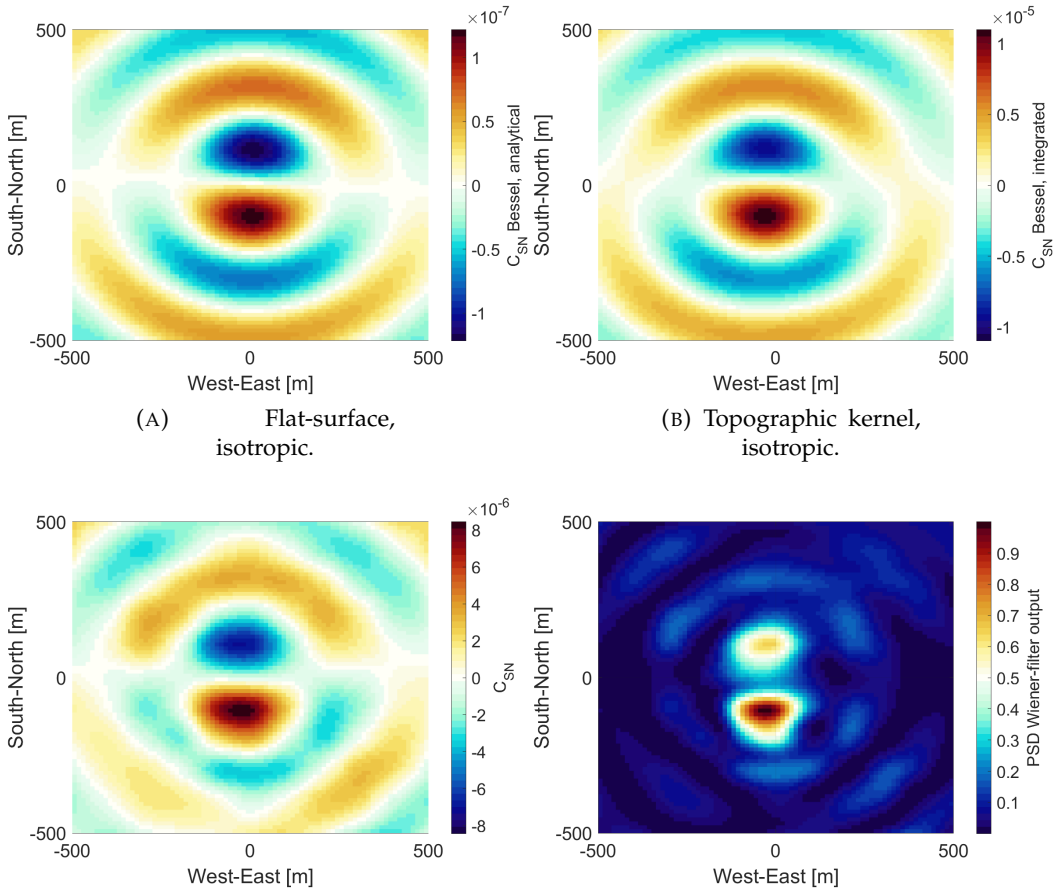

(A) Flat-surface, isotropic.

(B) Topographic kernel, isotropic.

(C) SPECFEM3D simulation.

(D) PSD Wiener filter.

FIGURE 2.15: Seismic-gravitational correlations of an ambient field at 5 Hz (a) – (c) in arbitrary, but consistent units. The normalized PSD of the Wiener-filter output is shown in (d). The test mass is located 100 m underground. The direction of gravity acceleration is along the A3 – A1 detector arm.

2.10 Bayesian seismic-array design

Since seismic measurements can only provide an incomplete understanding of seismic fields especially underground, estimates of NN and the optimization of sensor arrays can profit from numerical simulations. One needs to construct a surrogate model of the seismic field in terms of its two-point spatial correlations, which allows one to estimate seismic correlations between any two points in the field *i.e.* one needs cross-correlations as a continuous function of the coordinates of two points. For this, it is ideal to use both, information from seismic measurements and results from numerical simulations of seismic correlations. This can be done with a Bayesian approach, for example, using Gaussian Process Regression (GPR). This optimal modeling approach was developed for the Virgo detector, where however only displacements on the surface had to be considered (Badaracco et al., 2020). The task is computationally much more challenging for the simulation of seismic correlations in three dimensions. We had limited computational resources of only about 100-200 cores for calculating two-point spatial correlations for a surface array (Andric and Harms, 2020). Based on computational time in this case, the requirement for having the deeper model now and with a new estimate for how many pairs of points we need to simulate seismic correlations (which is much more in 3D), the computational time with old resources would be measured in months. So, we need to search for a new, suitable computer cluster.

For the Virgo array optimization, data from a very dense array were available, which means that the construction of the surrogate model was possible using only data (no numerical simulation of the seismic field was required). In Bayesian language, the analysis used uniform priors on seismic correlations. The situation will be different for ET with sparse sampling of underground seismic displacement. We cannot hope to have all the important seismic measurements (*e.g.* seismic displacements at all caverns), which provide likelihood in GPR. As a consequence, numerical models that implement topography and geology will be needed and used as priors of an otherwise data-based surrogate model of seismic correlations. The optimization of the array configuration will actually be based on a surrogate model of the Wiener filter, which depends on seismic correlations. The optimal array configuration minimizes the estimated residuals of a NN cancellation.

The Wiener filter surrogate model makes it possible to calculate the Wiener filter for an arbitrary number of seismometers placed at arbitrary locations. With this Bayesian seismic-array design we will be able to calculate the optimal sensor locations to maximize NN cancellation via Wiener filtering *i.e.* to optimize the array in 3D using multi-sensor numerical optimization routines, which will come with a great request for computational resources. Surrogate Wiener filter will allow us to make the best use of cross-correlation measurements. Another interesting result of the GPR is that it will tell us where to put sensors for more robust estimates *i.e.* at which locations we should put other seismometers during site-characterization campaigns to achieve a better overall estimate of the field of seismic correlations. It tells us where it becomes too model-dependent since in the places there is no data it relies too much on the prior. As one very important step, we would still need to investigate what type of seismic sensor helps most for efficient NN cancellation (Andric, 2022).

2.11 Conclusion

In this chapter, I presented synthetic seismic and gravitoelastic correlations between seismometers and a suspended underground test mass as part of the next-generation, gravitational-wave detector Einstein Telescope. The synthetics were calculated with the spectral-element SPECFEM3D Cartesian software. The main analysis was based on a topographic model centered at one of the vertices (A3) at a candidate site of the Einstein Telescope in Sardinia.

We found that A3-topography has generally a significant impact on seismic and gravitoelastic correlations. Specifically, calculations showed that Sardinian topography at vertex A3 scatters out energy from Rayleigh waves above 4 Hz protecting from the influence of distant seismic sources. As expected, symmetries of the field of gravitoelastic correlations are broken by topography leading to unique solutions of optimal seismometer placement for gravity-noise cancellation.

Since this work only addressed gravity perturbations from seismic surface displacement, an important future task is to extend the analysis to gravity perturbations resulting from (de)compression of rock by seismic waves, and from the displacement of underground cavern walls. In addition, geological inhomogeneities may be significant, which means that they should also be included in future modeling. SPECFEM3D can also tell us where we should improve our knowledge of geology. The current understanding of geology near the three vertex locations can be improved by drill-core and geoseismic studies, which would help to build a more accurate model and to improve simulation results.

The results are a powerful demonstration of SPECFEM3D's capability to model correlations in ambient seismic fields for the purpose of designing noise-cancellation systems using seismometer arrays. What is in fact proposed is to use the correlation results from numerical analysis to define priors for a Gaussian Process Regression, which then combines priors and observed seismic correlations for Bayesian inference of seismic correlations everywhere in the medium. This is a crucial step to calculate optimal array configurations for gravity-noise cancellation, which we expect to require several tens to hundreds of seismometers deployed in boreholes around 12 of the test masses of the Einstein Telescope. Bayesian seismic array design is close to the optimal that can be done to design a Newtonian noise cancellation system for Einstein Telescope. By doing this process properly we will decrease the required effort and therefore cost of a Newtonian noise mitigation system and increase the low-frequency sensitivity of Einstein Telescope.

Chapter 3

Lightsaber: A simulator of the angular sensing and control system for GW detectors

In this chapter, I will present the Lightsaber, an ASC time-domain simulator that can serve to test novel feedback-filter designs. This chapter is based on the paper by (Andric and Harms, 2021) (section 3.1) and on the work done during my Caltech visit (section 3.2).

3.1 LIGO-Lightsaber

In this section, I will present LIGO-Lightsaber. It represents ASC as used at LIGO Hanford Observatory (LHO) during O3.

3.1.1 Introduction

The Advanced LIGO detectors employ multiple levels of both active and passive seismic isolation systems. An active stage is providing a low-vibration platform and passive isolation system, a quadruple pendulum stage (QUAD), is suspended from it (Matichard et al., 2014; Matichard et al., 2015). Vibration noise is transferred to QUAD from the suspension platform, and QUAD reduces it by several orders of magnitude to reach LIGO's wanted displacement sensitivity of 10^{-19} m above 10 Hz. Like this, LIGO utilizes both active and passive vibration isolation systems to clear its way to detect GWs (*Vibration Isolation*; Abbott et al., 2016a), but this doesn't fully solve the problem of vibrational noise in LIGO.

The strain sensitivity improves as square-root of power in the high frequency (> 200 Hz) shot-noise-limited band. More light power in the arm cavities means stronger optomechanical couplings, leading to radiation pressure (RP) noise and to additional challenges with IFO control. More power also introduces the thermally induced side effects which need to be tackled for optimal IFO operation. So, the LIGO IFO is a complex optomechanical system whose angular mechanical transfer functions are dominated by radiation pressure effects (Dooley et al., 2013). A long-known concept is that RP creates torque, but optical torque's ability to destabilize optical cavities was first acknowledged in 1991 (Solimeno et al., 1991). Sidles and Sigg in 2006 were the first to completely model the theory of the RP's effect on angular mechanical transfer functions (tfs) (Sidles and Sigg, 2006). More elaboration on this topic can be found also in (Driggers, 2006; Fan et al., 2009; Hirose

et al., 2010). The concern arose that RP might be the factor limiting LIGO's ability to increase the arm cavities' light power.

It is important to have the test masses steady at low frequencies (below 3 Hz) in order to have the beams in the right spatial mode, to have the stable operation of the IFO at high power, to limit couplings to technical noise sources, and to maintain the good quality of interference at the antisymmetric port (Fritschel et al., 1998). Angular Sensing and Control is an important part of the control system to achieve this goal. The role of the ASC, apart from reducing the angular displacements, is to control optomechanical instabilities up to a few Hertz (Kasprzack, 2018). One of the most important measures of the effectiveness of the ASC is how much noise it contributes to the differential arm length change between the long Fabry-Perot arm cavities since DARM is the most sensitive degree of freedom to the passage of GWs (Allocca et al., 2020). DARM residual motion must be suppressed for the IFO to reach the desired sensitivity. The coupling between the DARM and ASC is in essence nonlinear since the coherence between these two signals is low. Nonlinear angle to length coupling is created by the combination of the angular mirror motion with the beam-spot motion on the mirror (Seymour et al., 2017; Buikema et al., 2020). As long as the DARM noise due to this coupling is well below the desired displacement sensitivity, and as long as the overall angular motion is sufficiently small so that the interferometer can be operated stably, the ASC performs well.

The problem for ASC is that in the process of controlling TMs at low frequencies, high-frequency noise is introduced in the observation band (above 10 Hz) originating mostly from the readout noise of sensors and less from imperfections of actuators at the penultimate mass (PUM) of the QUAD (Dooley, 2011; Dooley et al., 2013; Barsotti and Evans, 2011). This noise interferes directly with GW measurements. In ASC, requirements to reach sensitivity goals are to reduce RMS of angular TM motion below 1 nrad and to introduce the lowest possible noise in the angular TM motion above 10 Hz (Barsotti and Evans, 2011). Since during the O3 run the noise budget was dominated by the controls noise approximately between 10 Hz and 25 Hz, where it was 10–100 times higher than quantum noise and it was a significant noise source up to 55 Hz, it is crucial to mitigate this noise in order to achieve sensitivity improvements (Kasprzack, 2018; Buikema et al., 2020). Reducing it, the SNR of observable GW signals will increase and therefore enhance the astrophysical impact of the GW observatories (Hild et al., 2011; Maggiore et al., 2020). Specifically, early observation of the inspiral of NS binaries can be used to alert observatories of an upcoming merger (Chan et al., 2018), and detection of IMBH binaries would be greatly facilitated (Maggiore et al., 2020; Sathyaprakash et al., 2012; Abbott et al., 2020; Jani, Shoemaker, and Cutler, 2019). It is possible to follow the waveform evolution for a longer amount of time, which means more accurate estimates of some of the parameters of the binary systems including sky location (Grimm and Harms, 2020).

In this section, I present a time-domain simulator of the ASC at LHO. It incorporates the dominant nonlinear couplings of the optomechanical system consisting of the high-power cavity laser beam and the last two stages of suspension in LIGO with the control system. Input noises are laser power fluctuations, the motion of the Internal Seismic Isolation (ISI) platform, noise from the suspension damping loops, and the readout noises of the angular control. The local degrees of freedom are simulated and converted into a global angular basis for the angular control as done in the real system. Most input noises are simulated by spectral

methods, and second-order section (SOS) (Smith, 2007) models cover the last two stages of the suspension system and the angular controls. Nonlinear optomechanical couplings are included explicitly through equations of motion, *i.e.*, not as effective time-variant SOS models. The feed-forward radiation pressure compensation (RPC) path is implemented.

In section 3.1.2, the general overview of the LIGO-Lightsaber is given. In section 3.1.3, LIGO's seismic isolation system is described briefly including the active and passive isolation systems and the relevant noise inputs. In section 3.1.4, radiation-pressure effects and optomechanical couplings are introduced. In section 3.1.5, the feedback control of the ASC and the radiation pressure compensation path are described. In section 3.1.6, I present the main results of our simulation involving nonlinear angular mirror pitch motion to strain noise coupling.

3.1.2 Overview of the LIGO-Lightsaber

The LIGO-Lightsaber is the time-domain simulator of the ASC at LHO. The way in which LIGO-Lightsaber is built is that most of the input noises are simulated using spectral methods to avoid an unnecessarily large dimension of the second-order section models. The linear couplings of the simulation are based on zero-pole-gain (ZPK) models converted to the second-order section models, which cover the last two stages of the suspension system and the angular controls. This means that also the ZPK specifications of control filters are internally converted into SOS models. SOS models are convenient for continuous sampling of system coordinates. The main mechanical degree of freedom simulated in Lightsaber is the pitch motion of the test masses, which introduces the dominant angular noise in GW measurements. Pitch dynamics between PUM and TM are constructed by combining SOS models and non-linear optical features. So, the LIGO-Lightsaber plant model is constructed from several static second-order section models representing the mechanical and feedback system together with several nonlinear optomechanical couplings:

- Fluctuations of arm-cavity power depend nonlinearly on cavity length changes;
- Radiation-pressure torque is a bilinear term that contains the beam-spot motion as well as power fluctuations;
- Strain noise is produced as a bilinear coupling between angular motion of test masses and beam-spot motion.

The readout of the TM pitch motion is given a readout noise. A linear ASC feedback filter in a global basis is implemented as used at LHO during the O3 run. The filtered signal is fed back to PUM. The mechanical system is simulated in its local degrees of freedom, while the control is produced with respect to the global angular modes. There is the feed-forward radiation pressure compensation implemented as it was during the O3 run at the LHO (Andric and Harms, 2021). Since Lightsaber can serve to test novel feedback-filter designs, such as Reinforcement Learning, there is strain noise filtering implemented in the Postprocessing class of the Lightsaber. In order to be able to check the robustness of the RL controller, the scaling parameters for input noises are introduced. This is useful in order to have more control over the plant (more free parameters). For now, LIGO-Lightsaber

simulates one arm-cavity. Light propagation times inside the arm cavities are neglected, which means that the noise estimates are only accurate below 45 Hz corresponding to the arm-cavity pole (Buikema et al., 2020).

The simulation is run with a sampling frequency of 256 Hz and the duration of the entire simulation run (as used for the results presented in this thesis) is 1024 s. The Lightsaber is written completely in Python. Some of the libraries, apart from standard ones, needed to run the simulation are signal, control, slycot, absl-py, json5, tqdm. On a PC with 12 processors, it takes a few minutes for one simulation run.

The simulation was originally run with state-space models (Williamson, 1999), instead of SOS models. State-space models are also very convenient for continuous sampling of system coordinates. On a PC with 12 processors, it was taking approximately one hour for one simulation run in this case. Switching to SOS models showed to significantly speed up the code, and reduced numerical errors.

3.1.3 Mechanical system

State-of-the-art seismic isolation, for a typical ground motion of 10^{-6} m RMS, is required to reach minuscule enough relative mirror motions needed to detect GWs. Advanced LIGO combines Hydraulic External Pre-Isolator (HEPI), Internal Seismic Isolation, and multi-stage passive suspensions to provide vibration isolation at all frequencies (Matichard et al., 2014; Abbott et al., 2002; Abbott et al., 2004; Robertson et al., 2004). HEPI is based on the control techniques and quiet hydraulic actuators developed at Stanford (Hardham, 2005). This active platform is used to reject very low-frequency disturbances such as micro-seismic and tidal motion. It provides long-range alignment capability to all directions of rotation and translation. It gives inertial active isolation in the frequency band 0.1–10 Hz (Hua et al., 2004; Wen et al., 2014; Matichard et al., 2014). Large optical tables on which the core optics suspensions are mounted are contained in the ISI platforms (Matichard et al., 2013). The low noise instruments provide inertial isolation and alignment capability in the range of 0.1–30 Hz. There are two types of ISI systems: the BSC-ISI (Basic Symmetric Chambers-ISI) are two-stage platforms for the core optics which require further seismic isolation (Matichard et al., 2010), and the HAM-ISI (Horizontal Access Module-ISI) are single-stage platforms for the auxiliary optics, and power and signal recycling mirrors (Danaher, Hollander, et al., 2007; Kissel, 2010). BSC-ISI is installed in the large LIGO vacuum chambers. It contains a 2 m wide optical table that can support more than 1000 kg of optical payload. It is bringing residual displacement down to $10^{-11}\,\mathrm{m}/\sqrt{\mathrm{Hz}}$ at 1 Hz, and it can reduce it to less than $2 \times 10^{-13}\,\mathrm{m}/\sqrt{\mathrm{Hz}}$ above 10 Hz. There are five BSC-ISI unites in IFO (four for input and end TMs and one for BS) (*Vibration Isolation*; Fritschel et al., 2001; Matichard et al., 2014). These systems deploy position and vibration sensors (like seismometers) along with permanent-magnet actuators. The ground motion is taken care of in a feedforward scheme, and the platform's motion in a feedback scheme in order to produce a counter-motion, and suppress displacements to keep the IFO's components still (Marrocchesi et al., 2015; Schwartz et al., 2020). This motion is subsequently passed through the QUAD also causing angular motion of the TM. The spectra of ISI displacements along the direction of the interferometer arm (longitudinal) are shown in figure 3.1a. The channels used to calculate these spectra are H1:ISI-ITMX_SUSPOINT_ITMX_EUL_L_DQ, and H1:ISI-ETMX_SUSPOINT_ETMX_EUL_L_DQ for input test mass, and end

test mass, respectively. Using a spectral representation of this noise as the basis for its simulation means that non-stationarities are neglected, but this is a valid approximation for most of the time. In our notation, L represents longitudinal displacements along the arm direction and P pitch rotations. We focus on L motion since this is the most important ISI degree of freedom, *i.e.*, the one expected to produce the strongest pitch motion of the test mass.

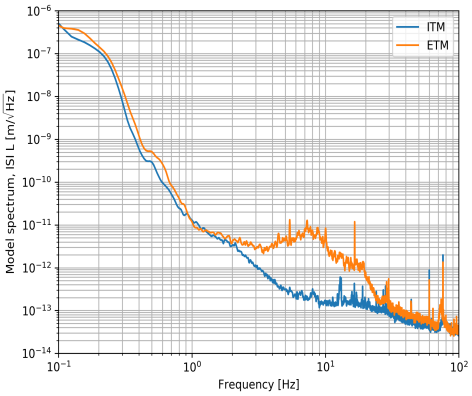

(A) ISI L

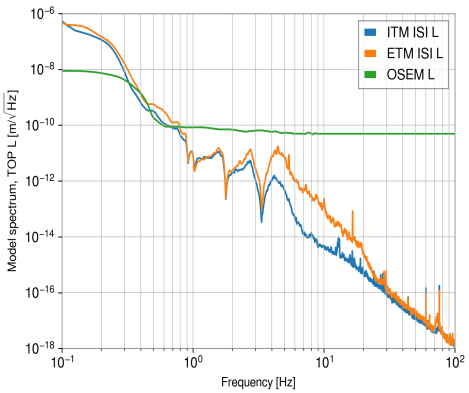

(B) TOP L

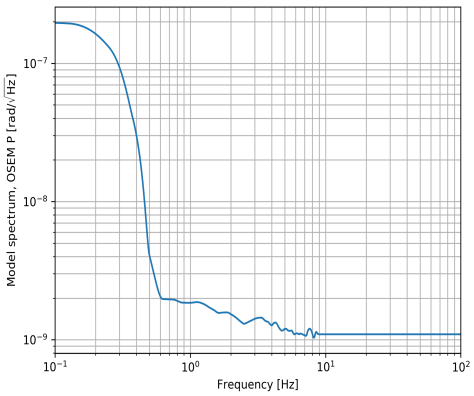

(C) OSEM P

FIGURE 3.1: Noise inputs passing through the QUAD. The spectra in (a) are directly obtained from LIGO Hanford O3 channel recordings. Plot (b) depends on a transfer function model from ISI L and TOP P to TOP L. The OSEM noise in (b) is simulated based on the spectral model shown in (c).

The suspensions of the test masses consist of a four-stage pendulum QUAD system, mounted on the ISI system, providing passive seismic isolation above a few Hertz. Apart from passive suspension, QUAD contains apparatus for additional local sensing, actuating, and controlling of this suspension, as well as actuator drivers and actuators for the global control of suspended optics (Advanced LIGO Systems Group, 2015). The masses of the four stages shown in figure 3.2 are called top mass (TOP), upper-intermediate mass (UIM), PUM, and the TM, and they sum up to about 120 kg, with the bottom two masses summing up to 80 kg. The mass of the 'Main chain' masses from top to bottom is about 20, 20, 40, 40 kg respectively. The QUAD is reducing displacements at 10 Hz by seven orders of

magnitude (Martynov, 2015). Steel wires are used for the suspension except for LIGO's TM's, which are suspended from 0.4 mm thick and 60 cm long fused-silica fibers bonded to PUM and TM (four fibers per TM). This final monolithic stage provides a high mechanical quality factor to lower thermal noise. Mechanical loss of the fused-silica is several orders of magnitude smaller than that of steel. It has a low density and high strength and this means that the fundamental violin mode of the fibers and the vertical eigenmode of the last suspension stage (bounce mode) are at higher and lower frequencies, respectively, than a corresponding steel wire, therefore violating less on the GW band (Advanced LIGO Systems Group, 2015; Abbott et al., 2016a). The first two masses of the 'Main Chain' are made out of steel, while PUM and TM are made of fused silica in order to preserve the low mechanical loss. A PUM is a cylinder whose axis of rotational symmetry is aligned with the TM. The ear-to-mass bonds are made with hydroxide-catalysis bonding (Advanced LIGO Systems Group, 2015). The 40 kg TM is cylindrical with a radius of 17 cm, and a thickness of 20 cm. In addition to the 'Main Chain', which faces the light beam and supports the TM, there is a nearly identical 'Reaction Chain' placed 5 mm behind it for the ETMs and 20 mm for the ITMs. The purpose of this chain is to be a quiet platform for applying control forces for longitudinal and angular DOFs, to filter any disturbances that could couple through the actuators, in order to hold the interferometer close to a dark fringe. The overall design of the two chains in terms of blades, wire lengths, attachment points, and masses are very similar to ease the manufacture and damping control. In LIGO, digital servo systems are used to feed control signals back. Forces are applied using either electromagnetic coils or electrostatic actuators (Aston et al., 2012; Carbone et al., 2012; Harry and LIGO Scientific Collaboration, 2010; Shapiro et al., 2015; Buikema et al., 2020; Barsotti and Evans, 2011; Abbott et al., 2016a). Gentle control forces are applied on the TM with the electrostatic drive. Electro-static actuators are on reaction masses, and magnetic actuators directly on the TMs are avoided to avoid direct magnetic noise coupling. The gold pattern is deposited on the face of the ultimate reaction mass and applies forces to the TM with an electrostatic field (Advanced LIGO Systems Group, 2015; *Vibration Isolation*; Buikema et al., 2020; Fritschel and LIGO Scientific Collaboration, 2015; Soni et al., 2021; Harry and LIGO Scientific Collaboration, 2010).

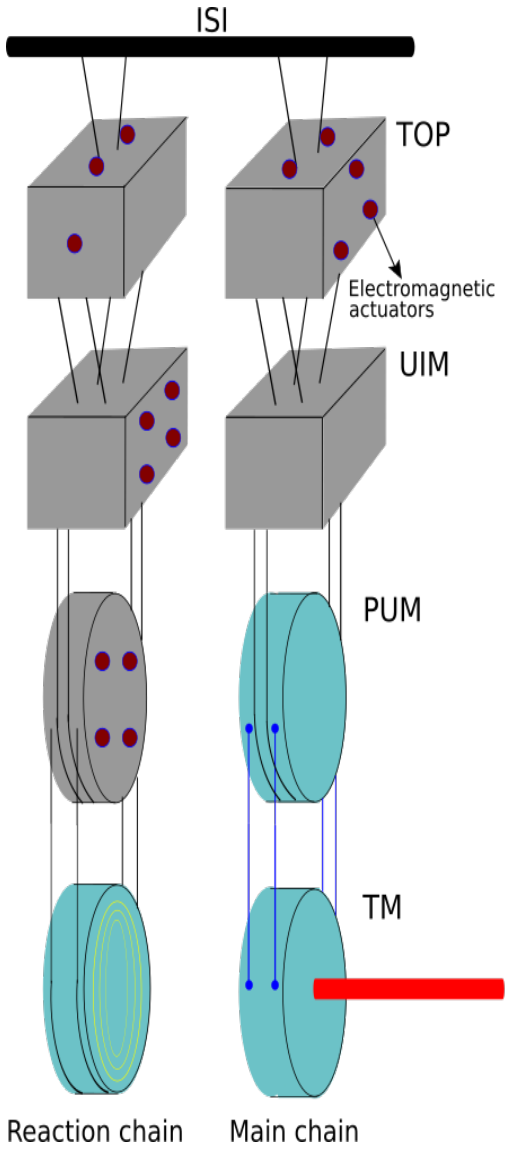

FIGURE 3.2: Schematic of the quadruple pendulum stage in LIGO.

The QUAD is designed to place the frequencies of its fundamental modes in different DOFs close to each other and well below 10 Hz to yield effective noise reduction in the GW observation band (*About "aLIGO"*; Andric and Harms, 2021). Each pendulum stage provides f^{-2} isolation above the resonant frequencies (Shapiro et al., 2015). The length change of the arm cavities should not vary more than a fraction of picometre in order to operate IFO successfully (*Vibration Isolation*; Aston et al., 2012). The suspended TMs respond like free masses to horizontal longitudinal forces above 10 Hz effectively. Pitch motion is the rotation of a TM about its horizontal axis, and yaw angular motion is the rotation of a TM about its vertical axis (Fritschel et al., 1998), with the main free pitch and yaw resonances being set to 0.55 Hz and 0.6 Hz, respectively (Yu, 2019; Barsotti and Evans, 2011). Length and pitch DOFs are coupled, which leaves an imprint of the longitudinal resonance at approximately 0.45 Hz in the pitch angular motion. The longitudinal-to-pitch coupling is also responsible for bigger pitch motion compared to yaw (3–5 times larger) being excited by longitudinal motion of the ISI (Kasprzack, 2018; Abbott et al., 2008).

To minimize pitch transmission from the suspension point, the TOP masses are suspended by two wires from the suspension point. In other cases, there are four wires. The four-stage pendulum QUAD system has many DOFs with low-frequency resonances. Fibers can ring up, there are rotational and translational resonances, in total 24. 22 out of the 24 pendulum modes are observable and controllable from the TOP mass. Therefore, local damping of all the low-frequency suspension modes is done with co-located Optical Sensors and Electro-Magnetic actuators (OSEMs) on the TOP mass to insure that any sensing noise will be well isolated from the TM. The basic OSEM components are a Light-Emitting Diode (LED), a photodiode, and a coil of wire. A flag blocks part of the LED light and produces a position-dependent signal from the PD. When there is current through the coil an actuation force is produced on a permanent magnet mounted under the flag (Shapiro et al., 2015; Carbone et al., 2012; Harry and LIGO Scientific Collaboration, 2010). These damping sensors and actuators are placed on the 'Main Chain', while the ASC signal, and other control signals, are applied from the 'Reaction Chain' (Buikema et al., 2020; Abbott et al., 2016a). 22 resonances are between 0.5 Hz and 5 Hz and are actively damped using feedback to TOP mass. Other 2 resonances exist at 9.7 and 13.8 Hz (which are the highest vertical and roll modes), which couple weakly to both input disturbances and the TM, and are damped by tuned-mass dampers (Robertson and Torrie, 2016; Fritschel, 2015; Aston et al., 2012; Fritschel and LIGO Scientific Collaboration, 2015; Shapiro et al., 2015). Attenuating low-frequency resonances using OSEMs, to avoid amplification of motion, the noise is introduced over a broad band of frequencies. This noise mainly comes from the briefly previously described shadow-sensing detection scheme, used to monitor the motion of a mass with a spectral density of about a few times $10^{-11}\,\mathrm{m/Hz^{1/2}}$ at 1 Hz per OSEM (Fritschel and LIGO Scientific Collaboration, 2015; Carbone et al., 2012; Martynov, 2015; Shapiro et al., 2015). Another smaller source of noise comes from the electromagnetic actuators. These noises are to be injected at the TOP mass and transferred to the TM (contribute to its pitch motion). The spectra of these noises are shown in figure 3.1(b, c), respectively. For comparison, also the ISI L contributions to the TOP L motion at ITM and ETM are shown in figure 3.1b. Seismic noise dominates approximately below 1 Hz and OSEM noises above 1 Hz. Together they form the main mechanical drivers of TM pitch motion. Transfer functions from ISI and TOP to TM are required to get the noise spectra at the TM level, and they are shown in figure 3.3(a, b, c). Note that while most angular transfer functions are in units rad/Nm, *i.e.*, the angular motion produced by a certain torque input, the transfer function for the OSEM noise in figure 3(c) has unit rad/rad since the noise is provided as an effective angular displacement produced by a damping loop that is not explicitly modeled in LIGO-Lightsaber. The spectra of the overall noise injected at ITM and ETM are shown in figure 3.4. The high-frequency plateau in this plot is due to the numerical limit of the simulation. These spectra are being used to generate a time series of Gaussian noise added sample-wise to the TM's angular motion during a time-domain simulation.

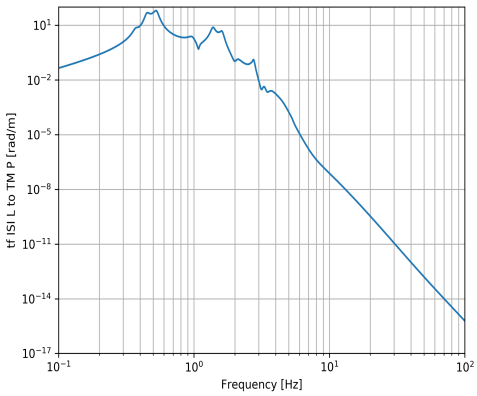

(A) tf ISI L to TM P

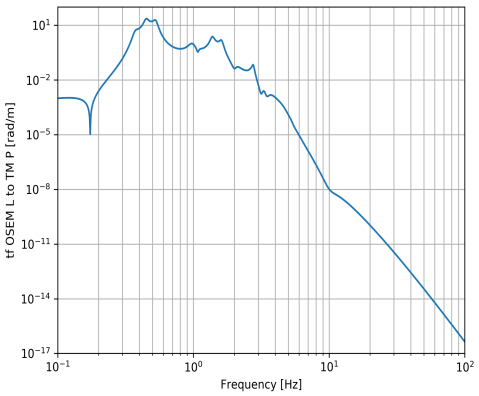

(B) tf OSEM L to TM P

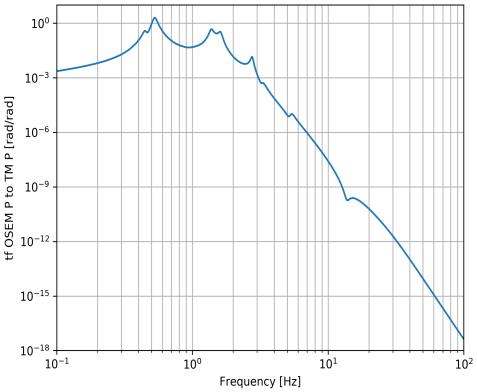

(C) tf OSEM P to TM P

FIGURE 3.3: QUAD suspension transfer functions. For OSEMs the transfer function magnitude is with respect to 1 rad/Nm.

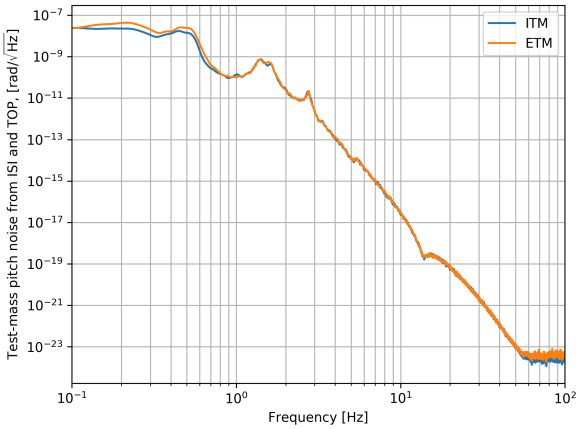

FIGURE 3.4: Simulated total noise passing through the suspension system for input and end test mass.

The mechanical transfer function is required from PUM pitch torque to TM P

angular motion. Since this part of the suspension system needs to be included in the dynamics of the time-domain simulation, it is represented as an SOS model. As a starting point, we use the ZPK model, which approximates all the dynamics of the QUAD suspension affecting this stage, *i.e.*, incorporating the effect of cross-couplings between DOFs and transmission from TM to PUM. The ZPK model is converted into an SOS model for the time-domain simulation (see figure 3.8 for a bode plot). The values of the parameters of the ZPK model are summarized in the table 3.1.

Zeros	Poles	Gain
-0.2107342 ± 2.871199j	-0.1543716 ± 2.727201j	93.52955
	-0.08732026 ± 3.492316j	
	-0.3149511 ± 9.411627j	

TABLE 3.1: ZPK model describing the transfer function from PUM P torque to TM P angular motion.

3.1.4 Optomechanical system

In the current generation of GW detectors, the optical power inside arm cavities is high (200 kW assumed in this simulation). It is important to examine the interaction between the mechanical system and the light field. In the regime of high circulating power, RP modifies the pendula dynamics and couples the angular motion of different suspended optics (Hirose et al., 2010). Since the amount of power stored in the arm cavities is much higher than in other parts of the IFO, optomechanical couplings in the recycling cavities can be neglected as a first step (Allocca et al., 2020). The fundamental RP coupling considered in the simulations is the torque produced by the light onto the suspended TMs (Seymour et al., 2017)

$$\tau_{\mathrm{RP}}(t) = \frac{2P_a(t)}{c} y(t), \tag{3.1}$$

assuming that all of the light is being reflected from the TMs. Torque fluctuations can be caused by power fluctuations $P_a(t)$ and/or beam-spot motion $y(t)$. Since the torque creates angular motion, which, in turn, creates beam-spot motion on the other TM, feedback is established leading to an optomechanical angular spring connecting the cavity mirrors (Allocca et al., 2020; Dooley et al., 2013). The cavity arms are long, which means that the small angular motion of one TM can create significant beam-spot motion on the other TM.

The cavity's mechanical tf is changed by optically induced torsional stiffness, as a function of the circulating power. To understand how the cavity dynamics are affected by RP, it is useful to diagonalize the coupled equations of the TMs' motions into normal cavity modes. The resulting decoupled equations of motion govern specific combinations of angular motions of the two TMs, the global modes, instead of the pitch or yaw of an individual TM. For yaw and pitch, we can thereby define the so-called *soft* and *hard* modes (Dooley et al., 2013; Dooley, 2011). The hard mode corresponds to a rotation of the cavity axis and the soft mode to a lateral offset of the cavity axis as shown in figure 3.5. So, a simple single resonance of a given TM splits into two, where frequency shifts are power-dependent.

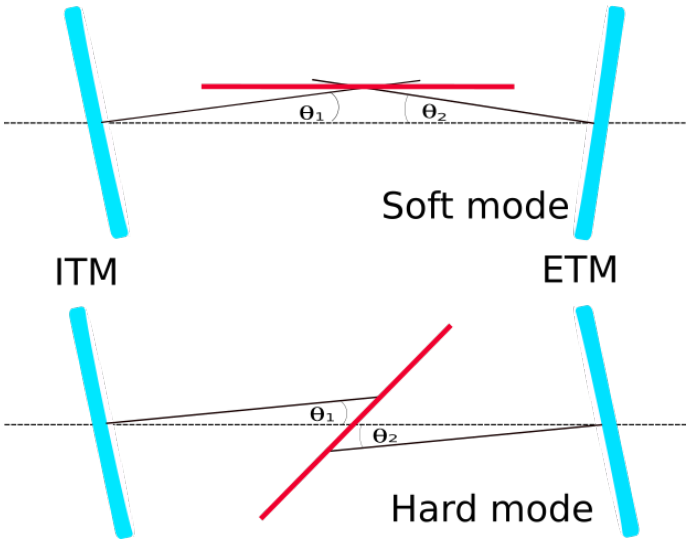

FIGURE 3.5: Visualization of global basis angles diagonalizing the torque stiffness matrix.

Since in the soft mode RP torque works against suspension torque (softens mechanical spring), its eigenfrequency is lower than the eigenfrequency of the suspension itself. The hard mode situation is the opposite, so the eigenfrequency of the hard mode is higher than the eigenfrequency of suspension (hardens/stiffens mechanical spring). Shifting of resonant frequencies increasing the arm-cavity power is shown in figure 3.6 (a, b) for soft and hard modes, respectively.

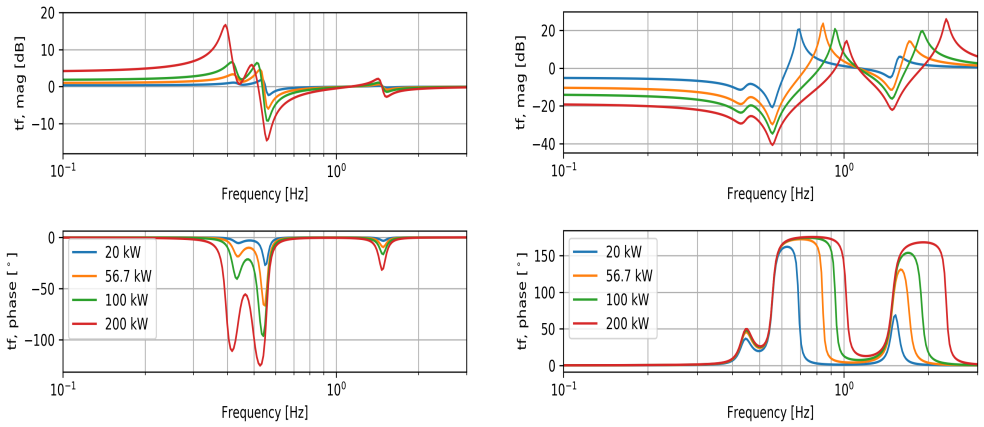

(A) Soft mode (B) Hard mode

FIGURE 3.6: Bode plot of Sidles-Sigg feedback transfer function with changing arm-cavity power.

Increasing the light power inside the arm cavities, RP torque can exceed restoring torque of the suspension, at which point the total torsional spring constant becomes negative making the resonance frequency of the soft mode imaginary and the entire system statically unstable. This creates a run-away situation where motion grows exponentially (Dooley et al., 2013; Barsotti, Evans, and Fritschel, 2010; Seymour et al., 2017; Hirose et al., 2010). To guarantee stability, the control filter

has to be properly shaped (Allocca et al., 2020). Particularly, the unity gain frequency (UGF) of the loop needs to be about 10 times higher than the frequency of the unstable resonance in order to provide overall stability (Barsotti, Evans, and Fritschel, 2010; Barsotti and Evans, 2011). On the other hand, the hard mode is always stable at DC, but external control is also needed to suppress the hard mode at its shifted resonant frequency (Yu, 2019). The complete derivation of the RP torsional spring constants is given in (Sidles and Sigg, 2006). The torques of soft and hard mode are

$$\tau_{S,H} = \kappa_{\mathrm{RP}} \frac{g_1 + g_2 \pm \sqrt{(g_1 - g_2)^2 + 4}}{2}, \tag{3.2}$$

where the plus sign corresponds to the soft mode and the minus sign to the hard mode and

$$\kappa_{\mathrm{RP}} = \frac{2P_a L_a}{c\,(g_1 g_2 - 1)}, \quad g_{1,2} = 1 - \frac{L_a}{R_{\mathrm{ITM,ETM}}}, \tag{3.3}$$

with P_a being the light power inside the cavity assumed to fluctuate around 200 kW, L_a is the arm-cavity length (3994.5 m) and, $R_{\mathrm{ITM,ETM}}$ are the radii of curvature of the ITM (1934 m) and the ETM (2245 m), respectively. With these values for the radii of curvature and corresponding g-factor, the soft mode is suppressed (Barsotti and Evans, 2011). The condition for the optical stability of a Fabry-Perot cavity is $0 < g_1 g_2 < 1$ (Sidles and Sigg, 2006).

The torque eigenvalues quantify the magnitude of the RP torsional spring constant for each of the modes and they are -2.7579 Nm/rad for the soft mode and 60.6795 Nm/rad for the hard mode for a cavity power of 200 kW. The eigenfrequencies of each of the optomechanical modes can then be written as:

$$f_{S,H} = \frac{1}{2\pi}\sqrt{\frac{\tau_p + \tau_{\mathrm{S,H}}}{I}}, \tag{3.4}$$

where τ_p is the restoring torque of the TM suspension and it is 9.72 Nm/rad for pitch and 9.41 Nm/rad for yaw. I is the TM's equivalent moment of inertia and for pitch, it is 0.757 kgm^2 and for yaw, it is equal to 0.663 kgm^2 (Barsotti and Evans, 2011). Resonant frequencies for pitch soft and hard mode are 0.4827 Hz and 1.5348 Hz, respectively, and for yaw, soft and hard mode are 0.5041 Hz and 1.6364 Hz, respectively. The critical arm-cavity power, for which the pitch soft mode becomes unstable is 705 kW, and for yaw, it is 682 kW. One more important coefficient is the beam offset to angle coefficient, which tells us how much beam offset is produced on a TM due to the angular motion of the other TM. It is given by the following formula:

$$\left.\frac{\mathrm{d}y}{\mathrm{d}\theta}\right|_{\mathrm{S,H}} = \frac{L_a}{2}\frac{(\mathrm{g}_2 + \mathrm{g}_1) \pm \sqrt{(\mathrm{g}_2 - \mathrm{g}_1)^2 + 4}}{(\,\mathrm{g}_2\mathrm{g}_1 - 1)}. \tag{3.5}$$

For the soft mode, it is approximately -2100 m/rad and for the hard mode, it is approximately 45000 m/rad (*aLIGO LLO Logbook*; Yu, 2019; Andric and Harms, 2021).

These changes introduced by RP are referred to as the Sidles-Sigg effect: a mirror's angular motion causes beam-spot motion on the other mirror, which in turn creates a torque that may lead to either less or more angular motion depending on the phase of the feedback. RP torque fluctuations on the TM can be also caused by power fluctuations, which is referred to as the $dP/d\theta$ effect. It is generally assumed

that power fluctuations contribute less to the torque than the Sidles-Sigg effect, but in accordance with equation (3.1), it might depend on whether there are any static beam offsets maintained during the IFO operation, and the difference in feedback mechanisms for these two couplings also influences the overall impact (Yu, 2019). In our simulation, where we use the exact nonlinear coupling in the time domain, they are both incorporated in the same time-domain equation for the RP torque and if they form, will appear automatically.

For future detectors, in order to handle optomechanical instabilities, special care will be taken about mirrors' masses, g-factors, multistage pendulum, and the power of the laser. What also can be done is to improve sensors, which would require a lot of money. So, for future detectors, the issue needs to be addressed already with their design.

3.1.5 The angular control system

The rudimentary requirement for the angular sensing and control scheme is to suppress the angular mirror motion at low frequencies, to overcome angular instabilities induced by RP, without reintroducing noise in the GW signal (Barsotti, Evans, and Fritschel, 2010; Yu et al., 2017). Quadrant photodiodes (QPDs) and wavefront sensors (WFSs) monitor beams' shapes and positions. The signal that they collect is filtered and fed back to PUM by means of four electromagnetic actuators producing torque to align the TMs. This process including the last two stages of suspension in LIGO with the control system is sketched in figure 3.7, and a more detailed description of the angular controls process can be found in (Dooley et al., 2013). The sensors' readout noise is injected along with the desired control signal. It is a combination of photodetector electronics noise, optical shot noise, and vibration noise, *e.g.*, from the acoustic field for components outside the vacuum system (Dooley et al., 2013; Martynov, 2015). Also, actuators produce additional noise, which is significantly lower than the readout noise of the sensors, and neglected in current LIGO-Lightsaber simulations. Since at PUM the actuation range is larger the TM is not pushed directly for angular control. So, the PUM stage is used instead of the TM stage which has a very small actuation range. If feedback is put higher in the QUAD chain, control authority would be significantly reduced. Taking also into consideration that by actuating the PUM, any actuation noise is filtered by the final stage's f^{-2}, is making the pushing at PUM the optimal solution. The ASC requirement is to reduce the RMS of the mirror angular motion to below 1 nrad and at the same time inject the lowest possible noise in the observational band above 10 Hz. In fact, the sensors' readout noises dominate the pitch motion of the TMs at higher frequencies. It limits strain sensitivity in the band 10 Hz to 25 Hz, and it remains significant to higher frequencies (Dooley et al., 2013; Buikema et al., 2020). Instead, thanks to the highly efficient QUAD suspension, the noise coming from the ISI and OSEMs is weak at 10 Hz (Harry and LIGO Scientific Collaboration, 2010). In addition to the ASC, optical levers are used for angular stabilization, but these are not engaged in low-noise operation (Dooley et al., 2013; Adhikari, 2004; Hirose et al., 2010).

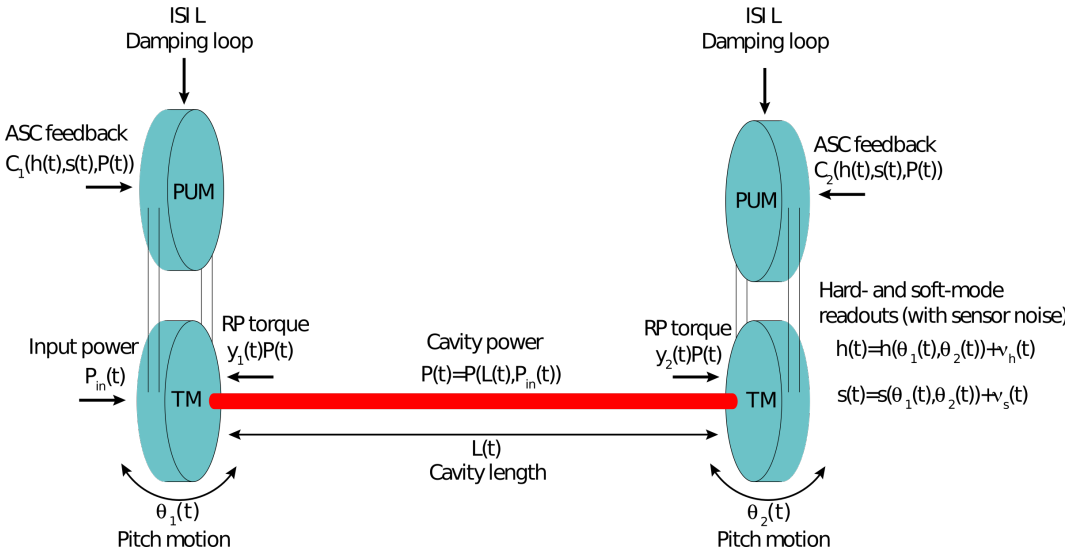

FIGURE 3.7: Diagram representing the simulated optomechanical system consisting of the high-power cavity laser beam and the last two stages of suspension in LIGO with the control system.

The LIGO-Lightsaber time-domain simulation uses local DOFs. As in the real ASC, a transformation to the global basis is required for the simulation of the feedback control, which implements filters acting on soft and hard modes. The filter outputs are converted back to the local basis for the actuator output at the two PUMs. The transformation into the global basis is also useful for analyzing the stability of the optomechanical system (Dooley et al., 2013). The transformation matrix connecting the angular motion of the TMs with the angle motion of the soft and hard modes is given by

$$\begin{bmatrix} \theta_{ITM} \\ \theta_{ETM} \end{bmatrix} = \begin{bmatrix} 1 & -r \\ r & 1 \end{bmatrix} \begin{bmatrix} \theta_{\mathrm{S}} \\ \theta_{\mathrm{H}} \end{bmatrix}, \tag{3.6}$$

where θ_{ITM} is the angular displacement of the ITM, θ_{ETM} is the angle of the ETM, θ_{S} is soft mode angle, θ_{H} hard mode angle, and r is defined as

$$r = \frac{(g_1 - g_2) + \sqrt{(g_1 - g_2)^2 + 4}}{2}. \tag{3.7}$$

The equation used for calculating beam-spots y_{ITM}, y_{ETM} on ITM and ETM is:

$$\mathbf{y} = \begin{bmatrix} y_{ITM} \\ y_{ETM} \end{bmatrix} = \frac{L_a}{1 - g_1 g_2} \begin{bmatrix} g_2 & 1 \\ 1 & g_1 \end{bmatrix} \begin{bmatrix} \theta_{ITM} \\ \theta_{ETM} \end{bmatrix}, \tag{3.8}$$

In order to get optical torque pitch noise, we need the response of TM pitch motion to RP torque, which in LIGO-Lightsaber is given by the ZPK model shown in table 3.2 (TM P to P transfer function). The bode plot of this transfer function is shown in figure 3.8. The spectra of the pitch motion due to optical torque for LIGO-Lightsaber are shown in figure 3.9. The Sidles-Sigg effect is a consequence of torque fluctuations due to beam-spot motion perturbing the TM angular motion, which causes beam-spot motion on the other TM, where the process repeats. These optomechanical dynamics form a loop that alters resonance frequencies as

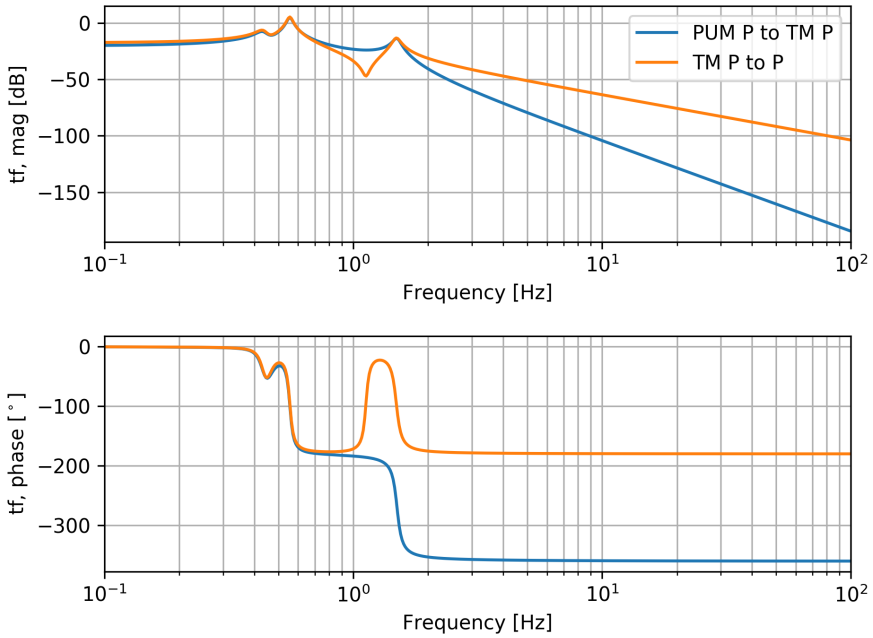

FIGURE 3.8: Bode plots of QUAD's last stage transfer functions. The transfer function magnitude is with respect to 1 rad/Nm.

discussed earlier. Optical torque noise superposes with external noise reaching the TMs from ISI and OSEMs. The controls signal is transferred from PUM to TM (PUM P to TM P in figure 3.8) and then summed with the other contributions to TM pitch motion. Another feedback path to consider is the radiation pressure compensation, which is explained below.

Zeros	Poles	Gain
-0.1772565 ± 2.866176j	-0.1393094 ± 2.737083j	2.567652
-0.1755293 ± 7.064508j	-0.08749749 ± 3.493148j	
	-0.3185553 ± 9.347665j	

TABLE 3.2: ZPK model describing optical torque to TM pitch angle transfer function (torque-to-angle response).

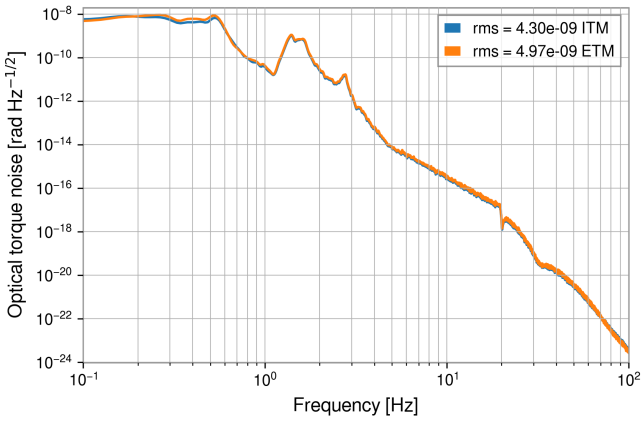

FIGURE 3.9: Spectra of ITM and ETM pitch motion due to the optical torque for 200 kW arm-cavity power.

With all contributions to the TM pitch angular motion summed up, LIGO-Lightsaber then simulates the readout of these motions in the global angular basis using the transformation in equation (3.6). WFSs sense the angular misalignment of the cavities with respect to their input beams and send a signal that corrects for the angle mismatch and QPDs see the beam transmitted through the arm cavities. QPDs maintain the alignment at low frequencies, primarily controlling beam-spot positions, while WFSs are performing it at frequencies up to several Hz (Dooley et al., 2013; Allocca et al., 2020). QPDs have four quadrants that sense the position of the impinging beam by comparing the amount of light present on each of them. WFSs give alignment signals by interference between the fundamental mode of the carrier/sidebands and the first higher order of transverse modes of the sidebands/carrier created by the misalignment of the IFO's optics. So, sensing of angular misalignments in the case of WFSs is done through a phase modulation–demodulation technique (Yu, 2019). More about WFS and QPD sensors and their placement and usage in IFOs can be found in (Yu, 2019; Fritschel and LIGO Scientific Collaboration, 2015). The sensing noise of the soft mode is $1 \times 10^{-13}\,\mathrm{rad/Hz^{1/2}}$ and of the hard mode it is $3 \times 10^{-14}\,\mathrm{rad/Hz^{1/2}}$. Due to the smaller bandwidth of soft mode loops with respect to the hard mode loops, their sensing noise contribution to the DARM noise is less severe than in the case of the hard modes (Yu, 2019). This signal is used for the ASC control signal including the radiation pressure compensation (both contained in the feedback 'C' in figure 3.7). The sensor outputs in our simulation have spectra shown in figure 3.10 (a, b), for the soft and hard modes, respectively.

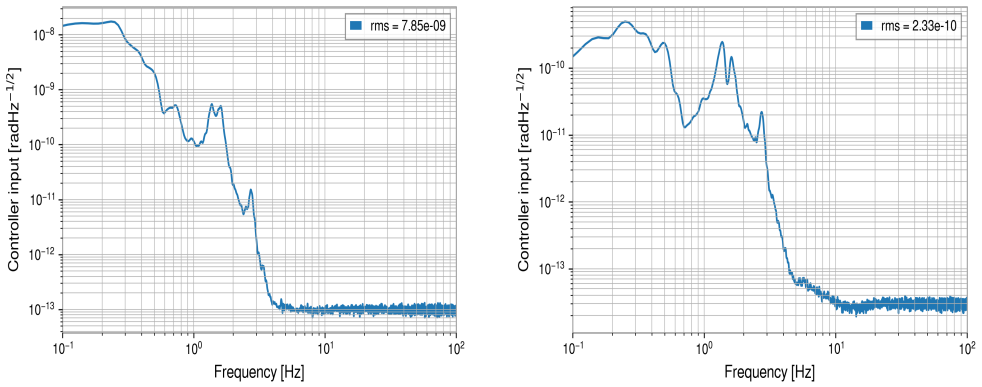

(A) (B)

FIGURE 3.10: Simulated spectra of the sensor outputs for the (**a**) soft and (**b**) hard mode.

Radiation pressure compensation

Arm-cavity RP effects are significant and hard mode resonant frequency is high (figure 3.6b) for 200 kW arm-cavity power. In order to handle these, at the LHO site the feed-forward radiation pressure compensation was implemented during the O3 run. The solution to stabilize the Sidles-Sigg effects comes from the fact that the torsional stiffness is a frequency-independent quantity that depends only on the cavity geometry (*i.e.*, the arm length, and the radius of curvature of TMs) and the arm-cavity power:

$$R_{\mathrm{S,H}} = \frac{2P_a}{c} \left.\frac{\mathrm{d}y}{\mathrm{d}\theta}\right|_{\mathrm{S,H}}. \tag{3.9}$$

The cavity geometry parameters are carefully measured with high accuracy prior to the installation of IFO, and the arm-cavity power can be measured in real-time. Therefore, the Sidles-Sigg feedback can be modeled accurately. The compensation is simply the addition of a parallel digital torque with the same shape but with the sign inverted as shown in figure 3.12. With this radiation pressure compensation path, having the arm-cavity power varying, the only parameter that needs to be adjusted is the DC gain (Yu, 2019). As a result, it is only needed to design a single controller that optimally stabilizes the system, and this filter will stay effective over at least a large range of input power levels. This will greatly facilitate the commissioning of the ASC at high-power operations (Buikema et al., 2020). While in the LIGO detectors, the compensation path is fed back onto PUM with the feedback filter containing an inversion of the PUM P to TM P mechanical tf, in LIGO-Lightsaber the compensation is directly given to TM P to avoid the tf inversion.

Both soft and hard Sidles-Sigg torques could be canceled entirely, but in practice, the introduction of a gain-adjustment factor in the path is necessary. This is because when the compensation is done for the hard mode, a digital torque corresponding to the soft mode is also sent to the suspension. If over-compensation accidentally happens it can cause destabilization of the system with the digital soft mode. This situation is avoided by performing under-compensation for the hard

mode. In RPC, the gain-adjustment factor is such that 200 kW is effectively reduced to 56.7 kW. In other words, with respect to the Sidles-Sigg optomechanics, the response function looks like a hard mode pendulum at an arm-cavity power of 56.7 kW, and small errors in the compensation path will not turn it into a destabilizing soft mode. The soft mode can be perfectly compensated, *i.e.*, reducing the arm-cavity power effectively to 0 W (Yu, 2019). In LIGO-Lightsaber, the ZPK model used in this compensation path is the same as the ZPK model describing optical torque to TM pitch angle transfer function, but with the gain obtained using equation 3.9 multiplied with the needed gain-adjustment factor (for the soft mode equal to 1, for the hard mode approximately 0.72). Before feeding back to the plant, this compensation signal is transformed into a local basis. Using this RPC technique is a much easier way of tackling the Sidles-Sigg effect than designing different frequency-dependent control filters at different power levels. This technique works well and it successfully eliminates the RP dependence in the response functions. More about it can be found in (Yu, 2019).

The sensing noise injection in the compensation path is actually quite low compared to the regular control path, but to avoid this noise contaminating the GW readout, an extra high-frequency cut-off filter is introduced. The design of this low-pass filter is quite flexible. Requirements are to have a phase delay $< 10^\circ$ at 3 Hz. What is used in our simulation is a second-order elliptic filter at 17 Hz with 40 dB attenuation above 17 Hz and 1 dB of ripple below 17 Hz. With this low-pass filter, the compensation path also meets aLIGO's requirement on the noise roll-off (Yu, 2019).

Feedback control

In order to stay at its nominal resonant condition, the IFO needs correct for angular motions. Filter design is typically obtained by a half-intuitive, half-quantitative method. It is difficult to design a filter that is stable over a relatively large span of input power and maintaining a high noise suppression at the same time. The controller is a linear filter providing stable feedback. It essentially takes the shape of a low-pass filter, with UGF tuned to the lowest possible value but providing high gain at lower frequencies (below 1 Hz) in order to reduce the motion of the TMs and with a relatively steep cut-off around 20 Hz, where the sensor noise dominates, to avoid sensing noise injection to GW channel. Steepening the cut-off can in principle reduce the noise introduced in the GW band, but with every pole used to reach the steeper drop-off, an extra 90° of phase loss is introduced. So limitation to the reduction of the TM motion comes from the nature of control loops. It is a compromise between servo's stability and sensing noise impression (Dooley, 2011; Martynov, 2015). The resulting need for a low-pass filter limits the achievable loops' bandwidth. One important thing to keep in mind during design is that the reduction of noise in the GW band is proportional to the UGF raised to the minus third or even minus fourth power (Dooley et al., 2013).

LIGO's ASC has feedback filters for soft and hard modes. The gain is chosen by the control system designer and must be chosen to achieve a stable system and sufficient RMS reduction. Brief description of calibration factors for LIGO-Lightsaber is given in appendix B, section B.1. The more complicated shape of the current control filters for the hard modes is partially to maintain the system's stability over a wide range of different input powers (Yu, 2019). It is not so difficult to control the soft mode, because the decreasing resonance naturally moves deeper into

the control bandwidth towards frequencies where the gain is higher (Fritschel and LIGO Scientific Collaboration, 2015). The stable, hard mode, is the one that poses the greater control challenge. Since the hard mode's natural frequency increases with power, it can potentially make the overall control loop unstable (Dooley et al., 2013). The price is that the control filter does not roll off fast enough to meet the LIGO's noise requirement in the 10–25 Hz band. A significant amount of control noise is injected in this band, contaminating the GW sensitivity (Yu, 2019; Yu et al., 2017).

The ZPK model for the soft mode controller is given in table 3.3 and for the hard mode controller in table 3.4. They consist of three components: control, low pass filter, and boosting component. In fact, most of the low-frequency actuation is sent to the upper stages of the suspensions to ensure a sufficient actuation range. In addition, the hard-mode readout is filtered and passed to the TOP mass to avoid instabilities in the reaction chain (Buikema et al., 2020). In LIGO-Lightsaber, this path is also directly given to PUM. The bode plots of the feedback soft and hard controllers are given in the figure 3.11. The simulation's controller output has spectra shown in figure 3.13 (a, b), for the soft and hard modes, respectively. The control signals are transformed to the local basis using equation 3.6. Then, tfs from PUM pitch input torque to TM pitch angular motion is used to calculate this signal at the level of the TM, and the loop is closed as shown in figure 3.12. The Simulink block diagrams for LIGO-Lightsaber are shown in appendix C, section C.1. The complete open-loop transfer function (OLTF) for soft and hard modes is given in the figure 3.14.

Component	Zeros	Poles	Gain
control	-0.88 $\pm$ 8.75j	-46 $\pm$ 100j	$9.34 \cdot 10^{8}$
	-1.885 + 0j	-39.2 $\pm$ 111j	
	0 $\pm$ 235.37221422j	-33.57836915 $\pm$ 47.32888881j	
	0 $\pm$ 115.38913934j	-7.29405346 $\pm$ 87.86565481j	
low pass	0 $\pm$ 93.32976848j	-21.09372154 $\pm$ 51.43961116j	0.35
	-4.45 $\pm$ 8.31j	-7.06 $\pm$ 6.245j	
boost	-1.07 $\pm$ 2.75j	-0.27 $\pm$ 2.94j	$1.32 \cdot 10^{-4}$

TABLE 3.3: ZPK model of the soft mode controller.

Component	Zeros	Poles	Gain
control	-0.3436 ± 4.11j	-78.77 ± 171.25j	5797.86
	-0.7854 ± 9.392j	-0.062832 + 0j	
		-628.32 + 0j	
top mass	-0.2π	0	1
low pass	0 ± 624.13953791j	-34.29016283 ± 56.5562509j	$3.16 \cdot 10^{-3}$
	0 ± 129.06849495j	-2.17157245 ± 126.18122121j	
	0 ± 193.59417786j	-46.61067471 ± 108.31124725j	
boost	-0.322 ± 0.299j	-0.161 ± 0.409j	841.52
	-0.786 ± 0.981j	-0.313 ± 1.217j	
	-1.068 ± 2.753j	-0.268 ± 2.941j	
	-1.53 ± 4.13j	-0.24 ± 4.39j	

TABLE 3.4: ZPK model of the hard mode controller.

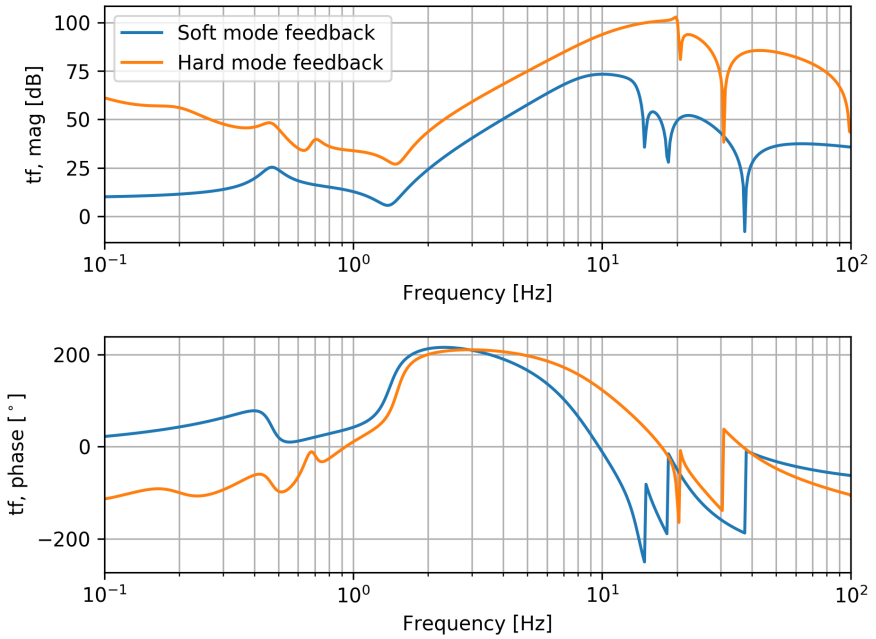

FIGURE 3.11: Bode plots of feedback control filters. The transfer function magnitude is with respect to 1 Nm/rad.

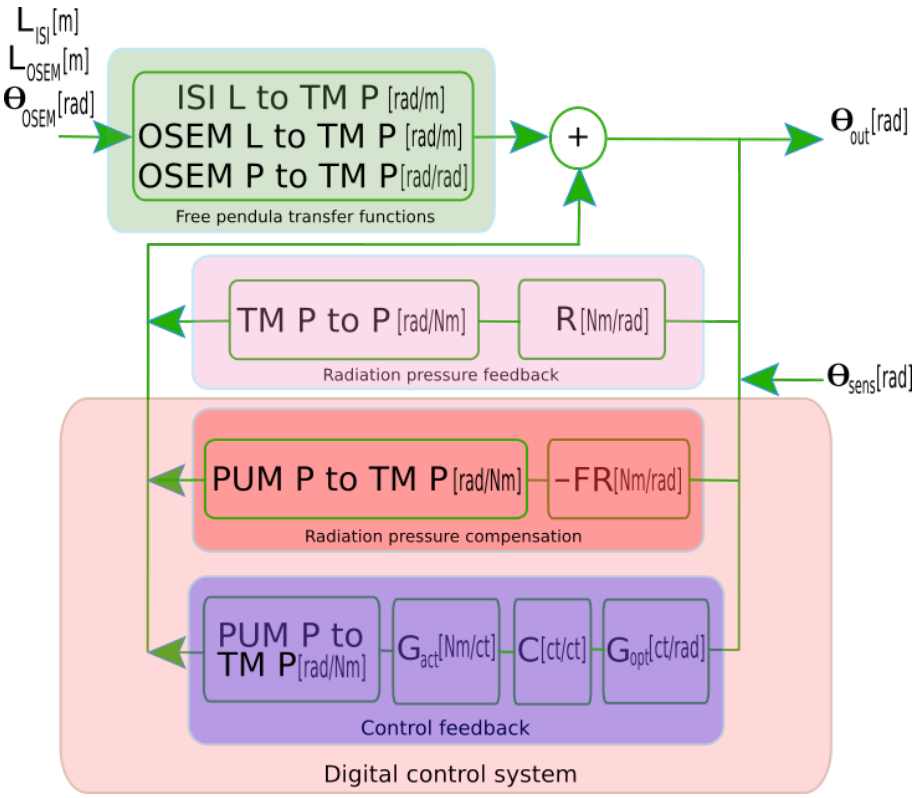

FIGURE 3.12: Diagram illustrating the components of the LIGO-Lightsaber simulation including RPC and feedback control. F is the gain-adjustment factor, G_{opt} converts angular motion into digital counts, and G_{act} converts digital counts into actuation torque.

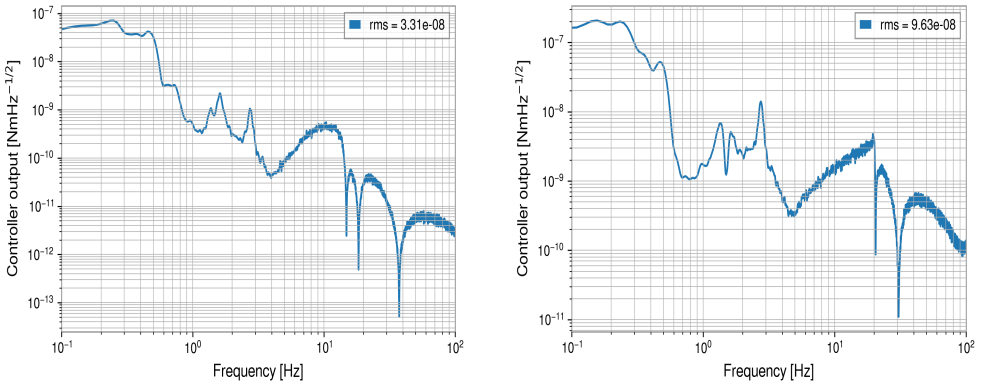

(A) (B)

FIGURE 3.13: Simulated spectra of the controller output for the (**a**) soft and (**b**) hard mode.

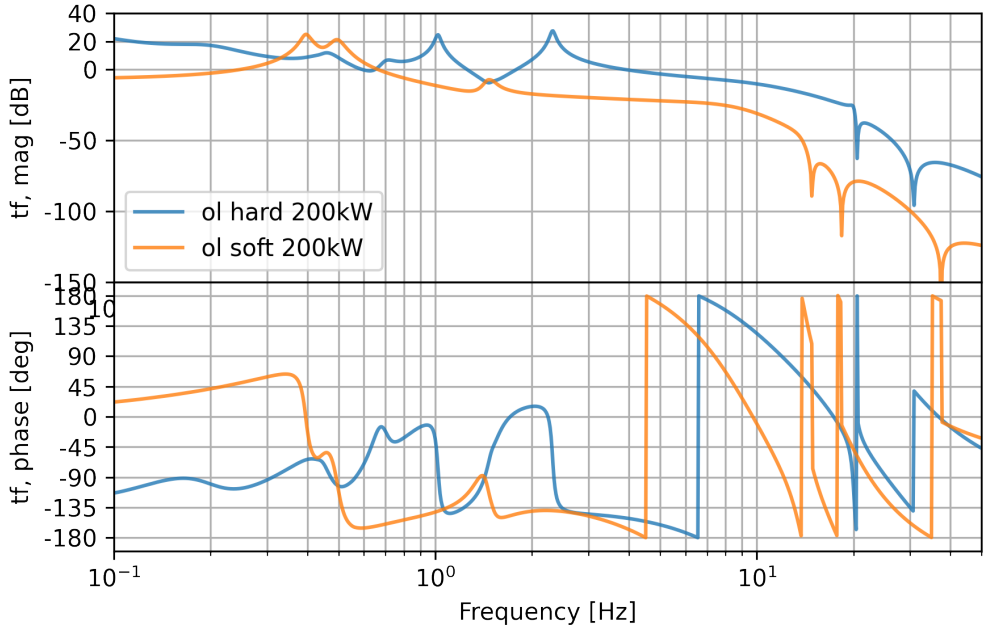

FIGURE 3.14: Bode plots of OLTFs for soft and hard modes.

3.1.6 Results

In LIGO-Lightsaber simulations, the ASC needs about a second to engage as shown in figure 3.15 for the hard mode. The simulation starts with a high RMS of hard mode angular motion and then it converges to the stationary situation. The spectra of simulated residual pitch angular motion for soft and hard modes are shown in figure 3.16.

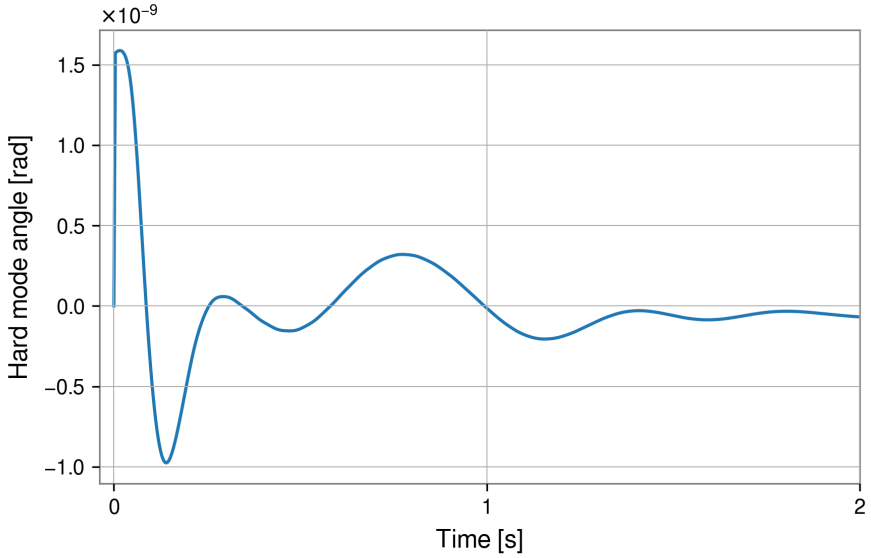

FIGURE 3.15: Demonstration of controls engagement in LIGO-Lightsaber in the case of the hard mode angular motion.

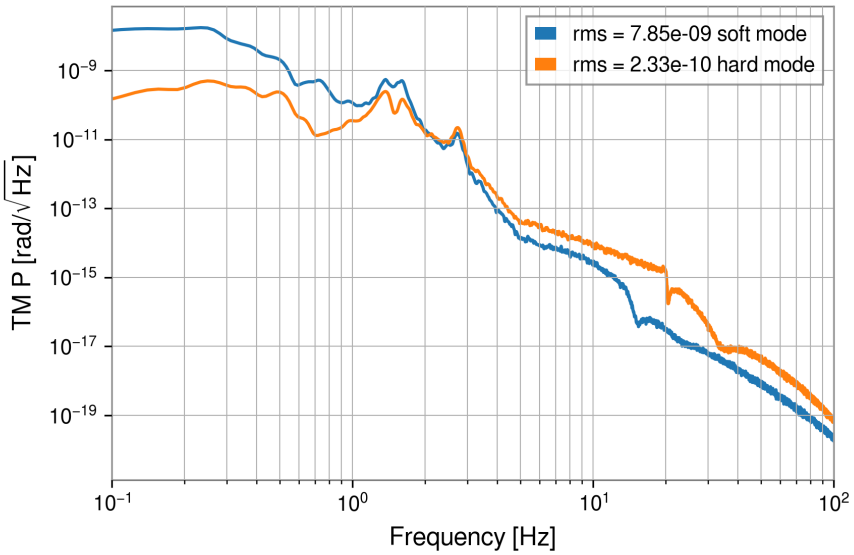

FIGURE 3.16: Simulated spectra of TM pitch motion for the soft and hard mode.

As explained earlier, important nonlinearity to be addressed in angular controls is that the strain noise coming from angular motion results as a product of beam-spot motion and angular motion. The beam-spot motion is relatively slow (mainly below 0.5 Hz), while angular motion is relevant at frequencies higher than 10 Hz (Barsotti, Evans, and Fritschel, 2010; Seymour et al., 2017). One of the problems here is that frequency components of spot position and angular motion could beat, creating hard-to-subtract noise (Driggers, 2013). The formula describing this bilinear process in the time domain using local angles is (Barsotti and Evans, 2011)

$$\Delta L_a(t) = y(t) \times \theta(t). \tag{3.10}$$

This coupling is easy to understand geometrically, as shown in figure 3.17. If the beam-spot position does not coincide with the mirror's rotational pivot, a length signal is created (Seymour et al., 2017). In order to evaluate angular noise coupled to the strain noise, we need to compute and add the length variation produced by each mirror. Beam spots are determined by angular motion (equation 3.8), and the coefficient $L_a/(1-g_1g_2)$ for LIGO is about $2 \cdot 10^4$ m/rad. The matrix's eigenvalues determine the coupling coefficients between beam-spot and angular motion for the soft and hard modes. According to the RMS values given in figure 3.16, the soft mode RMS is higher, but it produces smaller beam-spot motion and ultimately less strain noise as shown in figure 3.19a.

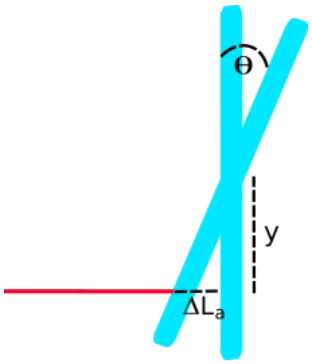

FIGURE 3.17: Angle-to-length coupling due to beam-spot miscentering.

The length change ΔL_a affects the arm-cavity power according to

$$P_a(t) = \frac{\tau_{ITM}^2 P_i(t)}{\left|1 - \rho_{ITM} \exp(4\pi j \frac{\Delta L_a(t)}{\lambda})\right|^2}, \tag{3.11}$$

where $P_i(t)$ is the input power that pumps the arm-cavity, τ_{ITM}, ρ_{ITM} assuming $\tau_{ITM}^2 + \rho_{ITM}^2 = 1$ are the transmissivity and reflectivity of the ITM (transmissivity of ITM is 1.4% and it is less than 6 ppm for the ETM (Harry and LIGO Scientific Collaboration, 2010)), and $\lambda = 1064$ nm is the wavelength of the laser light (Fritschel and LIGO Scientific Collaboration, 2015). The average input power is 705 W, and the spectrum of its relative fluctuations characteristic for the O3 run, commonly expressed as Relative Intensity Noise (RIN), is given in figure 3.18a [1]. Since LIGO-Lightsaber currently does not implement a length control, a simulation run, with DC offset, produces excess power fluctuations due to high length fluctuations entering the equation (3.11). As a temporary solution, a high-pass filter [2] is applied before inserting the length fluctuations into the equation (3.11), so the arm-cavity relative power fluctuations match input relative power fluctuations. Without beam offset, the power-to-angle-to-length-to-power loop is suppressed and excess power fluctuations cannot build up. The RIN with a high-pass filter satisfies the requirements on power stability in the control band given in (LIGO Laboratory / LIGO Scientific Collaboration, 2005). In the 0.1–0.4 Hz band, the RMS of RIN is approximately 10^{-3}, and in the 0.4–10 Hz band, it is approximately 10^{-4}. A typical simulated beam-spot motion has an RMS of about 0.02 mm with spectrum shown in figure 3.18b. Taking into account the ASC loops and the seismic inputs that are used, the RMS of beam-spot motion should be $\lesssim 0.1$ mm, which is consistent with the simulated result (Yu, 2019).

[1] RIN spectrum of the input beam is calculated from H1:ASC-X_TR_A_NSUM_OUT_DQ (transmission through end mirror), which is possible since the RIN of the simulated arm-cavity power, which generally depends on TM motion, is almost the same as the RIN of the simulated input power.

[2] It is a high-pass elliptic filter of 2nd order. The maximum ripple allowed below unity gain in the passband, specified in decibels, is 1. The minimum attenuation required in the stop band, specified in decibels, is 140. The critical frequency is 50 Hz.

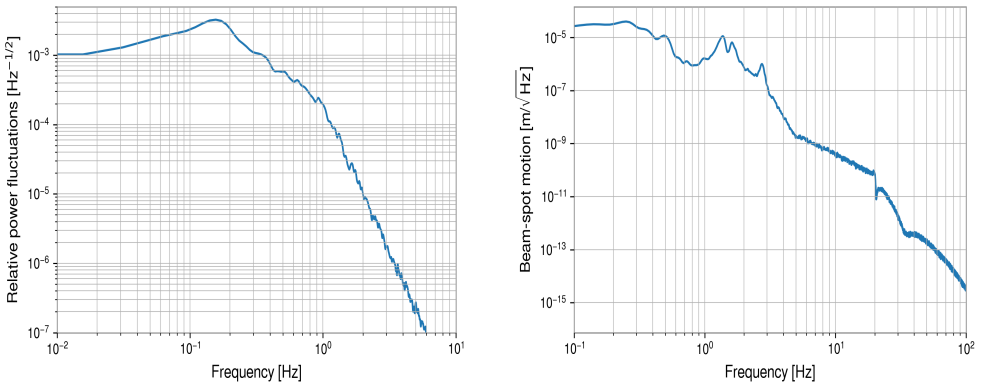

(A) (B)

FIGURE 3.18: (**a**) Spectrum of simulated relative power fluctuations, and (**b**) spectrum of simulated beam-spot motion on the test masses.

The main outcome of LIGO-Lightsaber is a model of the strain noise produced by the ASC. The first set of simulations concerns the case without static beam offset. The result of such a model is shown in figure 3.19a with 200 kW of optical power inside the arm-cavity (orange curve). The second ASC spectrum (blue curve) represents a 56.7 kW simulation without RPC. Since it is equivalent to the 200 kW simulation with RPC with respect to the Sidles-Sigg coupling, it allows us to infer the role of cavity-power fluctuations, which is overall minor at frequencies where ASC noise is important. The third ASC spectrum (green curve) is obtained including only the soft mode readout noise. As you can see, the hard mode readout noise contributes much more to the overall strain noise than the soft mode readout noise.

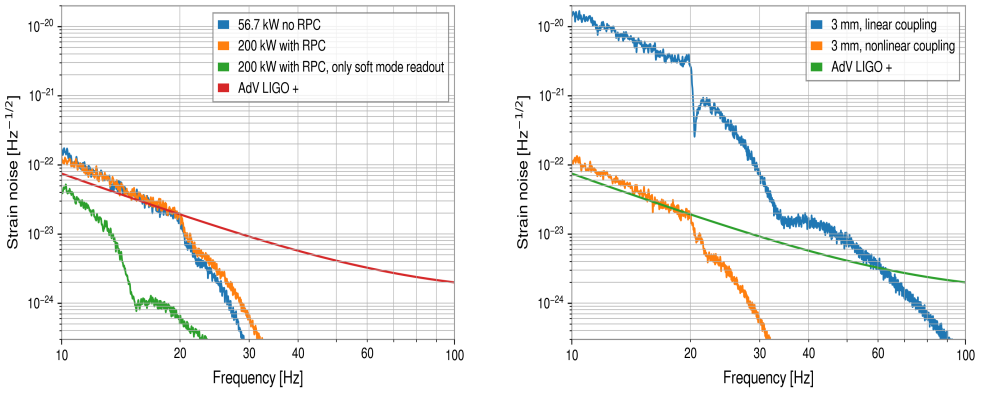

(A) (B)

FIGURE 3.19: (**a**) Simulated strain noise without static beam offset and (**b**) simulated strain noise obtained assuming a static beam offset of 3 mm in hard mode, in the case of both linear and nonlinear coupling, with radiation pressure compensation and 200 kW arm-cavity power.

The next set of simulations is with static beam offset. Intentional steering of

the beam from the center of rotation of the TM by as much as 3–5 mm (hard mode) offset was done in LIGO to reduce optical scatter and losses, *i.e.*, avoiding an overlap of the laser beam with major point defects on the TMs. In this case, the effect of power fluctuations on the angular motion of the TMs is enhanced, and the dynamics are strongly determined by a single angular mode (depending on whether the static offset is in hard or soft mode). In figure 3.19b, it can be seen that 3 mm beam offset in hard mode is sufficient to raise the ASC noise quite high in the case of linear coupling (blue curve). This is easily explained through the strain-noise coupling relation given in equation (3.10), but, in reality, the linear coupling is suppressed by the length to pitch feed-forward coupling (Yu, 2019). In the case of nonlinear coupling (orange curve), having DC torque optical pitch noise subtracted, the level of noise is much lower. The LIGO-Lightsaber simulation predicts angular noise to be an important contribution to detector noise, but the level of predicted noise is lower than in some of the past noise projections. Where the excess ASC noise comes from is still a mystery also for LIGO people. One possible explanation is higher beam-spot motion. The approximate value needed to explain the current ASC to strain noise coupling tells us that the RMS of beam-spot motion on each mirror should be approximately 1 mm. It is critical to note that this is the empirically determined offset for the hard mode. As a technical note, regarding beam offset in hard mode, hard mode's eigenvector is not $[-1, 1]$, but $[-0.867, 1]$.

3.2 Lightsaber-IMC

The Lightsaber is turning into a more universal simulation tool, and it finds applications in more than one plant model. As a first application, after the original LIGO-Lightsaber, I implemented it for the triangular cavity of the IMC at Caltech 40m prototype. I used the 40m Real-time Controls and Diagnostic System (RTCDS) in order to simulate the plant for IMC.

Caltech is hosting a smaller prototype version of the IFO, having arms of 40 m. The Caltech 40m IFO is a development and research testbed for improvements in configurations, readout systems, locking techniques, and control technologies, that will be incorporated into the LIGO IFOs (Ward et al., 2008; Adhikari et al., 2012).

In section 3.2.1, the general overview of the Lightsaber-IMC is given. In section 3.2.2, the IMC at Caltech 40m prototype is presented, with focus on the IMC's ASC. In section 3.2.3, the mechanical system and local damping loop at the IMC are introduced. In section 3.2.4, the main input noises, and the way I obtained them, are presented. In section 3.2.5 the feedback control of the ASC is described. In section 3.2.6, connection between beam-spot motion and angular motion, the radiation pressure effects, and some of Lightsaber-IMC results are given. Finally, in section 3.2.7, I present comparisons of Lightsaber-IMC outputs with real system channels.

3.2.1 Overview of the Lightsaber-IMC

Most of the things valid for LIGO-Lightsaber are also valid for Lightsaber-IMC (see section 3.1.2). The Lightsaber-IMC is the time-domain simulator of the ASC of the IMC at Caltech 40m prototype. The linear couplings are based on the second-order section models, which cover the suspension system, local damping, and feedback

angular controls. The main mechanical degree of freedom simulated in Lightsaber-IMC is the pitch motion of the IMC mirrors. The Lightsaber-IMC plant model is constructed from several static second-order section models representing the mechanical and feedback systems together with nonlinear optomechanical couplings. These couplings are the same as in LIGO-Lightsaber, apart from the fact that for the IMC, strain noise doesn't play any role, but still, we can look at the length change of the IMC cavity as a bilinear coupling between angular motion of mirrors and beam-spot motion.

The readout of the mirrors' pitch motion is given a sensing/electronics and excess readout noise. The main feedback control filters are implemented in a sensing basis. Apart from that, all other filters are in a local basis, including ASCPIT feedback control filters. In the local damping loop, OSEMs' noise is injected. The filtered signals from control feedback and local damping loops are fed back directly to mirrors. Light propagation time inside the cavity is neglected, which means that the outputs are accurate below 3.79 kHz corresponding to the IMC cavity pole (*Mode Cleaner*). On a PC with 12 processors, it takes around one minute for one simulation run.

3.2.2 Input Mode Cleaner

The brief description of the Input Mode Cleaner is given in section 1.2.1. In figure 3.20 the layout of the 40m's IMC ASC is shown. The 40m's IMC is a triangular cavity with two flat mirrors (MC1 and MC3) with a small separation (17.5 cm) and a spherical mirror (MC2) at the end. The longer side of the isosceles triangle is 13.458 m (Driggers, 2006). This arrangement makes the waist of the cavity eigenmode located in the middle of the two flat mirrors. For ASC, there are two WFSs at the MC1 reflection and a DC QPD at the transmission of the MC2. The WFSs use demodulation at 29.5 MHz. One of the WFS has a Gouy phase telescope to have the Gouy phase shift of 0° (or 360°) counted from the waist. The other one has the telescope tuned to have 90° shift. The MC2's DC QPD is sensitive to the beam position.

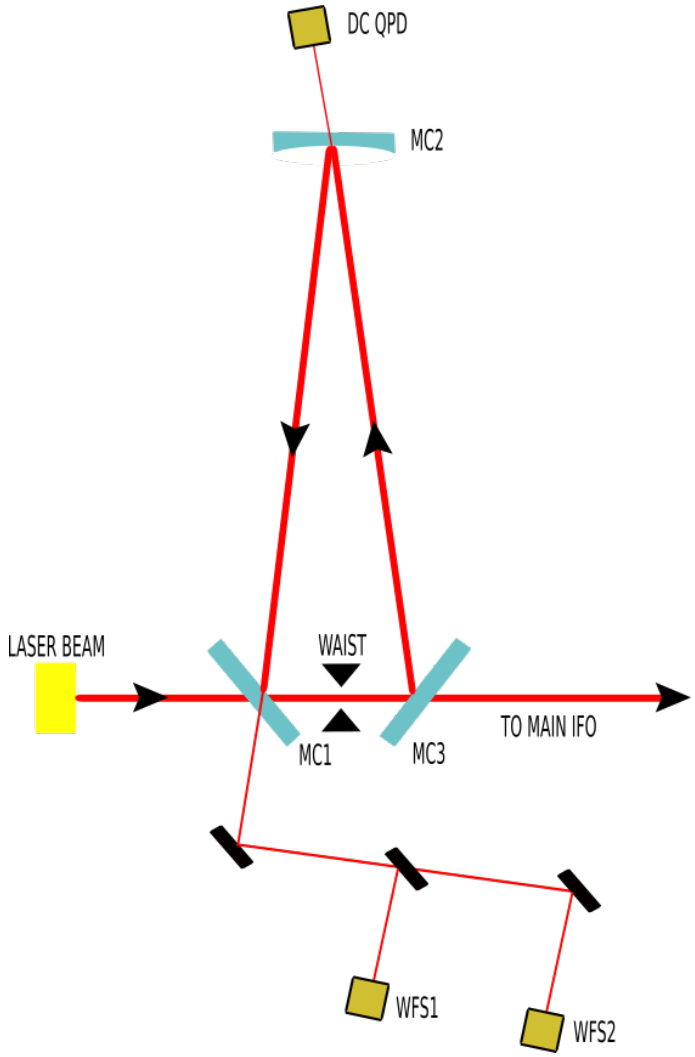

FIGURE 3.20: Simplified layout of the IMC at the 40m prototype at Caltech. It is a three-mirror ring cavity. The two flat mirrors are partially transmitting with T=0.2% (MC1, MC3), and the top mirror is curved (MC2, with transmissivity less than 0.001%) (*40m core optics*). Light comes in from the left, circulates between MC1, MC3, MC2, and back to MC1 before eventually exiting through MC3 toward the main IFO.

A WFS is a sensor that detects the difference between the beam axis and the cavity eigenmode axis. WFS1 (0°) is sensitive to the angular difference of these axes, and WFS2 90° is sensitive to the lateral difference of these axes as shown in figure 3.21. There are 4 DOFs *i.e.* (rotation and translation) x (vertical and horizontal). The two WFSs provide the error signal to control these 4 DOFs. Namely, if the WFS error signals are all zero, the input beam axis and the cavity axis match *i.e.* the main transmission is maximized.

FIGURE 3.21: WFS (0°) is sensing vertical and horizontal axis rotation. WFS (90°) is sensing axis translation.

3.2.3 Mechanical system and local damping

Passive seismic isolation system for IMC mirrors are multiple-stage seismic vibration isolation stacks. They consist of alternating layers of stiff masses and compliant springs providing passive filtering of ground vibration. It is a four-stage spring (elastomer) and stainless steel stack, having a table resting on three separated legs of three layers each as shown in figure 3.22. The elastomer springs' viscoelastic properties are used to dampen the normal modes of the stack and in the same time give fast roll-off of the stack transmission above these modal frequencies. The masses are very stiff so their internal resonance frequencies are above the important GW band. Separate legs of the mass-spring layers allow stiff masses to be incorporated into a larger structure that avoids elements with parasitic vibrational modes in the GW band. The stack's transmission from the base motion to the top motion at 100 Hz is 3×10^{-6} for vertical transmission (peak transmission is 11.3 at 6.9 Hz), and 10^{-7} for horizontal transmission (peak transmission is 9.4 at 1.8 Hz). The cross-coupling terms are between these values. More about passive isolation stacks you can find in (Giaime et al., 1996; Giaime, 1995).

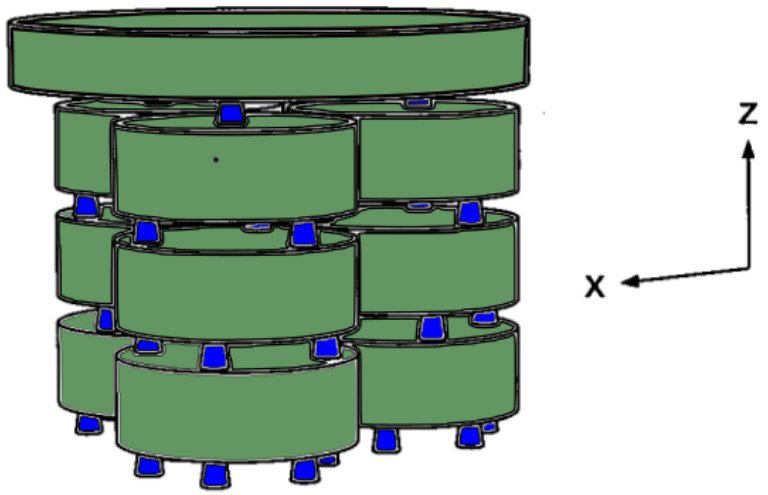

FIGURE 3.22: Passive isolation stack. The circular table is supported through springs by three separated legs of three mass-spring layers each. The width is 78 cm, and the overall height is 68 cm.

All MCs mirrors are suspended as single-stage pendula by a single loop of steel wire to provide isolation from ground motion as depicted in the figure 3.23. Each mirror is equipped with five magnet-coil actuators to control the mirror's angular and longitudinal DOFs. The length of the pendulum is 24.8 cm, the mirrors are cylinders made of fused silica, with a radius of 37.5 mm, and thickness of 25 mm (*40m core optics*; Kawamura and Hazel, 1997).

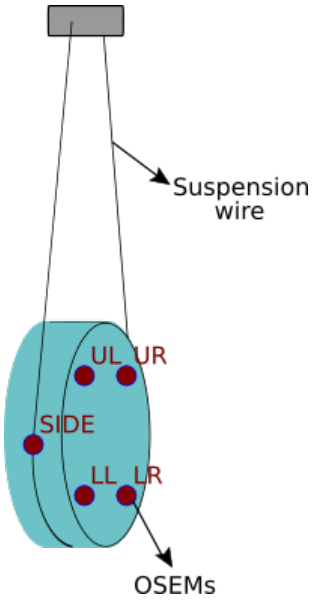

FIGURE 3.23: Sketch of the single stage suspension. All IMC mirrors are outfitted with magnet-coil actuators to control angular and longitudinal DOFs.

TM P to P transfer function for single stage pendulum determined with the following formula:

$$H(s) = \frac{1}{I} \frac{1}{\left[s + \omega_{0p}\left(\frac{1}{2Q} + \sqrt{\left(\frac{1}{2Q}\right)^2 - 1}\right)\right]\left[s + \omega_{0p}\left(\frac{1}{2Q} - \sqrt{\left(\frac{1}{2Q}\right)^2 - 1}\right)\right]}, \tag{3.12}$$

where I is moment of inertia of the mirror for pitch, and it is given with $I = \frac{1}{4}M_m R_m^2 + \frac{1}{12}M_m L_m^2$ where $M_m = 0.243$ kg is the mass of the mirror, R_m is radius of the mirror, and L_m is thickness of the mirror. $Q = 5$ is the quality factor, and ω_{0p} is free pitch angular resonance frequency. Free pitch resonance frequencies are 0.678, 0.748, 0.770 Hz, and free yaw resonance frequencies are 0.797, 0.815, 0.841 Hz for MC1, MC2, MC3, respectively. ZPK model for MCs for this tf has no zeros, the gain is equal to 10196, and poles are given in table 3.5.

MC1	MC2	MC3
-0.4260 ± 4.2386j	-0.4700 ± 4.6763j	-0.4838 ± 4.8138j

TABLE 3.5: Poles of TM P to P transfer function model for single suspension, describing torque to TM pitch angle transfer function.

Bode plot of TM P to P transfer function is shown in figure 3.24.

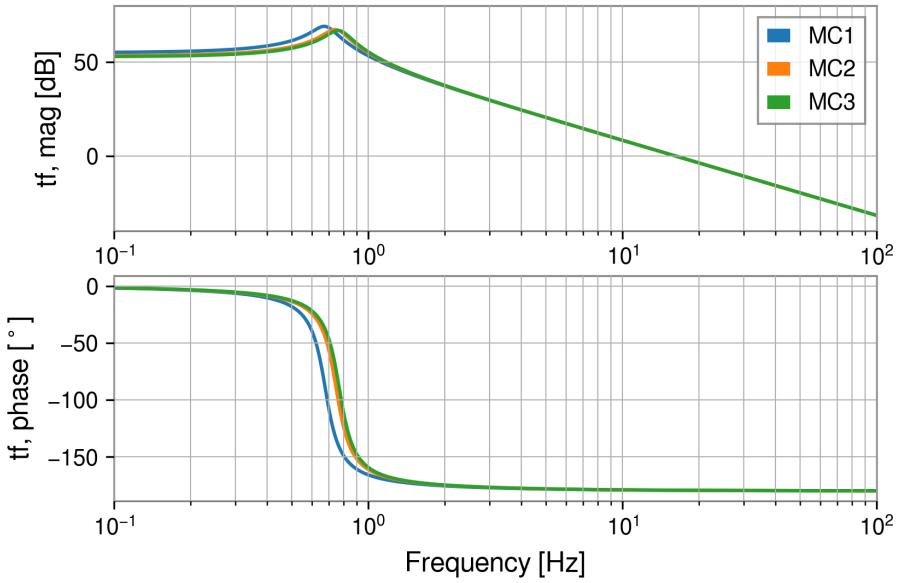

FIGURE 3.24: Bode plots of TM P to P transfer function for MC1, MC2, and MC3. The transfer function magnitude is with respect to 1 rad/Nm.

Local damping's ZPK model is the same for all MCs. Apart from the filter which ZPK model is $(0, -30 \times 2\pi, 10)$, there are two Chebyshev's and two elliptic filters. Chebyshev's filters are of the second and of the sixth order. The maximum ripple allowed below unity gain in the passband, specified in decibels, is 0.1 and 1. The critical frequency of the low-pass filter is 3 and 12 Hz. Filters have an additional gain of 1.13501. Elliptic filters are bandstop filters of 4th order. The maximum ripple allowed below unity gain in the passband, specified in decibels, is 1. The minimum attenuation required in the stop band, specified in decibels, is 40. Critical frequencies are 15.9–17.2 Hz and 23.5–24.7 Hz. Filters have an additional gain of 1.25893. Overall additional gains for local damping MC1, MC2, and MC3 are 60, 10, and 12, respectively. Bode plots of local damping are shown in figure 3.25. Here both OSEMs and counts to torque calibrations are included (more about calibration you can find in appendix B, section B.2). Adding the pendulum, it would be the complete local damping OLTF, of which comparison with the real system I will show later. Local damping loop is shown in the diagram in figure 3.26. The Simulink block diagrams for Lightsaber-IMC are shown in appendix C, section C.2.

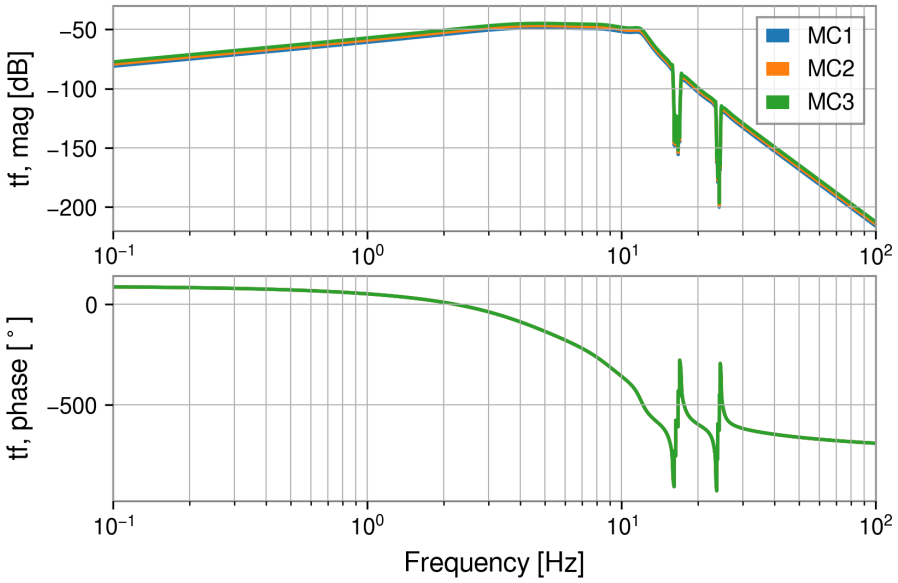

FIGURE 3.25: Bode plots of local damping for MC1, MC2, and MC3. The transfer function magnitude is with respect to 1 Nm/rad.

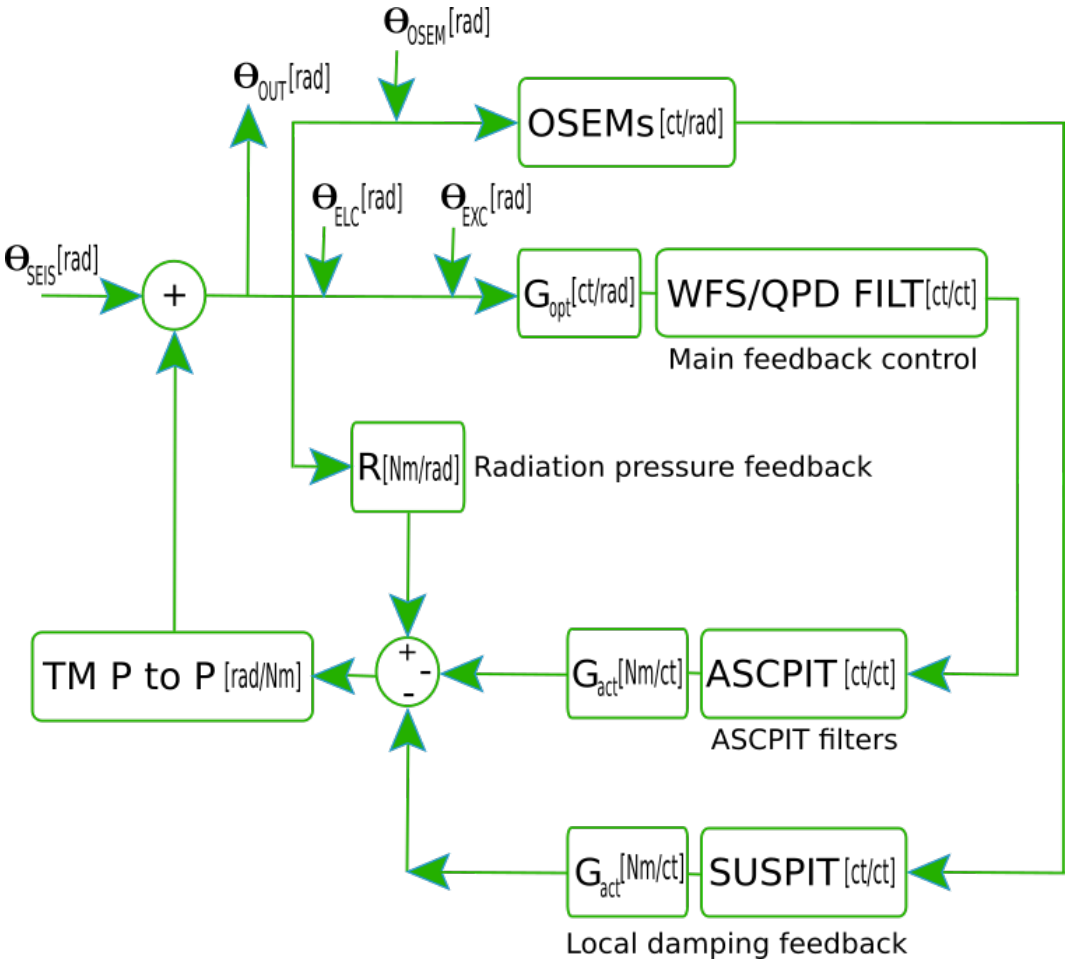

FIGURE 3.26: Diagram illustrating the components of the Lightsaber-IMC simulation including local damping feedback, control feedback, and radiation pressure feedback. All shown noise inputs are in terms of pitch angular motion. Θ_{SEIS}, Θ_{OSEM}, Θ_{ELC}, and Θ_{EXC} are seismic, damping OSEMs, electronics/sensing, and excess readout noise inputs. Note that damping OSEMs noise is originally measured in micrometers, and it needed to be calibrated to radians as it will be described later in the text. The electronics/sensing and excess readout noise inputs are originally in counts and are injected after G_{opt}. G_{opt} is the optical gain matrix that converts angular motion into digital counts, and G_{act} converts digital counts into actuation torque. WFS/QPD FILT are the main feedback filters in the sensors' basis, ASCPIT are output filters to suppress exciting bounce roll and other high order mechanical modes, and SUSPIT are local damping filters. Θ_{OUT} is the residual mirror's pitch motion.

3.2.4 Input noises

The calibration process for Lightsaber-IMC is given in appendix B, section B.2. During the calibration process, I obtained the optical gain matrix, which is basically a sensing matrix, needed to go from local to sensing basis. This matrix in figure 3.26 is labeled with G_{opt}, and converts angular motion from radians to counts.

The optical gain matrix in [cts/rad] is given with

$$G_{opt} = \begin{bmatrix} -32.3 \times 10^6 & 567.86 \times 10^6 & 164.47 \times 10^6 \\ -103.41 \times 10^6 & -473.22 \times 10^6 & 164.47 \times 10^6 \\ -1292.66 & -4732.2 & -2741.23 \end{bmatrix}. \tag{3.13}$$

Pitch dynamics is implemented with seismic, damping OSEMs, electronics/sensing noise, RIN, and excess readout noise inputs. These input noises are simulated by spectral methods to avoid an unnecessarily large dimension of the second-order section models.

Looking at the diagram in figure 3.26, and considering only the global feedback control loop, with some manipulations one can estimate external disturbances, which are mostly coming from residual seismic motion, as

$$\chi_{dist}(f) = \frac{1 + OLTF_{WFS/QPD}(f)}{O.G.} err_{WFS/QPD}(f), \tag{3.14}$$

where $O.G.$ is the optical gain, $OLTF_{WFS/QPD}$ is open loop transfer function of WFSs/QPD loops, err is the error signal in [cts Hz$^{-\frac{1}{2}}$]. These plots are shown in section 3.2.7. Like this, I directly obtained the amplitude-spectral density (ASD) of the input seismic noise in [rad Hz$^{-\frac{1}{2}}$]. Since WFSs' error signal is contaminated with excess readout noise I chose to use QPD in MC2 transmission for this calculation. This channel has a good coherence with the seismometer at the beamsplitter at lower frequencies (appendix B, figure B.4.) For WFSs channels this coherence is worse. At frequencies higher than a few Hertz this noise is contaminated with other noises, but for modeling purposes, this is more than good enough. The seismometer at BS didn't give credible data at higher frequencies. Otherwise, another option for getting seismic noise input would be seismometer data passed through passive stacks, and through the pendulum's platform to mirror's pitch motion transfer function. For $O.G.$ I took average absolute value of all MCs for QPD in MC2 in transmission (so of the last row of G_{opt} in 3.13). In the figure 3.27 external disturbance (seismic) noise spectrum in terms of pitch angular motion is shown.

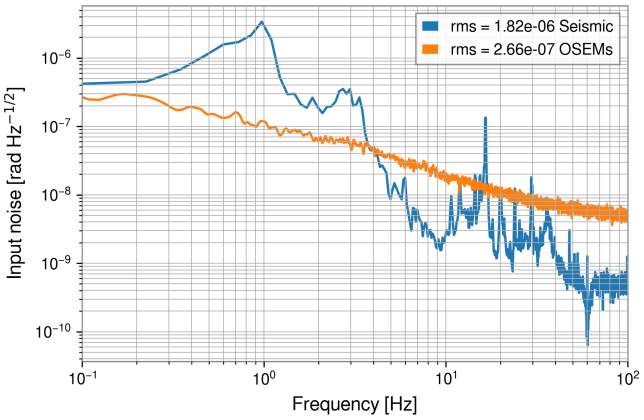

FIGURE 3.27: Seismic and local damping input noises in terms of mirror's pitch motion.

Next input noise is the local damping noise, coming from OSEMs (figure 3.27).

In order to get this spectrum, I used the already calculated null stream (aka butterfly mode) to find out the intrinsic OSEM noise. Butterfly mode is the following combination of OSEMs $(UL + LR) - (UR + LL)$ (see figure 3.23 for OSEMs placement) [3]. In order to get OSEMs' noise in terms of pitch motion, I was following the mirror's geometry. I divided the output of this null stream by the mirror's radius and $\sqrt{2}$, and then assuming these being incoherent noise sources, I multiplied it with 2 to get the final OSEMs noise (SIDE OSEM doesn't contribute to the pitch motion).

The electronics/sensing noise is the error signal measured with the Pre-stabilized Laser (PSL) system shutter closed. The noise measured with the PSL shutter closed is the sum of all the electronics/sensing noise from the WFS/QPD heads to Analog-to-Digital Converter (ADC). For WFSs (Adhikari, 2019), the noises absorbed here are dark noise of WFSs, electronics and phase noise from the local oscillator of the demodulation board (Arai, 2016), the noise of the whitening board (Heefner, 2005), and noise of ADC (Arai, 2021). For the DC QPD (Heefner, 2000) in MC2 transmission, noises absorbed here are dark noise of QPD, Optical Lever (OPLEV) board noise (Heefner, 2002), and ADC noise (Arai, 2021). There is supposed to be an Anti-Aliasing board before ADC, but for IMC, at the moment of data collection, it was not in function. Electronics/Sensing noise, in counts, for WFS1, WFS2 and DC QPD, together with error signal (*i.e.* with PSL shutter open), is shown in figure 3.28. I was injecting this noise before G_{opt} in radians by applying the inverse of G_{opt}. So, Θ_{ELC} [rad] $= G_{opt}^{-1}$ @ Θ_{ELC} [cts] in local basis is shown in the figure 3.29, and error signal is shown in subsection 3.2.7.

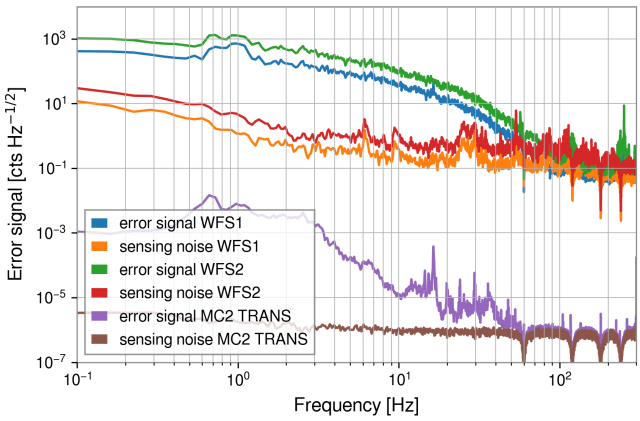

FIGURE 3.28: Error signal in counts with and without PSL shutter closed. Error signal with PSL shutter closed represents overall sensors' electronics/sensing noise denoted in the plot's legend as 'sensing noise'.

[3]The channels used here are C1:SUS-ITMX_SENSOR_UL, C1:SUS-ITMX_SENSOR_UR, C1:SUS-ITMX_SENSOR_LR, and C1:SUS-ITMX_SENSOR_LL and assumption is that OSEMs in IMC have the same spectra too.

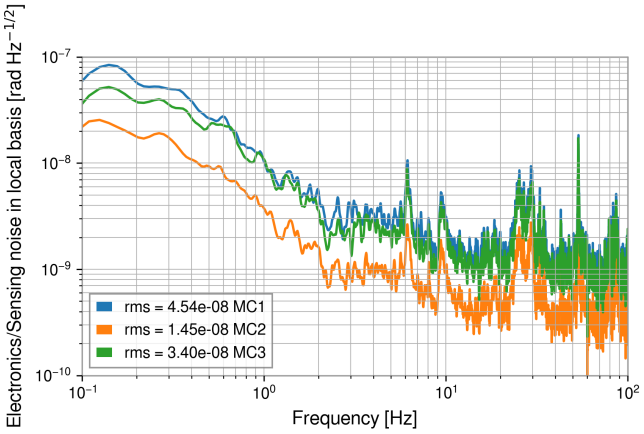

FIGURE 3.29: Electronics/Sensing noise in a local basis, as injected in Lightsaber-IMC.

Excess readout noise exists for WFSs, and not for DC QPD in MC2 transmission. In figure 3.28 in the error signal for WFSs there is a broad smooth noise between a few and a few tens of Hz. The suspect was that this noise comes from air turbulence in the WFS chamber (Sinclair et al., 2014; Enomoto, 2019), but the slope of the von Karman/Kolmogorov spectrum doesn't match the WFSs' error signal slope. In terms of counts this noise is shown in figure 3.30. I did again the same process as for electronics/sensing noise, and in a local basis, this noise is shown in figure 3.31.

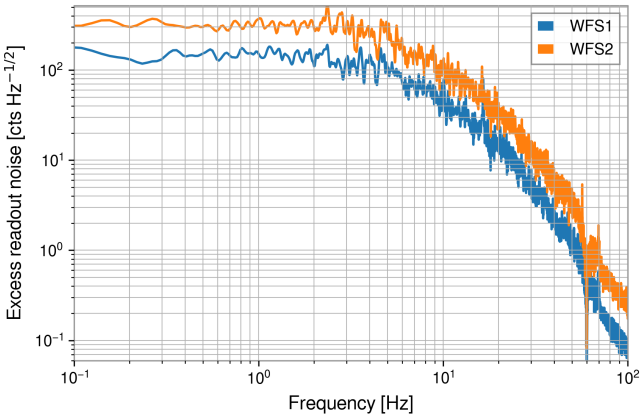

FIGURE 3.30: Excess readout noise of the WFSs.

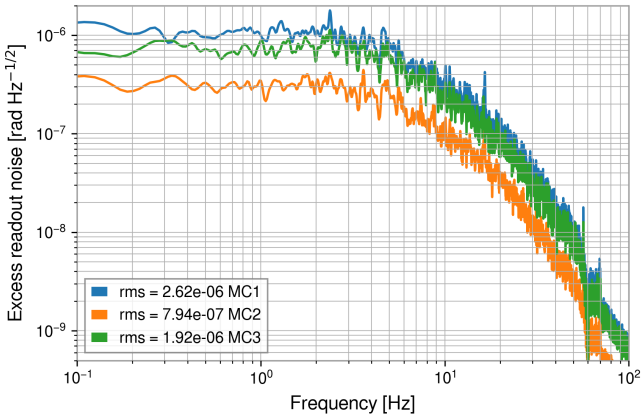

FIGURE 3.31: Excess readout noise in local basis.

The relative intensity noise (RIN) I obtained from the channel C1:IOO-MC_RFPD_DCMON, and it is given in the figure 3.32.

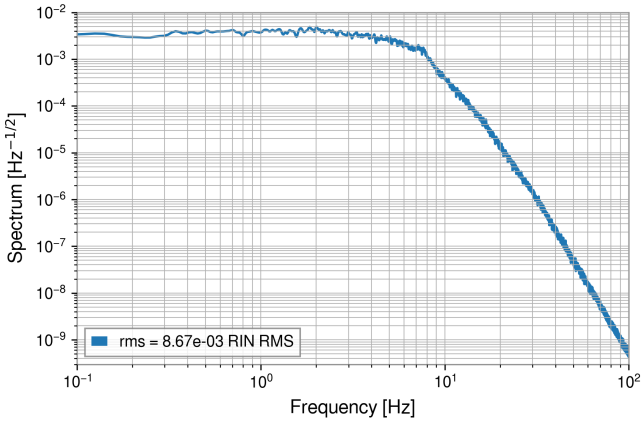

FIGURE 3.32: Spectrum of relative input power fluctuations for IMC.

For the same motivation as for LIGO-Lightsaber, the scaling parameters for all input noises are introduced.

3.2.5 Feedback control

The optical gain matrix transfers signal from the local to the sensors basis. For controlling pitch DOF at IMC, the main feedback filters are in the sensors' basis (denoted as 'WFS/QPD FILT' in figure 3.26, and shown in appendix D, figure D.7) given as ZPK models in table 3.6. WFS1 and WFS2 have the same filters.

After passing through these filters, the signal is converted to a local basis using the output control matrix

$$\begin{bmatrix} -1.59 & -0.902 & -0.559 \\ 0.962 & -0.57 & 0.172 \\ 0.425 & 1.61 & -0.516 \end{bmatrix},$$

Sensor	Zeros	Poles	Gain
WFS	-12.5663 ± 376.782j	-11.781 ± 45.6275j	2.01878
	-5.02655	-9.42478 ± 74.807j	
	-5.02655	-360.388 ± 514.688j	
	-345.575	0	
DC QPD	-12.5663 ± 376.782j	-30.2907 ± 36.099j	20187.8
	-5.02655	-9.42478 ± 74.807j	
	-5.02655	-360.388 ± 514.688j	
	-345.575	0	

TABLE 3.6: ZPK model of the IMC's WFS and QPD sensors' filters which are the main feedback filters for feedback control.

and then goes through ASCPIT filters. These output filters serve to suppress exciting bounce roll and other high order mechanical modes, and they are the same for all three MCs apart from an additional low-pass filter for MC2. There are four elliptic bandstop filters of 4th order. The maximum ripple allowed below unity gain in the passband, specified in decibels, is 1. The minimum attenuation required in the stop band, specified in decibels, is 40. Critical frequencies are 15.9–17.2 Hz, 23.5–24.7 Hz, 15.9–16.7 Hz, 23.5–24.3 Hz. Filters have an additional gain of 1.58463. Additional filter is given with ZPK model in table 3.7.

Zeros	Poles	Gain
-40.7838 ± 12867.9j	-628.827 ± 1665.23j	$4.91 \cdot 10^{13}$
	-246.001 ± 3930.22j	
	-1289.7 ± 12803.2j	

TABLE 3.7: ZPK model, part of ASCPIT filters.

For MC2 there is also the low-pass elliptic filter of 5th order. The maximum ripple allowed below unity gain in the passband, specified in decibels, is 1. The minimum attenuation required in the stop band, specified in decibels, is 50. The critical frequency is 28 Hz. Bode plots of control feedback filters are shown in figure 3.33. Here, both optical gain and counts to torque calibrations are included. Adding a pendulum, it would be the complete control feedback OLTF of which comparison with the real system I will show later. The control feedback loop is shown in the diagram in figure 3.26. Both local damping and control feedbacks are negative.

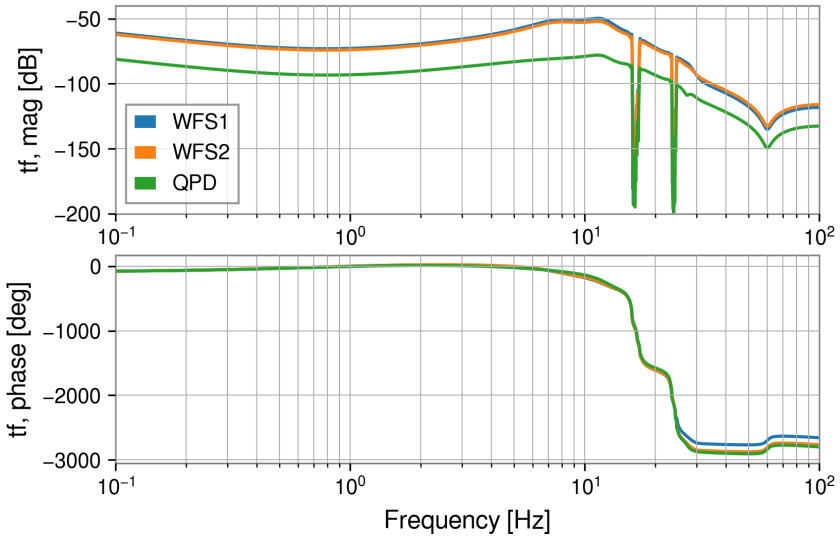

FIGURE 3.33: Bode plots of control feedback for WFS1, WFS2, and DC QPD in MC2 transmission (denoted as 'QPD' in this figure). ASCPIT filters are included in these plots also. The transfer function magnitude is with respect to 1 Nm/rad.

3.2.6 Beam-spot motion and optomechanics

The equation used for calculating beam-spots y_{MC1}, y_{MC2}, and y_{MC3} on MC1, MC2, and MC3 is (Tanioka et al., 2020; Kawazoe, Schilling, and Lück, 2011):

$$\mathbf{y} = \begin{bmatrix} y_{MC1} \\ y_{MC2} \\ y_{MC3} \end{bmatrix} = \begin{bmatrix} c_1 & -R_{MC2} & c_2 \\ R_{MC2}/\sqrt{2} & -R_{MC2} & R_{MC2}/\sqrt{2} \\ c_2 & -R_{MC2} & c_1 \end{bmatrix} \begin{bmatrix} \theta_{MC1} \\ \theta_{MC2} \\ \theta_{MC3} \end{bmatrix}, \tag{3.15}$$

where coefficients c_1 and c_2 are defined as $c_1 = \left(\frac{R_{MC2}-L_{IMC}-d_{IMC}}{\sqrt{2}}\right)$ and $c_2 = \left(\frac{R_{MC2}-L_{IMC}+d_{IMC}}{\sqrt{2}}\right)$. $R_{MC2} = 17.87$ m is the radius of curvature of MC2, L_{IMC} is the longer arm length in isosceles triangular mode cleaner, d_{IMC} is half of the shorter arm length in isosceles triangular mode cleaner (*40m core optics*). θ_{MC1}, θ_{MC2}, and θ_{MC1} are MC1, MC2, and MC3 mirrors' pitch motions, respectively. Simulated spectra of beam-spot motion for IMC is shown in figure 3.34. Beam-spot motion on distant MC2 is higher than on MC1 and MC3, which have almost identical beam-spot motion spectra. Residual mirrors' pitch motion is shown in the figure 3.35(A).

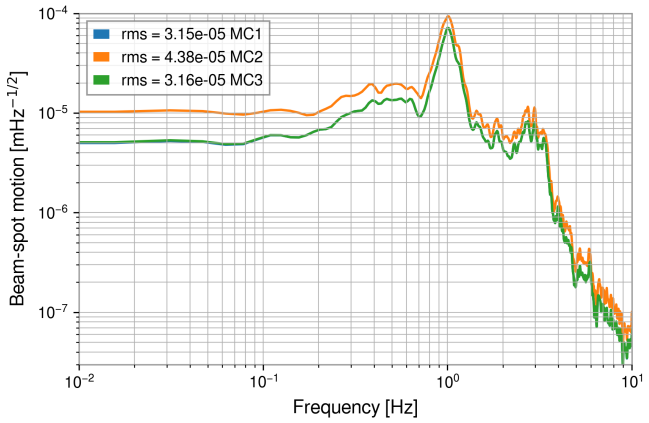

FIGURE 3.34: Spectra of beam-spot motion due to pitch angular motion at IMC mirrors.

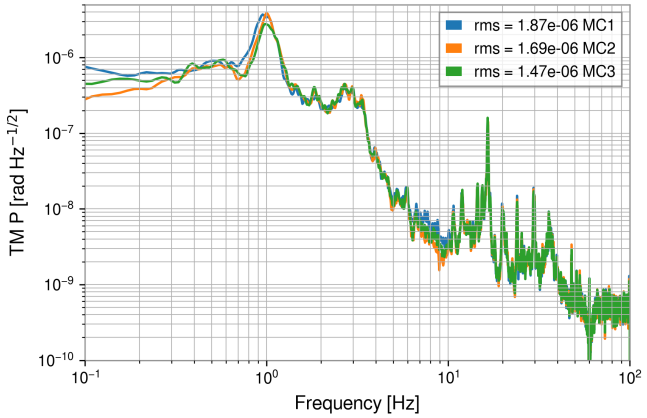

(A) Residual mirrors' pitch motion

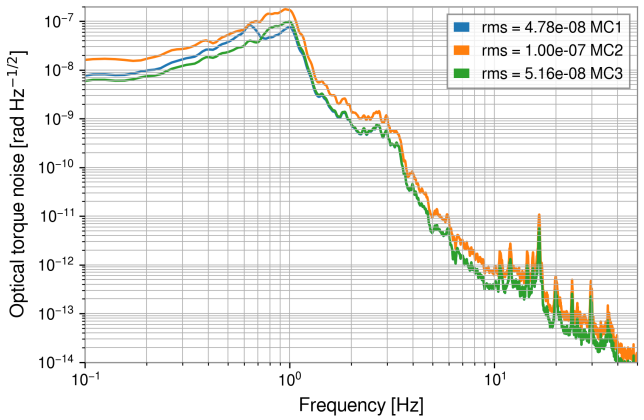

(B) Pitch motion due to optical torque

FIGURE 3.35: Spectra of the mirrors' pitch motion, (A) overall residual output pitch motion, and (B) pitch motion due to optical torque.

The optomechanical spring is not strong for IMC. The input power is 1 W, and the average cavity power is 500 W. The cavity power depends on the length change, which is calculated using 3.10 (now considering ΔL_{IMC} instead of ΔL_a). The total length change is the sum of length changes due to each mirror's pitch motion, its spectrum is shown in figure 3.36.

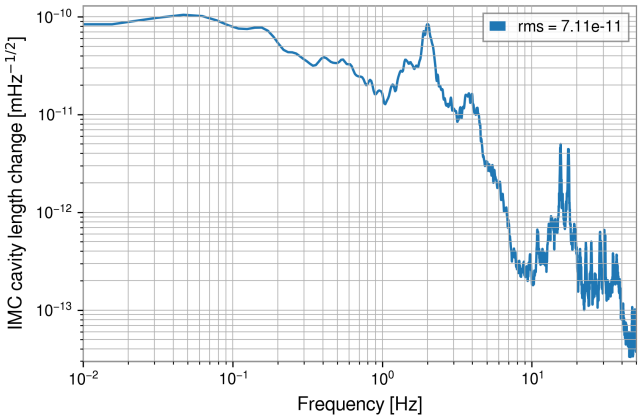

FIGURE 3.36: The spectrum of IMC length change due to mirrors' pitch motion and beam-spot motion.

Considering the geometry and beam circulation inside the cavity the length changes due to MC1 and MC3 motion are weighted with $\sqrt{2}$, and due to MC2 with 2. Then IMC cavity power is calculated using

$$P_{IMC}(t) = \frac{\tau_{MC1}^2 P_i(t)}{\left|1 - \rho_{MC1}\rho_{MC2}\rho_{MC3}\exp(2\pi j \frac{\Delta L_{IMC}(t)}{\lambda})\right|^2}, \tag{3.16}$$

where $P_i(t)$ is the input power that pumps the IMC cavity, τ_{MC1}, ρ_{MC1} assuming $\tau_{MC1}^2 + \rho_{MC1}^2 = 1$ are the transmissivity and reflectivity of the MC1, ρ_{MC2} and ρ_{MC3} are reflectivities of MC2 and MC3, respectively. Since Lightsaber-IMC does not implement a length control there is the same high-pass filter, as in LIGO-Lightsaber, mimicking it. Optical torque is calculated using equation 3.1 (now considering P_{IMC} instead of P_a), weighted with $1/\sqrt{2}$ for MC1 and MC3 mirrors. Spectra of optical torque noise is shown in figure 3.35(B). The optical torque noise produced by MC2 is higher than the optical torque noise produced by MC1 and MC3, which is expected regarding spectra of beam-spot motion shown in figure 3.34.

3.2.7 Comparisons with real system

In this section, I compare Lightsaber-IMC outputs with channels of the real system. In figure 3.37(A) are the error signal comparisons. The optical gain matrix is, apart from switching from local to sensor basis, also converting the signal from radians to counts. The error signal of IMC is in counts, and in order to get the signal plotted in 3.37(A) in radians, I inverted the optical gain matrix and applied it to the error signal.

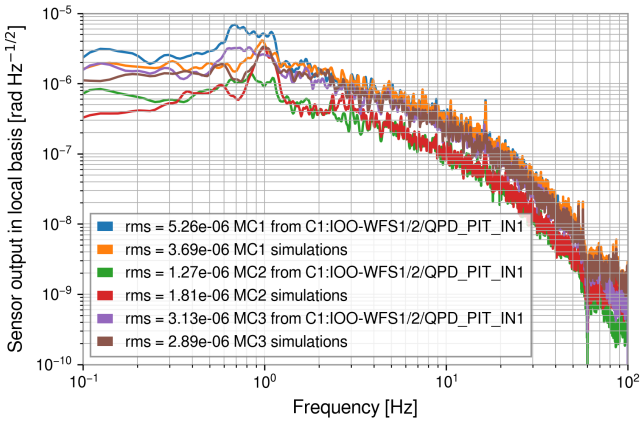

(A) Error signal

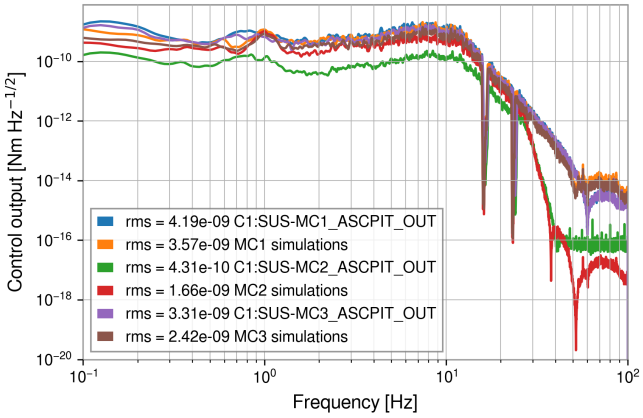

(B) Control output

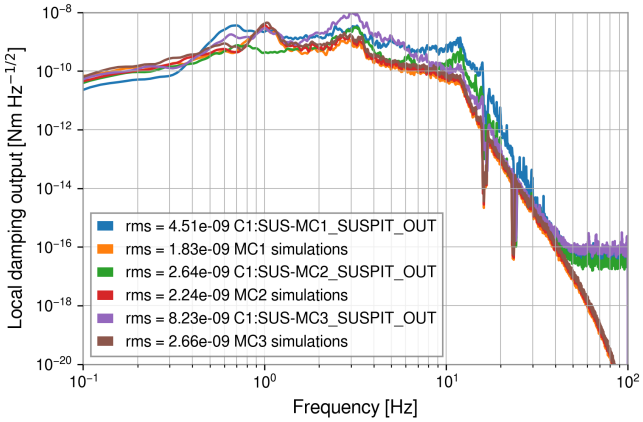

(C) Local damping output

FIGURE 3.37: Comparisons of Lightsaber-IMC observables with IMC channels. Note that in the legend 'QPD' is DC QPD in MC2 transmission.

In figure 3.37(B) controller outputs are compared, and in 3.37(C) local damping outputs are compared. Real system channels are again in counts (*e.g.* controller output shown in appendix B, figure B.5) and they needed to be calibrated to Nm in

order to compare them with Lightsaber-IMC outputs. What can be seen in 3.37(C) is that the IMC system suffers from quantization/loss of digits noise at higher frequencies. This level of noise is also present at higher frequencies of control output for MC2.

The measured OLTFs of the local damping of MCs is in appendix D. The UGF for MC2 and MC3 local damping loops is 0.9 Hz and 0.95 Hz, respectively. I could not take the resolution of measurements to be higher, since it was taking a long time to measure OLTF. In figure 3.38 are Lightsaber-IMC local damping OLTFs. UGF for MC1, MC2, and MC3 is 0.74 Hz, 0.83 Hz and 0.90 Hz, respectively. The measured OLTFs match pretty well the simulated Lightsaber-IMC OLTFs.

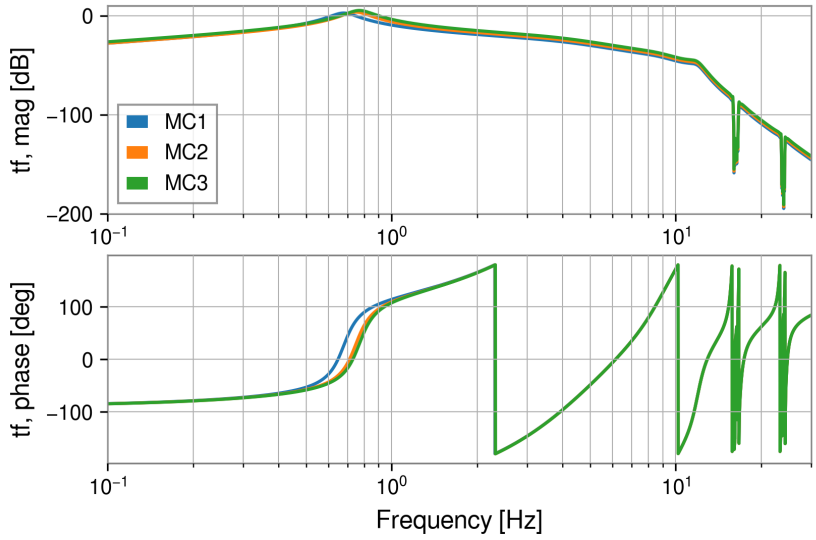

FIGURE 3.38: OLTF of local damping loops in Lightsaber-IMC.

The incomplete measured OLTF of control feedback for WFS1 is in appendix D [4]. The estimated UGF for WFS1 and WFS2 is less than 0.1 Hz, and for DC QPD loop is a few mHz. In figure 3.39 are Lightsaber-IMC control feedback OLTFs. The UGF for WFS1, WFS2, and DC QPD loop is 40 mHz, 40 mHz and 4 mHz, respectively. They agree pretty well with estimated ones from the real system.

[4] I didn't manage to measure the complete one for reasons explained in appendix D. The OLTFs for WFS2 and DC QPD in MC2 transimission I didn't manage to measure because sensors broke shortly afterwards.

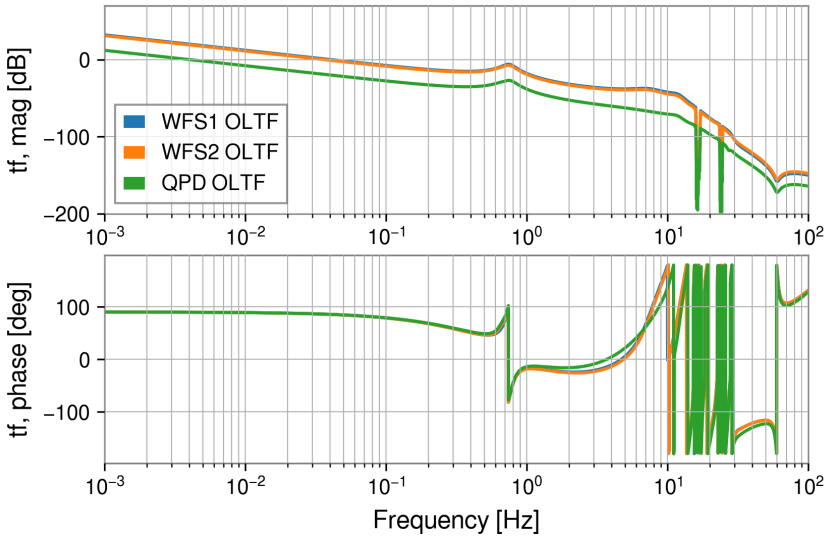

FIGURE 3.39: OLTF of control feedback loops in Lightsaber-IMC.

3.3 Conclusion

In this chapter, I presented the time-domain simulation Lightsaber of the angular sensing and control system at LHO, and the IMC of the 40m Caltech prototype. The ASC system is a complex component of the detector, which has proven to be difficult to model. This made it challenging to understand ASC noise in LIGO detectors, which however is known to be an important contribution to instrument noise below 25 Hz.

The complexity of the angular motion comes from the nonlinear optomechanical couplings between the suspended mirrors and the laser beam inside the cavity. Moreover, the angular motion of mirrors couples nonlinearly to differential arm length. The LIGO-Lightsaber is a nonlinear simulation of the optomechanical system consisting of the high-power cavity laser beam and the last two stages of suspension in LIGO with feedback control. For IMC the cavity power is not high, and there is a single suspension. The main noise inputs for LIGO-Lightsaber are power fluctuations from the input beam to the arm-cavity, readout noise of sensors of angular motion, seismic noise, and noise from dampers of suspension modes. The main noise inputs for Lightsaber-IMC are power fluctuations from the input beam to the cavity, electronics/sensing noise of sensors of angular motion (also there is excess WFSs' readout noise), seismic noise, and noise from dampers of suspension modes. For LIGO-Lightsaber, the mechanical system is simulated in its local degrees of freedom, while the control is produced with respect to the global angular modes. For Lightsaber-IMC the main feedback control is simulated in sensors' basis.

Lightsaber produces time series of all single-arm ASC observables of the LIGO detectors, which makes it possible to carry out detailed comparisons between simulation and real system at various levels. In the future, it will be interesting to make comparisons for LIGO-Lightsaber. Without very precise comparisons, at the moment, we see that, overall, the simulation reproduces the main characteristics

of the actual data, but the match is not completely satisfactory pointing to aspects of the noise inputs or ASC dynamics, which are not fully understood yet. It is difficult to get an accurate representation of the detector for the specific moment in time. For Lightsaber-IMC these comparisons are carried out and the simulations and real system outputs matching are excellent. The Lightsaber is sufficiently accurate to serve, at least, as a useful modeling tool especially when high precision is not required, *i.e.*, for noise budget calculations of current and future GW detectors. While the plant model is for the LIGO detectors, it is straightforward to modify the mechanical system, angular readouts, etc to represent other detectors (as done for IMC). The main work here is not on the simulation side, but for commissioners to have a sufficient understanding of the optomechanical plant and control system to feed the models.

Another application of Lightsaber, which will be explored in the next chapter, is that the fully nonlinear, time-domain representation allows researchers to test ASC controllers before implementing them in a detector. This can be especially valuable for certain nonstationary modern control schemes. In this context, Lightsaber serves as a development tool possibly leading to performance enhancements of future ASC systems parallel to nonlinear noise-cancellation techniques as another possible approach to reduce angular noise. As pointed out abundantly in the past, the ASC remains one of the big challenges of detector control, which needs to be addressed to be able to improve the low-frequency sensitivity of current detectors, and a detailed understanding of noise produced by the ASC is crucial to plan future generations of GW detectors.

Chapter 4

Machine-learning based ASC controller in LIGO

The Lightsaber is the nonlinear, time-domain representation that allows researchers to test ASC controllers before implementing them in a detector. This can be especially valuable for certain nonstationary and nonlinear modern control schemes. In this chapter, I will test a novel feedback-filter design, using Reinforcement Learning.

4.1 Introduction

The Reinforcement Learning based control should fulfill the fundamental requirements for the Angular Sensing and Control scheme, which are to suppress the angular mirror motion at low frequencies, to overcome angular instabilities induced by radiation pressure, and prevent reinjecting noise in the observational band (Barsotti, Evans, and Fritschel, 2010; Yu et al., 2017). So, the nonlinear ASC controller based on Reinforcement Learning should overcome the abilities of the optimal linear filter. Challenges in the problem are the high demands for the controller such as robustness, stability, and optimality. Control needs to be adaptable to changes in the detector (light power, temperature, mirror deformations, environmental noise). Reaching the sensitivity requirements at low frequencies is the most technologically challenging part of the GW detectors upgrade. Another upgrade that will happen in the upcoming scientific runs is to increase the circulating laser power in FPCs up to 750 kW, to reduce the shot noise contribution. This will further increase optomechanical instabilities, and the RL ASC controller should also handle them. As said as motivation in previous chapters, apart from other scientific drives, sub-30 Hz band is critical to both massive binary BHs and binary NS localizations (Yu et al., 2018). Therefore, improving low-frequency sensitivity is challenging but with high rewards.

In this chapter, in section 4.2 I will briefly introduce Reinforcement Learning and the type of algorithm and network used in this research. In section 4.3 I will describe the rewarding process and the results.

4.2 Reinforcement Learning

Machine Learning (ML), part of artificial intelligence, is the study of computer algorithms that improve automatically through experience. These algorithms leverage data in order to make predictions or decisions without being explicitly programmed to do so (Mitchell, 1997). Applications of ML algorithms are wide, such

as in computer vision, medicine, email filtering, controls (Hu et al., 2020). ML is divided into three categories, depending on the availability of the signal, or feedback to the learning system. These three categories are Supervised Learning, Unsupervised Learning, and Reinforcement Learning. In Supervised Learning the goal is to learn a function that maps an input to output, giving previously to the algorithm examples of input-output pairs (so, the training data are labeled) (Mohri, Rostamizadeh, and Talwalkar, 2018). An Unsupervised Learning algorithm learns patterns from unlabeled data. The algorithm is on its own to find the pattern/structure in the input data (Hinton and Sejnowski, 1999).

Reinforcement Learning is a category of ML which somewhat comes under the umbrella of unsupervised learning. It has close connections to both optimal control and adaptive control. In RL, an agent (an entity that perceives and acts) interacts with a dynamic environment in which it needs to achieve a certain goal. As it navigates, taking actions on an environment based on the current state of the environment, as shown, in discrete time, in the figure 4.1, it tries to maximize the cumulative reward. In contrast to most supervised and unsupervised learning settings, an RL agent must interact with an environment to generate its own training data. The desire is to see a sufficiently trained agent that takes the best action (the one which provides it the maximum future reward) for every state the environment could be in. It is inspired by natural learning mechanisms, where animals/humans adjust their actions based on reward and punishment stimuli received from the environment. The beauty of RL is that it starts from totally random trials and it finishes with sophisticated tactics (Busoniu et al., 2017; Mendel and McLaren, 1970). The RL algorithms are constructed on the idea that effective control decisions must be remembered, by means of a reinforcement signal, such that they become more likely to be used in the future. A carefully defined objective function is giving the reward to the agent. RL is focusing on finding a balance between so called exploration and exploitation (Sutton and Barto, 2015; Kaelbling, Littman, and Moore, 1996; *Key Concepts in RL*). Since many RL algorithms, due to the nature of the RL structure, use dynamic programming techniques, the environment is typically stated in the form of a Markov decision process (MDP) (Otterlo and Wiering, 2012). The main difference between the classical dynamic programming methods and RL algorithms is that the latter does not assume knowledge of an exact mathematical model of the MDP or become highly intractable to solve. Many dynamical decision problems can be formulated as MDPs including feedback control systems (Lewis, Vrabie, and Vamvoudakis, 2012). RL is used when there is no 'proper way' to perform the task. More about RL can be found in (Sutton and Barto, 2015; *Key Concepts in RL*).

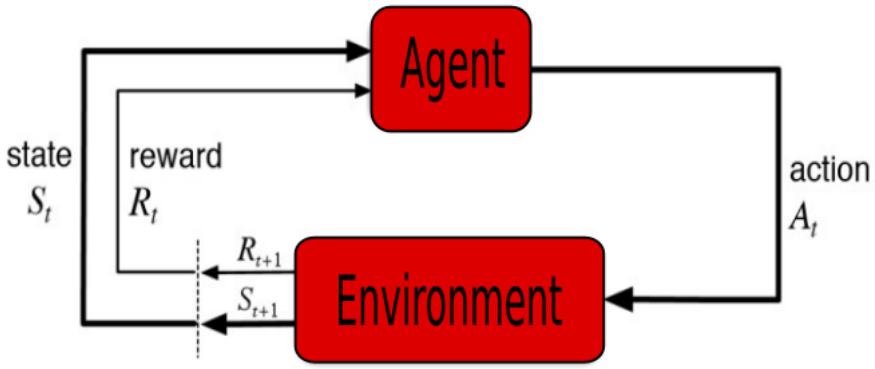

FIGURE 4.1: A basic Reinforcement Learning process. The agent interacts with the environment in discrete time steps. At each time step t agent receives the current state in which environment is (S_t), and reward (R_t). The agent then chooses an action (A_t) from the set of available actions, which is sent to the environment. The environment is now in a new state (S_{t+1}), the reward (R_{t+1}) associated with the transition (S_t, A_t, S_{t+1}) is determined, and this cycle continues.

What I used in this research is ACME. It is a library and framework of RL building blocks that strives to expose simple, efficient, research-oriented, and readable agents and algorithms. It is designed to enable simple descriptions of RL agents and their implementations, that can be run at many different scales of execution *i.e.* it allows for fast iteration of research ideas and scalable implementation of state-of-the-art agents. It provides tools and components for constructing agents at various levels of abstraction, from the lowest (*e.g.* networks, losses, policies) through to workers (actors, learners, replay buffers), and finally entire agents complete with the experimental apparatus necessary for robust measurement and evaluation, such as checkpointing, logging, and training loops. These agents serve both for providing strong baselines for algorithm performance and as reference implementations. Nonetheless, they should also provide enough simplicity and flexibility that they can be used as a starting block for novel research. ACME's building blocks are designed in such a way that the agents can be written at multiple scales (*e.g.* distributed agents, single-stream). Actors in ACME predominantly fall into one of two styles: feed-forward and recurrent (*ACME*; Hoffman et al., 2020). For TensorFlow agents, networks in ACME are typically implemented using the Sonnet neural network library (*Sonnet Documentation*).

The algorithm being used in this research is a bit more complex than the one given in figure 4.1. Namely, the data generation processes, the component that interacts most closely with the environment, will be referred as actor processes or more simply as actors. This is in contrast with the concept of learners, *i.e.* the processes which consume data in order to update policy parameters, usually by stochastic gradient descent. An illustration of an actor interacting with its environment, consuming observations produced by the environment, and producing actions that are in turn fed into the environment, is shown figure in 4.2. It illustrates the flow of information between an actor which produces actions and the environment which consumes those actions in order to produce rewards and novel observations. Afterward, the actor updates its internal state (its action-selection

policy). The learner component assesses the value of the action taken by the actor and usually takes the form of optimizing the weights of a neural network to minimize some algorithm-specific loss. Classically, these two processes of policy evaluation and policy improvement proceed in lockstep with one another. However, by making this explicit actor/learner distinction, we can also design agents which consist either of a single actor or many distributed actors which feed data to one or more learner processes. Overall, any agent interacting within this setting has to master two formidable challenges which align with these two processes. First, to obtain useful experiences, an agent must explore its environment effectively. Second, it has to learn effectively from these experiences (Hoffman et al., 2020; Bertsekas, 2009; Busoniu et al., 2017; Lewis, Vrabie, and Vamvoudakis, 2012; Sutton and Barto, 2015).

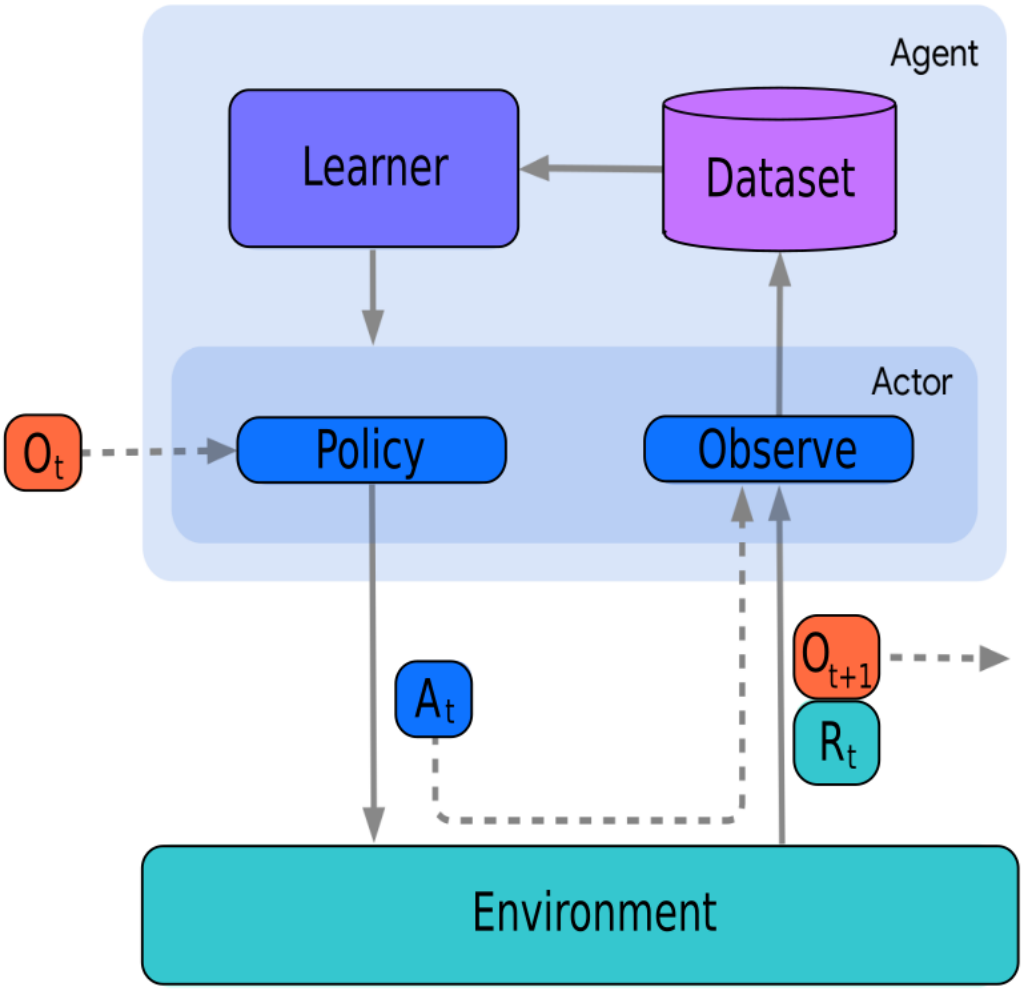

FIGURE 4.2: An environment loop, where the internals of learning components are also shown. The illustration shows how the actor and learner components interact. In particular, the actor pulls weights from the learner components in order to keep its action-selection up-to-date. Meanwhile, the learner pulls experiences observed by the actor through a dataset.

The algorithm used is Distributional Maximum a-posteriori Policy Optimisation (DMPO). It is an off-policy RL algorithm, but it exhibits the scalability, robustness, and hyperparameter insensitivity of on-policy algorithms while offering the high data-efficiency of off-policy, value-based methods. It is applicable to complex control problems (Abdolmaleki et al., 2018). The continuous control stochastic off-model DMPO agent is used. This agent distinguishes itself from the MPO agent by using a distributional critic (state-action value approximator, it allows the learning process to proceed as quickly as possible). The tool *Launchpad* enables distributed variants (Yang et al., 2021). Both the policy network and the critic network are simple multilayered perceptrons (MLP). The policy and critic network sizes are (256, 256, 256) and (512, 512, 256), respectively. MLP are a special case of a feedforward neural network (Sazli, 2006) where every layer is a fully connected layer, and in some definitions, the number of nodes in each layer is the same. Further, in many definitions the activation function across hidden layers is the same (*Feedforward Neural Networks and Multilayer Perceptrons*). Used MLP are actually the most simple feedforward network you can picture with a sprinkle of normalization needed to make it work. Exponential Linear Unit (ELU) activation function is used (also on the final layer of the neural network) (*Activation Functions*). The policy loss module is also MPO. The discount factor is a real value between 0 and 1, and takes care for the rewards agent achieved in the past, present, and future. In different words, it relates the rewards to time domain *i.e.* if it is 0 the agent cares for his first reward only, if it is 1, the agent cares for all future rewards. In my case discount factor is 0.99. Another parameter, epsilon, is to balance exploration and exploitation. If it is set to 0, algorithm never explores but always exploits the knowledge it already has. On the contrary, if epsilon set to 1, the algorithm always takes random actions and never uses past knowledge. Usually, epsilon is selected as a small number close to 0. For me it is 0.1 (Sutton and Barto, 2015; *Epsilon-Greedy Q-learning*; *Penalizing the Discount Factor in Reinforcement Learning*).

In this research, I was training an RL agent against LIGO-Lightsaber. LIGO-Lightsaber simulation is working with the RL environment wrapper. The wrapper is also rescaling and stabilizing the system. The environment rescales the control and observations to roughly Gaussian normal based on the closed-loop behavior of the linear controller. Actions are scaled back to the original scale before being passed to the base environment. The plan is that the RL agent takes care of feedback control as shown in figure 4.3. For the future RL agent should also take care of the RPC path. The impression of sensor noise cannot be avoided entirely in the presence of feedback (Dooley, 2011) and the hope is that RL can do better (without compromising the strain sensitivity of the detector). The first 500 timesteps are run without an RL agent, only using the linear controller in order to stabilize the system. After this RL agent takes over, without the linear controller. This setting makes sense since if the linear controller is on, it will inject some noise and the neural network has to exactly cancel that one out again.

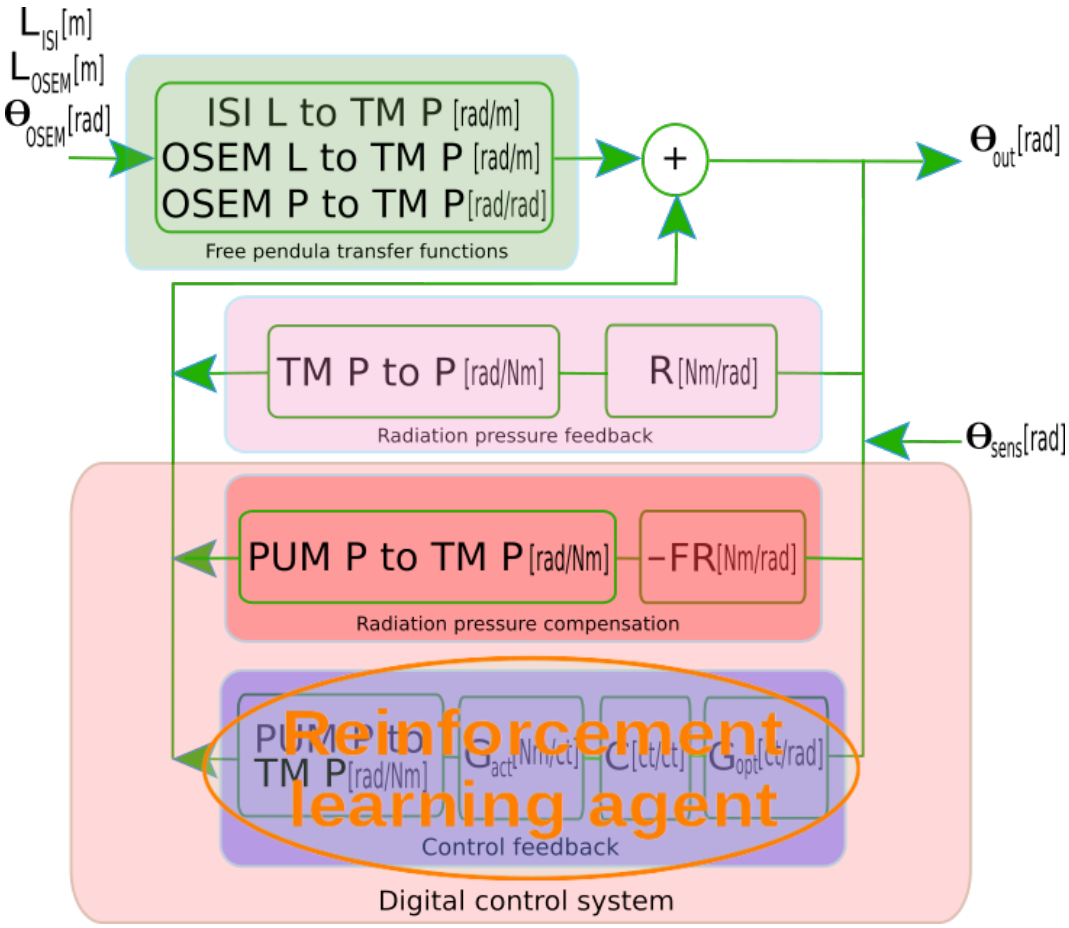

FIGURE 4.3: Diagram representing the simulated optomechanical system consisting of the high-power cavity laser beam and the last two stages of suspension in LIGO with the control system being replaced with a Reinforcement Learning agent.

4.3 Results

In RL, the art of designing reward functions is crucial. The policy evaluation step is performed by observing from the environment the results of applying current actions. These results are evaluated using a performance index, or value function that quantifies how close the current action is to optimal. Performance or value can be defined in terms of optimality objectives such as maximum reward (Lewis, Vrabie, and Vamvoudakis, 2012). What I used is frequency dependant reward filter, which includes observed pitch motion and whitened strain noise. Since the frequencies below 10 Hz and above 40 Hz would dominate during the rewarding process, and controls noise is relevant between 10 Hz and 25 Hz I needed to whiten the strain noise to make the rewards dominated by the noise in this frequency band. The idea is to use the readout signal to score for achieving the control objective, which is reducing the RMS of pitch angular motion in the 'DC band' (0 – 3 Hz), and to use the whitened strain noise, which spectrum is shown in figure 4.4, to score for noise reduction in the observational band (10 – 25 Hz) *i.e.* the strain noise should be as low as possible in that band. For scoring on observed pitch

motion L2 norm is used. The final reward is the summation of rewards scoring on observed pitch motion and on whitened strain noise.

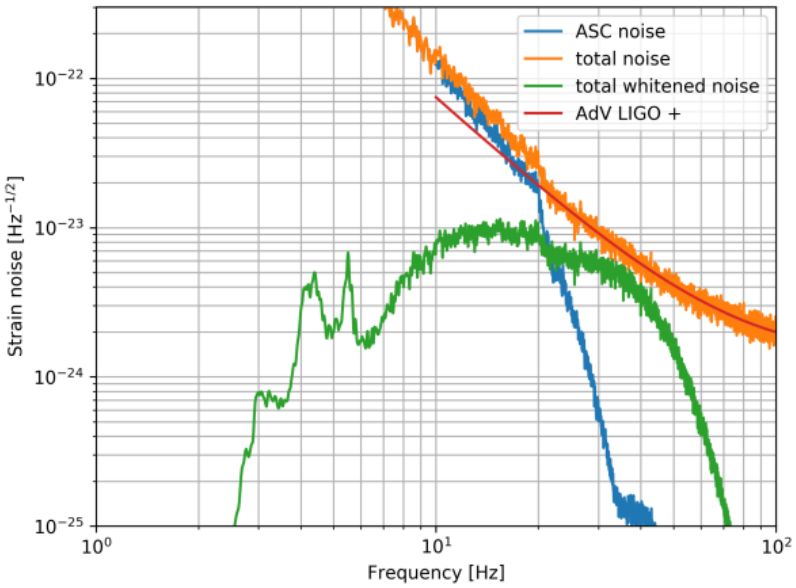

FIGURE 4.4: Whitened strain noise (green curve) so the rewards are dominated by the noise in the desired frequency band. Total strain noise in LIGO-Lightsaber is the sum of ASC noise and other noises (orange curve). It is basically ASC noise plus the optimistic sensitivity scenario for Adv LIGO during O5 represented with the red curve.

The residual TM pitch motions comparisons for ITM and ETM, using linear controller and RL agent are shown in figure 4.5. In the interesting observation band (10–25 Hz) there is a significant reduction of TM pitch motion, while the RMS requirement in lower frequencies is not satisfied. The reduction of TM pitch motion using RL agent with respect to the linear controller is 6–8 times in 15–20 Hz frequency band, where the reduction is the highest. The possibility why scoring on observed pitch motion is not fixing RMS is that the reward I have is not giving a gradient if the pitch is large (*i.e.* in the 10^{-8} range), and it would need to be changed to something that gives a small gradient even if the numbers are that large. One more thing to take into consideration for the future is that policies must be somehow prevented from taking inappropriate actions when there is a glitch or a GW event in the strain channel. I evaluated the results after 10 episodes of training. I was running it on 25 CPUs and 1 Tesla T4 GPU on LNGS-GPU cluster, and one run with 10 episodes and an evaluation episode was taking around 18 hours.

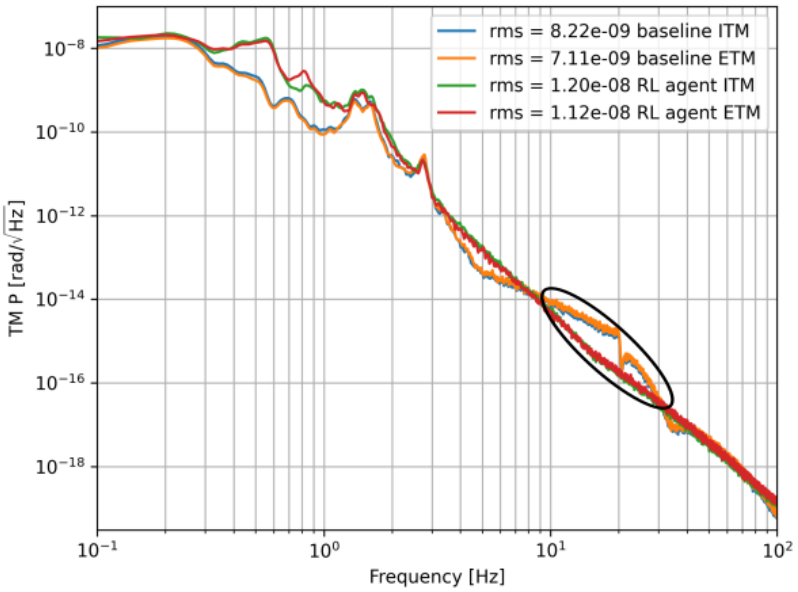

FIGURE 4.5: Comparison of residual test mass pitch motion for ITM and ETM in cases of RL agent and linear controller taking actions.

4.4 Conclusion

The Lightsaber finds application in the testing nonlinear ASC controllers before implementing them in a detector. One such nonstationary modern control scheme that can improve feedback control is Reinforcement Learning. Reinforcement Learning is a method for solving optimization problems that involves an actor/agent that interacts with its environment and modifies its actions (or control policies) based on stimuli received in response to its actions. RL control needs to meet the requirements on both the cutoff of high-frequency sensing noise and the suppression of low-frequency input motion. So, the RL algorithm should be clever enough to reduce pitch motion, to suppress the injection of readout noise, in the 10–25 Hz band, but still to maintain the ability to control below 3 Hz, in order to get better results than commissioners with the linear controller. This is the way to achieve low-frequency sensitivity. LIGO needs a solution for this now, and ET will need it also.

What I obtained is the reduction of residual test mass pitch motion in the observational band, but still, the RMS requirement is not satisfied. The reduction of TM pitch motion using the RL agent with respect to the linear controller is 6–8 times in 15–20 Hz frequency band. The RL agent is successfully controlling optomechanical instabilities. Playing with reward filters showed to have a huge impact and there is justified optimism for further improvements (*i.e.* by scoring on other more robust observables).

One last thing to clarify here is the necessity of the Lightsaber-IMC. There was a need for another simulator to train against in order to do the transfer experiments (to test Reinforcement Learning control in practice). The reason for choosing this

system is that it is very robust and has much more uptime than the actual 40m prototype. First tests at the Caltech 40m prototype with the IMC control successfully demonstrated the use of Reinforcement Learning in interferometer control.

Conclusions

This thesis work aims to improve the low-frequency sensitivity of gravitational-wave detectors, focusing on seismic Newtonian noise and angular controls and sensing noises.

I worked on problems in terrestrial gravity with the goal to characterize the seismic Newtonian noise. I presented synthetic seismic and gravitoelastic correlations between seismometers and a suspended underground test mass, which are required for an optimized deployment of seismometers for gravity noise cancelation. The synthetics were calculated with the spectral-element SPECFEM3D Cartesian software. The main analysis was based on a topographic model centered at one of the vertices (A3) at a candidate site of the Einstein Telescope in Sardinia. What was found is that A3 topography has generally a significant impact on seismic and gravitoelastic correlations. Specifically, calculations showed that Sardinian topography at vertex A3 scatters out energy from Rayleigh waves above 4 Hz protecting from the influence of distant seismic sources. As expected, symmetries of the field of gravitoelastic correlations are broken by topography leading to unique solutions of optimal seismometer placement for gravity-noise cancellation. These simulated seismic correlations will be implemented as priors in a Gaussian Process Regression and combined with observed seismic correlations for Bayesian inference of correlations everywhere in the medium. So, all pieces together for a Bayesian seismic-array design for Newtonian noise cancelation are outlined. Bayesian seismic array design is close to the optimal that can be done to design a Newtonian noise cancellation system for Einstein Telescope. By doing this process properly we will decrease the required effort and therefore cost of a Newtonian noise mitigation system and increase the low-frequency sensitivity of Einstein Telescope.

The Angular Sensing and Control system remains one of the big challenges of detector control, which needs to be addressed to be able to improve the low-frequency sensitivity of current detectors, and a detailed understanding of noise produced by the ASC is crucial to plan future generations of GW detectors. I presented the new time-domain simulation Lightsaber of the ASC at LIGO Hanford and at the Input Mode Cleaner of the 40m Caltech prototype. The complexity of the angular motion comes from the nonlinear optomechanical couplings between the suspended mirrors and the laser beam inside the cavities. Moreover, the angular motion of mirrors couples nonlinearly to differential arm length. The main noise inputs for Lightsaber are power fluctuations from the input beam to the cavity, readout noise of sensors of angular motion, seismic noise, and local damping noise. In the simulation, there is local (mirrors)-global (sensing) basis conversion. Lightsaber produces time series of all ASC observables, which makes it possible to carry out detailed comparisons between simulation and real system at various levels. For Lightsaber-IMC these comparisons are carried out and matching of the simulations and real system outputs are excellent. The Lightsaber can serve for noise budget calculations of current and future gravitational wave detectors. The Lightsaber can be transferred to represent other detectors' plant models.

Being the fully nonlinear, time-domain representation, Lightsaber allows researchers to test ASC controllers before implementing them in a detector. This

can be especially valuable for certain nonstationary and nonlinear modern control schemes, such as Reinforcement Learning. The Reinforcement Learning based controller is supposed to overcome the abilities of the optimal linear filter. It needs to meet the requirements on both the cutoff of the high-frequency sensing noise and the suppression of low-frequency input motion. What I obtained is the reduction of residual test mass pitch motion in the observational band, but still, the RMS requirement is not satisfied. The reduction of TM pitch motion using the Reinforcement Learning agent with respect to the linear controller is 6–8 times in 15–20 Hz frequency band. These results give optimism regarding future improvements. Once this controller is developed and tested with the time-domain simulations, the idea is to bring it to the Caltech 40m prototype for the first experimental test.

Appendix A

SPECFEM3D Cartesian plots

The surface propagation of the simulated ensemble forward wavefield for flat and topography models is shown in the sequence of snapshots in the figures A.1 and A.2, respectively. The ensemble forward field first converges on $\mathbf{x}^{\alpha}$ and then passes through the point and spreads out. The ensemble forward wavefield $\mathbf{\Phi}^{\alpha}$ would consist of isotropic concentric circles centered on $\mathbf{x}^{\alpha}$ if the model domain were the entire infinite flat plane, and the noise uniform across that flat plane (Tromp et al., 2010). However, because we are restricting the simulation domain and also in the topography model having a non-flat free surface, the ensemble forward wavefield is not isotropic. In this example the first and the second receiver were placed in the middle of the free surface of the models. The distance between them is 130 m.

The A3-topography surface normals for 500 m $\times$ 500 m area around TM are shown in the A.3.

The variation of power spectral densities of vertical surface displacement in the case of the flat free surface model is shown in figure A.4.

The result in figure A.5 tells us where a single seismometer should be placed, in the case of the flat-surface model, to obtain the best reduction of NN by coherent cancellation with a Wiener filter.

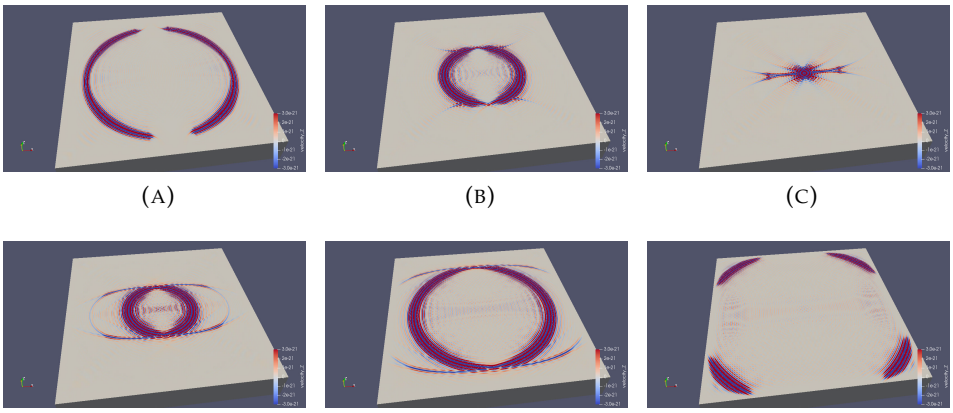

(A) (B) (C)

(D) (E) (F)

FIGURE A.1: The simulated ensemble forward wavefield for the flat-surface model.

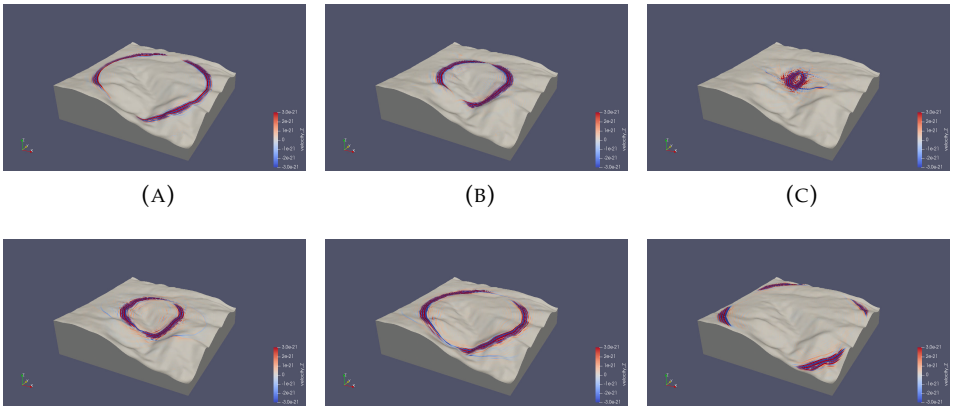

(A) (B) (C)

(D) (E) (F)

FIGURE A.2: The simulated ensemble forward wavefield for the A3-topography model.

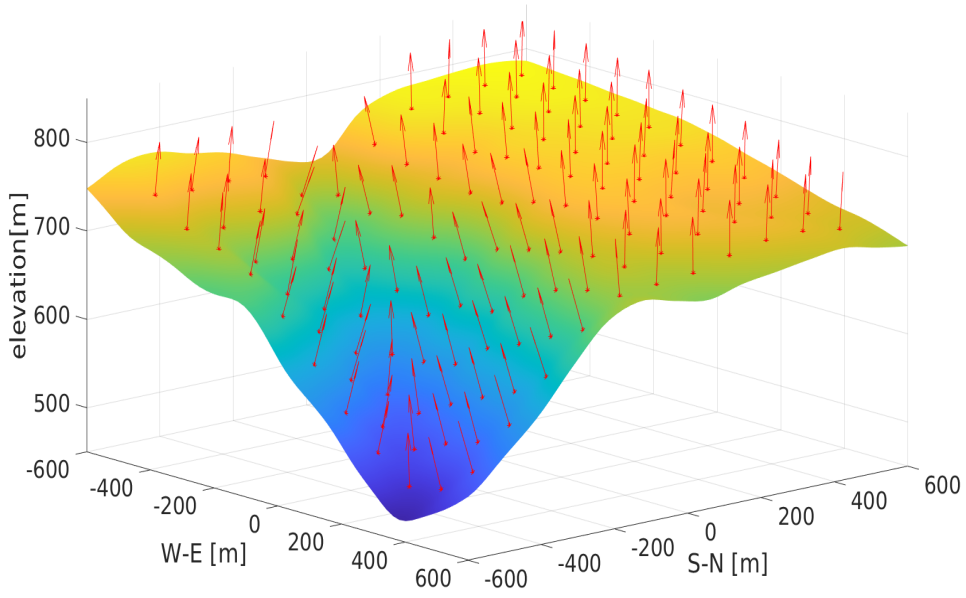

FIGURE A.3: Topography, stations, and normals of the topographic surface in the place of stations, in the vicinity of cavern A3. The stations used in the simulation are marked with red stars (from which normals arise).

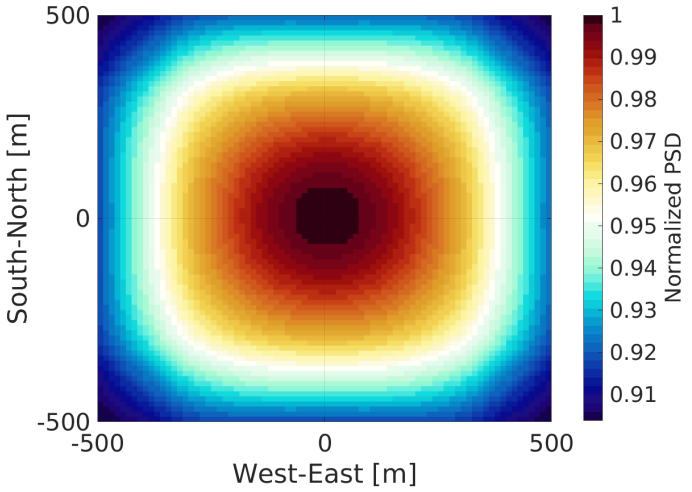

FIGURE A.4: Normalized spectral densities calculated for an ambient field with SPECFEM3D at 5 Hz for a flat-surface model.

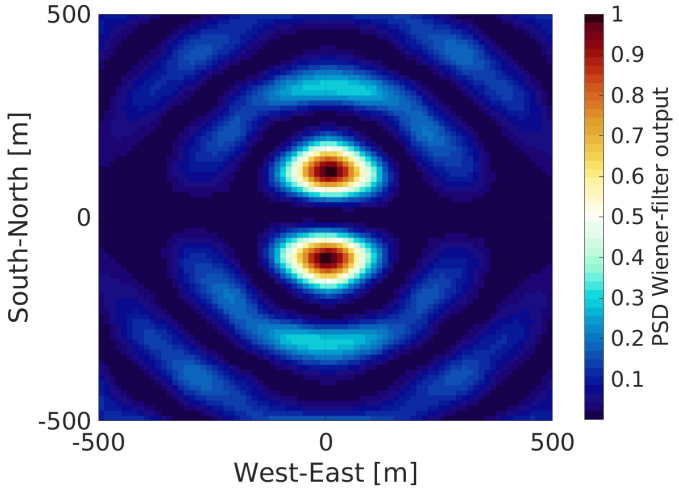

FIGURE A.5: The normalized PSD of the Wiener-filter output in the case of flat-surface model. The test mass is located 100 m underground. The direction of gravity acceleration is along the A3 – A1 detector arm.

Appendix B

Calibration for Lightsaber

Calibration means finding the proportionality factors between measured signals and the corresponding physical quantities. It is a critical aspect of characterization of any system.

B.1 LIGO-Lightsaber

DC gain is chosen by the control designers and above 30 it can cause instability of the control loop while choosing it to be lower than 30 doesn't give enough reduction of RMS of TM angular motion (weaker control of the system). DC gain for the soft controller is 20, and for the hard one, it is 30. Further, the optical response for the soft one is 10419 [ct/rad], while for the hard controller it is 4.44×10^{10} [ct/rad]. The digitized output of the controller needs to be converted to the analog signal, so in the actuator, it is converted to torque, therefore we need counts to torque factor which is equal for both soft and hard mode controllers and it is 6.32×10^{-10} [Nm/ct]. Overall gain is equal to the product of DC gain, optical response, and counts to torque factor. For the soft controller, it is 1.32×10^{-4} and for the hard one, it is 841.52. These calibration factors we got from our Caltech collaborators.

B.2 Lightsaber-IMC

In the case of Lightsaber-IMC, calibration is mostly finding proportionality factors between digital counts and physical quantities. The interface MEDM (Motif Editor and Display Manager) screen of single suspension RTCDS for MC1 is given in the figure B.1(A). MC2 and MC3 ones look similar to it. In order to get the actuators response, I was shaking mirrors using *LOCKIN2* as shown in the figure B.1(B). I was shaking them with N number of counts at 3 Hz, and looking at the time-domain sensor's OSEM output using *ndscope* tool [1]. Important was to shake in pitch, setting output filter to coil matrix as shown in figure B.1(C). To get actuator response in terms of pitch motion I was following the mirror's geometry. I divided the sensor's OSEM output by the mirror's radius and $\sqrt{2}$, and then divided it by the number of counts, N I was shaking with. What I obtained as actuators' responses at 3 Hz for MC1, MC2, MC3 are 7.736×10^{-8} $\frac{\text{rad}}{\text{cts}}$, 5.283×10^{-8} $\frac{\text{rad}}{\text{cts}}$, and 5.472×10^{-8} $\frac{\text{rad}}{\text{cts}}$, respectively. It was needed to scale this number back to DC, and

[1] The channels I looked at are C1:SUS-MC1_ULSEN_OUTPUT, C1:SUS-MC1_URSEN_OUTPUT, C1:SUS-MC1_LRSEN_OUTPUT, and C1:SUS-MC1_LLSEN_OUTPUT for MC1 mirror. The output of these channels is in micrometers. For actuator response for one mirror, I was taking the average of these.

with small manipulations with ratios, these responses need to be multiplied with 13 in order to get actuators' responses at DC.

Actuators' response is important in order to obtain optical gain matrix, which is basically sensing matrix, needed to go from local to sensing basis. Having actuators' response A, I was shaking MCs, using *LOCKIN2* as previously, in pitch with B counts at 3 Hz and getting WFS1, WFS2, and DC QPD error signals [2] of C counts at 3 Hz (using *ndscope* tool again, as shown in figure B.2), that means WFS1, WFS2, and DC QPD optical gain is $D\ \frac{\text{cts}}{\text{rad}} = \frac{C}{A \times B}$. I was shaking all 3 MCs, in order to obtain all nine elements of the optical gain matrix given in 3.13. The sign of optical gain matrix I was obtaining comparing the phase of the excitation and the phase of the error signal.

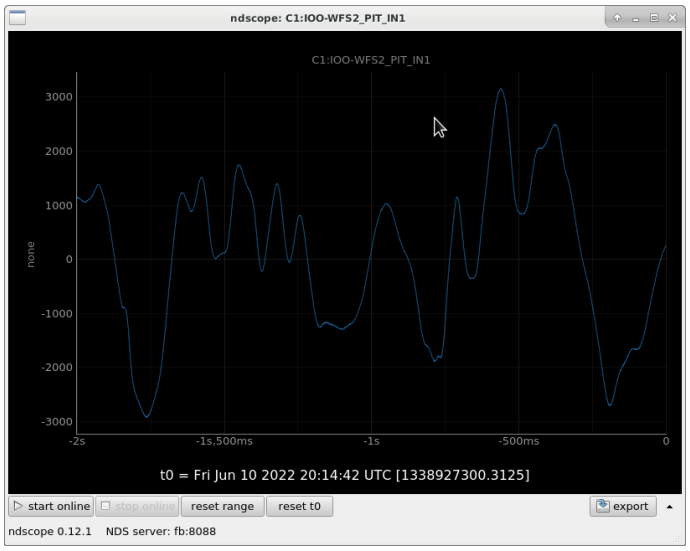

FIGURE B.2: Example of monitoring of WFS2 error pitch signal time-series using *ndscope* tool.

In order to get counts to torque calibration, I considered the transfer function of the rigid pendulum

$$H(\omega) = \frac{k}{I} \frac{1}{-\omega^2 + \omega_0^2 + i\frac{\omega\omega_0}{Q}}, \tag{B.1}$$

Where k is given in [Nm/cts]. Having excitation done at 3 Hz, and wanting calibration at DC, k is given with

$$k = I \times (-2\pi \times 3)^2 \times H(3Hz), \tag{B.2}$$

where $H(3Hz)$ is actuators' responses at 3 Hz. Counts to torque factor is 2.6958×10^{-9} [Nm/cts], 1.8410×10^{-9} [Nm/cts], and 1.9069×10^{-9} [Nm/cts] for MC1, MC2, and MC3, respectively.

In order to get the OSEM calibration factor in the local damping loop, I was looking at the suspension input matrix for pitch degree of freedom shown in figure B.3. These outputs are in counts per micrometer, then again looking at the

[2] The error signal channels are C1:IOO-WFS1_PIT_IN1, C1:IOO-WFS2_PIT_IN1, and C1:IOO-MC2_TRANS_PIT_IN1.

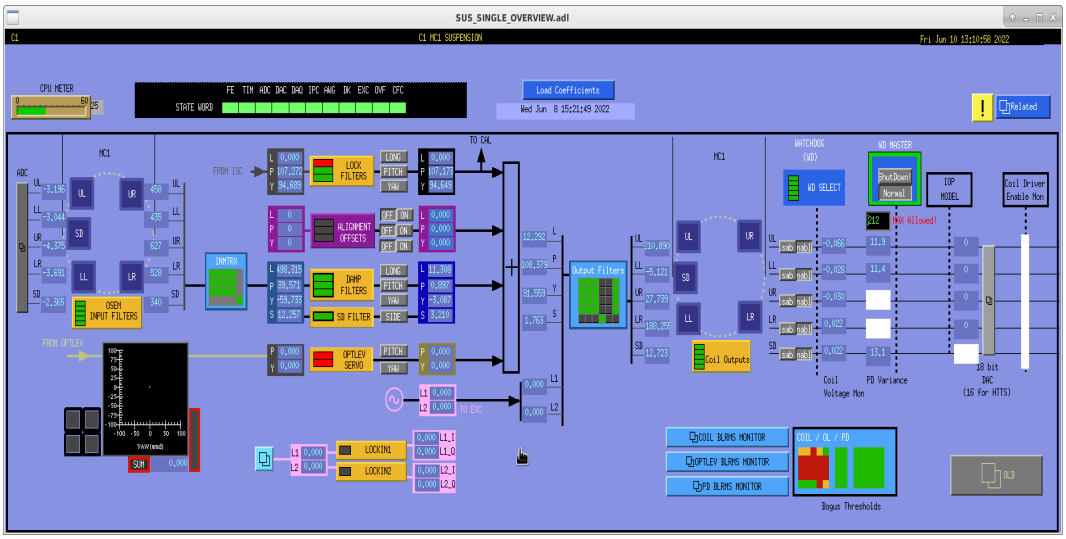

(A) The interface MEDM screen of single suspension RTCDS for MC1

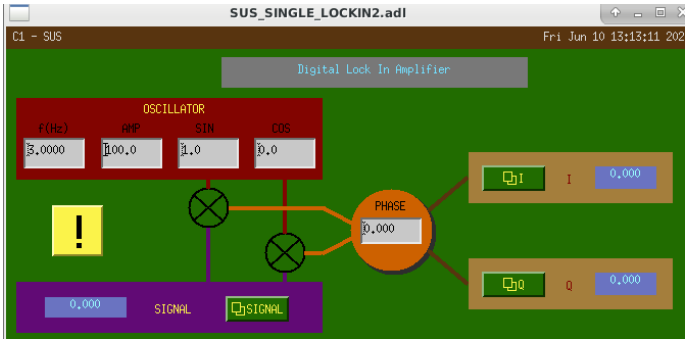

(B) *LOCKIN2* used in calibration procedure

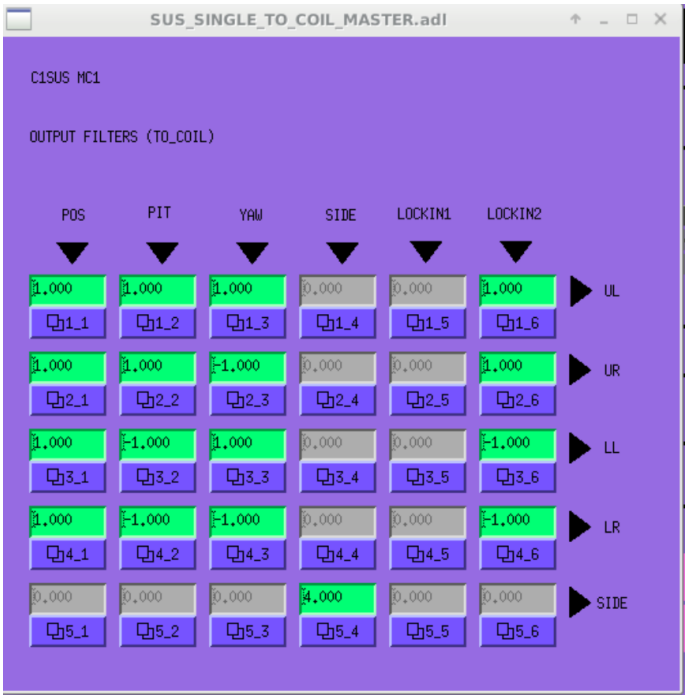

(C) Setting output filter to coil matrix to excite pitch DOF using *LOCKIN2*

FIGURE B.1: Screenshots describing calibration procedure using Simulink digital interface.

geometry of the mirror I got OSEM calibration factors to be 16377 [cts/rad] for MC1 and 176595 [cts/rad] for MC2 and MC3.

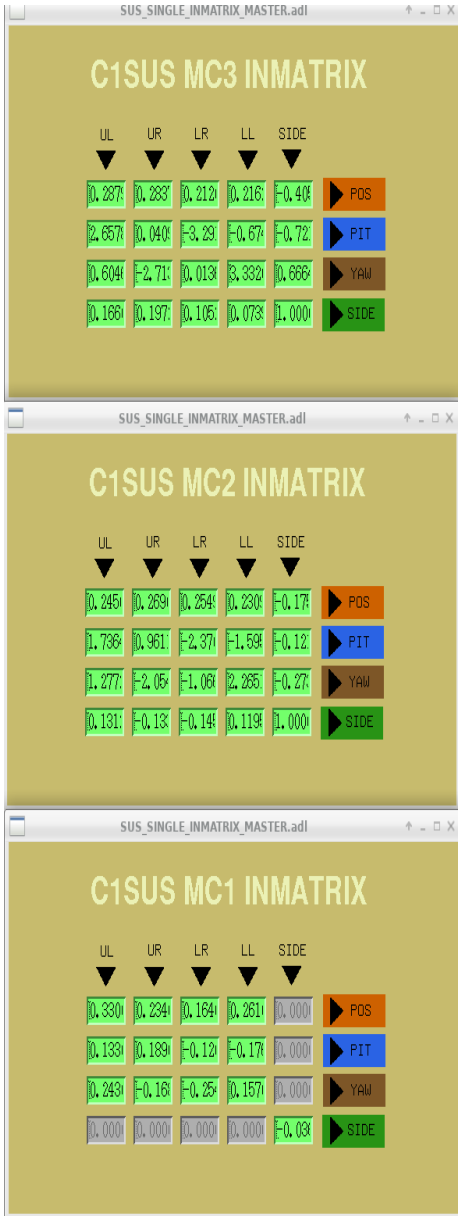

FIGURE B.3: Suspension input matrices for MCs.

The figure B.4 is showing coherence between the error signal and seismometer at the beamsplitter. The resolution of the figure is bad, but the purple line denotes coherence between the error signal of DC QPD in MC2 transmission with BS seismometer.

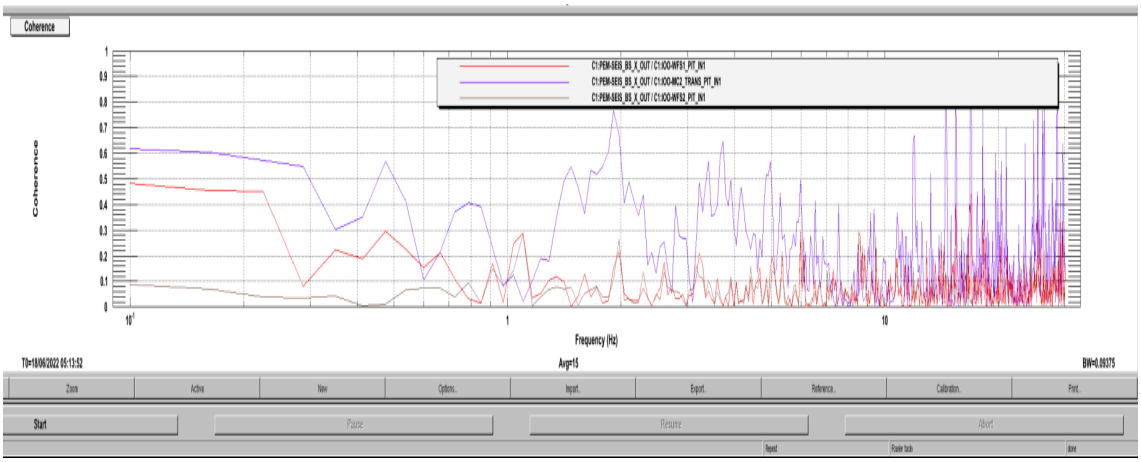

FIGURE B.4: Measured coherence between error signal and seismometer at the beamsplitter.

The figure giving ASD of feedback controller output in counts is shown in B.5.

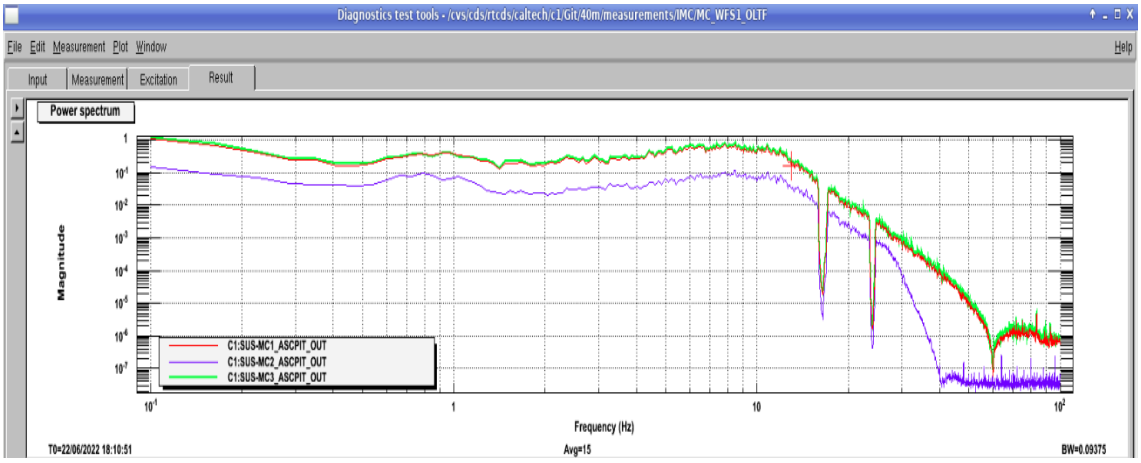

FIGURE B.5: Measured ASD of feedback controller output for MCs.

Appendix C

Simulink block diagrams for Lightsaber

The real-time models are drawn as block diagrams in Simulink, then run through a code generator. So when making the translation for this system, the first task is to go through the python code, follow all the signals around the loop, and track the operations that are done to them. It helped that the Lightsaber code is structured like a block diagram, with separate classes for the various subsystems. The block diagrams for LIGO-Lightsaber are given in section C.1, and for Lightsaber-IMC in section C.2.

C.1 LIGO-Lightsaber

In the next 20 pages there are, respectively: full LIGO-Lightsaber system, control system, eigenbasis to local basis matrix, RL policy, RPC gain, eigenbasis to local basis in RPC path, plant, arm, cavity geometry calculations, beam-spot, arm-cavity power, torque for ETM, torque for ITM, input power, reset, suspension and summing pitch motions for ETM, suspension and summing pitch motions for ITM, readout, local basis to eigenbasis matrix, reset.

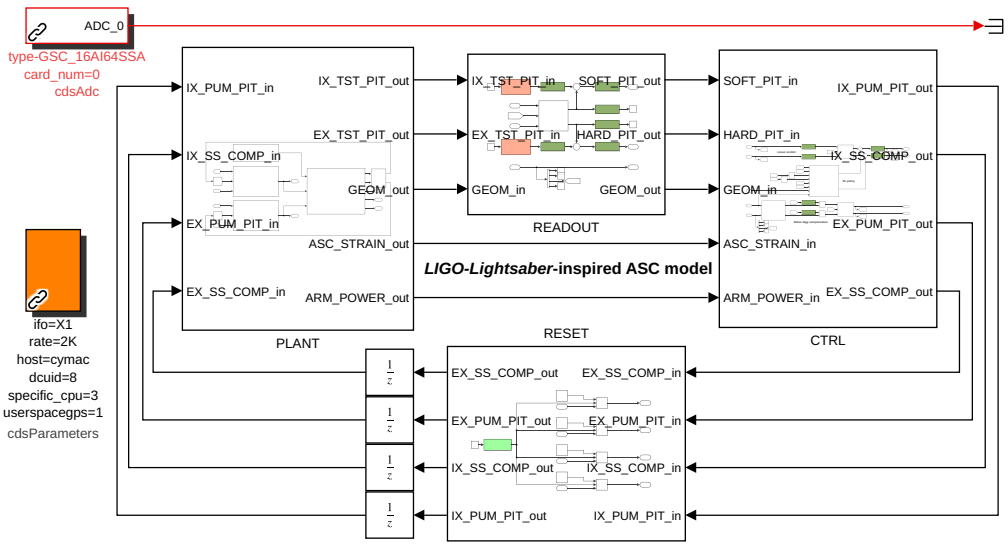
ADC_0
type-GSC_16AI64SSA
card_num=0
cdsAdc
ifo=X1
rate=2K
host=cymac
dcuid=8
specific_cpu=3
userspacegps=1
cdsParameters
IX_PUM_PIT_in
IX_TST_PIT_out
EX_TST_PIT_out
IX_SS_COMP_in
GEOM_out
EX_PUM_PIT_in
ASC_STRAIN_out
EX_SS_COMP_in
ARM_POWER_out
PLANT
IX_TST_PIT_in
SOFT_PIT_out
EX_TST_PIT_in
HARD_PIT_out
GEOM_in
GEOM_out
READOUT
SOFT_PIT_in
IX_PUM_PIT_out
HARD_PIT_in
IX_SS_COMP_out
GEOM_in
EX_PUM_PIT_out
ASC_STRAIN_in
ARM_POWER_in
EX_SS_COMP_out
CTRL
LIGO-Lightsaber-inspired ASC model
RESET
EX_SS_COMP_out
EX_SS_COMP_in
EX_PUM_PIT_out
EX_PUM_PIT_in
IX_SS_COMP_out
IX_SS_COMP_in
IX_PUM_PIT_out
IX_PUM_PIT_in

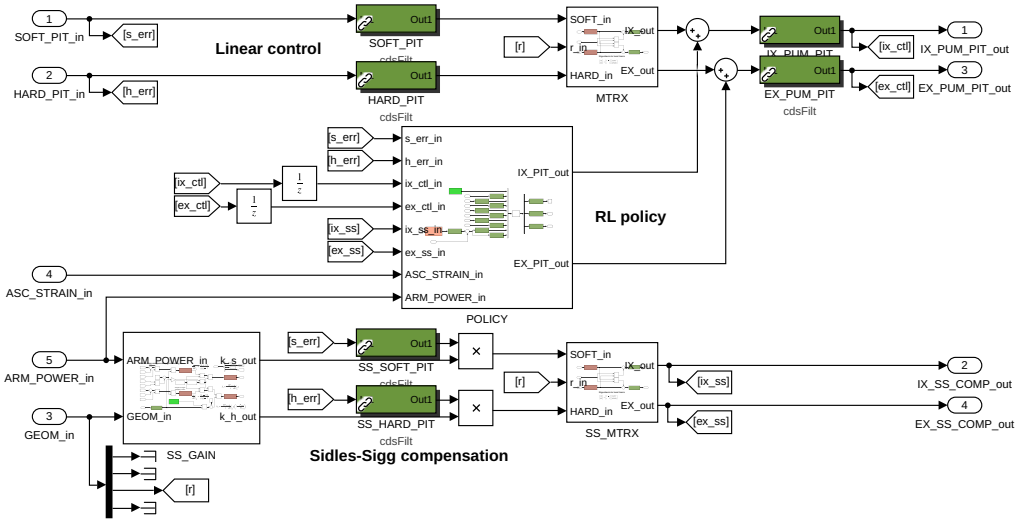
1
SOFT_PIT_in
[s_err]
Linear control
Out1
SOFT_PIT
cdsFilt
2
HARD_PIT_in
[h_err]
Out1
HARD_PIT
cdsFilt
[r]
SOFT_in
r_in
HARD_in
IX_out
EX_out
MTRX
Out1
IX_PUM_PIT
[ix_ctl]
1
IX_PUM_PIT_out
Out1
EX_PUM_PIT
cdsFilt
[ex_ctl]
3
EX_PUM_PIT_out
[s_err]
[h_err]
[ix_ctl]
[ex_ctl]
[ix_ss]
[ex_ss]
s_err_in
h_err_in
ix_ctl_in
ex_ctl_in
ix_ss_in
ex_ss_in
ASC_STRAIN_in
ARM_POWER_in
IX_PIT_out
EX_PIT_out
POLICY
RL policy
4
ASC_STRAIN_in
5
ARM_POWER_in
3
GEOM_in
ARM_POWER_in
GEOM_in
k_s_out
k_h_out
SS_GAIN
[r]
[s_err]
Out1
SS_SOFT_PIT
cdsFilt
[h_err]
Out1
SS_HARD_PIT
cdsFilt
Sidles-Sigg compensation
SOFT_in
r_in
HARD_in
IX_out
EX_out
SS_MTRX
[ix_ss]
[ex_ss]
2
IX_SS_COMP_out
4
EX_SS_COMP_out

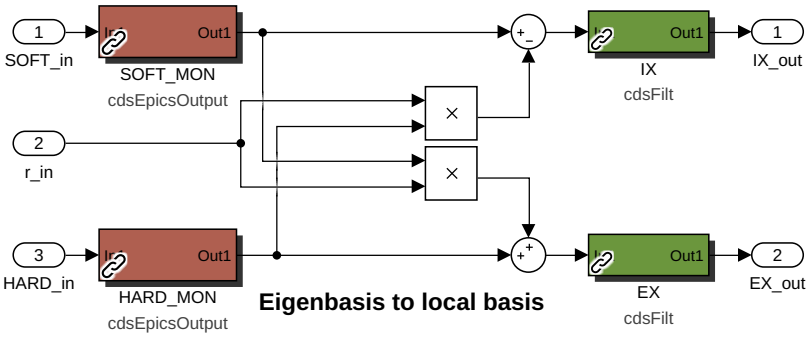
1
SOFT_in
In1
Out1
SOFT_MON
cdsEpicsOutput
2
r_in
3
HARD_in
In1
Out1
HARD_MON
cdsEpicsOutput
+
−
×
×
+
+
In1
Out1
IX
cdsFilt
In1
Out1
EX
cdsFilt
1
IX_out
2
EX_out
Eigenbasis to local basis
$\begin{bmatrix} IX \\ EX \end{bmatrix} = \begin{bmatrix} 1 & -r \\ r & 1 \end{bmatrix} \begin{bmatrix} SOFT \\ HARD \end{bmatrix}$

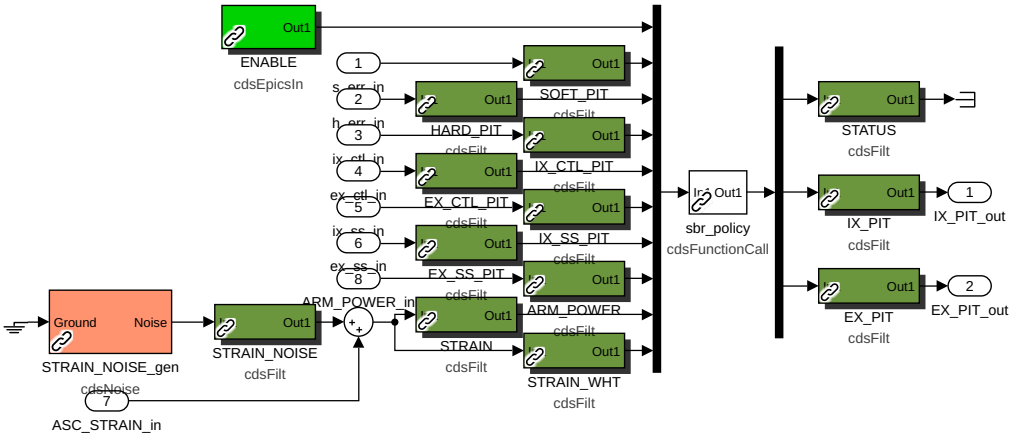
Out1
ENABLE
cdsEpicsIn
1
2
3
4
5
6
8
7
ASC_STRAIN_in
Out1
SOFT_PIT
cdsFilt
HARD_PIT
IX_CTL_PIT
EX_CTL_PIT
IX_SS_PIT
EX_SS_PIT
ARM_POWER
STRAIN
STRAIN_WHT
Ground
Noise
STRAIN_NOISE_gen
cdsNoise
STRAIN_NOISE
ARM_POWER_in
sbr_policy
cdsFunctionCall
STATUS
IX_PIT
IX_PIT_out
EX_PIT
EX_PIT_out

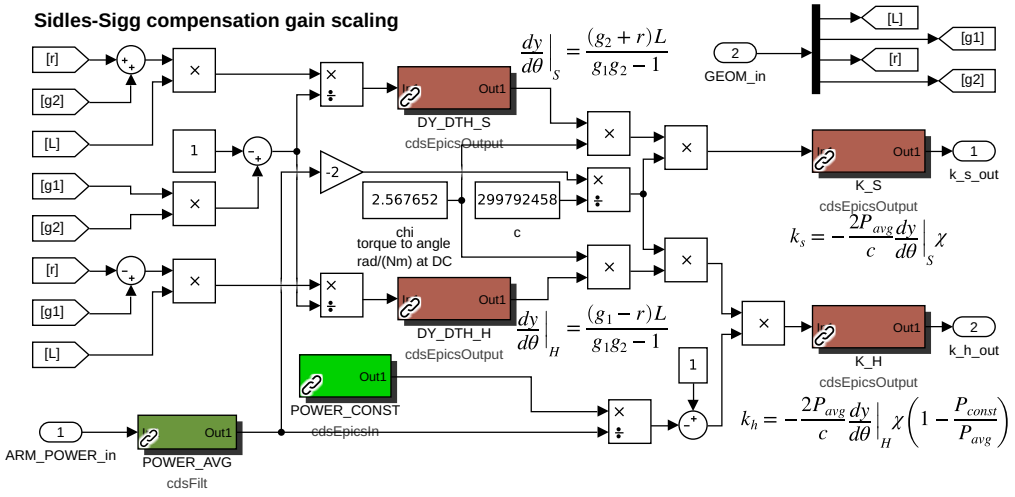
Sidles-Sigg compensation gain scaling
[r]
[g2]
[L]
[g1]
[g2]
[r]
[g1]
[L]
1
-2
2.567652
chi
torque to angle
rad/(Nm) at DC
299792458
c
Out1
DY_DTH_S
cdsEpicsOutput
DY_DTH_H
cdsEpicsOutput
POWER_CONST
cdsEpicsIn
1
ARM_POWER_in
Out1
POWER_AVG
cdsFilt
2
GEOM_in
[L]
[r]
[g1]
[g2]
K_S
cdsEpicsOutput
k_s_out
K_H
cdsEpicsOutput
k_h_out
$\left.\frac{dy}{d\theta}\right|_S = \frac{(g_2 + r)L}{g_1 g_2 - 1}$
$\left.\frac{dy}{d\theta}\right|_H = \frac{(g_1 - r)L}{g_1 g_2 - 1}$
$k_s = -\frac{2P_{avg}}{c}\left.\frac{dy}{d\theta}\right|_S \chi$
$k_h = -\frac{2P_{avg}}{c}\left.\frac{dy}{d\theta}\right|_H \chi\left(1 - \frac{P_{const}}{P_{avg}}\right)$

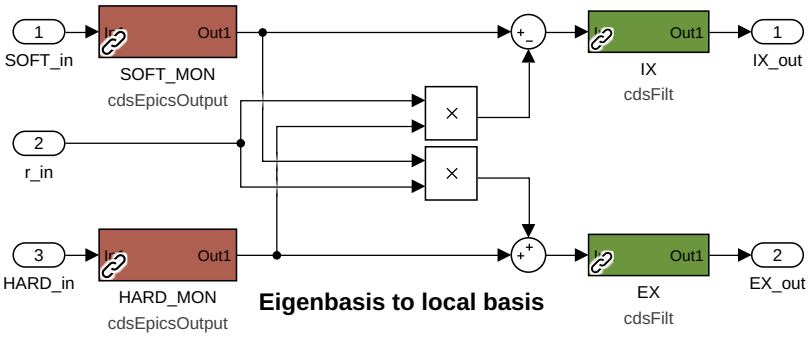
1
SOFT_in
In1
Out1
SOFT_MON
cdsEpicsOutput
2
r_in
3
HARD_in
In1
Out1
HARD_MON
cdsEpicsOutput
+
−
×
×
+
+
In1
Out1
IX
cdsFilt
In1
Out1
EX
cdsFilt
1
IX_out
2
EX_out
Eigenbasis to local basis
$\begin{bmatrix} IX \\ EX \end{bmatrix} = \begin{bmatrix} 1 & -r \\ r & 1 \end{bmatrix} \begin{bmatrix} SOFT \\ HARD \end{bmatrix}$

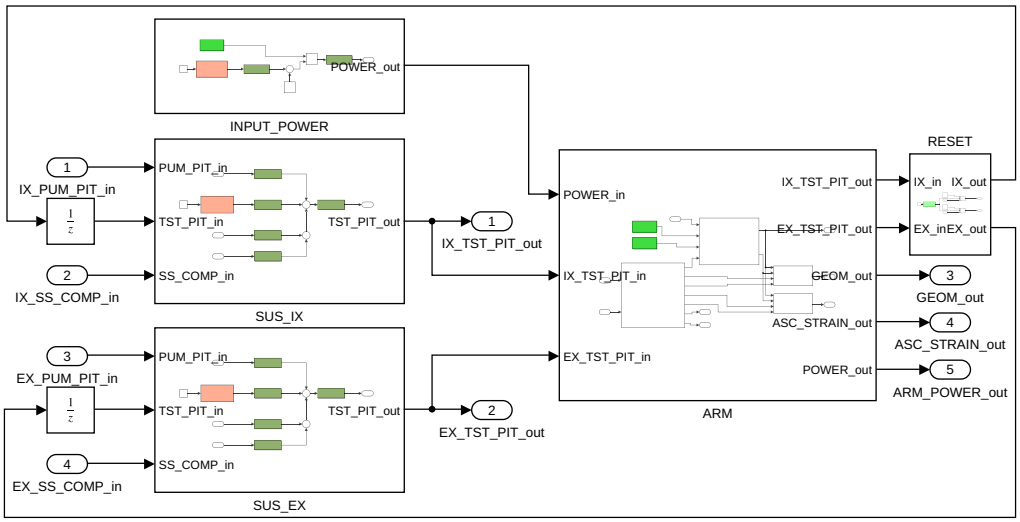
POWER_out
INPUT_POWER
1
IX_PUM_PIT_in
2
IX_SS_COMP_in
PUM_PIT_in
TST_PIT_in
SS_COMP_in
TST_PIT_out
SUS_IX
1
IX_TST_PIT_out
3
EX_PUM_PIT_in
4
EX_SS_COMP_in
PUM_PIT_in
TST_PIT_in
SS_COMP_in
TST_PIT_out
SUS_EX
2
EX_TST_PIT_out
POWER_in
IX_TST_PIT_in
EX_TST_PIT_in
IX_TST_PIT_out
EX_TST_PIT_out
GEOM_out
ASC_STRAIN_out
POWER_out
ARM
RESET
IX_in
IX_out
EX_in
EX_out
3
GEOM_out
4
ASC_STRAIN_out
5
ARM_POWER_out

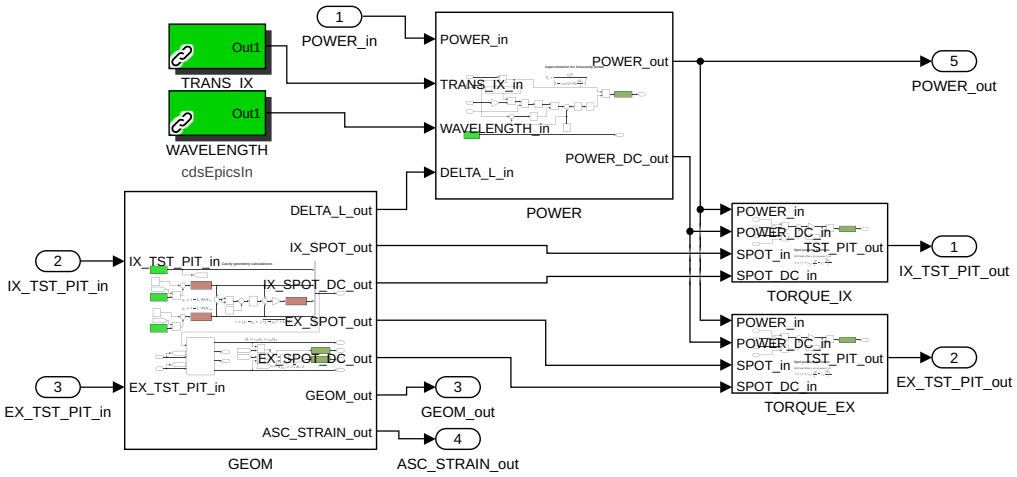
1
POWER_in
Out1
TRANS_IX
Out1
WAVELENGTH
cdsEpicsIn
POWER_in
TRANS_IX_in
WAVELENGTH_in
DELTA_L_in
POWER_out
POWER_DC_out
POWER
5
POWER_out
DELTA_L_out
IX_SPOT_out
IX_SPOT_DC_out
EX_SPOT_out
EX_SPOT_DC_out
GEOM_out
ASC_STRAIN_out
2
IX_TST_PIT_in
3
EX_TST_PIT_in
IX_TST_PIT_in
EX_TST_PIT_in
GEOM
3
GEOM_out
4
ASC_STRAIN_out
POWER_in
POWER_DC_in
SPOT_in
SPOT_DC_in
TST_PIT_out
TORQUE_IX
1
IX_TST_PIT_out
POWER_in
POWER_DC_in
SPOT_in
SPOT_DC_in
TST_PIT_out
TORQUE_EX
2
EX_TST_PIT_out

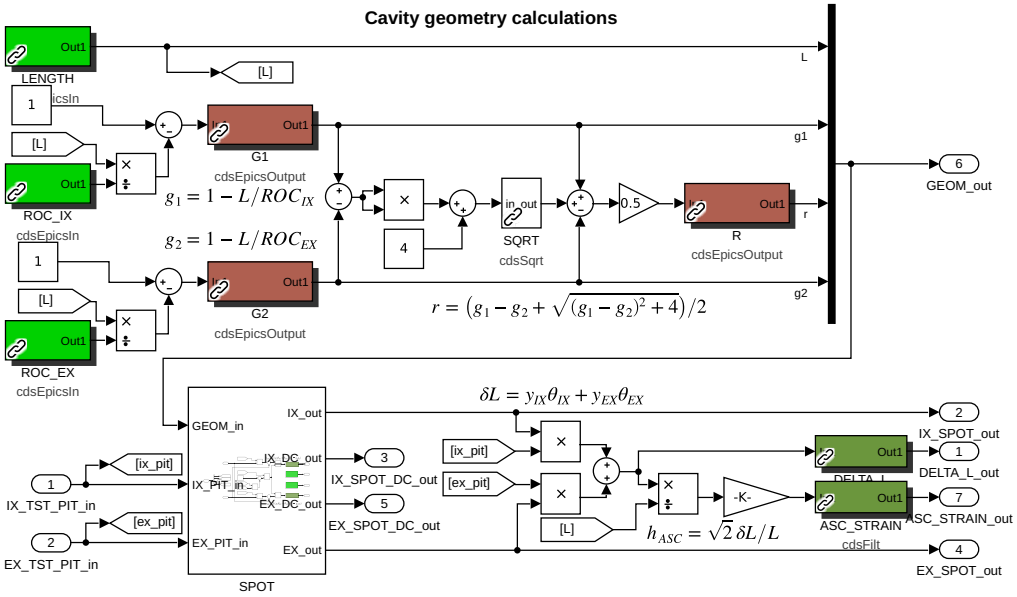
Cavity geometry calculations
Out1
LENGTH
[L]
L
1
icsIn
G1
cdsEpicsOutput
g1
[L]
Out1
ROC_IX
cdsEpicsIn
$g_1 = 1 - L/ROC_{IX}$
$g_2 = 1 - L/ROC_{EX}$
4
in_out
SQRT
cdsSqrt
0.5
R
cdsEpicsOutput
r
6
GEOM_out
1
[L]
Out1
ROC_EX
cdsEpicsIn
G2
cdsEpicsOutput
g2
$r = (g_1 - g_2 + \sqrt{(g_1 - g_2)^2 + 4})/2$
$\delta L = y_{IX}\theta_{IX} + y_{EX}\theta_{EX}$
GEOM_in
IX_out
IX_DC_out
IX_PIT_in
EX_DC_out
EX_PIT_in
EX_out
SPOT
[ix_pit]
[ex_pit]
1
IX_TST_PIT_in
2
EX_TST_PIT_in
3
IX_SPOT_DC_out
5
EX_SPOT_DC_out
2
IX_SPOT_out
1
DELTA_L_out
7
ASC_STRAIN_out
4
EX_SPOT_out
-K-
Out1
ASC_STRAIN
cdsFilt
$h_{ASC} = \sqrt{2}\,\delta L/L$

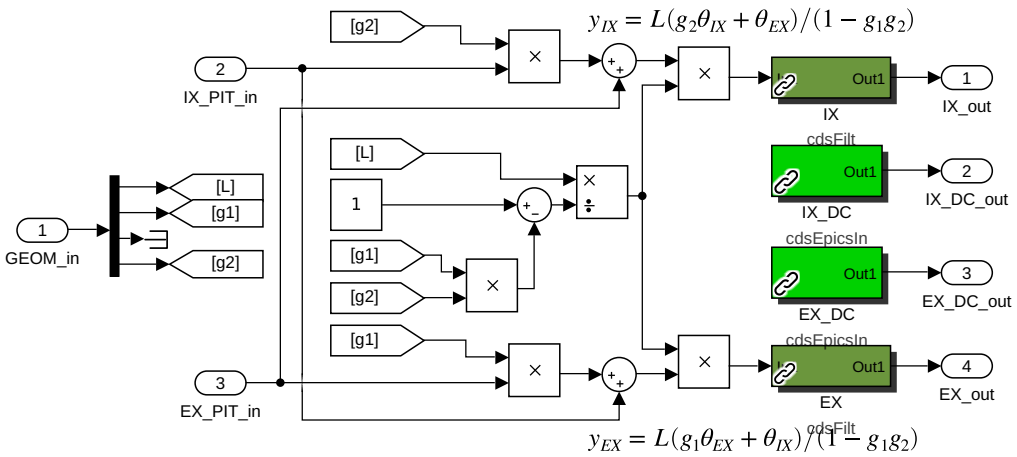
$y_{IX} = L(g_2\theta_{IX} + \theta_{EX})/(1 - g_1g_2)$
[g2]
2
IX_PIT_in
[L]
[g1]
[g2]
1
GEOM_in
[L]
1
[g1]
[g2]
[g1]
3
EX_PIT_in
Out1
IX
1
IX_out
cdsFilt
Out1
IX_DC
2
IX_DC_out
cdsEpicsIn
Out1
EX_DC
3
EX_DC_out
cdsEpicsIn
Out1
EX
4
EX_out
cdsFilt
$y_{EX} = L(g_1\theta_{EX} + \theta_{IX})/(1 - g_1g_2)$

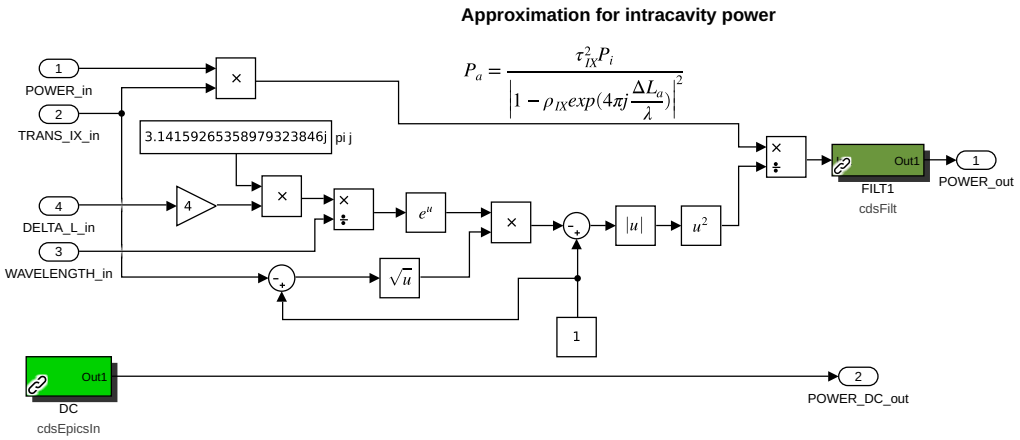
Approximation for intracavity power
$P_a = \frac{\tau_{IX}^2 P_i}{\left|1 - \rho_{IX} exp(4\pi j \frac{\Delta L_a}{\lambda})\right|^2}$
1
POWER_in
2
TRANS_IX_in
3.14159265358979323846j
pi j
4
4
DELTA_L_in
3
WAVELENGTH_in
e^u
$\sqrt{u}$
$|u|$
u^2
1
Out1
FILT1
cdsFilt
1
POWER_out
Out1
DC
cdsEpicsIn
2
POWER_DC_out

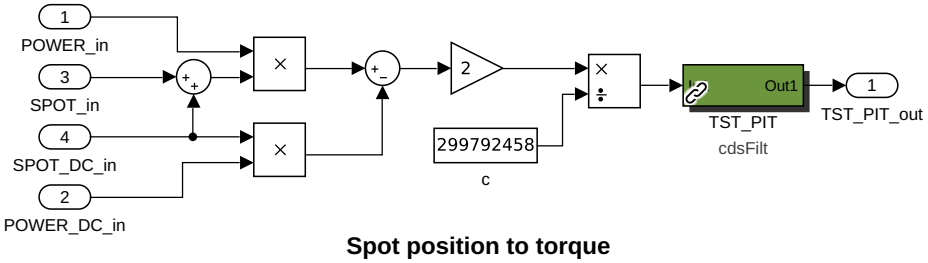

Spot position to torque

With fixed offset y_dc at power P_dc

$$\tau = (y + y_{dc})\frac{2P}{c} - y_{dc}\frac{2P_{dc}}{c}$$

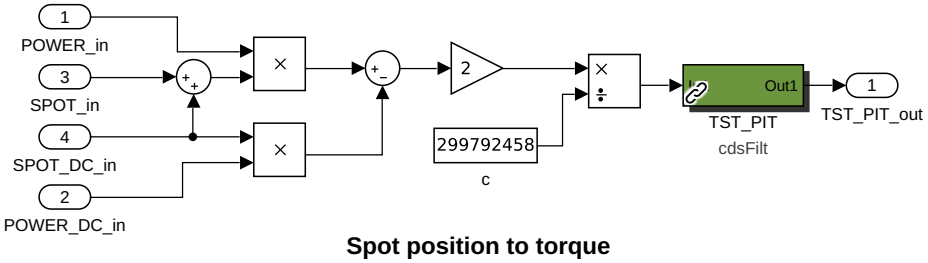

Spot position to torque

With fixed offset y_dc at power P_dc

$$\tau = (y + y_{dc})\frac{2P}{c} - y_{dc}\frac{2P_{dc}}{c}$$

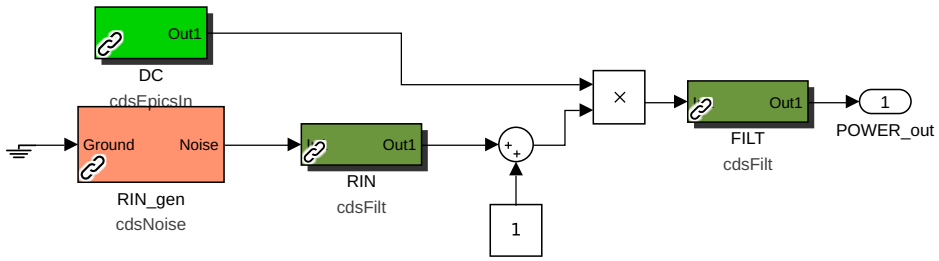
Out1
DC
cdsEpicsIn
Ground
Noise
RIN_gen
cdsNoise
Out1
RIN
cdsFilt
+
+
1
×
Out1
FILT
cdsFilt
1
POWER_out

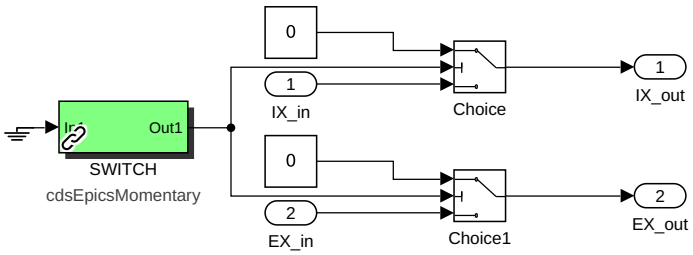
0
1
IX_in
Choice
1
IX_out
Out1
SWITCH
cdsEpicsMomentary
0
2
EX_in
Choice1
2
EX_out

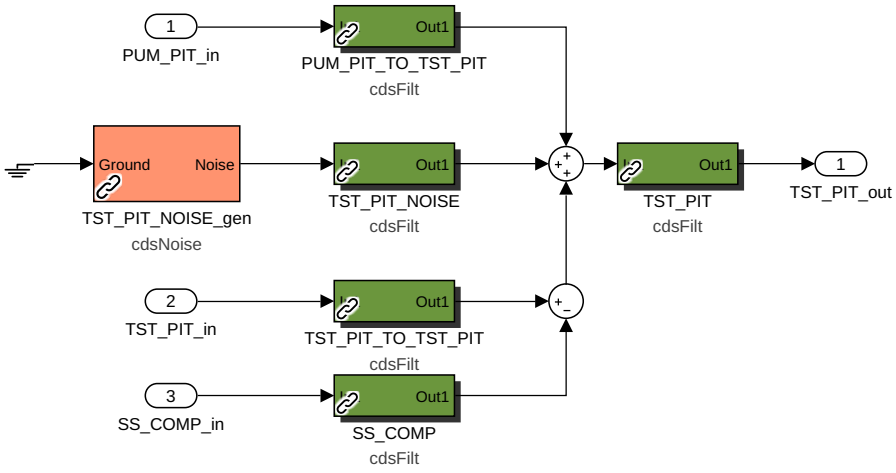
1
PUM_PIT_in
Out1
PUM_PIT_TO_TST_PIT
cdsFilt
Ground
Noise
TST_PIT_NOISE_gen
cdsNoise
Out1
TST_PIT_NOISE
cdsFilt
Out1
TST_PIT
cdsFilt
1
TST_PIT_out
2
TST_PIT_in
Out1
TST_PIT_TO_TST_PIT
cdsFilt
3
SS_COMP_in
Out1
SS_COMP
cdsFilt

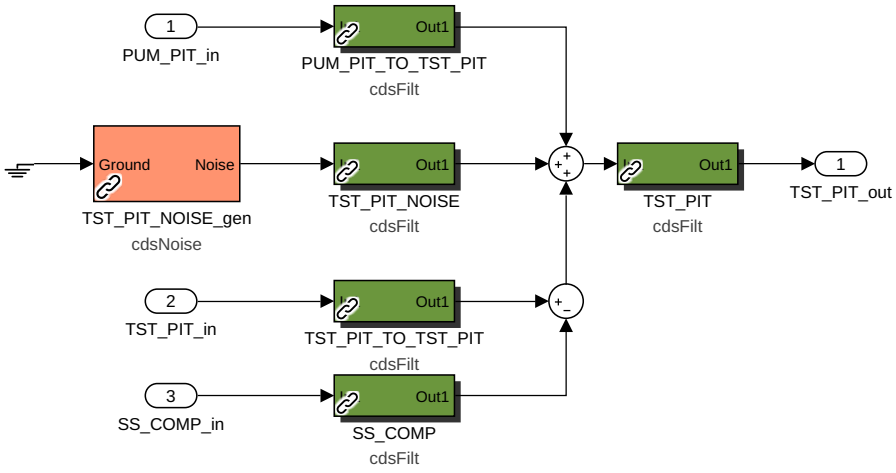
1
PUM_PIT_in
Out1
PUM_PIT_TO_TST_PIT
cdsFilt
Ground
Noise
TST_PIT_NOISE_gen
cdsNoise
Out1
TST_PIT_NOISE
cdsFilt
Out1
TST_PIT
cdsFilt
1
TST_PIT_out
2
TST_PIT_in
Out1
TST_PIT_TO_TST_PIT
cdsFilt
3
SS_COMP_in
Out1
SS_COMP
cdsFilt

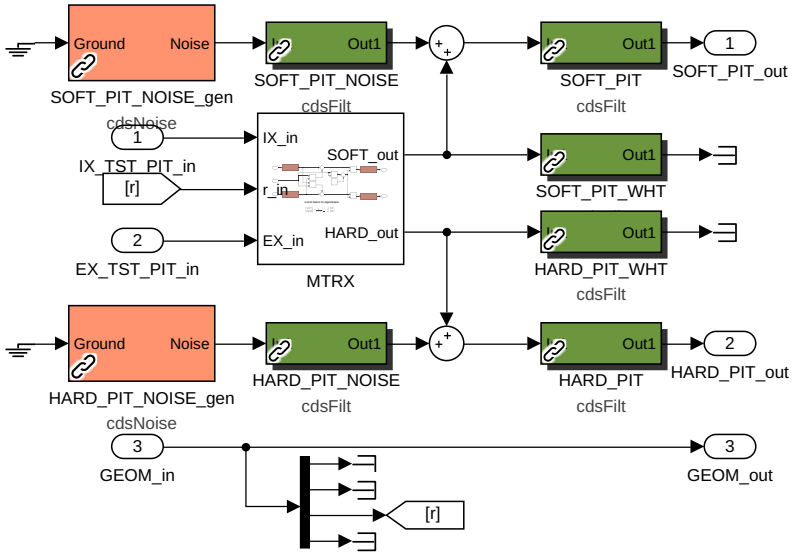
Ground
Noise
SOFT_PIT_NOISE_gen
cdsNoise
Out1
SOFT_PIT_NOISE
cdsFilt
Out1
SOFT_PIT
cdsFilt
1
SOFT_PIT_out
1
IX_TST_PIT_in
[r]
IX_in
r_in
SOFT_out
HARD_out
EX_in
MTRX
Out1
SOFT_PIT_WHT
2
EX_TST_PIT_in
Out1
HARD_PIT_WHT
cdsFilt
Ground
Noise
HARD_PIT_NOISE_gen
cdsNoise
Out1
HARD_PIT_NOISE
cdsFilt
Out1
HARD_PIT
cdsFilt
2
HARD_PIT_out
3
GEOM_in
3
GEOM_out
[r]

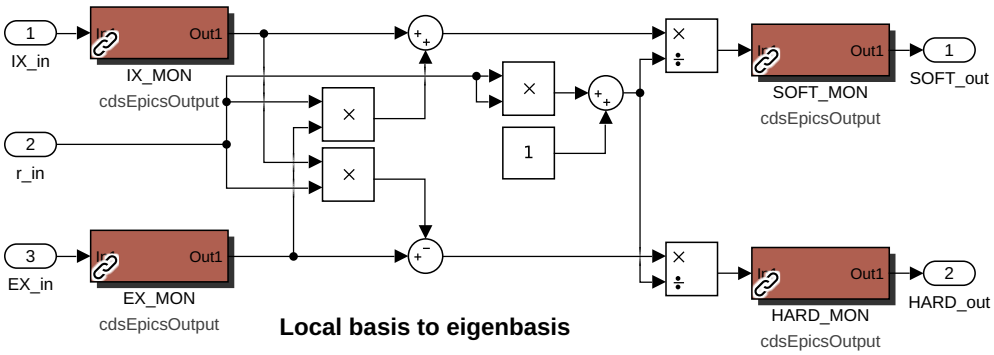
1
IX_in
Out1
IX_MON
cdsEpicsOutput
2
r_in
3
EX_in
Out1
EX_MON
cdsEpicsOutput
1
SOFT_MON
cdsEpicsOutput
SOFT_out
2
HARD_MON
cdsEpicsOutput
HARD_out
Local basis to eigenbasis
$\begin{bmatrix} SOFT \\ HARD \end{bmatrix} = \frac{1}{1+r^2} \begin{bmatrix} 1 & r \\ -r & 1 \end{bmatrix} \begin{bmatrix} IX \\ EX \end{bmatrix}$

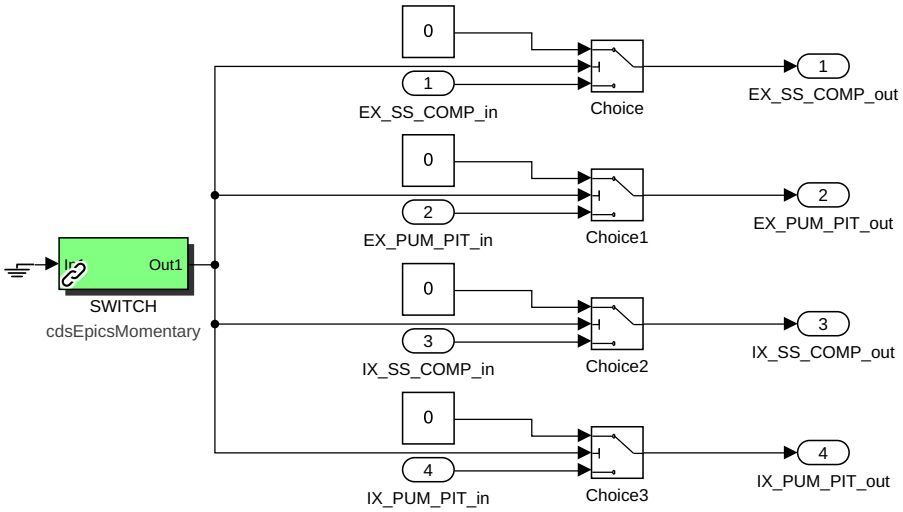
0
1
EX_SS_COMP_in
Choice
1
EX_SS_COMP_out
0
2
EX_PUM_PIT_in
Choice1
2
EX_PUM_PIT_out
In1
Out1
SWITCH
cdsEpicsMomentary
0
3
IX_SS_COMP_in
Choice2
3
IX_SS_COMP_out
0
4
IX_PUM_PIT_in
Choice3
4
IX_PUM_PIT_out

C.2 Lightsaber-IMC

In the next 22 pages there are, respectively: full Lightsaber-IMC system, ASCPIT control, control output matrix, main feedback control, RL policy, local damping, plant, cavity, cavity geometry calculations, beam-spot, IMC cavity power, torque for MC1, torque for MC2, torque for MC3, input power, reset, suspension and summing pitch motions for MC1, suspension and summing pitch motions for MC2, suspension and summing pitch motions for MC3, readout, local to sensor basis matrix, reset.

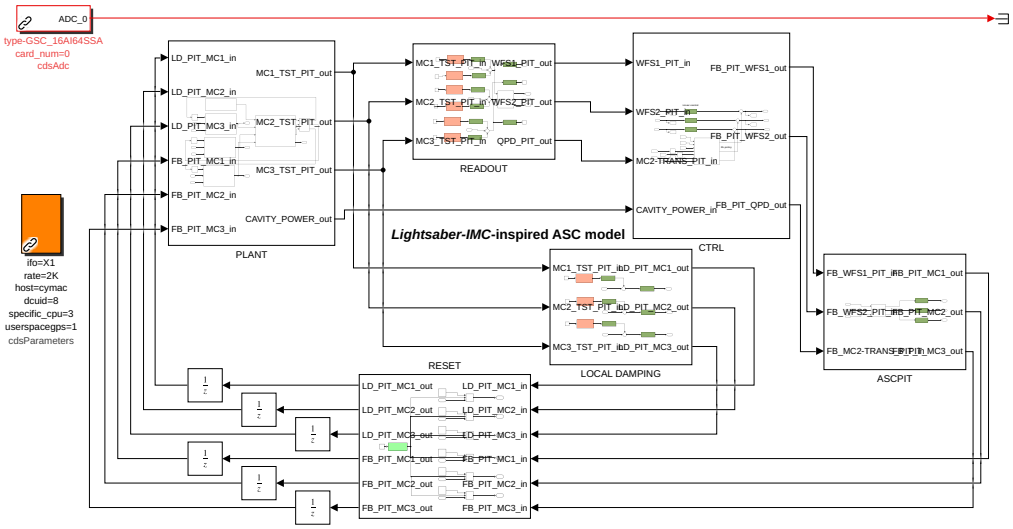
ADC_0
type-GSC_16AI64SSA
card_num=0
cdsAdc
ifo=X1
rate=2K
host=cymac
dcuid=8
specific_cpu=3
userspacegps=1
cdsParameters
LD_PIT_MC1_in
LD_PIT_MC2_in
LD_PIT_MC3_in
FB_PIT_MC1_in
FB_PIT_MC2_in
FB_PIT_MC3_in
MC1_TST_PIT_out
MC2_TST_PIT_out
MC3_TST_PIT_out
CAVITY_POWER_out
PLANT
MC1_TST_PIT_in
MC2_TST_PIT_in
MC3_TST_PIT_in
WFS1_PIT_out
WFS2_PIT_out
QPD_PIT_out
READOUT
WFS1_PIT_in
WFS2_PIT_in
MC2-TRANS_PIT_in
CAVITY_POWER_in
FB_PIT_WFS1_out
FB_PIT_WFS2_out
FB_PIT_QPD_out
CTRL
Lightsaber-IMC-inspired ASC model
MC1_TST_PIT_in
MC2_TST_PIT_in
MC3_TST_PIT_in
LD_PIT_MC1_out
LD_PIT_MC2_out
LD_PIT_MC3_out
LOCAL DAMPING
FB_WFS1_PIT_in
FB_WFS2_PIT_in
FB_MC2-TRANS_PIT_in
FB_PIT_MC1_out
FB_PIT_MC2_out
FB_PIT_MC3_out
ASCPIT
RESET
LD_PIT_MC1_out
LD_PIT_MC2_out
LD_PIT_MC3_out
FB_PIT_MC1_out
FB_PIT_MC2_out
FB_PIT_MC3_out
LD_PIT_MC1_in
LD_PIT_MC2_in
LD_PIT_MC3_in
FB_PIT_MC1_in
FB_PIT_MC2_in
FB_PIT_MC3_in

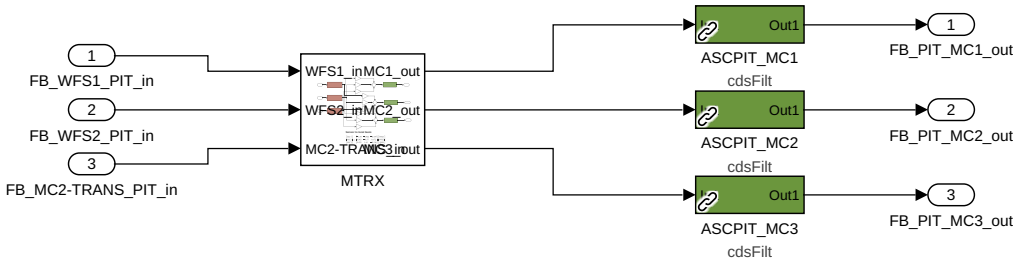
1
FB_WFS1_PIT_in
2
FB_WFS2_PIT_in
3
FB_MC2-TRANS_PIT_in
WFS1_inMC1_out
WFS2_inMC2_out
MC2-TRANS_inMC3_out
MTRX
Out1
ASCPIT_MC1
cdsFilt
Out1
ASCPIT_MC2
cdsFilt
Out1
ASCPIT_MC3
cdsFilt
1
FB_PIT_MC1_out
2
FB_PIT_MC2_out
3
FB_PIT_MC3_out

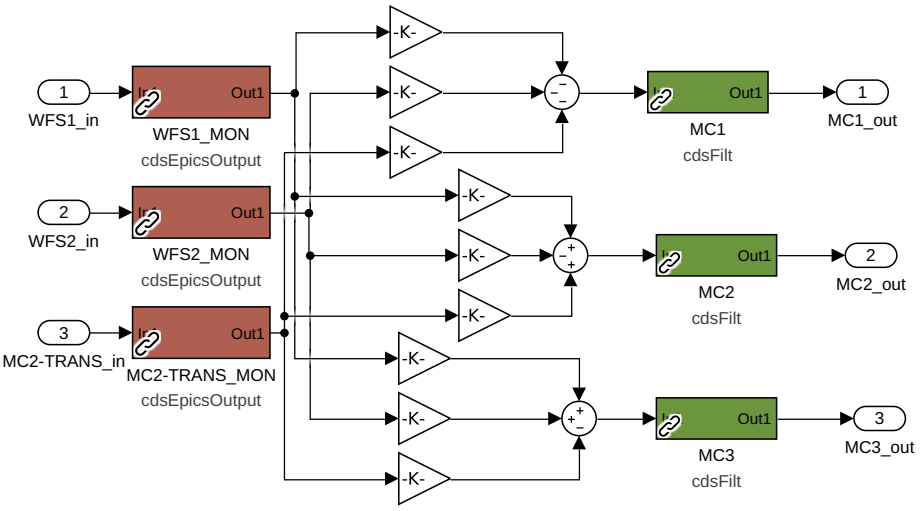

Sensor to local basis

$$\begin{bmatrix} MC1 \\ MC2 \\ MC3 \end{bmatrix} = \begin{bmatrix} -1.59 & -0.902 & -0.559 \\ 0.962 & -0.57 & 0.172 \\ 0.425 & 1.61 & -0.516 \end{bmatrix} \begin{bmatrix} WFS1 \\ WFS2 \\ QPD \end{bmatrix}$$

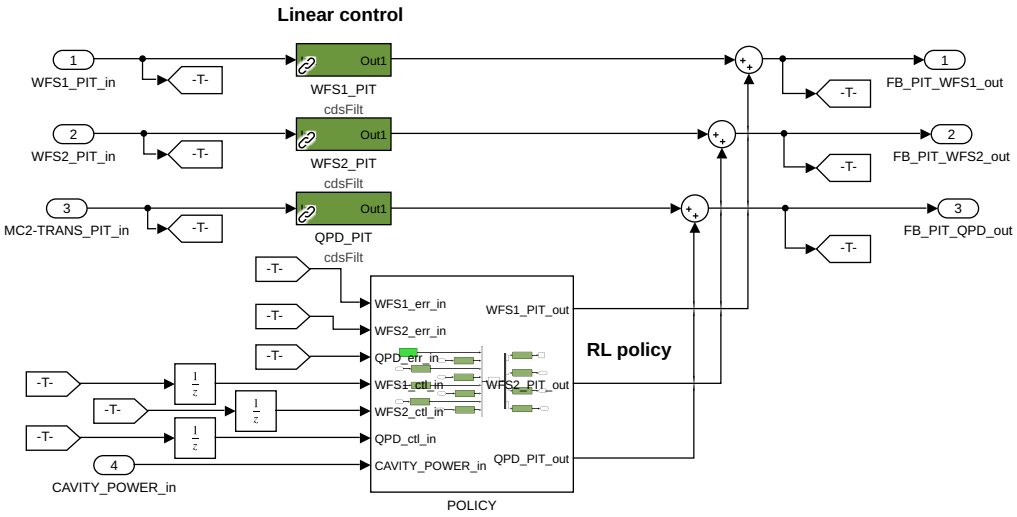
Linear control
1
WFS1_PIT_in
-T-
Out1
WFS1_PIT
cdsFilt
2
WFS2_PIT_in
-T-
Out1
WFS2_PIT
cdsFilt
3
MC2-TRANS_PIT_in
-T-
Out1
QPD_PIT
cdsFilt
-T-
-T-
-T-
-T-
-T-
-T-
4
CAVITY_POWER_in
WFS1_err_in
WFS2_err_in
QPD_err_in
WFS1_ctl_in
WFS2_ctl_in
QPD_ctl_in
CAVITY_POWER_in
WFS1_PIT_out
WFS2_PIT_out
QPD_PIT_out
RL policy
POLICY
1
FB_PIT_WFS1_out
-T-
2
FB_PIT_WFS2_out
-T-
3
FB_PIT_QPD_out
-T-

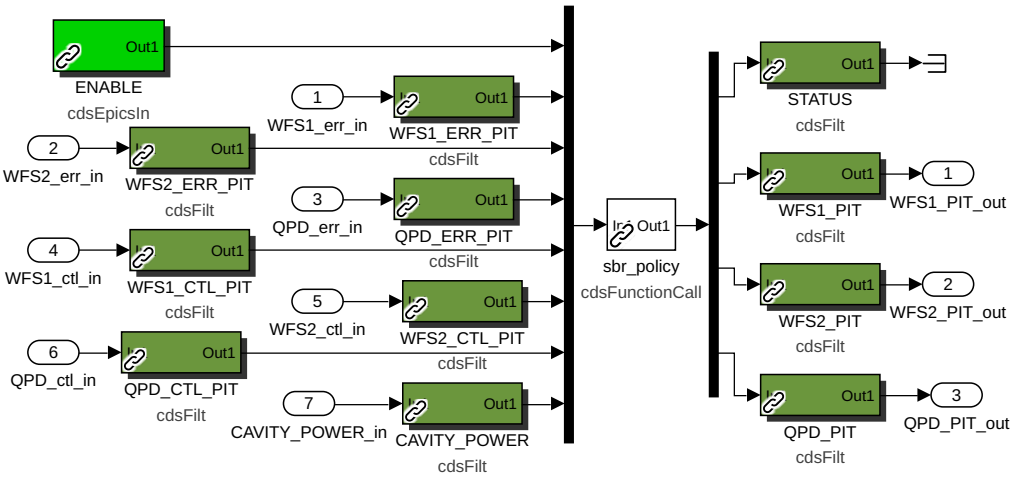
Out1
ENABLE
cdsEpicsIn
1
WFS1_err_in
Out1
WFS1_ERR_PIT
cdsFilt
2
WFS2_err_in
Out1
WFS2_ERR_PIT
cdsFilt
3
QPD_err_in
Out1
QPD_ERR_PIT
cdsFilt
4
WFS1_ctl_in
Out1
WFS1_CTL_PIT
cdsFilt
5
WFS2_ctl_in
Out1
WFS2_CTL_PIT
cdsFilt
6
QPD_ctl_in
Out1
QPD_CTL_PIT
cdsFilt
7
CAVITY_POWER_in
Out1
CAVITY_POWER
cdsFilt
Out1
sbr_policy
cdsFunctionCall
Out1
STATUS
cdsFilt
Out1
WFS1_PIT
cdsFilt
1
WFS1_PIT_out
Out1
WFS2_PIT
cdsFilt
2
WFS2_PIT_out
Out1
QPD_PIT
cdsFilt
3
QPD_PIT_out

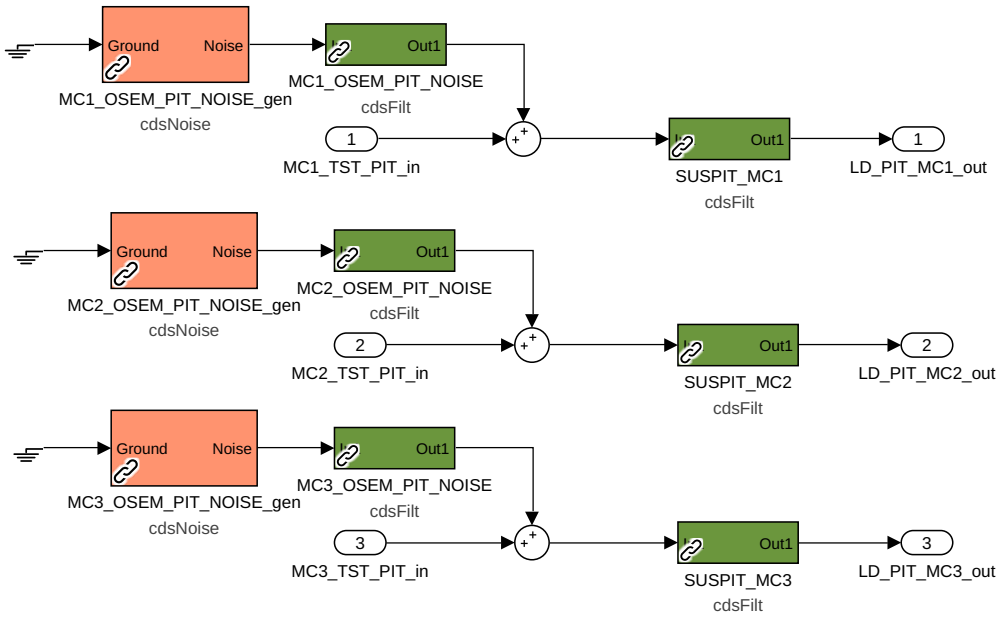
Ground
Noise
MC1_OSEM_PIT_NOISE_gen
cdsNoise
Out1
MC1_OSEM_PIT_NOISE
cdsFilt
1
MC1_TST_PIT_in
Out1
SUSPIT_MC1
cdsFilt
1
LD_PIT_MC1_out
Ground
Noise
MC2_OSEM_PIT_NOISE_gen
cdsNoise
Out1
MC2_OSEM_PIT_NOISE
cdsFilt
2
MC2_TST_PIT_in
Out1
SUSPIT_MC2
cdsFilt
2
LD_PIT_MC2_out
Ground
Noise
MC3_OSEM_PIT_NOISE_gen
cdsNoise
Out1
MC3_OSEM_PIT_NOISE
cdsFilt
3
MC3_TST_PIT_in
Out1
SUSPIT_MC3
cdsFilt
3
LD_PIT_MC3_out

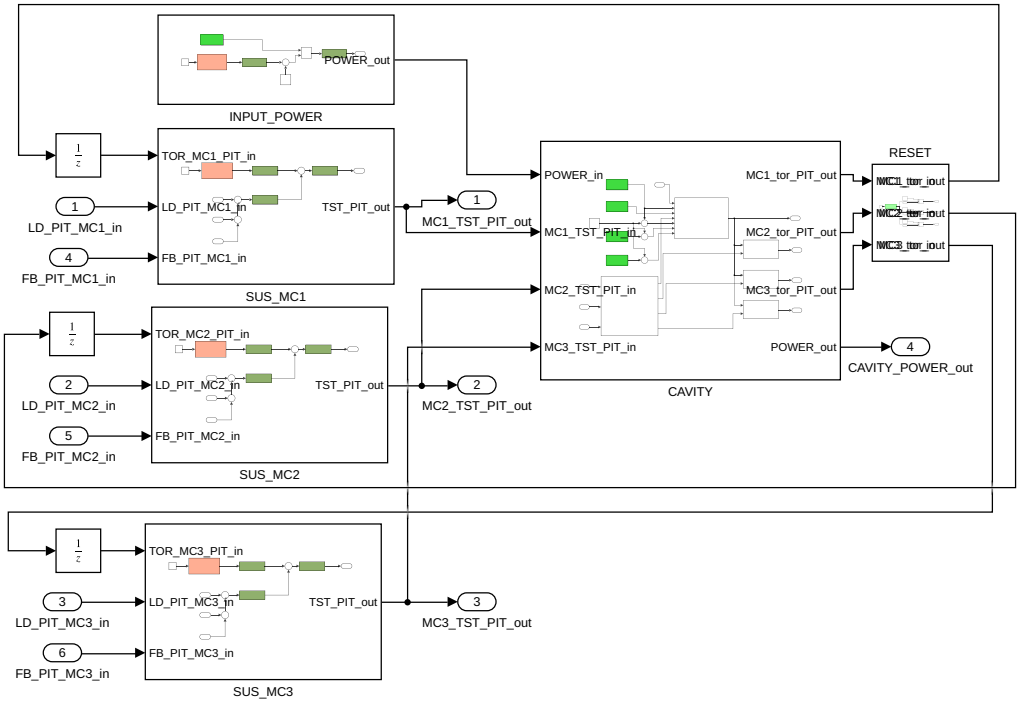
POWER_out
INPUT_POWER
TOR_MC1_PIT_in
LD_PIT_MC1_in
TST_PIT_out
FB_PIT_MC1_in
SUS_MC1
1
LD_PIT_MC1_in
4
FB_PIT_MC1_in
1
MC1_TST_PIT_out
TOR_MC2_PIT_in
LD_PIT_MC2_in
TST_PIT_out
FB_PIT_MC2_in
SUS_MC2
2
LD_PIT_MC2_in
5
FB_PIT_MC2_in
2
MC2_TST_PIT_out
TOR_MC3_PIT_in
LD_PIT_MC3_in
TST_PIT_out
FB_PIT_MC3_in
SUS_MC3
3
LD_PIT_MC3_in
6
FB_PIT_MC3_in
3
MC3_TST_PIT_out
POWER_in
MC1_TST_PIT_in
MC2_TST_PIT_in
MC3_TST_PIT_in
MC1_tor_PIT_out
MC2_tor_PIT_out
MC3_tor_PIT_out
POWER_out
CAVITY
4
CAVITY_POWER_out
RESET

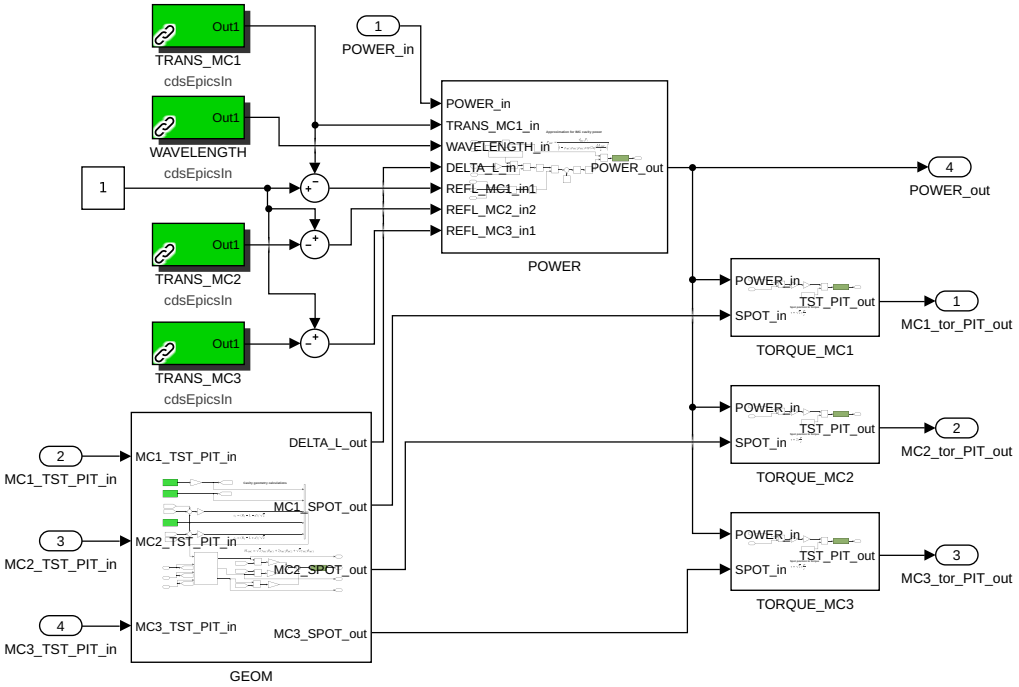
Out1
TRANS_MC1
cdsEpicsIn
Out1
WAVELENGTH
cdsEpicsIn
1
Out1
TRANS_MC2
cdsEpicsIn
Out1
TRANS_MC3
cdsEpicsIn
1
POWER_in
POWER_in
TRANS_MC1_in
WAVELENGTH_in
DELTA_L_in
REFL_MC1_in1
REFL_MC2_in2
REFL_MC3_in1
POWER_out
POWER
4
POWER_out
POWER_in
SPOT_in
TST_PIT_out
TORQUE_MC1
1
MC1_tor_PIT_out
POWER_in
SPOT_in
TST_PIT_out
TORQUE_MC2
2
MC2_tor_PIT_out
POWER_in
SPOT_in
TST_PIT_out
TORQUE_MC3
3
MC3_tor_PIT_out
2
MC1_TST_PIT_in
3
MC2_TST_PIT_in
4
MC3_TST_PIT_in
MC1_TST_PIT_in
MC2_TST_PIT_in
MC3_TST_PIT_in
DELTA_L_out
MC1_SPOT_out
MC2_SPOT_out
MC3_SPOT_out
GEOM

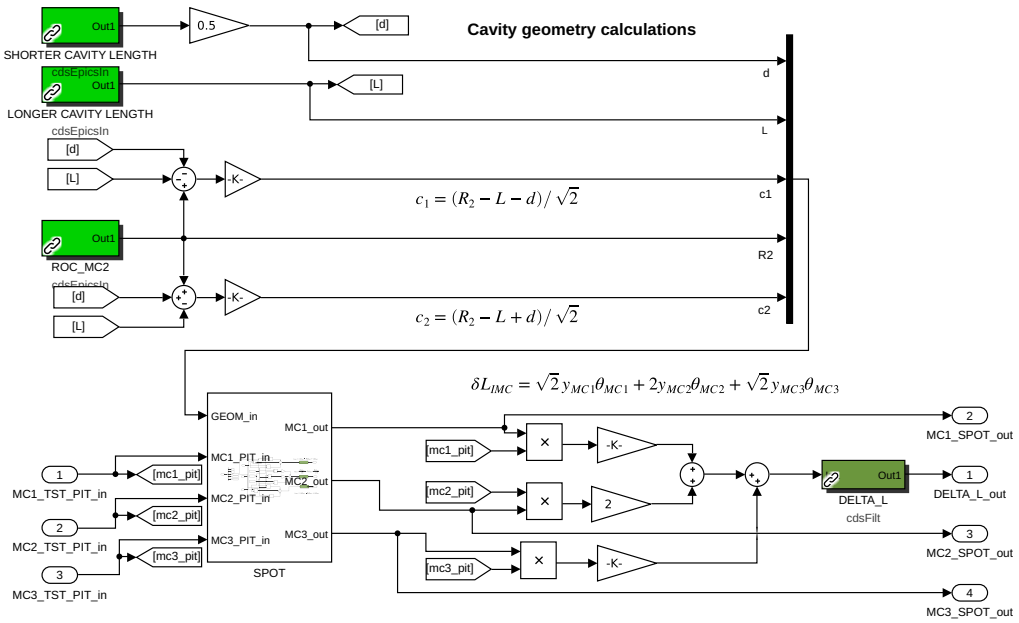
Cavity geometry calculations
Out1
SHORTER CAVITY LENGTH
0.5
[d]
d
cdsEpicsIn
Out1
LONGER CAVITY LENGTH
[L]
L
cdsEpicsIn
[d]
[L]
-K-
$c_1 = (R_2 - L - d)/\sqrt{2}$
c1
Out1
ROC_MC2
R2
cdsEpicsIn
[d]
[L]
-K-
$c_2 = (R_2 - L + d)/\sqrt{2}$
c2
$\delta L_{IMC} = \sqrt{2}\, y_{MC1}\theta_{MC1} + 2 y_{MC2}\theta_{MC2} + \sqrt{2}\, y_{MC3}\theta_{MC3}$
GEOM_in
MC1_PIT_in
MC2_PIT_in
MC3_PIT_in
MC1_out
MC2_out
MC3_out
SPOT
1
MC1_TST_PIT_in
2
MC2_TST_PIT_in
3
MC3_TST_PIT_in
[mc1_pit]
[mc2_pit]
[mc3_pit]
[mc1_pit]
[mc2_pit]
[mc3_pit]
×
×
×
-K-
2
-K-
Out1
DELTA_L
cdsFilt
2
MC1_SPOT_out
1
DELTA_L_out
3
MC2_SPOT_out
4
MC3_SPOT_out

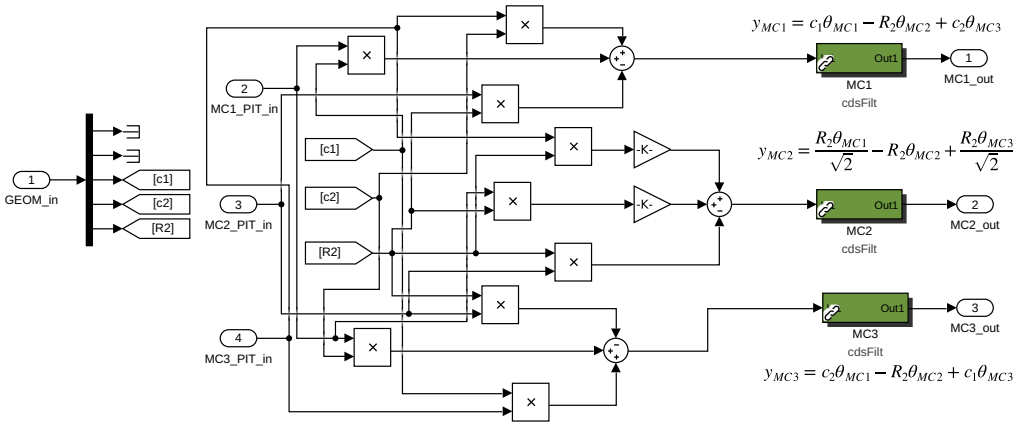
$y_{MC1} = c_1\theta_{MC1} - R_2\theta_{MC2} + c_2\theta_{MC3}$
$y_{MC2} = \frac{R_2\theta_{MC1}}{\sqrt{2}} - R_2\theta_{MC2} + \frac{R_2\theta_{MC3}}{\sqrt{2}}$
$y_{MC3} = c_2\theta_{MC1} - R_2\theta_{MC2} + c_1\theta_{MC3}$
1
GEOM_in
[c1]
[c2]
[R2]
2
MC1_PIT_in
3
MC2_PIT_in
4
MC3_PIT_in
-K-
-K-
Out1
MC1
cdsFilt
1
MC1_out
Out1
MC2
cdsFilt
2
MC2_out
Out1
MC3
cdsFilt
3
MC3_out

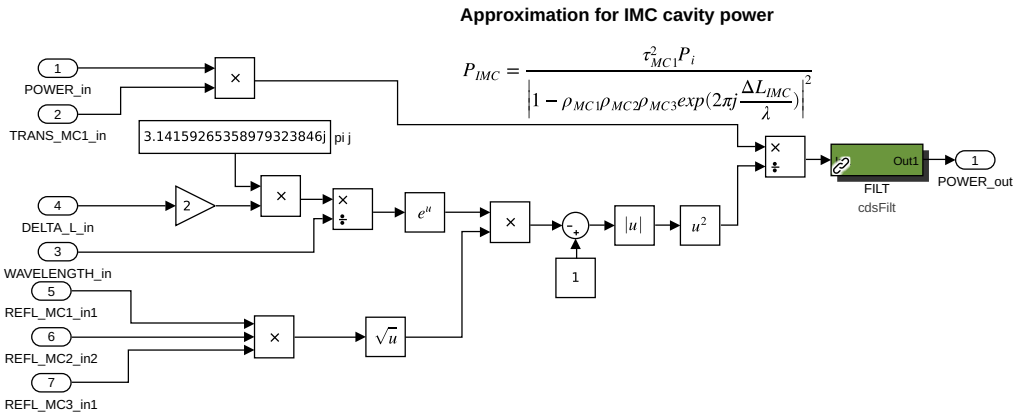
Approximation for IMC cavity power
$P_{IMC} = \frac{\tau_{MC1}^2 P_i}{\left|1 - \rho_{MC1}\rho_{MC2}\rho_{MC3} exp(2\pi j \frac{\Delta L_{IMC}}{\lambda})\right|^2}$
1
POWER_in
2
TRANS_MC1_in
3.14159265358979323846j
pi j
4
DELTA_L_in
2
3
WAVELENGTH_in
5
REFL_MC1_in1
6
REFL_MC2_in2
7
REFL_MC3_in1
e^u
$\sqrt{u}$
1
$|u|$
u^2
Out1
FILT
cdsFilt
1
POWER_out

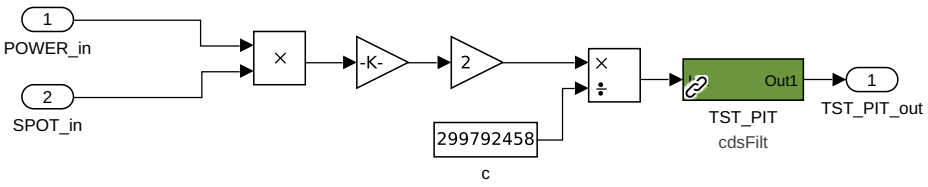

Spot position to torque

$$\tau = \sqrt{2}\, y \frac{P}{c}$$

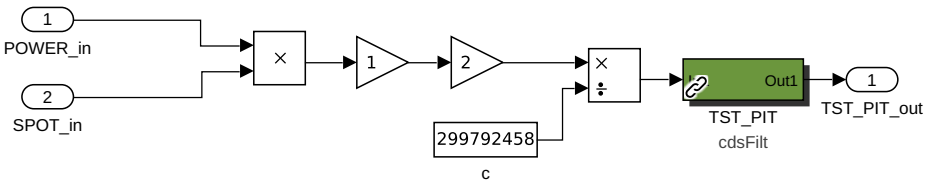

Spot position to torque

$$\tau = 2y\frac{P}{c}$$

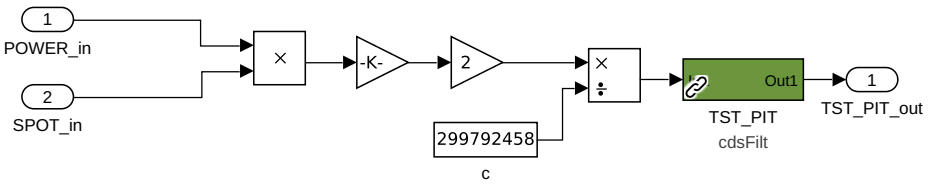

Spot position to torque

$$\tau = \sqrt{2}\, y \frac{P}{c}$$

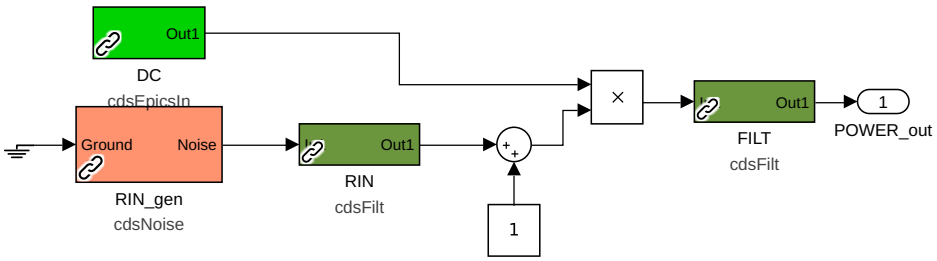
Out1
DC
cdsEpicsIn
Ground
Noise
RIN_gen
cdsNoise
Out1
RIN
cdsFilt
+
+
1
×
Out1
FILT
cdsFilt
1
POWER_out

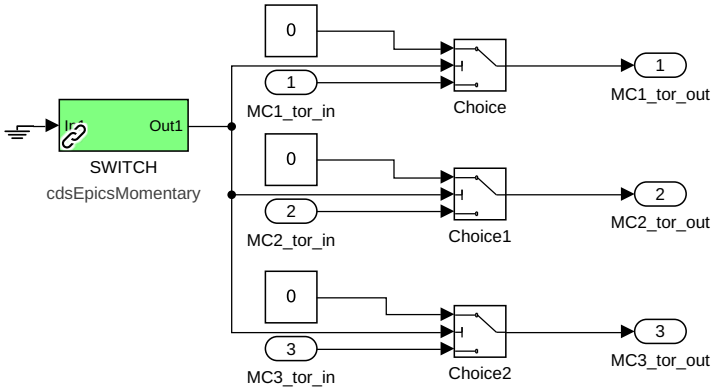
0
1
MC1_tor_in
Choice
1
MC1_tor_out
Out1
SWITCH
cdsEpicsMomentary
0
2
MC2_tor_in
Choice1
2
MC2_tor_out
0
3
MC3_tor_in
Choice2
3
MC3_tor_out

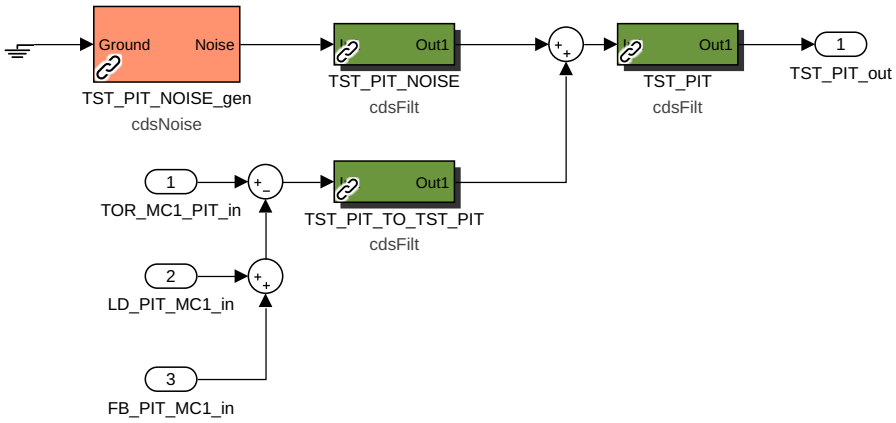
Ground
Noise
TST_PIT_NOISE_gen
cdsNoise
Out1
TST_PIT_NOISE
cdsFilt
Out1
TST_PIT
cdsFilt
1
TST_PIT_out
1
TOR_MC1_PIT_in
Out1
TST_PIT_TO_TST_PIT
cdsFilt
2
LD_PIT_MC1_in
3
FB_PIT_MC1_in

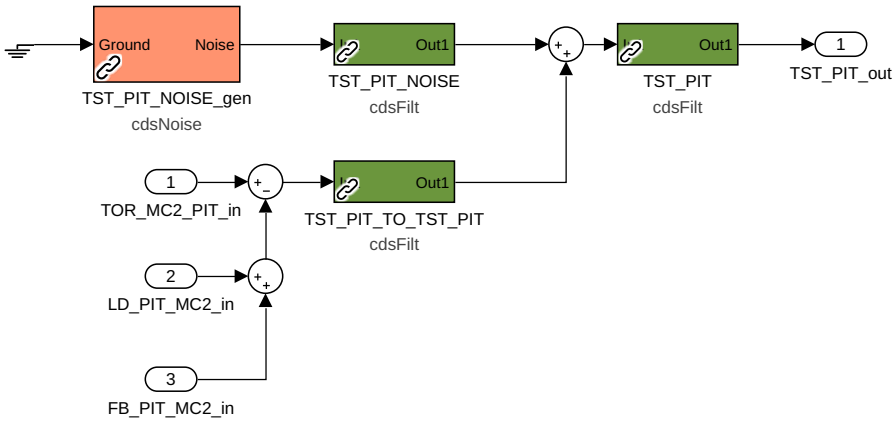
Ground
Noise
TST_PIT_NOISE_gen
cdsNoise
Out1
TST_PIT_NOISE
cdsFilt
Out1
TST_PIT
cdsFilt
1
TST_PIT_out
1
TOR_MC2_PIT_in
Out1
TST_PIT_TO_TST_PIT
cdsFilt
2
LD_PIT_MC2_in
3
FB_PIT_MC2_in

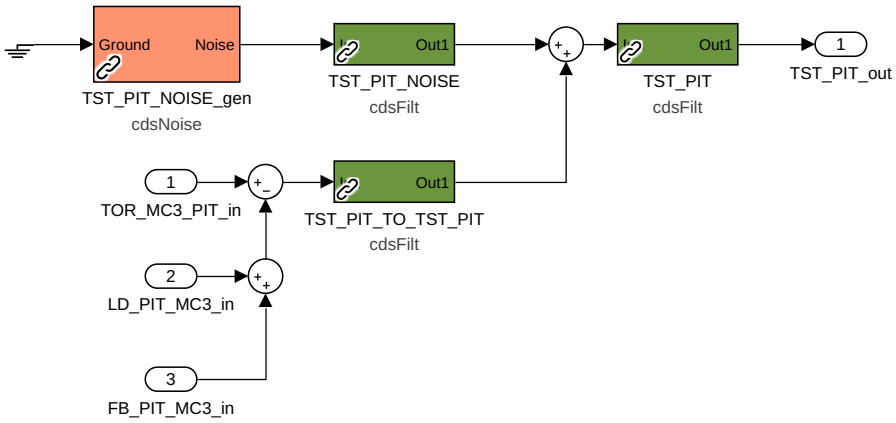
Ground
Noise
TST_PIT_NOISE_gen
cdsNoise
Out1
TST_PIT_NOISE
cdsFilt
Out1
TST_PIT
cdsFilt
1
TST_PIT_out
1
TOR_MC3_PIT_in
Out1
TST_PIT_TO_TST_PIT
cdsFilt
2
LD_PIT_MC3_in
3
FB_PIT_MC3_in

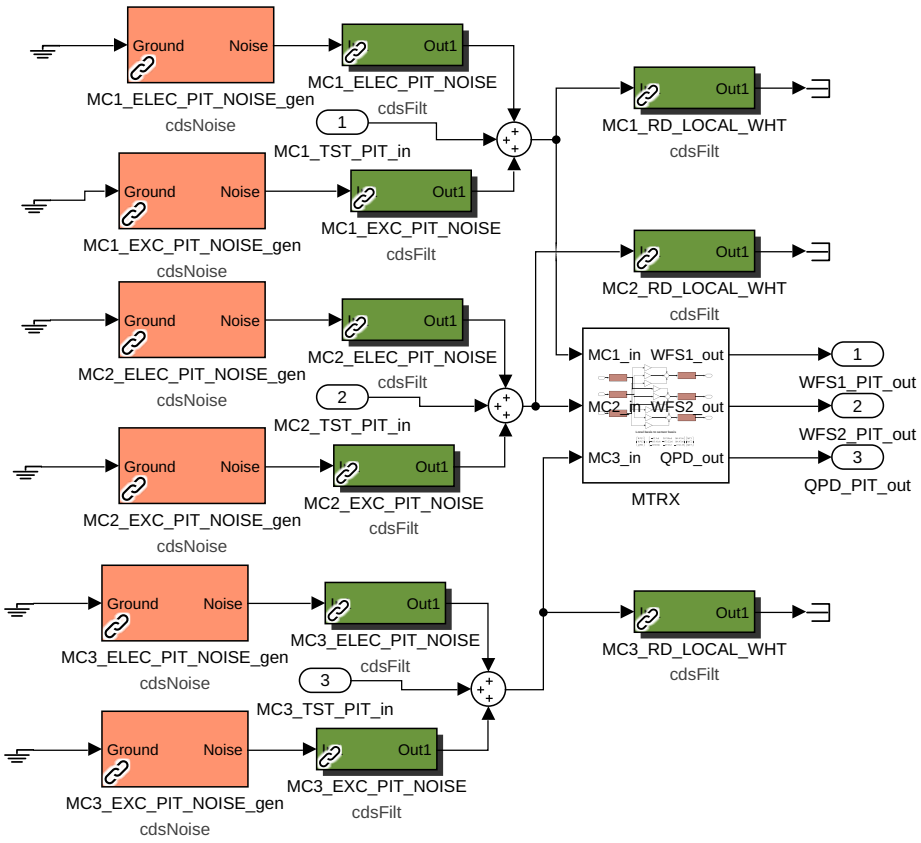
Ground
Noise
MC1_ELEC_PIT_NOISE_gen
cdsNoise
Out1
MC1_ELEC_PIT_NOISE
cdsFilt
1
MC1_TST_PIT_in
MC1_EXC_PIT_NOISE_gen
MC1_EXC_PIT_NOISE
MC2_ELEC_PIT_NOISE_gen
MC2_ELEC_PIT_NOISE
2
MC2_TST_PIT_in
MC2_EXC_PIT_NOISE_gen
MC2_EXC_PIT_NOISE
MC3_ELEC_PIT_NOISE_gen
MC3_ELEC_PIT_NOISE
3
MC3_TST_PIT_in
MC3_EXC_PIT_NOISE_gen
MC3_EXC_PIT_NOISE
MC1_RD_LOCAL_WHT
MC2_RD_LOCAL_WHT
MC3_RD_LOCAL_WHT
MC1_in
MC2_in
MC3_in
WFS1_out
WFS2_out
QPD_out
MTRX
WFS1_PIT_out
WFS2_PIT_out
QPD_PIT_out

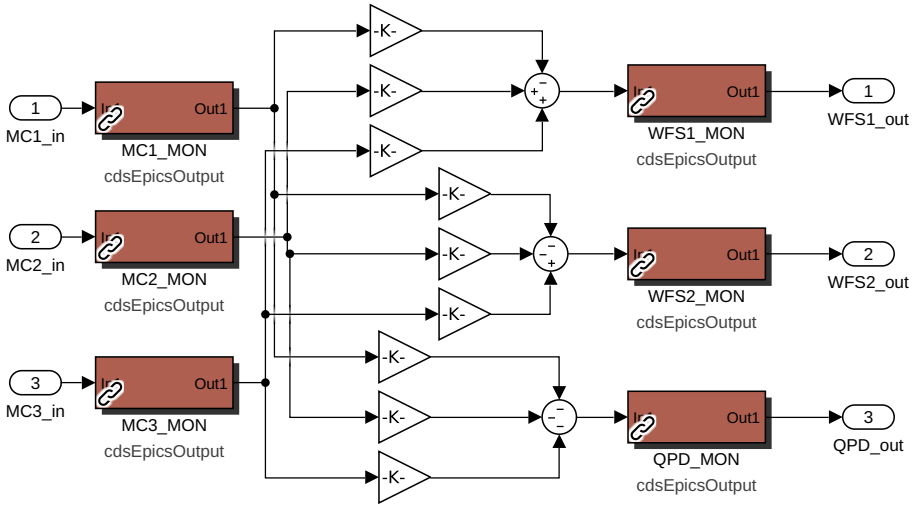

Local basis to sensor basis

$$\begin{bmatrix} WFS1 \\ WFS2 \\ QPD \end{bmatrix} = \begin{bmatrix} -32.3e6 & 567.86e6 & 164.47e6 \\ -103.41e6 & -473.22e6 & 164.47e6 \\ -1292.66 & -4732.2 & -2741.23 \end{bmatrix} \begin{bmatrix} MC1 \\ MC2 \\ MC3 \end{bmatrix}$$

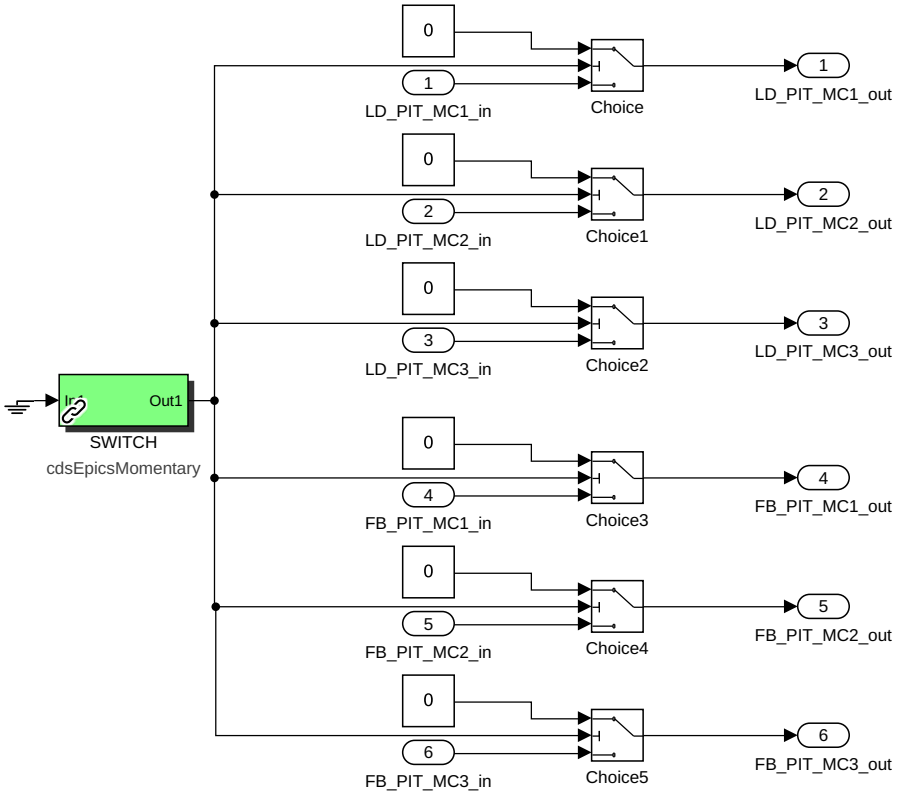
0
1
LD_PIT_MC1_in
Choice
1
LD_PIT_MC1_out
0
2
LD_PIT_MC2_in
Choice1
2
LD_PIT_MC2_out
0
3
LD_PIT_MC3_in
Choice2
3
LD_PIT_MC3_out
In1
Out1
SWITCH
cdsEpicsMomentary
0
4
FB_PIT_MC1_in
Choice3
4
FB_PIT_MC1_out
0
5
FB_PIT_MC2_in
Choice4
5
FB_PIT_MC2_out
0
6
FB_PIT_MC3_in
Choice5
6
FB_PIT_MC3_out

Appendix D

Open-loop transfer function measurements for Lightsaber-IMC

I compared the OLTFs of local damping and the real system. OLTF of local damping loops I measured using swept sine at 3 Hz. Setup for MC3 please find in figure D.1 (setup for MC1 and MC2 is basically the same). For MC1 measured local damping OLTF please find in figure D.2. It seems this loop is not doing anything and needs a gain increase. The mistake that might have happened here is that the resolution is very low, and I missed UGF. I couldn't have gone with a higher number of points since measurements were taking too long time, and since I was exciting the system at that time the 40m team couldn't do their work. For MC2 please find it in figure D.3, and for MC3 in figure D.4.

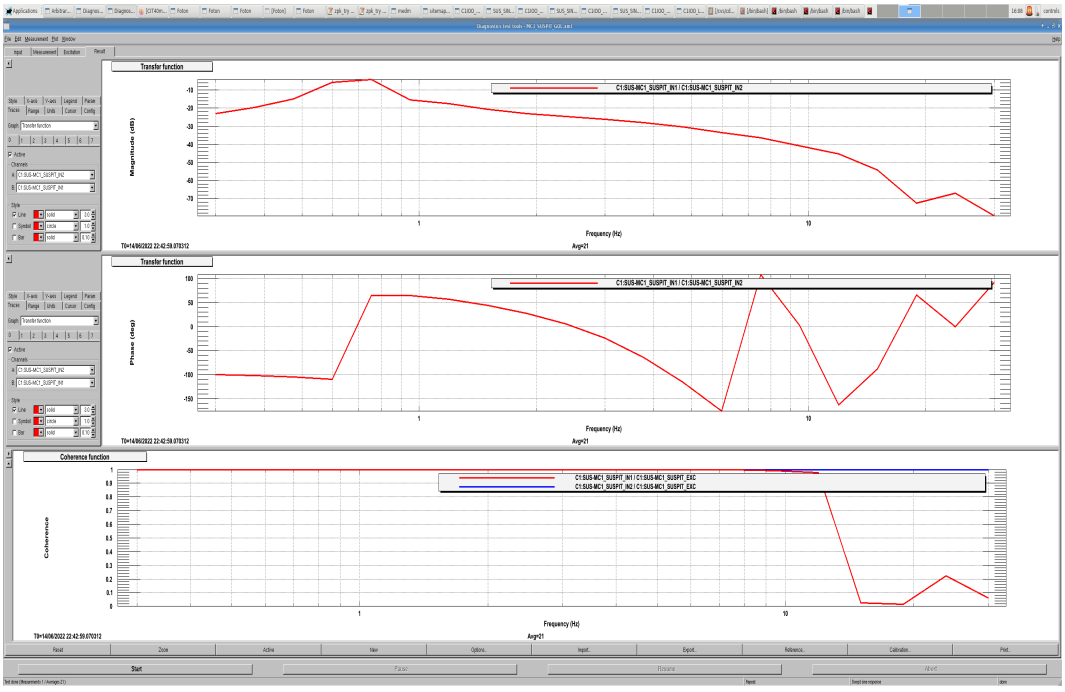

FIGURE D.2: MC1 local damping loop OLTF. Coherence (3rd row) is excelent for relevant frequencies.

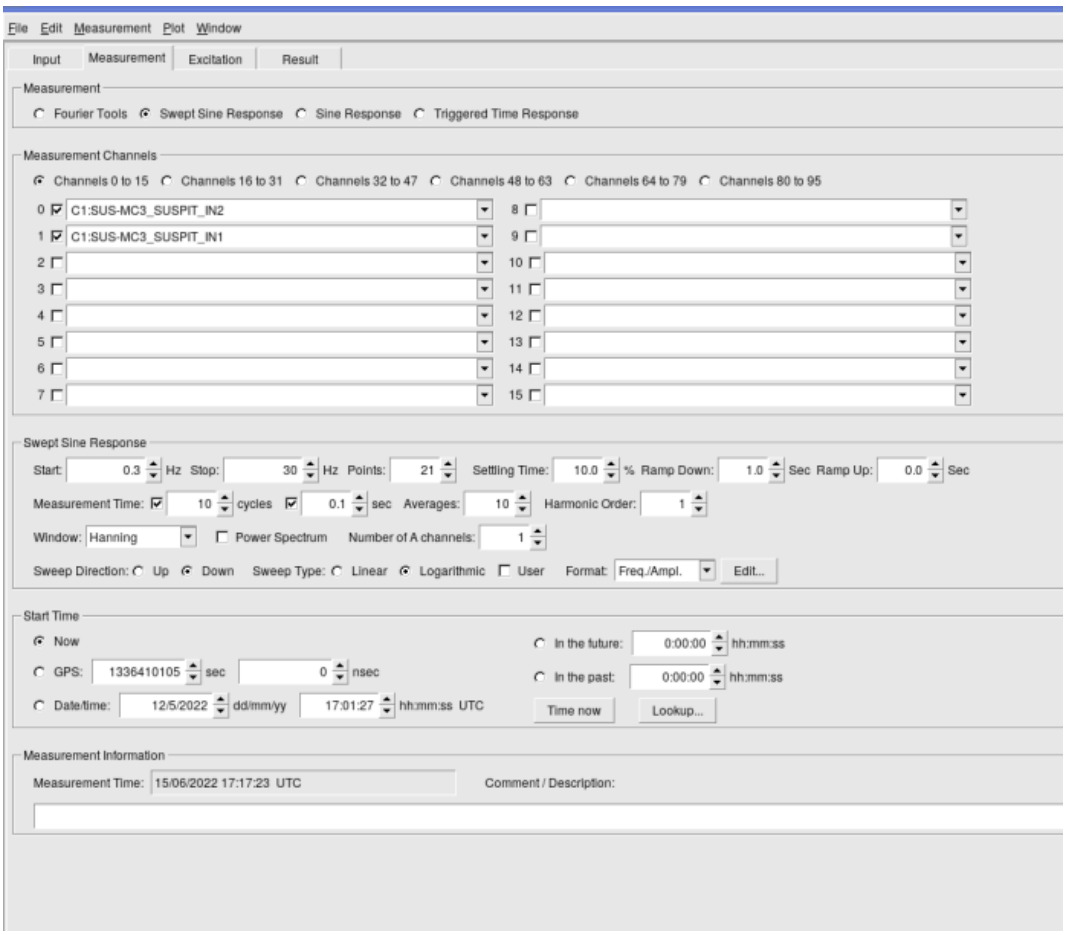

(A)

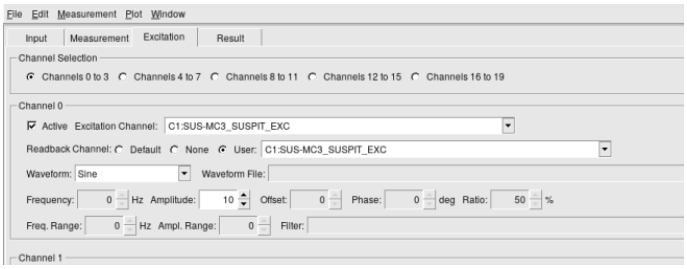

(B)

FIGURE D.1: Screenshots of setup for OLTF measurement of local damping loops.

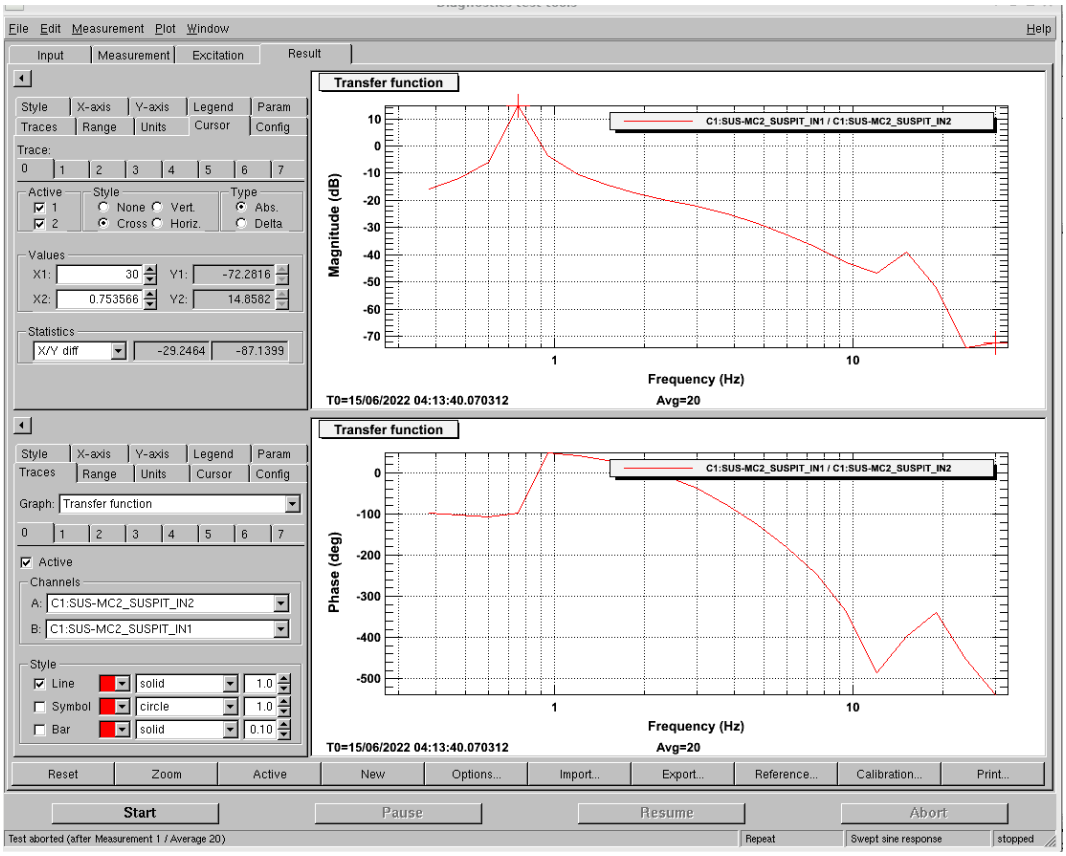

FIGURE D.3: MC2 local damping loop OLTF. Unfortunately, I didn't screenshot the coherence for this OLTF.

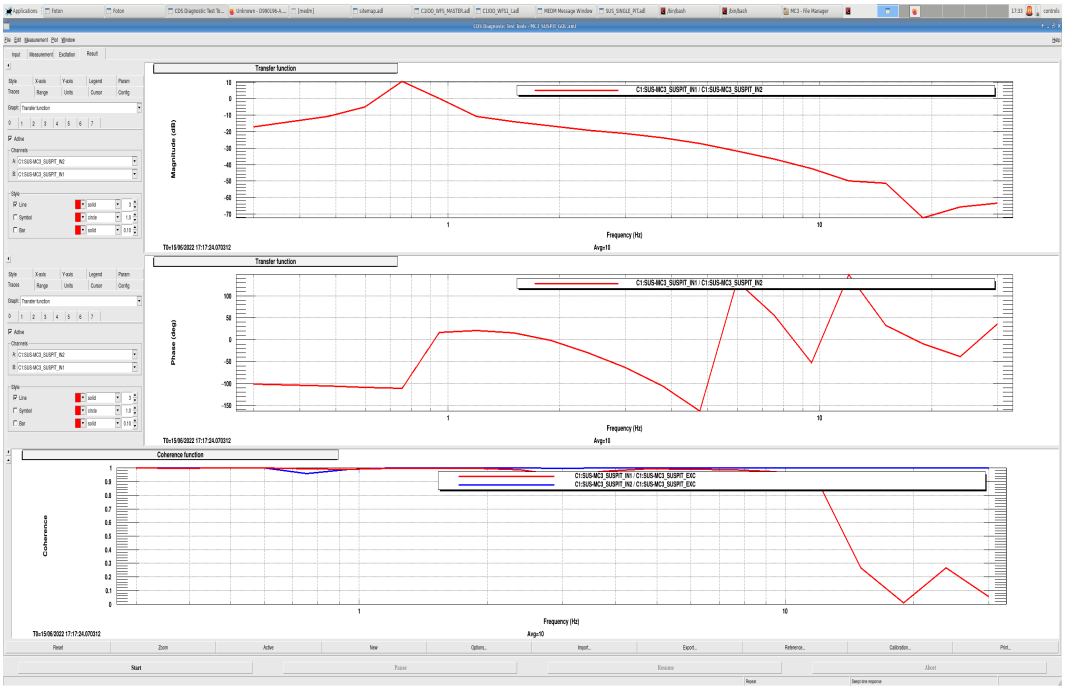

FIGURE D.4: MC3 local damping loop OLTF. Coherence (3rd row) is excelent for relevant frequencies.

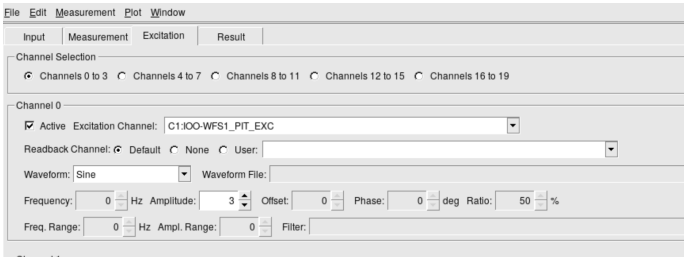

(A)

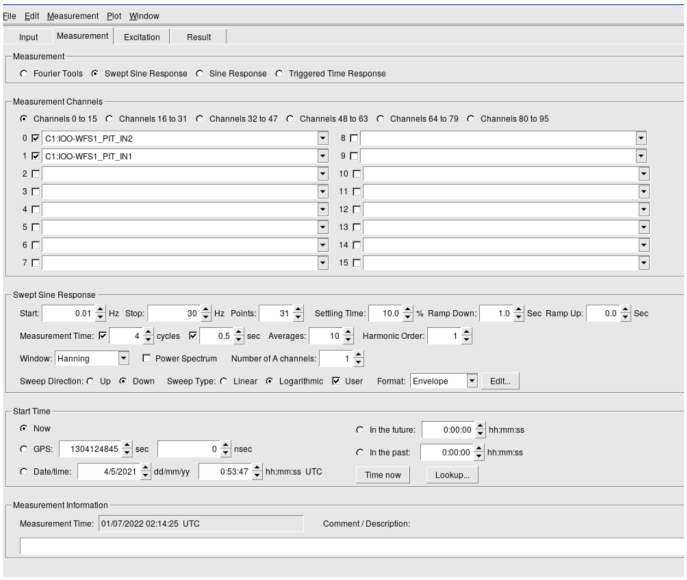

(B)

FIGURE D.5: Screenshots of setup for OLTF measurement of WFS1 feedback control loop.

I compared the OLTF of the control feedback and the real system for WFS1. OLTF of the control feedback loop I measured using swept sine at 3 Hz. Setup for WFS1 OLTF please find in figure D.5. For WFS1 measured OLTF please find in figure D.6. I needed to stop measurement since it was taking way too long, and the the 40m team couldn't have done anything in the meanwhile. For WFS2 and DC QPD in MC2 transmission I couldn't do it since sensors broke shortly afterwards. As you can see in the plot UGF would be like 25 mHz (it almost crossed zero), maybe even higher since as you can see coherence (third row) started falling at these frequencies (and maybe it would have crossed zero earlier if coherence remained good). So, this measurement is in excellent agreement with what Lightsaber-IMC gives.

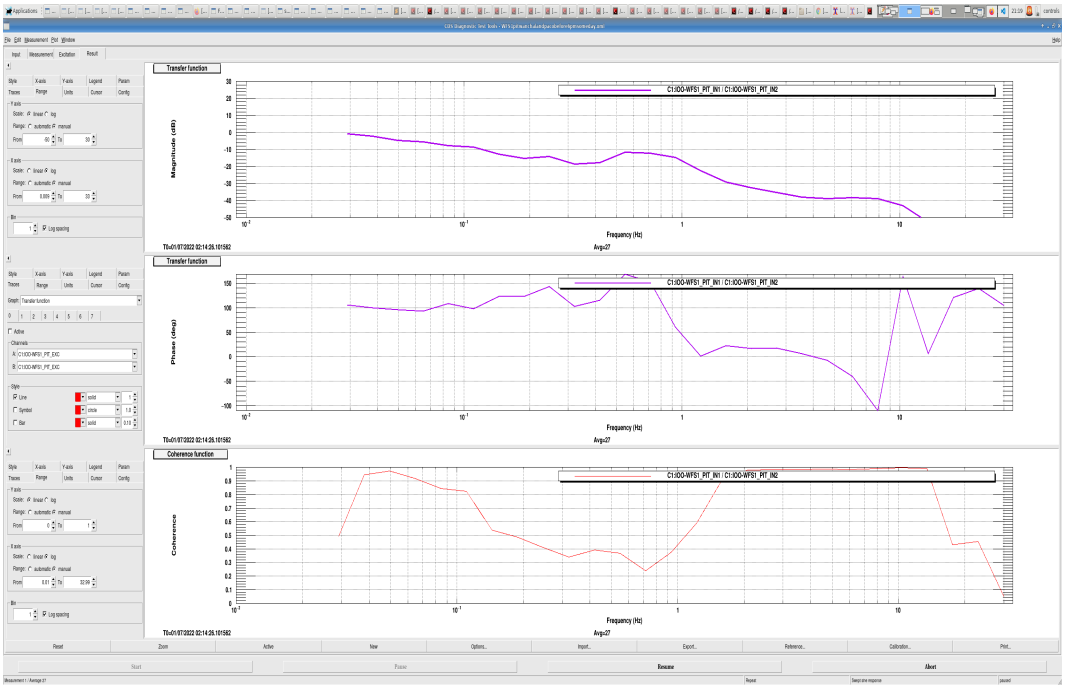

FIGURE D.6: Measured WFS1's control feedback OLTF.

In the figure D.7 the interface MEDM screen of the sensors' RTCDS is shown.

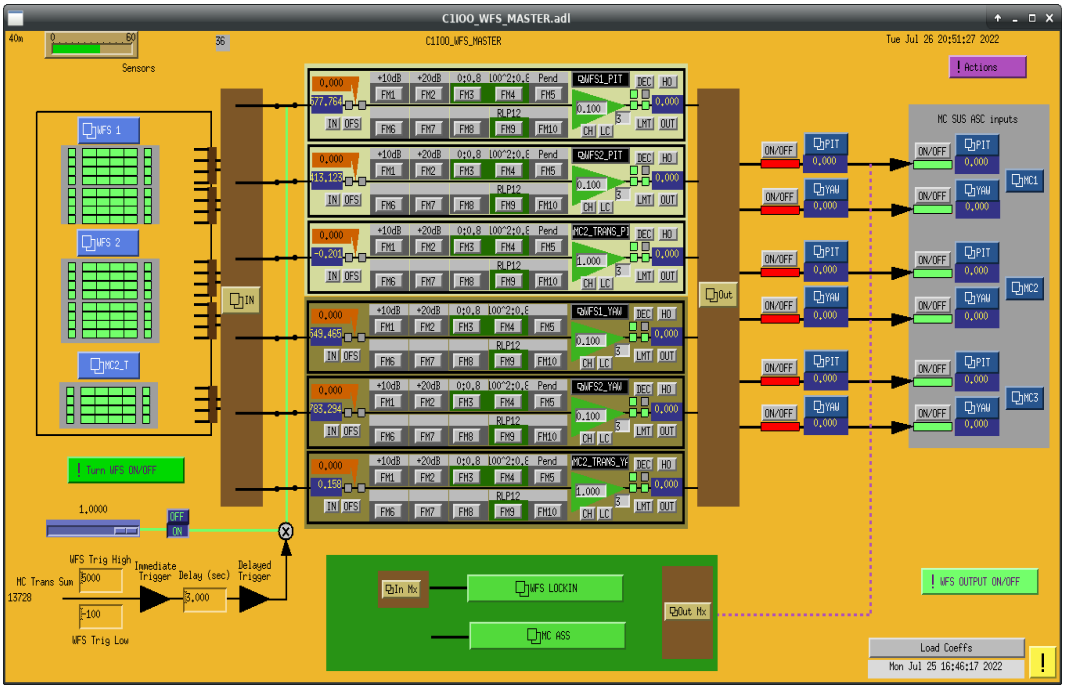

FIGURE D.7: Sensors' RTCDS.

Bibliography

40m core optics. Available online: https://wiki-40m.ligo.caltech.edu/Core_Optics. Accessed: 24-July-2022.

Abadie, J. et al. (2010). "First Search for Gravitational Waves from the Youngest Known Neutron Star". In: *The Astrophysical Journal* 722.2, pp. 1504–1513. DOI: 10.1088/0004-637x/722/2/1504. URL: https://doi.org/10.1088/0004-637x/722/2/1504.

Abadie, J. et al. (2011). "Search for gravitational waves from binary black hole inspiral, merger, and ringdown". In: *Physical Review D* 83.12, 122005, p. 122005. DOI: 10.1103/PhysRevD.83.122005. arXiv: 1102.3781 [gr-qc].

Abbott, B. P. et al. (2009). "Search for gravitational-wave bursts in the first year of the fifth LIGO science run". In: *Physical Review D* 80.10, 102001, p. 102001. DOI: 10.1103/PhysRevD.80.102001. arXiv: 0905.0020 [gr-qc].

Abbott, B. P. et al. (2016a). "GW150914: The Advanced LIGO Detectors in the Era of First Discoveries". In: *Physical Review Letters* 116 (13), p. 131103. DOI: 10.1103/PhysRevLett.116.131103. URL: http://link.aps.org/doi/10.1103/PhysRevLett.116.131103.

Abbott, B. P. et al. (2016b). "Observation of Gravitational Waves from a Binary Black Hole Merger". In: *Phys. Rev. Lett.* 116 (6), p. 061102. DOI: 10.1103/PhysRevLett.116.061102. URL: http://link.aps.org/doi/10.1103/PhysRevLett.116.061102.

Abbott, B. P. et al. (2020a). "A guide to LIGO-Virgo detector noise and extraction of transient gravitational-wave signals". In: *Classical and Quantum Gravity* 37.5, 055002, p. 055002. DOI: 10.1088/1361-6382/ab685e. arXiv: 1908.11170 [gr-qc].

Abbott, B. P. et al. (2020b). "Prospects for observing and localizing gravitational-wave transients with Advanced LIGO, Advanced Virgo and KAGRA". In: *Living Reviews in Relativity* 23.1, 3, p. 3. DOI: 10.1007/s41114-020-00026-9. URL: https://link.springer.com/article/10.1007/s41114-020-00026-9.

Abbott, R. et al. (2002). "Seismic isolation for Advanced LIGO". In: *Classical and Quantum Gravity* 19.7, pp. 1591–1597. DOI: 10.1088/0264-9381/19/7/349. URL: https://iopscience.iop.org/article/10.1088/0264-9381/19/7/349.

Abbott, R et al. (2004). "Seismic isolation enhancements for initial and Advanced LIGO". In: *Classical and Quantum Gravity* 21.5, S915. URL: http://stacks.iop.org/0264-9381/21/i=5/a=081.

Abbott, R. et al. (2020). "Properties and Astrophysical Implications of the 150 SM Binary Black Hole Merger GW190521". In: *The Astrophysical Journal* 900, p. L13. DOI: 10.3847/2041-8213/aba493. URL: https://iopscience.iop.org/article/10.3847/2041-8213/aba493.

Abbott, Rich et al. (2008). *AdvLIGO Interferometer Sensing and Control Conceptual Design. LIGO-T070247-v1*. Tech. rep. LIGO-Caltech-MIT. URL: https://dcc.ligo.org/LIGO-T070247/public.

Abdolmaleki, Abbas et al. (2018). *Maximum a Posteriori Policy Optimisation*. DOI: 10.48550/ARXIV.1806.06920. URL: https://arxiv.org/abs/1806.06920.

About "aLIGO". Available online: https://www.ligo.caltech.edu/page/about-aligo. Accessed: 24-March-2021.

Abubakar, Iya (1962). "Scattering of plane elastic waves at rough surfaces. I". In: *Mathematical Proceedings of the Cambridge Philosophical Society* 58 (01), pp. 136–157. ISSN: 1469-8064. DOI: 10.1017/S030500410003629X. URL: https://www.cambridge.org/core/journals/mathematical-proceedings-of-the-cambridge-philosophical-society/article/scattering-of-plane-elastic-waves-at-rough-surfaces-i/93B5053EA67AF32B3300FC95C959FAC1.

— (1963). "Scattering of plane elastic waves at rough surfaces. II". In: *Mathematical Proceedings of the Cambridge Philosophical Society* 59, pp. 231 –248. DOI: 10.1017/S0305004100002176. URL: https://www.cambridge.org/core/journals/mathematical-proceedings-of-the-cambridge-philosophical-society/article/scattering-of-plane-elastic-waves-at-rough-surfaces-ii/D4C52A3034A736F8C54B59DAA837C205.

Acernese, F. et al. (2010). "Measurements of Superattenuator seismic isolation by Virgo interferometer". In: *Astroparticle Physics* 33.3, pp. 182 –189. ISSN: 0927-6505. DOI: http://dx.doi.org/10.1016/j.astropartphys.2010.01.006. URL: http://www.sciencedirect.com/science/article/pii/S0927650510000253.

Acernese, F et al. (2015). "Advanced Virgo: a second-generation interferometric gravitational wave detector". In: *Classical and Quantum Gravity* 32.2, p. 024001. DOI: 10.1088/0264-9381/32/2/024001. URL: http://stacks.iop.org/0264-9381/32/i=2/a=024001.

ACME. Available online: https://dm-acme.readthedocs.io/en/latest/index.html. Accessed: 01-September-2022.

Activation Functions. Available online: https://ml-cheatsheet.readthedocs.io/en/latest/activation_functions.html. Accessed: 03-September-2022.

Adhikari, R X et al. (2020). "A cryogenic silicon interferometer for gravitational-wave detection". In: *Classical and Quantum Gravity* 37.16, p. 165003. DOI: 10.1088/1361-6382/ab9143. URL: https://doi.org/10.1088%2F1361-6382%2Fab9143.

Adhikari, Rana (2004). "Sensitivity and Noise Analysis of 4 km Laser Interferometric Gravitational Wave Antennae". PhD dissertation. Massachusetts Institute of Technology.

— (2019). *Wavefront Sensor: 40m Rev of initial LIGO WFS. LIGO Document D1900268-v1*. Tech. rep. LIGO-Caltech. URL: https://dcc.ligo.org/LIGO-D1900268.

Adhikari, Rana et al. (2012). *Status of the LIGO 40m Prototype*. LVC Collaboration Meeting held on 10 Sep 2012 in Sapienza University, Rome, Italy. URL: https://dcc.ligo.org/LIGO-G1200903.

Advanced LIGO Systems Group (2015). *Advanced LIGO Systems Design*. Tech. rep. Caltech-MIT-LIGO Laboratory. URL: https://dcc.ligo.org/LIGO-T010075.

Aki, K. and P. G. Richards (2009). *Quantitative Seismology, 2nd edition*. University Science Books.

Akutsu, T. et al. (2019). "KAGRA: 2.5 Generation Interferometric Gravitational Wave Detector". In: *Nature Astronomy* 3.1, pp. 35–40. DOI: 10.1038/s41550-018-0658-y. URL: https://www.nature.com/articles/s41550-018-0658-y.

aLIGO LLO Logbook. Available online: https://alog.ligo-la.caltech.edu/aLOG/index.php?callRep=41815. Accessed: 01-April-2021.

Allen, Bruce (1996). "The stochastic gravity-wave background: sources and detection". In: DOI: 10.48550/ARXIV.GR-QC/9604033. URL: https://arxiv.org/abs/gr-qc/9604033.

— (2005). "χ^2 time-frequency discriminator for gravitational wave detection". In: *Physical Review D* 71 (6), p. 062001. DOI: 10.1103/PhysRevD.71.062001. URL: https://link.aps.org/doi/10.1103/PhysRevD.71.062001.

Allen, Bruce and Joseph D. Romano (1999). "Detecting a stochastic background of gravitational radiation: Signal processing strategies and sensitivities". In: *Phys. Rev. D* 59 (10), p. 102001. DOI: 10.1103/PhysRevD.59.102001. URL: http://link.aps.org/doi/10.1103/PhysRevD.59.102001.

Allocca, Annalisa et al. (2020). "Interferometer Sensing and Control for the Advanced Virgo Experiment in the O3 Scientific Run". In: *Galaxies* 8, p. 85. DOI: 10.3390/galaxies8040085. URL: https://www.mdpi.com/2075-4434/8/4/85.

Amann, Florian et al. (2020). "Site-selection criteria for the Einstein Telescope". In: *Review of Scientific Instruments* 91.9, p. 094504. DOI: 10.1063/5.0018414. URL: https://doi.org/10.1063%2F5.0018414.

Amico, P. et al. (2001). "Thermal noise limit in the Virgo mirror suspension". In: *Nuclear Instruments and Methods in Physics Research A* 461.1-3, pp. 297–299. DOI: 10.1016/S0168-9002(00)01256-0. URL: https://www.sciencedirect.com/science/article/abs/pii/S0168900200012560?via%3Dihub.

Ando, Masaki et al. (2010). "Torsion-Bar Antenna for Low-Frequency Gravitational-Wave Observations". In: *Phys. Rev. Lett.* 105 (16), p. 161101. DOI: 10.1103/PhysRevLett.105.161101. URL: http://link.aps.org/doi/10.1103/PhysRevLett.105.161101.

Andric, Tomislav (2022). "Providing priors to Bayesian array optimization for the Sardinian candidate site of the Einstein Telescope". In: *Il nuovo cimento C* 45.183 (6), pp. 1–4. DOI: 10.1393/ncc/i2022-22183-7. URL: https://www.sif.it/riviste/sif/ncc/econtents/2022/045/06/article/26.

Andric, Tomislav and Jan Harms (2020). "Simulations of Gravitoelastic Correlations for the Sardinian Candidate Site of the Einstein Telescope". In: *Journal of Geophysical Research (Solid Earth)* 125.10, e20401. DOI: 10.1029/2020JB020401. URL: https://agupubs.onlinelibrary.wiley.com/doi/10.1029/2020JB020401.

Andric, Tomislav and Jan Harms (2021). "Lightsaber: A Simulator of the Angular Sensing and Control System in LIGO". In: *Galaxies* 9.3. ISSN: 2075-4434. DOI: 10.3390/galaxies9030061. URL: https://www.mdpi.com/2075-4434/9/3/61.

Arai, Koji (2016). *IMC WFS Demodulator Board, Rev. 40m. LIGO Document D1600503-v2*. Tech. rep. LIGO-Caltech. URL: https://dcc.ligo.org/LIGO-D1600503.

— (2021). *40m End ADC Adapter Unit. LIGO Document D2100016-v1*. Tech. rep. LIGO-Caltech. URL: https://dcc.ligo.org/LIGO-D2100016.

Arai, Koji et al. (2013). *Output Mode Cleaner Design. LIGO-T1000276-v5*. Tech. rep. Caltech-MIT-LIGO. URL: https://dcc.ligo.org/LIGO-T1000276/public.

Aston, S et al. (2012). "Update on quadruple suspension design for Advanced LIGO". In: *Classical and Quantum Gravity* 29.23, p. 235004. DOI: 10.1088/0264-9381/29/23/235004. URL: https://iopscience.iop.org/article/10.1088/0264-9381/29/23/235004.

Ayachit, Utkarsh (2019). *The ParaView Guide, Community Edition [software]*. Kitware (USA).

Badaracco, F and J Harms (2019). "Optimization of seismometer arrays for the cancellation of Newtonian noise from seismic body waves". In: *Classical and Quantum Gravity* 36.14, p. 145006. DOI: 10.1088/1361-6382/ab28c1. URL: https://iopscience.iop.org/article/10.1088/1361-6382/ab28c1.

Badaracco, Francesca (2020). "Newtonian Noise Studies in 2nd and 3rd Generation Gravitational-Wave Interferometric Detectors". PhD dissertation. Gran Sasso Science Institute.

Badaracco, Francesca et al. (2020). "Machine learning for gravitational-wave detection: surrogate Wiener filtering for the prediction and optimized cancellation of Newtonian noise at Virgo". In: *Classical and Quantum Gravity* 37.19, p. 195016. DOI: 10.1088/1361-6382/abab64. URL: https://iopscience.iop.org/article/10.1088/1361-6382/abab64.

Bard, Pierre-Yves (1982). "Diffracted waves and displacement field over two-dimensional elevated topographies". In: *Geophysical Journal International* 71.3, pp. 731–760. ISSN: 0956-540X. DOI: 10.1111/j.1365-246X.1982.tb02795.x. URL: https://doi.org/10.1111/j.1365-246X.1982.tb02795.x.

Barsotti, Lisa and Matthew Evans (2011). *Modeling of Alignment Sensing and Control for Advanced LIGO. LIGO-T0900511-v4*. Tech. rep. LIGO-MIT. URL: https://dcc.ligo.org/LIGO-T0900511/public.

Barsotti, Lisa, Jan Harms, and Roman Schnabel (2018). "Squeezed vacuum states of light for gravitational wave detectors". In: *Reports on Progress in Physics* 82.1, p. 016905. DOI: 10.1088/1361-6633/aab906. URL: https://iopscience.iop.org/article/10.1088/1361-6633/aab906.

Barsotti, Lorenzo, M Evans, and P Fritschel (2010). "Alignment sensing and control in advanced LIGO". In: *Classical and Quantum Gravity* 27.8, p. 084026. DOI: 10.1088/0264-9381/27/8/084026. URL: https://iopscience.iop.org/article/10.1088/0264-9381/27/8/084026.

Basini, P., Q. Liu, and C. Tape (2012). "Ambient-noise Tomography of the Southern California Lithosphere". In: *AGU Fall Meeting Abstracts*. Vol. 2012, S41A–2415.

Basini, P. et al. (2013). "The influence of nonuniform ambient noise on crustal tomography in Europe". In: *Geochemistry, Geophysics, Geosystems* 14.5, pp. 1471–1492. DOI: 10.1002/ggge.20081. URL: https://agupubs.onlinelibrary.wiley.com/doi/full/10.1002/ggge.20081.

Bassan, Massimo (2013). *Advanced Interferometers and the Search for Gravitational Waves*. Vol. 404. Springer. ISBN: 978-3-319-03791-2. DOI: 10.1007/978-3-319-03792-9.

Beccaria, M et al. (1998). "Relevance of Newtonian seismic noise for the VIRGO interferometer sensitivity". In: *Classical and Quantum Gravity* 15.11, p. 3339. URL: https://iopscience.iop.org/article/10.1088/0264-9381/15/11/004.

Beker, M G, J F J van den Brand, and D S Rabeling (2015). "Subterranean ground motion studies for the Einstein Telescope". In: *Classical and Quantum Gravity* 32.2, p. 025002. DOI: https://doi.org/10.1088/0264-9381/32/2/025002. URL: http://stacks.iop.org/0264-9381/32/i=2/a=025002.

Beker, M G et al. (2012). "Newtonian noise and ambient ground motion for gravitational wave detectors". In: *Journal of Physics: Conference Series* 363.1, p. 012004. DOI: https://doi.org/10.1088/1742-6596/363/1/012004. URL: http://stacks.iop.org/1742-6596/363/i=1/a=012004.

Beker, M.G. et al. (2011). "Improving the sensitivity of future GW observatories in the 1 - 10Hz band: Newtonian and seismic noise". In: *General Relativity and*

Gravitation 43.2, pp. 623–656. ISSN: 0001-7701. DOI: 10.1007/s10714-010-1011-7. URL: http://dx.doi.org/10.1007/s10714-010-1011-7.

Benesty, Jacob, Yiteng(Arden) Huang, and Jingdong Chen (2008). "Wiener and Adaptive Filters". English. In: *Springer Handbook of Speech Processing*. Ed. by Jacob Benesty, M.Mohan Sondhi, and Yiteng(Arden) Huang. Springer Berlin Heidelberg, pp. 103–120. ISBN: 978-3-540-49125-5. DOI: 10.1007/978-3-540-49127-9_6. URL: http://dx.doi.org/10.1007/978-3-540-49127-9_6.

Bertsekas, Dimitri P. (2009). "Neuro-dynamic programmingNeuro-Dynamic Programming". In: *Encyclopedia of Optimization*. Ed. by Christodoulos A. Floudas and Panos M. Pardalos. Boston, MA: Springer US, pp. 2555–2560. ISBN: 978-0-387-74759-0. DOI: 10.1007/978-0-387-74759-0_440. URL: https://doi.org/10.1007/978-0-387-74759-0_440.

Blacker, T et al. (2019). *Trelis v16.5 [software]*. Sandia National Laboratories (USA).

Bondu, François, Patrice Hello, and Jean-Yves Vinet (1998). "Thermal noise in mirrors of interferometric gravitational wave antennas". In: *Physics Letters A* 246.3-4, pp. 227–236. DOI: 10.1016/S0375-9601(98)00450-2. URL: https://www.sciencedirect.com/science/article/abs/pii/S0375960198004502?via%3Dihub.

Bonnefoy-Claudet, Sylvette, Fabrice Cotton, and Pierre-Yves Bard (2006). "The nature of noise wavefield and its applications for site effects studies: A literature review". In: *Earth-Science Reviews* 79.3-4, pp. 205 –227. ISSN: 0012-8252. DOI: http://dx.doi.org/10.1016/j.earscirev.2006.07.004. URL: http://www.sciencedirect.com/science/article/pii/S0012825206001012.

Braginsky, V. B., M. L. Gorodetsky, and S. P. Vyatchanin (1999). "Thermodynamical fluctuations and photo-thermal shot noise in gravitational wave antennae". In: *Phys. Lett. A* 264, p. 1.

Buikema, A. et al. (2020). "Sensitivity and performance of the Advanced LIGO detectors in the third observing run". In: *Physical Review D* 102 (6), p. 062003. DOI: 10.1103/PhysRevD.102.062003. URL: https://link.aps.org/doi/10.1103/PhysRevD.102.062003.

Busoniu, Lucian et al. (2017). *Reinforcement learning and dynamic programming using function approximators*. CRC press.

Callen, Herbert B. and Theodore A. Welton (1951). "Irreversibility and Generalized Noise". In: *Physical Review* 83.1, pp. 34–40. DOI: 10.1103/PhysRev.83.34. URL: https://journals.aps.org/pr/abstract/10.1103/PhysRev.83.34.

Canuel, B. et al. (2020). "ELGAR – European Laboratory for Gravitation and Atom-interferometric Research". In: *Classical and Quantum Gravity* 37.22, 225017, p. 225017. DOI: 10.1088/1361-6382/aba80e. arXiv: 1911.03701 [physics.atom-ph].

Carbone, L et al. (2012). "Sensors and actuators for the Advanced LIGO mirror suspensions". In: *Classical and Quantum Gravity* 29.11, p. 115005. DOI: 10.1088/0264-9381/29/11/115005. URL: https://doi.org/10.1088/0264-9381/29/11/115005.

Carroll, Sean M. (1997). *Lecture Notes on General Relativity*. DOI: 10.48550/ARXIV.GR-QC/9712019. URL: https://arxiv.org/abs/gr-qc/9712019.

Caves, Carlton M. (1981). "Quantum-mechanical noise in an interferometer". In: *Phys. Rev. D* 23 (8), pp. 1693–1708. DOI: 10.1103/PhysRevD.23.1693. URL: http://link.aps.org/doi/10.1103/PhysRevD.23.1693.

Cella, G. (2000). "Off-Line Subtraction of Seismic Newtonian Noise". In: *Recent Developments in General Relativity*. Ed. by B. Casciaro et al. Springer Milan, pp. 495–

503. ISBN: 978-88-470-0068-1. DOI: 10.1007/978-88-470-2113-6_44. URL: http://dx.doi.org/10.1007/978-88-470-2113-6_44.

Cerdonio, M. et al. (2001). "Wideband Dual Sphere Detector of Gravitational Waves". In: *Phys. Rev. Lett.* 87 (3), p. 031101. DOI: 10.1103/PhysRevLett.87.031101. URL: http://link.aps.org/doi/10.1103/PhysRevLett.87.031101.

Chan, Man Leong et al. (2018). "Binary neutron star mergers and third generation detectors: Localization and early warning". In: *Physical Review D* 97 (12), p. 123014. DOI: 10.1103/PhysRevD.97.123014. URL: https://link.aps.org/doi/10.1103/PhysRevD.97.123014.

Chen, Y. (2003). "Sagnac interferometer as a speed-meter-type, quantum-nondemolition gravitational-wave detector". In: *Phys. Rev. D* 67, p. 122004.

Chen, Yanbei et al. (2006). "Interferometers for Displacement-Noise-Free Gravitational-Wave Detection". In: *Laser Physics Letters* 97.15, 151103, p. 151103. DOI: 10.1103/PhysRevLett.97.151103. arXiv: gr-qc/0603054 [gr-qc].

Christensen, Nelson (1990). "On Measuring the Stochastic Gravitational Radiation Background with Laser Interferometric Antennas". PhD dissertation. Massachusetts Institute of Technology.

Coughlin, M and J Harms (2012). "Seismic topographic scattering in the context of GW detector site selection". In: *Classical and Quantum Gravity* 29.7, p. 075004. DOI: 10.1088/0264-9381/29/7/075004. URL: https://doi.org/10.1088/0264-9381/29/7/075004.

Coughlin, M et al. (2016). "Towards a first design of a Newtonian-noise cancellation system for Advanced LIGO". In: *Classical and Quantum Gravity* 33.24, p. 244001. DOI: 10.1088/0264-9381/33/24/244001. URL: https://doi.org/10.1088/0264-9381/33/24/244001.

Coughlin, M. et al. (2019). "Coherence-Based Approaches for Estimating the Composition of the Seismic Wavefield". In: *Journal of Geophysical Research: Solid Earth* 124.3, pp. 2941–2956. DOI: 10.1029/2018JB016608. eprint: https://agupubs.onlinelibrary.wiley.com/doi/pdf/10.1029/2018JB016608. URL: https://agupubs.onlinelibrary.wiley.com/doi/abs/10.1029/2018JB016608.

Coughlin, M. W. et al. (2018). "Implications of Dedicated Seismometer Measurements on Newtonian-Noise Cancellation for Advanced LIGO". In: *Phys. Rev. Lett.* 121 (22), p. 221104. DOI: 10.1103/PhysRevLett.121.221104. URL: https://link.aps.org/doi/10.1103/PhysRevLett.121.221104.

Cupillard, Paul and Yann Capdeville (2010). "On the amplitude of surface waves obtained by noise correlation and the capability to recover the attenuation: A numerical approach". In: *Geophysical Journal International* 181 (3), pp. 1687 – 1700. DOI: 10.1111/j.1365-246X.2010.04586.x. URL: https://academic.oup.com/gji/article/181/3/1687/606203.

Dahlen, FA, and J Tromp (1998). *Theoretical global seismology*. Princeton university press.

Danaher, C, B Hollander, et al. (2007). *Advanced LIGO single stage HAM vibration isolation table*. Tech. rep. LIGO Laboratory. URL: https://dcc.ligo.org/LIGO-G070156/public.

Danilishin, Stefan L. and Farid Ya. Khalili (2012). "Quantum Measurement Theory in Gravitational-Wave Detectors". In: *Living Reviews in Relativity* 15.5. DOI: 10.12942/lrr-2012-5. URL: http://www.livingreviews.org/lrr-2012-5.

DeRosa, Ryan et al. (2012). "Global feed-forward vibration isolation in a km scale interferometer". In: *Classical and Quantum Gravity* 29.21, p. 215008. DOI: 10.

1088/0264-9381/29/21/215008. URL: https://doi.org/10.1088/0264-9381/29/21/215008.

Deville, Michel, P. Fischer, and E.H. Mund (2003). "High-Order Methods for Incompressible Fluid Flow". In: *Applied Mechanics Reviews* 56, p. 528. DOI: 10.1115/1.1566402. URL: https://asmedigitalcollection.asme.org/appliedmechanicsreviews/article/56/3/B43/446365/High-Order-Methods-for-Incompressible-Fluid-Flow.

Di Giovanni, Matteo (2021). *Summary of long term seismic characterization activities at Sos Enattos*. Presentation for workshop on ET site studies and characterization.

Dooley, Katherine et al. (2013). "Angular control of optical cavities in a radiation-pressure-dominated regime: the Enhanced LIGO case". In: *Journal of the Optical Society of America A* 30, pp. 2618–26. DOI: 10.1364/JOSAA.30.002618. URL: https://opg.optica.org/josaa/abstract.cfm?uri=josaa-30-12-2618.

Dooley, Laird Katherine (2011). "Design and performance of high laser power interferometers for gravitational-wave detection". PhD dissertation. University of Florida.

Driggers, J. C. et al. (2019). "Improving astrophysical parameter estimation via offline noise subtraction for Advanced LIGO". In: *Phys. Rev. D* 99 (4), p. 042001. DOI: 10.1103/PhysRevD.99.042001. URL: https://link.aps.org/doi/10.1103/PhysRevD.99.042001.

Driggers, Jenne (2006). *Optomechanical Alignment Instability in LIGO Mode Cleaners. LIGO document T060240-00-R*. Tech. rep. LIGO Laboratory. URL: https://dcc.ligo.org/LIGO-T060240/public.

— (2013). *Noise Cancellation for Gravitational Wave Detectors*. LIGO Seminar, Caltech, Pasadena, USA.

Driggers, Jennifer C., Jan Harms, and Rana X. Adhikari (2012). "Subtraction of Newtonian noise using optimized sensor arrays". In: *Physiscal Review D* 86 (10), p. 102001. DOI: 10.1103/PhysRevD.86.102001. URL: http://link.aps.org/doi/10.1103/PhysRevD.86.102001.

Driggers, Jennifer C. et al. (2012). "Active noise cancellation in a suspended interferometer". In: *Review of Scientific Instruments* 83.2, pp. 024501–024501–6. ISSN: 0034-6748. DOI: 10.1063/1.3675891. URL: https://aip.scitation.org/doi/10.1063/1.3675891.

Edwards, T. et al. (2000). *LISA: Study of the Laser Interferometer Space Antenna: Final Technical Report (FTR), Dornier Satellitensysteme GmbH*. Tech. rep. DSS Report No. LI-RP-DS-009.

Einstein, Albert (2014). *The Meaning of Relativity: Including the Relativistic Theory of the Non-Symmetric Field - Fifth Edition*. Princeton University Press. ISBN: 9780691080079. DOI: 10.2307/j.ctv3hh4zg. URL: https://www.jstor.org/stable/j.ctv3hh4zg.

Enomoto, Yutaro (2019). "Interferometer Locking Scheme for Advanced Gravitational-Wave Detectors and Beyond". PhD dissertation. University of Tokyo.

Epsilon-Greedy Q-learning. Available online: https://www.baeldung.com/cs/epsilon-greedy-q-learning. Accessed: 07-September-2022.

Estevez, Dimitri (2020). "Upgrade of Advanced Virgo photon calibrators and first intercalibration of Virgo and LIGO detectors for the observing run O3". PhD dissertation. Université Savoie Mont Blanc.

ET Science Team (2011). "Einstein gravitational wave Telescope conceptual design study". In: *available from European Gravitational Observatory, document number ET-0106C-10*.

Evans, Matthew et al. (2021). *A Horizon Study for Cosmic Explorer: Science, Observatories, and Community*. DOI: 10.48550/ARXIV.2109.09882. URL: https://arxiv.org/abs/2109.09882.

Fabry, Ch. and A. Perot (1901). "On a New Form of Interferometer". In: *The Astrophysical Journal* 13, p. 265. DOI: 10.1086/140817.

Fan, Yaohui et al. (2009). "Observation of optical torsional stiffness in a high optical power cavity". In: *Applied Physics Letters* 94.8, 081105, p. 081105. DOI: 10.1063/1.3088850. URL: https://aip.scitation.org/doi/10.1063/1.3088850.

Fan, Yuanzhong and Roel Snieder (2009). "Required source distribution for interferometry of waves and diffusive fields". In: *Geophysical Journal International* 179.2, pp. 1232–1244. DOI: 10.1111/j.1365-246X.2009.04358.x. URL: https://academic.oup.com/gji/article/179/2/1232/663424.

Feedforward Neural Networks and Multilayer Perceptrons. Available online: https://boostedml.com/2020/04/feedforward-neural-networks-and-multilayer-perceptrons.html. Accessed: 03-September-2022.

Fiorucci, Donatella et al. (2018). "Impact of infrasound atmospheric noise on gravity detectors used for astrophysical and geophysical applications". In: *Physical Review D* 97 (6), p. 062003. DOI: 10.1103/PhysRevD.97.062003. URL: https://link.aps.org/doi/10.1103/PhysRevD.97.062003.

Fricke, Tobin T. et al. (2012). "DC readout experiment in Enhanced LIGO". In: *Classical and Quantum Gravity* 29.6, 065005, p. 065005. DOI: 10.1088/0264-9381/29/6/065005. arXiv: 1110.2815 [physics.ins-det].

Fritschel, P et al. (2001). *Seismic Isolation Subsystem Design Requirements Document*. Tech. rep. Caltech-MIT-LIGO Laboratory. URL: https://dcc.ligo.org/LIGO-E990303/public.

Fritschel, Peter (2015). *Concept for a bounce and roll mode damper for the quad suspensions. T1500343-v1*. Tech. rep. LIGO-Caltech-MIT. URL: https://dcc.ligo.org/LIGO-T1500343.

Fritschel, Peter and the LIGO Scientific Collaboration (2015). "Advanced LIGO". In: *Classical and Quantum Gravity* 32.7, p. 074001. ISSN: 1361-6382. DOI: 10.1088/0264-9381/32/7/074001. URL: http://dx.doi.org/10.1088/0264-9381/32/7/074001.

Fritschel, Peter et al. (1998). "Alignment of an Interferometric Gravitational Wave Detector". In: *Applied optics* 37.28, pp. 6734–47. DOI: 10.1364/AO.37.006734. URL: https://opg.optica.org/ao/abstract.cfm?uri=ao-37-28-6734.

Geuzaine, Christophe and Jean-François Remacle (2009). "Gmsh: A three-dimensional finite element mesh generator with built-in pre-and post-processing facilities". In: *International Journal for Numerical Methods in Engineering* 79 (11), 1309–1331. DOI: https://doi.org/10.1002/nme.2579. URL: https://onlinelibrary.wiley.com/doi/10.1002/nme.2579.

Giaime, J. A. et al. (2003). "Feedforward reduction of the microseism disturbance in a long-base-line interferometric gravitational-wave detector". In: *Review of Scientific Instruments* 74.1, pp. 218–224. DOI: http://dx.doi.org/10.1063/1.1524717. URL: http://scitation.aip.org/content/aip/journal/rsi/74/1/10.1063/1.1524717.

Giaime, Joseph et al. (1996). "A passive vibration isolation stack for LIGO: Design, modeling, and testing". In: *Review of Scientific Instruments* 67, pp. 208 –214. DOI: 10.1063/1.1146573.

Giaime, Jospeh Anthony (1995). "Studies of Laser Interferometer Design and a Vibration Isolation System for Interferometric Gravitational Wave Detectors". PhD dissertation. Massachusetts Institute of Technology.

Gilbert, Freeman and Leon Knopoff (1960). "Seismic scattering from topographic irregularities". In: *Journal of Geophysical Research* 65.10, pp. 3437–3444. ISSN: 2156-2202. DOI: 10.1029/JZ065i010p03437. URL: http://dx.doi.org/10.1029/JZ065i010p03437.

Giunchi, Carlo et al. (2020). *Seismic noise characterization of the Sos Enattos Mine (Sardinia), a candidate site for the next generation of terrestrial gravitational waves detectors*. EGU General Assembly 2020, Online, EGU2020-9692. DOI: https://doi.org/10.5194/egusphere-egu2020-9692.

Grimm, Stefan and Jan Harms (2020). "Multiband gravitational-wave parameter estimation: A study of future detectors". In: *Physical Review D* 102.2 (2), p. 022007. DOI: 10.1103/PhysRevD.102.022007. URL: https://link.aps.org/doi/10.1103/PhysRevD.102.022007.

Gropp, W., E. Lusk, and A. Skjellum (1994). *Using MPI, portable parallel programming with the Message-Passing Interface*. Cambridge, USA: MIT Press. ISBN: 978-0-262-57104-3. DOI: 10.7551/mitpress/7056.001.0001. URL: https://direct.mit.edu/books/book/3812/Using-MPIPortable-Parallel-Programming-with-the.

Hanasoge, S. et al. (2012). "Non-linear iterative inversions for the distribution of noise sources". In: *AGU Fall Meeting Abstracts*. Vol. 2012, S53C–2513.

Harada, Tomohiro, B. J. Carr, and Takahisa Igata (2018). "Complete conformal classification of the Friedmann-Lemaître-Robertson-Walker solutions with a linear equation of state". In: *Classical and Quantum Gravity* 35.10, 105011, p. 105011. DOI: 10.1088/1361-6382/aab99f. arXiv: 1801.01966 [gr-qc].

Hardham, Corwin (2005). *Quiet hydraulic actuators for LIGO*. Stanford University.

Harms, J et al. (2010). "Characterization of the seismic environment at the Sanford Underground Laboratory, South Dakota". In: *Classical and Quantum Gravity* 27.22, p. 225011. DOI: 10.1088/0264-9381/27/22/225011. URL: https://doi.org/10.1088/0264-9381/27/22/225011.

Harms, J. et al. (2020). "Observation of a potential future sensitivity limitation from ground motion at LIGO Hanford". In: *Physical Review D* 101 (10), p. 102002. DOI: 10.1103/PhysRevD.101.102002. URL: https://link.aps.org/doi/10.1103/PhysRevD.101.102002.

Harms, Jan (2019). "Terrestrial gravity fluctuations". In: *Living Reviews in Relativity* 22.1, p. 6. ISSN: 1433-8351. DOI: 10.1007/s41114-019-0022-2. URL: https://doi.org/10.1007/s41114-019-0022-2.

Harms, Jan and Stefan Hild (2014). "Passive Newtonian noise suppression for gravitational-wave observatories based on shaping of the local topography". In: *Classical and Quantum Gravity* 31.18, p. 185011. DOI: https://doi.org/10.1088/0264-9381/31/18/185011. URL: http://stacks.iop.org/0264-9381/31/i=18/a=185011.

Harms, Jan and Conor M. Mow-Lowry (2018). "Suspension-thermal noise in spring-antispring systems for future gravitational-wave detectors". In: *Classical and*

Quantum Gravity 35.2, 025008, p. 025008. DOI: 10.1088/1361-6382/aa9e28. arXiv: 1707.07309 [gr-qc].

Harms, Jan et al. (2003). "Squeezed-input, optical-spring, signal-recycled gravitational-wave detectors". In: *Phys. Rev. D* 68 (4), p. 042001. DOI: 10.1103/PhysRevD.68.042001. URL: http://link.aps.org/doi/10.1103/PhysRevD.68.042001.

Harms, Jan et al. (2013). "Low-frequency terrestrial gravitational-wave detectors". In: *Phys. Rev. D* 88 (12), p. 122003. DOI: 10.1103/PhysRevD.88.122003. URL: http://link.aps.org/doi/10.1103/PhysRevD.88.122003.

Harms, Jan et al. (2021). "Lunar Gravitational-wave Antenna". In: *The Astrophysical Journal* 910.1, 1, p. 1. DOI: 10.3847/1538-4357/abe5a7. arXiv: 2010.13726 [gr-qc].

Harry, Gregory M and the LIGO Scientific Collaboration (2010). "Advanced LIGO: the next generation of gravitational wave detectors". In: *Classical and Quantum Gravity* 27.8, p. 084006. DOI: https://doi.org/10.1088/0264-9381/27/8/084006. URL: http://stacks.iop.org/0264-9381/27/i=8/a=084006.

Hawking, Stephen and Werner Israel (1989). *300 Years of Gravitation*. Cambridge University press. ISBN: 9780521379762.

Heefner, Jay (2000). *Generic Quad Photodiode Interface Module. LIGO Document D990692-x0.* Tech. rep. LIGO-Caltech. URL: https://dcc.ligo.org/LIGO-D990692.

— (2002). *Optical Lever PD Interface Board. LIGO Document D010033-x0.* Tech. rep. LIGO-Caltech. URL: https://dcc.ligo.org/LIGO-D010033.

— (2005). *WFS Whitening and Interface Board. LIGO Document D990196-x0.* Tech. rep. LIGO-Caltech. URL: https://dcc.ligo.org/LIGO-D990196.

Hild, S et al. (2009). "A xylophone configuration for a third-generation gravitational wave detector". In: *Classical and Quantum Gravity* 27.1, p. 015003. DOI: 10.1088/0264-9381/27/1/015003. URL: https://doi.org/10.1088\%2F0264-9381\%2F27\%2F1\%2F015003.

Hild, S et al. (2011). "Sensitivity studies for third-generation gravitational wave observatories". In: *Classical and Quantum Gravity* 28.9, p. 094013. DOI: https://doi.org/10.1088/0264-9381/28/9/094013. URL: http://stacks.iop.org/0264-9381/28/i=9/a=094013.

Hinton, Geoffrey and Terrence Sejnowski (1999). *Unsupervised Learning: Foundations of Neural Computation*. The MIT Press, p. 415. ISBN: 978-0262581684.

Hirose, Eiichi et al. (2010). "Angular instability due to radiation pressure in the LIGO gravitational-wave detector". In: *Applied optics* 49.18, pp. 3474–84. DOI: 10.1364/AO.49.003474. URL: https://opg.optica.org/ao/abstract.cfm?uri=ao-49-18-3474.

Hobson, M. P. et al. (2007). "General Relativity: An Introduction for Physicists". In: *Physics Today* 60.3, p. 62. DOI: 10.1063/1.2718760. URL: https://physicstoday.scitation.org/doi/10.1063/1.2718760.

Hoffman, Matt et al. (2020). "Acme: A Research Framework for Distributed Reinforcement Learning". In: *CoRR* abs/2006.00979. arXiv: 2006.00979. URL: https://arxiv.org/abs/2006.00979.

Hu, Junyan et al. (2020). "Voronoi-Based Multi-Robot Autonomous Exploration in Unknown Environments via Deep Reinforcement Learning". In: *IEEE Transactions on Vehicular Technology* 69.12, pp. 14413–14423. DOI: 10.1109/TVT.2020.3034800. URL: https://ieeexplore.ieee.org/document/9244647.

Hua, Wensheng et al. (2004). "Low-frequency active vibration isolation for advanced LIGO". In: *Gravitational Wave and Particle Astrophysics Detectors*. Ed. by

James Hough and Gary H. Sanders. Vol. 5500. Society of Photo-Optical Instrumentation Engineers (SPIE) Conference Series, pp. 194–205. DOI: 10.1117/12.552518. URL: https://www.spiedigitallibrary.org/conference-proceedings-of-spie/5500/1/Low-frequency-active-vibration-isolation-for-advanced-LIGO/10.1117/12.552518.short?SSO=1.

Huang, X, L Huang, and M Gong (2008). "Q-switched operation with Fox-Smith-Michelson laser cavity". In: *Laser Physics Letters* 5.3, pp. 189–192. DOI: 10.1002/lapl.200710110. URL: https://doi.org/10.1002/lapl.200710110.

Hudson, J. A. (1967). "Scattered Surface Waves from a Surface Obstacle". In: *Geophysical Journal International* 13.4, pp. 441–458. DOI: 10.1111/j.1365-246X.1967.tb03143.x. eprint: http://gji.oxfordjournals.org/content/13/4/441.full.pdf+html. URL: http://gji.oxfordjournals.org/content/13/4/441.abstract.

Hudson, J. A. et al. (1973). "The scattering of longitudinal elastic waves at a rough free surface". In: *Journal of Physics D Applied Physics* 6.18, pp. 2174–2186. DOI: 10.1088/0022-3727/6/18/303. URL: https://iopscience.iop.org/article/10.1088/0022-3727/6/18/303.

Hudson, J.A. and L. Knopoff (1967). "Statistical properties of Rayleigh waves due to scattering by topography". In: *Bulletin of the Seismological Society of America* 57, pp. 83–90.

Hughes, Scott A. and Kip S. Thorne (1998). "Seismic gravity-gradient noise in interferometric gravitational-wave detectors". In: *Physical Review D* 58 (12), p. 122002. DOI: 10.1103/PhysRevD.58.122002. URL: http://link.aps.org/doi/10.1103/PhysRevD.58.122002.

Hulse, R. A. and J. H. Taylor (1975). "Discovery of a pulsar in a binary system". In: *The Astrophysical Journal Letters* 195, pp. L51–L53. DOI: 10.1086/181708.

Jani, Karan, Deirdre Shoemaker, and Curt Cutler (2019). "Detectability of intermediate-mass black holes in multiband gravitational wave astronomy". In: *Nature Astronomy* 4, pp. 1–6. ISSN: 2397-3366. DOI: 10.1038/s41550-019-0932-7. URL: https://doi.org/10.1038/s41550-019-0932-7.

Kaelbling, L Pack, Michael L Littman, and Andrew W Moore (1996). "Reinforcement Learning: A Survey". In: *Journal of Articial Intelligence Research* 4, pp. 237–285. DOI: https://doi.org/10.1613/jair.301. URL: https://www.jair.org/index.php/jair/article/view/10166.

Karypis, George and Vipin Kumar (1999). "Kumar, V.: A Fast and High Quality Multilevel Scheme for Partitioning Irregular Graphs. SIAM Journal on Scientific Computing". In: *Siam Journal on Scientific Computing* 20 (1), pp. 359–392. DOI: 10.1137/S1064827595287997. URL: https://epubs.siam.org/doi/10.1137/S1064827595287997.

Kasprzack, Marie (2018). *Seismic motion to Angular Control: Challenges and Prospects in Advanced LIGO*. Low-Frequency Workshop presentation, Birmingham, UK.

Kawamura, Seiji and Janeen Hazel (1997). *Small Optics Suspension (SOS) Final Design (Mechanical System). LIGO Document T970135-x0.* Tech. rep. LIGO-Caltech-MIT. URL: https://dcc.ligo.org/LIGO-T970135.

Kawazoe, Fumiko, R Schilling, and Harald Lück (2011). "Eigenmode changes in a misaligned triangular optical cavity". In: *Journal of Optics* 13.5, p. 055504. DOI: 10.1088/2040-8978/13/5/055504. URL: https://iopscience.iop.org/article/10.1088/2040-8978/13/5/055504.

Kerr, Roy P. (1963). "Gravitational Field of a Spinning Mass as an Example of Algebraically Special Metrics". In: *Phys. Rev. Lett.* 11 (5), pp. 237–238. DOI: 10.1103/PhysRevLett.11.237. URL: https://link.aps.org/doi/10.1103/PhysRevLett.11.237.

Key Concepts in RL. Available online: https://spinningup.openai.com/en/latest/spinningup/rl_intro.html. Accessed: 05-September-2022.

Kissel, Jeffrey S (2010). "Calibrating and Improving the Sensitivity of the LIGO Detectors". PhD dissertation. Louisiana State University.

Komatitsch, D. (2004). "Simulations of Ground Motion in the Los Angeles Basin Based upon the Spectral-Element Method". In: *The Bulletin of the Seismological Society of America* 94.1, pp. 187–206. DOI: 10.1785/0120030077. URL: https://pubs.geoscienceworld.org/ssa/bssa/article-abstract/94/1/187/103056/Simulations-of-Ground-Motion-in-the-Los-Angeles?redirectedFrom=fulltext.

Komatitsch, D et al. (2018). *SPECFEM 3D Cartesian v3.0 [software]*. Computational Infrastructure for Geodynamics.

Komatitsch, Dimitri, Jesús Labarta, and David Michéa (2008). "A simulation of seismic wave propagation at high resolution in the inner core of the Earth on 2166 processors of MareNostrum". In: *Lecture Notes in Computer Science* 5336, pp. 364–377. DOI: 10.1007/978-3-540-92859-1_33. URL: https://link.springer.com/chapter/10.1007/978-3-540-92859-1_33.

Komatitsch, Dimitri and Roland Martin (2007). "An unsplit convolutional perfectly matched layer improved at grazing incidence for the seismic wave equation". In: *Geophysics* 72.5, SM155. DOI: https://doi.org/10.1190/1.2757586. URL: https://library.seg.org/doi/10.1190/1.2757586.

Komatitsch, Dimitri and Jeroen Tromp (1999). "Introduction to the spectral element method for three-dimensional seismic wave propagation". In: *Geophysical Journal International* 139.3, pp. 806–822. ISSN: 1365-246X. DOI: 10.1046/j.1365-246x.1999.00967.x. URL: http://dx.doi.org/10.1046/j.1365-246x.1999.00967.x.

— (2002a). "Spectral-element simulations of global seismic wave propagation I. Validation". In: *Geophysical Journal International* 149.2, pp. 390–412. DOI: 10.1046/j.1365-246X.2002.01653.x. eprint: http://gji.oxfordjournals.org/content/149/2/390.full.pdf+html. URL: http://gji.oxfordjournals.org/content/149/2/390.abstract.

— (2002b). "Spectral-element simulations of global seismic wave propagation—II. Three-dimensional models, oceans, rotation and self-gravitation". In: *Geophysical Journal International* 150.1, pp. 303–318. DOI: 10.1046/j.1365-246X.2002.01716.x. eprint: https://onlinelibrary.wiley.com/doi/pdf/10.1046/j.1365-246X.2002.01716.x. URL: https://onlinelibrary.wiley.com/doi/abs/10.1046/j.1365-246X.2002.01716.x.

Komatitsch, Dimitri and Jean-Pierre Vilotte (1998). "The spectral element method: An efficient tool to simulate the seismic response of 2D and 3D geological structures". In: *Bulletin of the Seismological Society of America* 88.2, pp. 368–392. ISSN: 0037-1106. DOI: 10.1785/BSSA0880020368. eprint: https://pubs.geoscienceworld.org/ssa/bssa/article-pdf/88/2/368/5344788/bssa0880020368.pdf. URL: https://doi.org/10.1785/BSSA0880020368.

Komatitsch, Dimitri et al. (1999). "The spectral element method for elastic wave equations—application to 2-D and 3-D seismic problems". In: *International Journal for Numerical Methods in Engineering* 45.9, pp. 1139–1164. DOI: 10.1002/(SICI)1097-0207(19990730)45:9<1139::AID-NME617>3.0.CO;2-T. URL: https://onlinelibrary.wiley.com/doi/10.1002/(SICI)1097-0207(19990730)45:9%3C1139::AID-NME617%3E3.0.CO;2-T.

Komatitsch, Dimitri et al. (2003). "A 14.6 billion degrees of freedom, 5 teraflops, 2.5 terabyte earthquake simulation on the Earth Simulator". In: *Proceedings of the SC'03 ACM/IEEE conference on Supercomputing*. Gordon Bell Prize winner article. Phoenix, Arizona, USA: ACM, pp. 4–11. ISBN: 1-58113-695-1. DOI: 10.1145/1048935.1050155. URL: https://dl.acm.org/doi/10.1145/1048935.1050155.

Landau, Lev Davidovich and E. M. Lifshitz (1975). *The classical theory of fields*. Elsevier. ISBN: 9780750627689.

Lewis, Frank L., Draguna Vrabie, and Kyriakos G. Vamvoudakis (2012). "Reinforcement Learning and Feedback Control: Using Natural Decision Methods to Design Optimal Adaptive Controllers". In: *IEEE Control Systems Magazine* 32.6, pp. 76–105. DOI: 10.1109/MCS.2012.2214134. URL: https://ieeexplore.ieee.org/document/6315769.

LIGO Laboratory / LIGO Scientific Collaboration (2005). *ADVANCED LIGO, Pre-Stabilized Laser Design Requirements. LIGO-T050036-00-D*. Tech. rep. LIGO-Caltech-MIT. URL: https://dcc.ligo.org/public/0000/T050036/002/LIGO-T050036-00-D%20%28Pre-Stabilized%20Laser%20Design%20Requirements%29.pdf.

LIGO sources. Available online: https://www.ligo.caltech.edu/page/gw-sources. Accessed: 10-May-2022.

LIGO what. Available online: https://www.ligo.caltech.edu/page/what-are-gw. Accessed: 10-May-2022.

LIGO why. Available online: https://www.ligo.caltech.edu/page/why-detect-gw. Accessed: 10-May-2022.

Liu, Q. and J. Tromp (2006). "Finite-Frequency Kernels Based on Adjoint Methods". In: *The Bulletin of the Seismological Society of America* 96.6, pp. 2383–2397. DOI: 10.1785/0120060041. URL: https://pubs.geoscienceworld.org/ssa/bssa/article-abstract/96/6/2383/146674/Finite-Frequency-Kernels-Based-on-Adjoint-Methods?redirectedFrom=fulltext.

Liu, Qinya and Jeroen Tromp (2008). "Finite-frequency sensitivity kernels for global seismic wave propagation based upon adjoint methods". In: *Geophysical Journal International* 174.1, pp. 265–286. DOI: 10.1111/j.1365-246X.2008.03798.x. URL: https://academic.oup.com/gji/article/174/1/265/577094.

Lobkis, Oleg I. and Richard L. Weaver (2001). "On the emergence of the Green's function in the correlations of a diffuse field". In: *The Journal of the Acoustical Society of America* 110.6, pp. 3011–3017. DOI: 10.1121/1.1417528. URL: https://doi.org/10.1121/1.1417528.

Look Deeper. Available online: https://www.ligo.caltech.edu/page/look-deeper. Accessed: 10-May-2022.

Maday, Yvon and Anthony T. Patera (1989). "Spectral element methods for the incompressible Navier-Stokes equations". In: *IN: State-of-the-art surveys on computational mechanics (A90-47176 21-64). New York*, pp. 71–143.

Maggiore, Michele (2008). *Gravitational waves: Volume 1: Theory and experiments*. Vol. 1. Oxford university press. ISBN: 9780198570745. DOI: 10.1093/acprof:oso/9780198570745.001.0001. URL: https://academic.oup.com/book/41655.

Maggiore, Michele et al. (2020). "Science case for the Einstein telescope". In: *Journal of Cosmology and Astroparticle Physics* 2020.03, pp. 050–050. DOI: 10.1088/1475-7516/2020/03/050. URL: https://doi.org/10.1088\%2F1475-7516\%2F2020\%2F03\%2F050.

Mandic, Vuk et al. (2018). "A 3D Broadband Seismometer Array Experiment at the Homestake Mine". In: *Seismological Research Letters* 89.6, p. 2420. DOI: 10.1785/0220170228. eprint: /gsw/content_public/journal/srl/89/6/10.1785_0220170228/3/srl-2017228.1.pdf. URL: http://dx.doi.org/10.1785/0220170228.

Maradudin, Alexei and D.L Mills (1976). "Attenuation of Rayleigh surface waves by surface roughness". In: *Annals of Physics* 100, pp. 262–309. DOI: 10.1016/0003-4916(76)90063-4. URL: https://www.sciencedirect.com/science/article/abs/pii/0003491676900634?via%3Dihub.

Marrocchesi, Alessandra et al. (2015). *A prototype for a tilt-free seismometer. LIGO-T1500485–v1*. Tech. rep. LIGO-Caltech-MIT. URL: https://dcc.ligo.org/LIGO-T1500485/public.

Martin, Roland and Dimitri Komatitsch (2009). "An unsplit convolutional perfectly matched layer technique improved at grazing incidence for the viscoelastic wave equation". In: *Geophysical Journal International* 179.1, pp. 333–344. DOI: 10.1111/j.1365-246X.2009.04278.x. URL: https://onlinelibrary.wiley.com/doi/abs/10.1111/j.1365-246X.2009.04278.x.

Martin, Roland et al. (2010). "A High-Order Time and Space Formulation of the Unsplit Perfectly Matched Layer for the Seismic Wave Equation Using Auxiliary Differential Equations (ADE-PML)". In: *Computer Modelling in Engineering and Sciences - CMES* 56. DOI: 10.3970/cmes.2010.056.017. URL: https://www.techscience.com/CMES/v56n1/25463.

Martynov, Denis (2015). "Lock Acquisition and Sensitivity Analysis of Advanced LIGO Interferometers". PhD dissertation. California Institute of Technology.

Matichard, F. et al. (2014). "Advanced LIGO two-stage twelve-axis vibration isolation and positioning platform. Part 1: Design and production overview". In: *Precision Engineering* 40.0, pp. –. ISSN: 0141-6359. DOI: http://dx.doi.org/10.1016/j.precisioneng.2014.09.010. URL: http://www.sciencedirect.com/science/article/pii/S0141635914001561.

— (2015). "Advanced LIGO two-stage twelve-axis vibration isolation and positioning platform. Part 2: Experimental investigation and tests results". In: *Precision Engineering* 40, pp. 287 –297. ISSN: 0141-6359. DOI: http://dx.doi.org/10.1016/j.precisioneng.2014.11.010. URL: //www.sciencedirect.com/science/article/pii/S0141635914002098.

Matichard, Fabrice et al. (2010). "Prototyping, testing and performance of the two-stage seismic isolation system for advanced ligo gravitational wave detectors". In: *Proceedings - ASPE Spring Topical Meeting on Control of Precision Systems, ASPE 2010* 48. URL: https://www.scopus.com/record/display.uri?eid=2-s2.0-84884361583&origin=inward&txGid=bd124187c1e9a2fc9feadef734810be7.

Matichard, Fabrice et al. (2013). "Ligo vibration isolation and alignment platforms: An overview of systems, performance and features of interest for the field of precision positioning and manufacturing". In: *Proceedings - ASPE Spring Topical*

Meeting on Control of Precision Systems, ASPE 2013 55, pp. 94–99. URL: https://www.scopus.com/record/display.uri?eid=2-s2.0-84884361583&origin=inward&txGid=bd124187c1e9a2fc9feadef734810be7.

Mendel, JM and RW McLaren (1970). "8 reinforcement-learning control and pattern recognition systems". In: *Mathematics in science and engineering*. Vol. 66. Elsevier, pp. 287–318.

Michelson, A. A. and E. W. Morley (1887). "On the relative motion of the Earth and the luminiferous ether". In: *Am. J. Sci.* 34, p. 333.

Michéa, David and Dimitri Komatitsch (May 2010). "Accelerating a 3D finite-difference wave propagation code using GPU graphics cards". In: *Geophysical Journal International* 182, pp. 389–402. DOI: 10.1111/j.1365-246X.2010.04616.x. URL: https://academic.oup.com/gji/article/182/1/389/563062.

Misner, C. W., K. S. Thorne, and J. A. Wheeler (1973). *Gravitation*. Freeman. ISBN: 0716703343.

Mitchell, Tom (1997). *Machine Learning*. McGraw-Hill Science/Engineering/Math, p. 432. ISBN: 0070428077.

Mode Cleaner. Available online: https://wiki-40m.ligo.caltech.edu/Mode_Cleaner. Accessed: 27-July-2022.

Mohri, Mehryar, Afshin Rostamizadeh, and Ameet Talwalkar (2018). *Foundations of Machine Learning*. The MIT Press, p. 505. ISBN: 9780262039406.

Montagner, J.-P. et al. (2012). "Time-reversal method and cross-correlation techniques by normal mode theory: a three-point problem". In: *Geophysical Journal International* 191.2, pp. 637–652. ISSN: 0956-540X. DOI: 10.1111/j.1365-246X.2012.05619.x. URL: https://doi.org/10.1111/j.1365-246X.2012.05619.x.

Mooney, H. M. (1976). "The seismic wave system from a surface impact". In: *Geophysics* 41.2, pp. 243–265. DOI: 10.1190/1.1440614. eprint: http://geophysics.geoscienceworld.org/\\content/41/2/243.full.pdf+html. URL: http://geophysics.geoscienceworld.org/content\\/41/2/243.abstract.

Mueller, Chris (2014). *The Advanced LIGO Input Mode Cleaner*. Presentation for the Detector Characterization Group.

Naticchioni, L et al. (2014). "Microseismic studies of an underground site for a new interferometric gravitational wave detector". In: *Classical and Quantum Gravity* 31.10, p. 105016. DOI: https://doi.org/10.1088/0264-9381/31/10/105016. URL: http://stacks.iop.org/0264-9381/31/i=10/a=105016.

Ogilvy, J A (1987). "Wave scattering from rough surfaces". In: *Reports on Progress in Physics* 50.12, p. 1553. DOI: 10.1088/0034-4885/50/12/001. URL: http://stacks.iop.org/0034-4885/50/i$=$12/a$=$001.

Olsen, K. B., R. Madariaga, and R. J. Archuleta (1997). "Three-Dimensional Dynamic Simulation of the 1992 Landers Earthquake". In: *Science* 278, pp. 834–838. DOI: 10.1126/science.278.5339.834. URL: https://www.science.org/doi/10.1126/science.278.5339.834.

Orfanidis, Sophocles J (2007). *Optimum signal processing: an introduction*. Macmillan publishing company.

Otterlo, Martijn van and Marco Wiering (2012). "Reinforcement Learning and Markov Decision Processes". In: *Reinforcement Learning: State-of-the-Art*. Ed. by Marco Wiering and Martijn van Otterlo. Berlin, Heidelberg: Springer Berlin Heidelberg, pp. 3–42. ISBN: 978-3-642-27645-3. DOI: 10.1007/978-3-642-27645-3_1. URL: https://doi.org/10.1007/978-3-642-27645-3_1.

Otto, O. W. (1977). "Scattering of Rayleigh waves from topographic irregularities at oblique incidence". In: *Journal of Applied Physics* 48.12, pp. 5105–5110. DOI: 10.1063/1.323587. URL: https://aip.scitation.org/doi/10.1063/1.323587.

Pacheco, P. S. (1997). *Parallel programming with MPI*. San Francisco, USA: Morgan Kaufmann Press.

Paik, Ho Jung (2018). "SOGRO (Superconducting Omni-directional Gravitational Radiation Observatory)". In: European Physical Journal Web of Conferences 168, 01005, p. 01005. DOI: 10.1051/epjconf/201816801005. URL: https://www.epj-conferences.org/articles/epjconf/abs/2018/03/epjconf_icgaxiii-ik2018_01005/epjconf_icgaxiii-ik2018_01005.html.

Patera, A. T. (1984). "A Spectral Element Method for Fluid Dynamics: Laminar Flow in a Channel Expansion". In: *Journal of Computational Physics* 54.3, pp. 468–488. DOI: 10.1016/0021-9991(84)90128-1. URL: https://www.sciencedirect.com/science/article/pii/0021999184901281?via%3Dihub.

Pellegrini, François and Jean Roman (1996). "SCOTCH: A Software Package for Static Mapping by Dual Recursive Bipartitioning of Process and Architecture Graphs". In: vol. 1067, pp. 493–498. ISBN: 978-3-540-61142-4. DOI: 10.1007/3-540-61142-8_588. URL: https://link.springer.com/chapter/10.1007/3-540-61142-8_588.

Penalizing the Discount Factor in Reinforcement Learning. Available online: https://towardsdatascience.com/penalizing-the-discount-factor-in-reinforcement-learning-d672e3a38ffe. Accessed: 07-September-2022.

Peter, D. et al. (2007). "Surface wave tomography: global membrane waves and adjoint methods". In: *Geophysical Journal International* 171.3, pp. 1098–1117. DOI: 10.1111/j.1365-246X.2007.03554.x. URL: https://academic.oup.com/gji/article/171/3/1098/716936.

Peter, Daniel et al. (2011). "Forward and adjoint simulations of seismic wave propagation on fully unstructured hexahedral meshes". In: *Geophysical Journal International* 186.2, pp. 721–739. DOI: 10.1111/j.1365-246X.2011.05044.x. URL: https://academic.oup.com/gji/article/171/3/1098/716936.

Prince, Thomas et al. (2006). "LISA: Probing the Universe with Gravitational Waves". In: *LISA-LIST-RP-436* 1, pp. 1–117. eprint: https://sci.esa.int/documents/35005/36499/1567256267249-LISA_Science_Case.pdf. URL: https://sci.esa.int/web/lisa/-/41272-lisa-probing-the-universe-with-gravitational-waves.

Priolo, Enrico, José M. Carcione, and Géza Seriani (1994). "Numerical simulation of interface waves by high-order spectral modeling techniques". In: *Acoustical Society of America Journal* 95.2, pp. 681–693. DOI: 10.1121/1.408428. URL: https://asa.scitation.org/doi/10.1121/1.408428.

Punturo, M et al. (2010). "The Einstein Telescope: a third-generation gravitational wave observatory". In: *Classical and Quantum Gravity* 27.19, p. 194002. DOI: https://doi.org/10.1088/0264-9381/27/19/194002. URL: http://stacks.iop.org/0264-9381/27/i=19/a=194002.

Reitze, David et al. (2019). "Cosmic Explorer: The U.S. Contribution to Gravitational-Wave Astronomy beyond LIGO". In: *Bulletin of the American Astronomical Society*. Vol. 51. arXiv: 1907.04833 [astro-ph.IM].

Rey Vega, Leonardo and Hernan Rey (2013). "Wiener Filtering". English. In: *A Rapid Introduction to Adaptive Filtering*. SpringerBriefs in Electrical and Computer Engineering. Springer Berlin Heidelberg, pp. 7–17. ISBN: 978-3-642-30298-5. DOI: 10.1007/978-3-642-30299-2_2. URL: http://dx.doi.org/10.1007/978-3-642-30299-2_2.

Robertson, Norna and Calum Torrie (2016). *A Tale of Two Dampers: Bounce and Roll Mode Damping for the Quads*. Talk for the LVC meeting, G1600371-v3.

Robertson, Norna A. et al. (2004). "Seismic isolation and suspension systems for Advanced LIGO". In: *Gravitational Wave and Particle Astrophysics Detectors*. Ed. by James Hough and Gary H. Sanders. Vol. 5500. Society of Photo-Optical Instrumentation Engineers (SPIE) Conference Series, pp. 81–91. DOI: 10.1117/12.552469. URL: https://www.spiedigitallibrary.org/conference-proceedings-of-spie/5500/1/Seismic-isolation-and-suspension-systems-for-Advanced-LIGO/10.1117/12.552469.short?SSO=1.

Rothman, Tony (2018). "The Secret History of Gravitational Waves". In: *American Scientist* 106.2, p. 96. DOI: 10.1511/2018.106.2.96. URL: https://doi.org/10.1511/2018.106.2.96.

Sanchez-Sesma, F.J. and M. Campillo (1991). "Diffraction of P, SV and Rayleigh waves by topographic features: a boundary integral formulation". In: *Bulletin - Seismological Society of America* 81.6, pp. 2234–2253.

Sathyaprakash, B et al. (2012). "Scientific objectives of Einstein Telescope". In: *Classical and Quantum Gravity* 29.12, p. 124013. DOI: 10.1088/0264-9381/30/7/079501. URL: http://stacks.iop.org/0264-9381/29/i=12/a=124013.

Saulson, Peter R. (1990). "Thermal noise in mechanical experiments". In: *Phys. Rev. D* 42 (8), pp. 2437–2445. DOI: 10.1103/PhysRevD.42.2437. URL: http://link.aps.org/doi/10.1103/PhysRevD.42.2437.

Saulson, Peter R. (1994). *Fundamentals of Interferometric Gravitational Wave Detectors*. World Scientific Publishing Co Pte Ltd. ISBN: 9789813146204. DOI: 10.1142/2410. URL: https://www.worldscientific.com/worldscibooks/10.1142/2410#t=aboutBook.

Sazli, Murat (2006). "A brief review of feed-forward neural networks". In: *Communications, Faculty Of Science, University of Ankara* 50, pp. 11–17. DOI: 10.1501/0003168. URL: https://www.semanticscholar.org/paper/A-brief-review-of-feed-forward-neural-networks-Sazli/5a45fb35ffad65c904da2edeef443dcf11219de7.

Schnier, D. et al. (1997). "Power recycling in the Garching 30 m prototype interferometer for gravitational-wave detection". In: *Physics Letters A* 225.4, pp. 210–216. DOI: 10.1016/S0375-9601(96)00893-6. URL: https://www.sciencedirect.com/science/article/abs/pii/S0375960196008936?via%3Dihub.

Schwartz, E. et al. (2020). "Improving the robustness of the advanced LIGO detectors to earthquakes". In: *Classical and Quantum Gravity* 37.23, 235007, p. 235007. DOI: 10.1088/1361-6382/abbc8c. URL: https://iopscience.iop.org/article/10.1088/1361-6382/abbc8c.

Schwarzschild, K. (1999). "On the gravitational field of a mass point according to Einstein's theory". In: DOI: 10.48550/ARXIV.PHYSICS/9905030. URL: https://arxiv.org/abs/physics/9905030.

Seriani, Géza and Enrico Priolo (2012). "Spectral Element Method for acoustic wave simulation in heterogeneous media". In: *Finite Elements in Analysis and Design* 16, pp. 337–348. DOI: 10.1016/0168-874X(94)90076-0. URL: https:

//www.sciencedirect.com/science/article/abs/pii/0168874X94900760?via%3Dihub.

Seymour, Brian C. et al. (2017). *Characterization of Nonlinear Angular Noise Coupling into Differential Arm Length of the LIGO Livingston Detector. LIGO-T1700343-v1*. Tech. rep. LIGO. URL: https://dcc.ligo.org/LIGO-T1700343/public.

Shapiro, Brett et al. (2015). "Noise and control decoupling of Advanced LIGO suspensions". In: *Classical and Quantum Gravity* 32.1, p. 015004. DOI: 10.1088/0264-9381/32/1/015004. URL: https://iopscience.iop.org/article/10.1088/0264-9381/32/1/015004.

Sidles, John A. and Daniel Sigg (2006). "Optical torques in suspended Fabry-Pérot interferometers". In: *Physics Letters A* 354.3, pp. 167 –172. ISSN: 0375-9601. DOI: http://dx.doi.org/10.1016/j.physleta.2006.01.051. URL: http://www.sciencedirect.com/science/article/pii/S0375960106001381.

Sinclair, L. C. et al. (2014). "Optical phase noise from atmospheric fluctuations and its impact on optical time-frequency transfer". In: *Phys. Rev. A* 89 (2), p. 023805. DOI: 10.1103/PhysRevA.89.023805. URL: https://link.aps.org/doi/10.1103/PhysRevA.89.023805.

Smith, J.O. (2007). *Introduction to Digital Filters: With Audio Applications*. Music signal processing series. W3K. ISBN: 9780974560717. eprint: https://books.google.it/books?id=pC1iCQUAsHEC&printsec=frontcover&source=gbs_ge_summary_r&cad=0#v=onepage&q&f=false. URL: https://books.google.it/books?id=pC1iCQUAsHEC.

Snieder, Roel (1986). "The influence of topography on the propagation and scattering of surface waves". In: *Physics of the Earth and Planetary Interiors* 44.3, pp. 226–241. DOI: 10.1016/0031-9201(86)90072-5. URL: https://www.sciencedirect.com/science/article/abs/pii/0031920186900725?via%3Dihub.

Solimeno, S. et al. (1991). "Fabry-Pérot resonators with oscillating mirrors". In: *Physical Review A* 43 (11), pp. 6227–6240. DOI: 10.1103/PhysRevA.43.6227. URL: https://link.aps.org/doi/10.1103/PhysRevA.43.6227.

Soni, S et al. (2021). "Reducing scattered light in LIGO's third observing run". In: *Classical and Quantum Gravity* 38.2, p. 025016. DOI: 10.1088/1361-6382/abc906. URL: https://doi.org/10.1088/1361-6382/abc906.

Sonnet Documentation. Available online: https://sonnet.readthedocs.io/en/latest/. Accessed: 03-September-2022.

Souradeep, Tarun (2016). "LIGO-India". In: *Resonance* 21 (3), pp. 225 –231. DOI: 10.1007/s12045-016-0316-6. URL: https://doi.org/10.1007/s12045-016-0316-6.

Sutton, Richard and Andrew Barto (2015). *Reinforcement Learning: An Introduction*. The MIT Press, p. 548. ISBN: 78-0-262-19398-6.

Tanioka, Satoshi et al. (2020). *Angular response of a triangular optical cavity analyzed by a linear approximation method*. DOI: 10.48550/ARXIV.2002.02703. URL: https://arxiv.org/abs/2002.02703.

Taylor, J H and J M Weisberg (1982). "New test of general relativity: Gravitational radiation and the binary pulsar PSR 1913+16". In: *The Astrophysical Journal* 253, pp. 908–920. DOI: 10.1086/159690. URL: https://www.osti.gov/biblio/5130227.

Tromp, Jeroen, Dimitri Komatitsch, and Qinya Liu (2008). "Spectral-element and adjoint methods in seismology". In: *Communications in Computational Physics*

3.1, pp. 1–32. eprint: https://www.global-sci.org/v1/cicp/openaccess/v3_1.pdf.

Tromp, Jeroen, Carl Tape, and Qinya Liu (2005). "Seismic tomography, adjoint methods, time reversal and banana-doughnut kernels". In: *Geophysical Journal International* 160.1, pp. 195–216. DOI: 10.1111/j.1365-246X.2004.02453.x. URL: https://academic.oup.com/gji/article/160/1/195/712020.

Tromp, Jeroen et al. (2010). "Noise cross-correlation sensitivity kernels". In: *Geophysical Journal International* 183.2, pp. 791–819. DOI: 10.1111/j.1365-246X.2010.04721.x. URL: https://academic.oup.com/gji/article/183/2/791/656248.

Tsai, Victor C. and Morgan P. Moschetti (2010). "An explicit relationship between time-domain noise correlation and spatial autocorrelation (SPAC) results". In: *Geophysical Journal International* 182.1, pp. 454–460. DOI: 10.1111/j.1365-246X.2010.04633.x. URL: https://academic.oup.com/gji/article/182/1/454/563758.

Tsuboi, Seiji et al. (2003). "Broadband modeling of the 2002 Denali fault earthquake on the Earth Simulator". In: *Physics of the Earth and Planetary Interiors* 139.3-4, pp. 305–313. DOI: 10.1016/j.pepi.2003.09.012. URL: https://www.sciencedirect.com/science/article/abs/pii/S0031920103002115?via%3Dihub.

Vibration Isolation. Available online: https://www.ligo.caltech.edu/page/vibration-isolation. Accessed: 24-March-2021.

Virieux, Jean (1986). "P-SV wave propagation in heterogeneous media: Velocity-stress finite-difference method". In: *Geophysics* 51.4, pp. 889–901. DOI: 10.1190/1.1442147. URL: https://library.seg.org/doi/10.1190/1.1442147.

Wapenaar, Kees, Evert Slob, and Roel Snieder (2006). "Unified Green's Function Retrieval by Cross Correlation". In: *Physical Review Letters* 97.23, 234301, p. 234301. DOI: 10.1103/PhysRevLett.97.234301. URL: https://journals.aps.org/prl/abstract/10.1103/PhysRevLett.97.234301.

Ward, R et al. (2008). "dc readout experiment at the Caltech 40m prototype interferometer". In: *Classical and Quantum Gravity* 25. DOI: 10.1088/0264-9381/25/11/114030. URL: https://iopscience.iop.org/article/10.1088/0264-9381/25/11/114030.

Weber, J. (1960). "Detection and Generation of Gravitational Waves". In: *Physical Review* 117.1, pp. 306–313. DOI: 10.1103/PhysRev.117.306. URL: https://journals.aps.org/pr/abstract/10.1103/PhysRev.117.306.

Weinberg, Steven (1972). *Gravitation and cosmology: Principle and applications of general theory of relativity*. John Wiley and Sons. ISBN: 0471925675.

Wen, S. et al. (2014). "Hydraulic external pre-isolator system for LIGO". In: *Classical and Quantum Gravity* 31.23, 235001, p. 235001. DOI: 10.1088/0264-9381/31/23/235001. arXiv: 1309.5685 [gr-qc].

Williamson, Darrell (1999). *Discrete-time Signal Processing*. Springer. ISBN: 978-1-85233-161-0. DOI: 10.1007/978-1-4471-0541-1. URL: https://link.springer.com/book/10.1007/978-1-4471-0541-1.

Woodard, M. F. (1997). "Implications of Localized, Acoustic Absorption for Heliotomographic Analysis of Sunspots". In: *The Astrophysical Journal* 485.2, pp. 890–894. DOI: 10.1086/304468. URL: https://iopscience.iop.org/article/10.1086/304468.

Woods, R. D. (1968). "Screening of Surface Waves in Soils". In: *Journal of the Soil Mechanics and Foundations Division: proceedings of the American Society of Civil Engineers* 94.4, pp. 951–979.

Xie, Zhinan et al. (2014). "Improved forward wave propagation and adjoint-based sensitivity kernel calculations using a numerically stable finite-element PML". In: *Geophysical Journal International* 198.3, pp. 1714–1747. DOI: 10.1093/gji/ggu219. URL: https://academic.oup.com/gji/article/198/3/1714/588126.

Yang, Fan et al. (2021). *Launchpad: A Programming Model for Distributed Machine Learning Research*. DOI: 10.48550/ARXIV.2106.04516. URL: https://arxiv.org/abs/2106.04516.

Yu, Hang (2019). "Astrophysical signatures of neutron stars in compact binaries and experimental improvements on gravitational-wave detectors". PhD dissertation. Massachusetts Institute of Technology.

Yu, Hang et al. (2017). "Prospects for Detecting Gravitational Waves at 5 Hz with Ground-Based Detectors". In: *Physical Review Letters* 120.14, 141102, p. 141102. DOI: 10.1103/PhysRevLett.120.141102. URL: https://journals.aps.org/prl/abstract/10.1103/PhysRevLett.120.141102.

Yu, Hang et al. (2018). *Low-freq Workshop at U Birmingham*. Low-Frequency Workshop presentation, Birmingham, UK.